Geofluids

Brines Linked to Ore Deposits and Oil/Gas Accumulation

Lead Guest Editor: Rongxi Li
Guest Editors: Yonggang Feng and Guo Xiang Chi

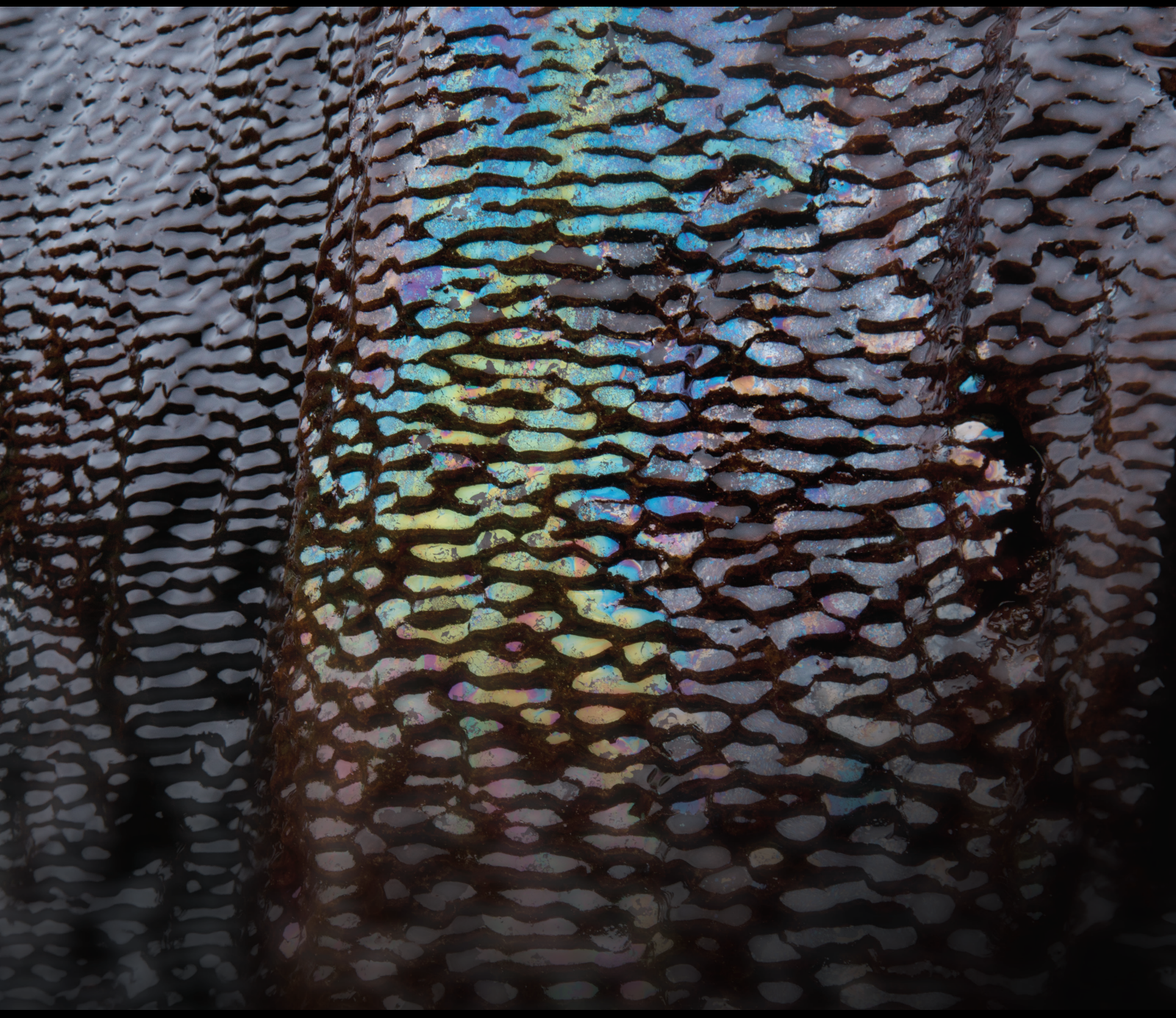

Brines Linked to Ore Deposits and Oil/Gas Accumulation

Geofluids

Brines Linked to Ore Deposits and Oil/ Gas Accumulation

Lead Guest Editor: Rongxi Li
Guest Editors: Yonggang Feng and Guo Xiang Chi

Contents

Hindawi
Geofluids
Volume 2022, Article ID 6255886, 13 pages
https://doi.org/10.1155/2022/6255886

Research Article

Reconstruction of Polyhalite Ore-Formed Temperature from Late Middle Pleistocene Brine Temperature Research in Kunteyi Playa, Western China

Jun Li,[1,2,3] Wenxia Li,[1,2,3] Weiliang Miao,[1,2] Qiliang Tang,[1,2] Yongshou Li,[1,2] Xiaolong Yuan,[1,2] Qingyu Hai,[1,2] Yongsheng Du,[1,2] and Xiying Zhang[1,2]

[1]*Key Laboratory of Comprehensive and Highly Efficient Utilization of Salt Lake Resources, Qinghai Institute of Salt Lakes, Chinese Academy of Sciences, Xining, Qinghai 810008, China*
[2]*Qinghai Provincial Key Laboratory of Geology and Environment of Salt Lakes Xining, Qinghai 810008, China*
[3]*University of Chinese Academy of Sciences, Beijing 100049, China*

Correspondence should be addressed to Xiying Zhang; xyzhchina@isl.ac.cn

Received 27 May 2021; Revised 18 November 2021; Accepted 23 November 2021; Published 13 January 2022

Academic Editor: Jinze Xu

Kunteyi Salt Lake (KSL), located in the northwest of the Qaidam Basin (QB), is rich in polyhalite resources. However, there is no relevant research on the ore-formed temperature of polyhalite in nature, such as KSL. The homogenization temperature (T_h) of salt mineral inclusions can directly reveal the form temperature of minerals. In view of the poor diagenesis of polyhalite in KSL, almost no polyhalite crystals are formed. Therefore, the ore-formed temperature of polyhalite in KSL is revealed by using the T_h of fluid inclusions in halite associated with polyhalite as a substitute index. A total of 472 T_h data from 34 halite samples and 34 maximum homogenization temperature (T_{hMAX}) data ranged from 17.1°C to 35.5°C, among which 24 data were concentrated at 17-23°C and the average value is 22.1°C. Brine temperature of other salt lakes in QB and paleoclimate characteristics of the study area were combined. It suggests that the temperature conditions of polyhalite mineralization in the study area are generally low. However, under the overall low-temperature background, polyhalite seems to be easily enriched at relatively high temperature; for example, the content of polyhalite is generally high in the first relatively dry and hot salt-forming period, and the brine temperature at the peak stage of polyhalite at 45 m is relatively high, which indicates that the high temperature conditions promote the formation of polyhalite in KSL. As far as the overall relationship between temperature and polyhalite is concerned, polyhalite is deposited at both low temperature and relatively high temperature, which verifies the previous understanding that polyhalite is a mineral with wide temperature phase, and also shows that temperature has a limited effect on polyhalite formation under natural conditions. In addition, combined with the chemical composition of halite fluid inclusions, it is found that the concentration of Mg^{2+} in nature has an influence on the temperature measurement process. According to the previous experimental research, speculate that the actual temperature of ancient brine and ore-formed temperature of polyhalite in KSL are lower than the measured T_h. The confirmation of the influence of Mg^{2+} on temperature measurement is convenient for more accurate reconstruction of the metallogenic temperature of evaporite such as polyhalite. The research on the ore-formed temperature of KSL polyhalite enriches and perfects the polyhalite mineralization theory and provides theoretical basis for the basic and applied research of polyhalite.

1. Introduction

As a hydrated K, Ca, and Mg sulfate mineral $K_2Ca_2Mg(SO_4)_4{\cdot}2H_2O$, polyhalite is widely distributed in evaporite deposits, although the phase diagram study shows that the metallogenic conditions are harsh. It is a new trend in the development of international potash fertilizer industry to make potassium sulfate (SOP) from polyhalite [1, 2]. Therefore, the

research on polyhalite has never been interrupted. With the bottleneck of searching for potassium salt deposits in China and the depletion of potassium salt resources, polyhalite as a potassium-bearing mineral will become an important continuous potassium resource. Some typical foreign polyhalite deposits, such as Permian in England, Drawell Basin in America, and Great Kavir Basin in Iran and Spain, are mainly marine sediments and mostly metasomatic secondary minerals [3–5]. The Triassic polyhalite in the Sichuan Basin is the most typical in China. Studies have shown that it was formed by metasomatism of anhydrite from foreign K^+- and Mg^{2+}-rich solutions, and some scholars believe that it was formed by metasomatism of gypsum by seawater concentration [6–8]. Polyhalite also have been discovered in the Tertiary salt-bearing series in Lop Nur, Jianghan Basin, and Bohai Bay [9–11]. The polyhalite in the Qaidam Basin (QB) is mainly distributed in KSL in the northwest of the basin, and other salt lakes are also distributed but not large-scale. Kunteyi polyhalite was located in the prospecting stage in the early stage and has been further studied in recent years. The study shows that the polyhalite produced in the halite layer is widely distributed and low in content, while the clastic layer is narrow in distribution and high in content, and it is considered that the polyhalite in the halite layer is a primary mineral [12, 13]. Metallogenic simulation study proves that its formation is related to Tertiary oilfield brine upwelling along the fault, and the higher the temperature, the more favorable it is for mineralization [14]. In recent years, the laboratory experimental study of polyhalite has increased, the effect of high-temperature calcination on the mineral structure of polyhalite was observed [15, 16], and thermodynamics and metallogenic facies area of natural polyhalite were studied [17–19]. It can be seen that the research on polyhalite has been comprehensive, but there are few reports on the ore-formed temperature of polyhalite in nature.

The polyhalite produced in the halite layer of KSL is a primary mineral, which provides the possibility to study its ore-formed temperature by using the T_h of the fluid inclusions in the primary halite associated with polyhalite. Fluid inclusions in halite can provide direct, quantitative paleotemperature data. The "cooling nucleation" method of pure liquid-phase primary halite fluid inclusion [20] can accurately test the brine temperature during the crystallization of halite. The T_h of the primary single liquid-phase halite fluid inclusions distributed in cumulate and chevron halite crystal growth bands can reflect the temperature and variation characteristics of ancient brine during salt formation [21–26]. The T_h recorded by halite fluid inclusions in shallow water is similar to atmospheric temperature, which is widely used in paleoclimate research [27–32]. The reliability of the T_h index of halite fluid inclusions and the maturity of its testing technology are further explained. In this work, the temperature of KSL brine is reconstructed by studying the T_h of the primary halite fluid inclusions in the core halite salt layer; finally, the ore-formed temperature of polyhalite is revealed directly.

The ore-formed temperature of salt minerals is mostly studied directly by using fluid inclusions in the minerals. Because all the salt lakes in QB are inland Quaternary modern salt lakes, the polyhalite minerals deposited in them have poor diagenesis, are mostly soil-like cements, and have no inclusions developed, so it is impossible to directly use their inclusions to study the ore-formed temperature. Therefore, the study of ancient brine temperature indirectly indicates the characteristics of polyhalite ore-formed temperature, which is rarely reported in the study of evaporite mineralization temperature. It is feasible in theory, an exploratory study, and a certain initiative. The initiation and implementation of this research method will greatly facilitate the revelation of the significance of temperature to potassium salt minerals such as carnallite and sylvinite and other evaporated salt minerals with unsatisfactory inclusions. Although this research is groundbreaking and distinctive, at the same time, there are some shortcomings. A total of 34 samples were collected in the evaporation salt layer of about 51 m, and 472 temperature data were measured. This data is small, and the data closer to the actual situation cannot be obtained from the statistical significance to the maximum extent.

2. Geological Setting

KSL is a secondary faulted basin in the northwest of QB, which consists of Kunteyi Dry Salt Lake, Kunteyi Lake, and Potassium Lake (Figure 1). It is a chloride-type comprehensive deposit with dry salt lake and brine lake coexisting, mainly composed of halite and potassium salt [33]. At the end of the early Pleistocene, with the separation of Qaidam ancient lakes, the Kunteyi Basin became a secondary lake basin in QB and gradually evolved into a dry salt lake [34]. This area is located in the tectonic units—Kunlun fold system and Qilian fold system, which was formed under the strong influence of Altun Mountain strike-slip fault, showing well-developed fault blocks and strong folds, with many faults developed and having an important impact on the mineralization of salt lakes [35, 36]. There is no surface recharge water body in the study area. The ice and snow melt water in the northern Altun Mountain replenishes the groundwater in front of the mountain through bedrock fissures and surface flood infiltration. The deep water discharge as seeps along the fault and the confined water at the front of the alluvial fan also account for a certain proportion of recharge [37]. In addition, the large (small) Haerten River supplies the salt lake by underground undercurrent after entering Sugan Lake, which is an important river supply source in the lake area [1]. Borehole ZK3608 is located near the mineral deposition center of Kunteyi Playa. The average sedimentation rate of Kunteyi Salt Lake since 730 ka is 4 m/10^4a [38]. According to this deposition rate, the age of 75.25 m of the ZK3608 final hole is about 188 ka. ZK3208 is adjacent to ZK3608 and has the same stratigraphic sequence. Based on the chronological data of ZK3208 [39], it is calculated that the final pore age of ZK3608 is about 180 ka, which is basically consistent with the age obtained by the sedimentation rate, so it is determined to be the late Middle Pleistocene.

The study of the salt-forming period in western QB shows that the cold and dry climate since the middle and late Pleistocene has led to the concentration of lake water until it dried up, which is an important salt-forming period [41]. Through the study of minerals and elements in the core

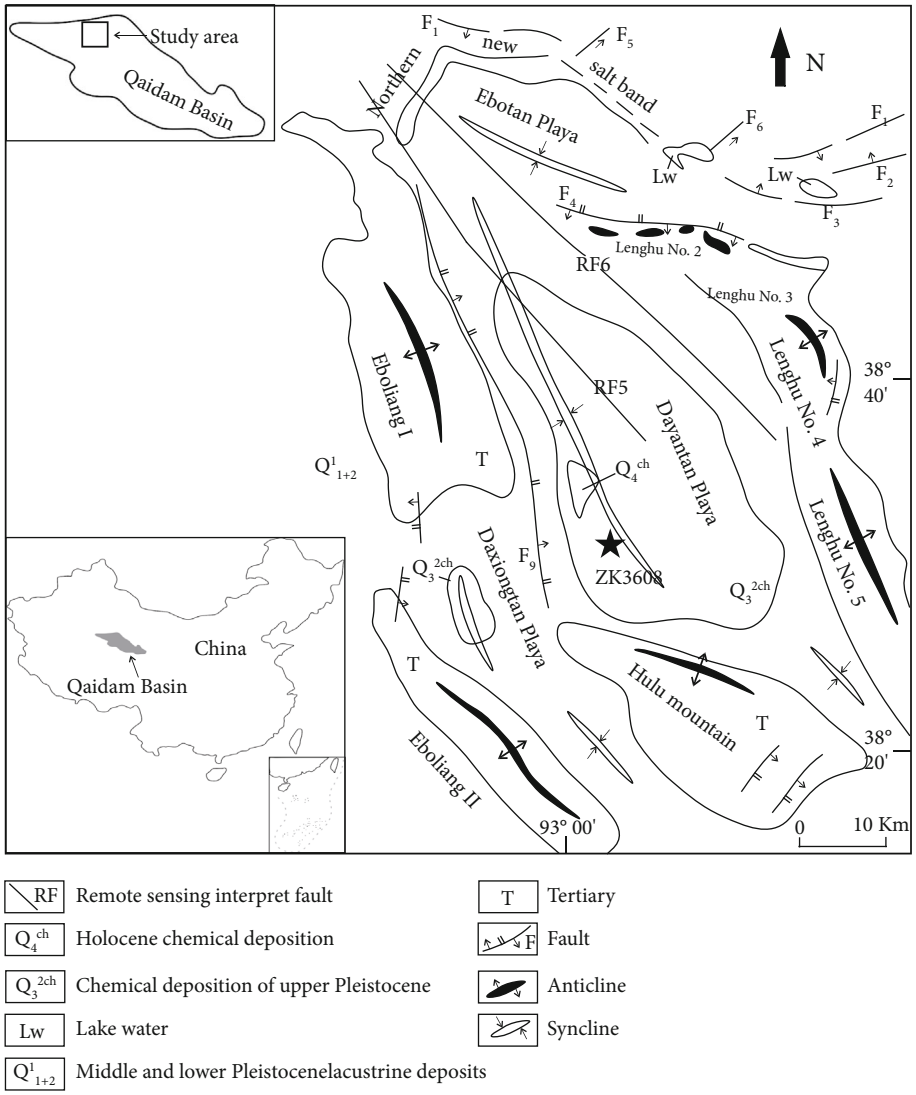

Figure 1: Schematic geological map of Kunteyi Playa in QB, China, and the location of core ZK3608 (modified after [40]).

section ZK3208 of Dayantan, it is found that the salt layer was formed in dry and cold acidic oxidation environment, and the salt-forming environment in the middle and late stage was mainly dry and cold [28]. The study of δ^{37}Cl of rock salt shows that the climate in the study area has developed from 240 ka to a drier and colder direction [42]. The CONISS clustering program divides the sediments from borehole 1045 in the Kunteyi Basin since the late Pleistocene into three mineral assemblage zones, all of which reflect the dry and cold climate [43]. It shows that the climate environment is mainly dry and cold in the middle and late salt-forming stage of Kunteyi Salt Lake.

3. Materials and Method

The petrographic observation instrument of halite and fluid inclusions is a Zeiss polarizing microscope (Axioskop 40 Pol); a Linkam THMS 600 (manufactured in England) cooling and heating stage frozen using liquid nitrogen was employed for the measurement of T_h. The temperature range measured by this instrument is -196 to +600°C, and the error is ±1°C.

3.1. Materials. Halite samples for T_h analysis were collected from the borehole ZK3608 in the Dayantan depression in the Kunteyi Playa of northwest QB (Figure 1). ZK3608 lithology has a depth of 75.25 m and contains 9 evaporite-clastic sedimentary cycles [13]. According to the systematic sorting and cataloging of core profiles, the halite layer is 51.1 m in total and primary polyhalite is widely distributed in the halite layer (Figure 2). A total of 45 halite samples were obtained by high-resolution sampling of the halite layer. Preliminary screening of lithosol particles with obvious primary characteristics, such as self-crystallization, was performed for systematic observation of petrography. Primary halite refers to the halite evaporated from lake water, and the crystals are mostly cumulate crystals and chevron crystals [44–46]. Cumulate crystals and chevron crystals

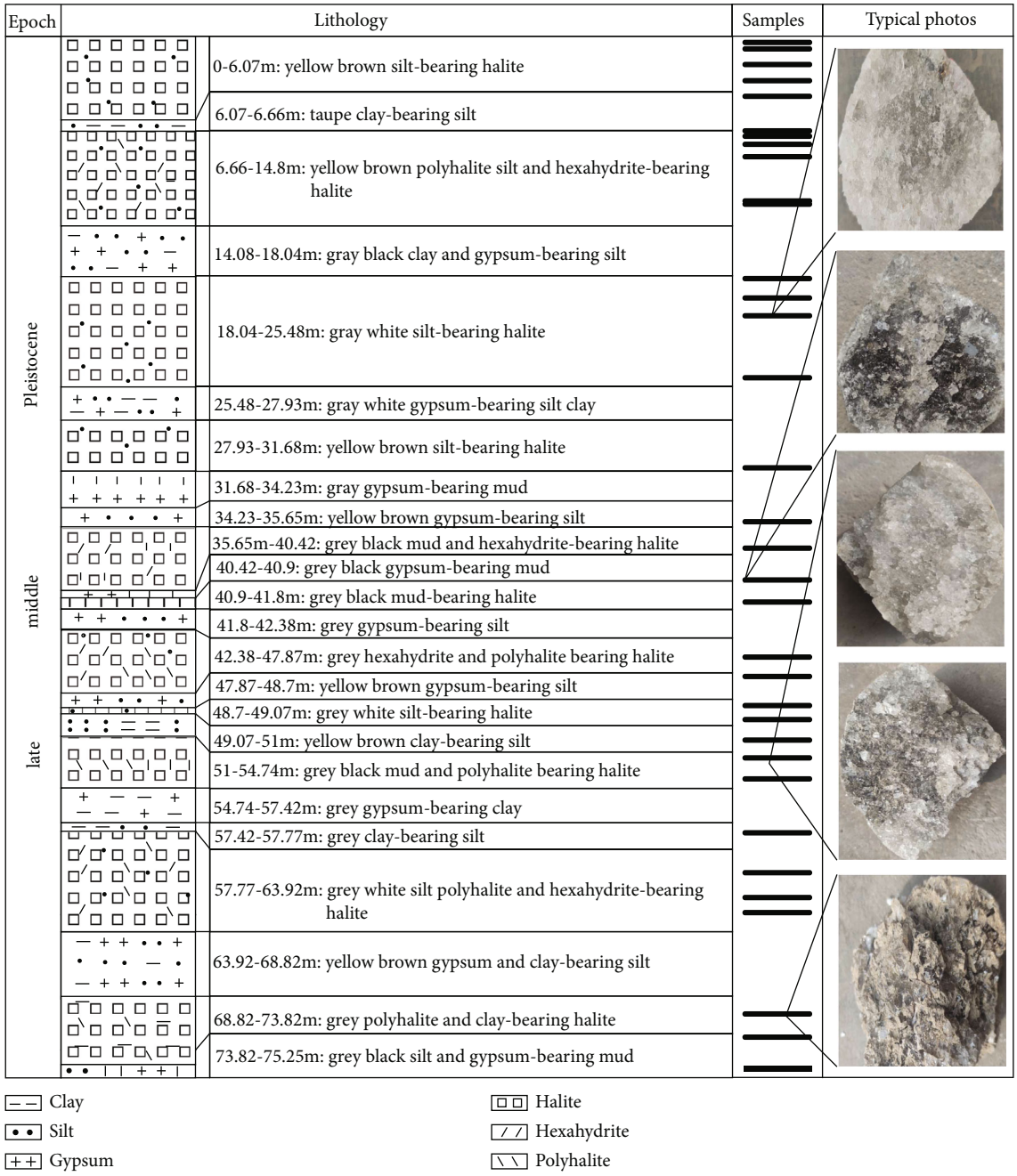

Figure 2: ZK3608 lithology description, sampling point location, and typical hand specimen.

dominate these samples (Figure 3). The primary fluid inclusions are mostly distributed along the growth zone of primary halite and also show cumulate and chevron distribution characteristics. The sample analytical methods followed those work [23]. Halite chips were prepared by cleaving 2–3 mm thick fragments with a razor blade. The prepared halite slices containing primary fluid inclusions are stored in a plastic box with a desiccant for temperature measurement. Some inclusions are gas-liquid two-phase because they cannot provide accurate temperature. Only the primary single-phase aqueous liquid inclusions within cloudy fluid inclusion bands in chevron and cumulate crystals were selected in our study for homogenization temperature analysis. Through observation of the whole rock sample of the halite salt layer, typical primary polyhalite is found, which is associated with halite. The boundary between the two minerals is clear, and there is no sign of metasomatism, which is the primary mineral precipitated from brine (Figure 4). It can be seen from hand specimen observation that gray-white polyhalite minerals are associated with halite (Figure 4). This provides direct mineralogical evidence for retrieving the ore-formed temperature of polyhalite from the temperature of ancient brine.

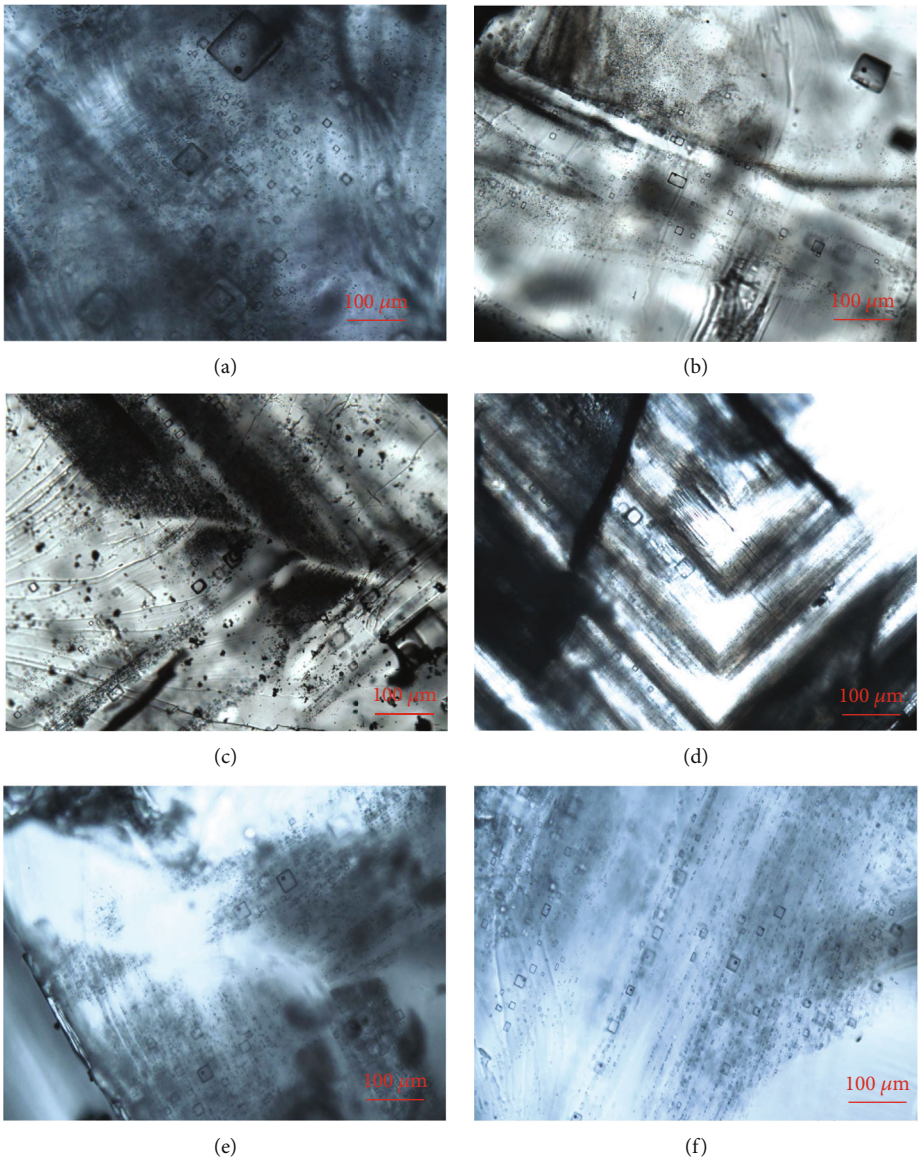

Figure 3: Petrologic characteristics of halite fluid inclusions: (a, b) fluid inclusion banding containing gas-liquid two-phase inclusion; (c, d) chevron fluid inclusion banding distribution structure; (e, f) a large number of gas-liquid two-phase inclusions appear after freezing with liquid nitrogen.

3.2. Method. There are two ways to freeze and nucleate halite fluid inclusions: one is to freeze slowly in the refrigerator for about two weeks and the other is to freeze quickly with liquid nitrogen on the cold and hot stage. Through the experimental study on the T_h of synthetic halite fluid inclusions, it is proven that the rapid freezing of liquid nitrogen can also provide reliable temperature data [47, 48]. We used liquid nitrogen rapid freezing and refrigerator slow freezing methods to test the T_h of artificially synthesized halite fluid inclusions and found that the maximum T_h data obtained by the two methods are very close to the set constant temperature evaporation temperature [49]. This method is also widely used in the study of T_h of fluid inclusions in salt-bearing strata such as the Jialingjiang Formation in the Sichuan Basin, Shashi Formation in the Jiangling Sag, Mengyejing in Yunnan, and Qarhan Bieletan section and Cordillera de los Andes in South America [50–54]. It shows that it is feasible to use liquid nitrogen to freeze and nucleate directly on the cold and hot stage, and this temperature measurement work is also carried out by using a liquid nitrogen rapid freezing method.

Firstly, the sheet to be measured is placed on a cold and hot stage, connected with liquid nitrogen and cooled to -18°C. On the premise of ensuring that the inclusions do not freeze and not damage the size and shape, some single liquid-phase halite inclusions appear to have bubbles due to condensation and contraction, forming gas-liquid two-phase inclusions. Then, after enough gas-liquid two-phase inclusions appear, the temperature rise test is carried out. In order to ensure the data to be as accurate as possible, the temperature rise rate is 0.5°C/min within 15°C, and the rate drops to 0.1°C/min when the temperature is above 15°C [23, 24]. The temperature at which the vapor bubbles disappeared was recorded. All the sample

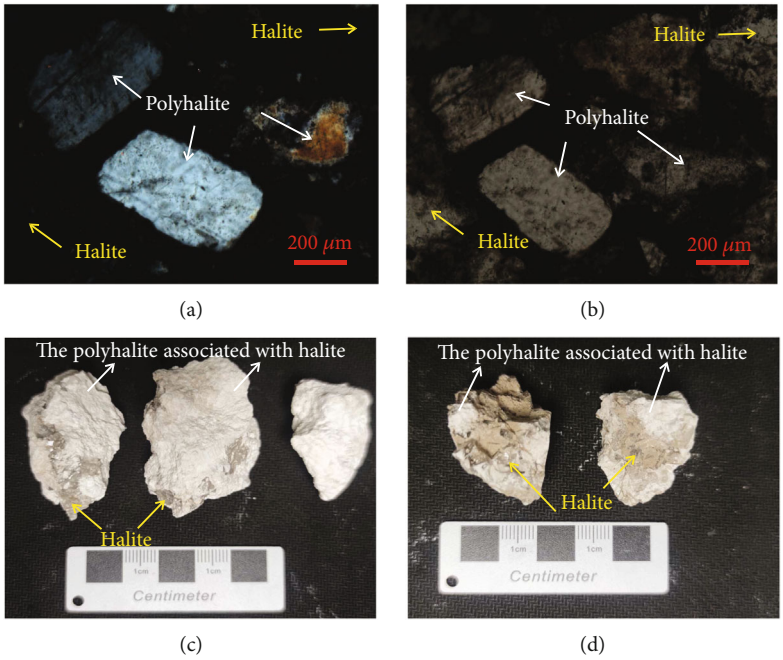

Figure 4: The microscopic morphology of polyhalite in KSL: (a, b) the relationship between polyhalite and halite in the halite layer; (c, d) relationship between polyhalite and halite in the hand specimen (from [55]).

preparation and microthermometric works were made in Minerals Lab, Qinghai Institute of Salt Lakes, Chinese Academy of Sciences.

4. Results and Discussion

Although a total of 45 halite samples were obtained, among them, 5 halite samples (nos. 4, 27, 28, 33, and 37) did not develop fluid inclusions and 6 samples (nos. 16, 17, 23, 24, 26, and 31) did not freeze out bubbles needed for temperature measurement after long-term freezing. So an amount to 472 fluid T_h data was observed and measured from 34 halite samples (Table 1). In 472 temperature data, the minimum is 4.5°C, the maximum is 35.5°C, and the average value is 17.0°C (Table 1). Characteristics of temperature data of 34 halite samples are shown in Table 1. Since the T_{hMAX} is often used to study brine temperature, this paper mainly discusses the characteristics of the T_{hMAX} of 34 halite samples. The T_{hMAX} of 34 halite samples ranges from 17.1 to 35.5°C, with an average value of 22.1°C, among which the temperature of 24 samples is between 17 and 23°C (Figure 5). In a word, the overall temperature is low.

4.1. Fluid Inclusion T_h and K^+, Mg^{2+}, and Ca^{2+} in KSL Halite. Thirty-four samples with enough T_h data were frozen by liquid nitrogen, so that the bubble appearance time was basically within 1.7 h. However, the freezing time of no. 16, 17, 23, 24, 26, and 31 samples was close to or exceeded 5 h, respectively (Table 2); still, no bubbles appear, so give up the T_h test. The scholar pointed out that freezing nucleation is difficult for some halite samples buried deep and deposited with potassium and magnesium salts [56]. Besides the experimental study on the effects of K^+, Mg^{2+}, and Ca^{2+} content on the T_h of fluid inclusions in halite, it was found that the higher the Mg^{2+} content, the more difficult it is to freeze and nucleate, and the content of K^+ has certain influence but is not the main factor [48]. The 40 halite samples obtained from ZK3608 not only tested the homogenization temperature of fluid inclusions but also tested the chemical composition of fluid inclusions [57]. The mean contents of K^+ and Mg^{2+} in 40 halite fluid inclusions are 17.1 g/l and 41.2 g/l, respectively, and the median contents of K^+ and Mg^{2+} are 12.5 g/l and 39.4 g/l, respectively [57]. The sample information of 6 unfrozen nucleation and adjacent horizons is shown in Table 2, and the composition data of sample 26 without inclusion is also shown. Samples 23, 24, and 26 have high K^+ and Mg^{2+} content; in particular, Mg^{2+} content far exceeds the average and median of Mg^{2+} in 40 halite fluid inclusions. In addition, it was found that samples 16, 17, and 31 had high K^+ and Mg^{2+} contents, especially Mg^{2+} contents, and samples in adjacent 5horizons (15, 18, 30, and 32) had the same high K^+ and Mg^{2+} contents. Even though a few inclusion data were obtained, the freezing time was longer (Table 2). It shows that not only the contents of K^+ and Mg^{2+}, especially Mg^{2+}, have an influence on freezing nucleation during temperature measurement of fluid inclusions in halite under laboratory conditions, but also the same scientific problems exist under actual natural conditions.

In addition, the experimental study shows that compared with the simple sodium chloride system, the existence of K^+, Mg^{2+}, and Ca^{2+} will cause the T_{hMAX} of halite fluid inclusions to be higher than the actual brine temperature during crystallization; in particular, K^+ has a significant impact [48]. The existence of K^+ and Mg^{2+}, especially Mg^{2+}, has an impact on the temperature measurement process. It is reasonable to believe that the existence of K^+, Mg^{2+}, and Ca^{2+} under natural

Table 1: Summary of homogenization temperatures of halite fluid inclusions.

Serial no.	T_{hMIN} (°C)	T_{hMAX} (°C)	T_{hAVG} (°C)	Depth (m)	N	Serial no.	T_{hMIN} (°C)	T_{hMAX} (°C)	T_{hAVG} (°C)	Depth (m)	N
01	12.7	23.0	17.2	1.0	13	18	10.7	19.0	14.8	37.6	16
02	14.0	22.0	17.4	1.5	15	19	9.5	25.0	17.2	39.9	24
03	15.2	25.6	20.2	2.6	15	20	9.0	22.5	16.2	41.5	8
04	15.6	25.4	19.1	3.8	20	21	15.5	31.0	22.4	45.5	8
05	19.8	35.5	25.8	4.9	12	22	10.5	19.3	15.3	46.9	19
06	15.5	22.0	18.2	7.4	13	23	4.5	22.0	9.9	49.0	18
07	12.0	22.0	16.3	7.8	9	24	12.0	22.0	16.1	50.0	14
08	11.6	30.0	21.8	8.4	17	25	13.0	19.5	15.9	51.5	16
09	9.3	18.6	15.8	9.3	6	26	10.2	19.3	14.3	52.8	12
10	13.0	21.0	15.8	12.5	7	27	13.0	25.8	21.2	54.3	6
11	15.1	26.1	20.6	12.7	12	28	16.1	28.0	23.1	58.2	14
12	9.9	17.5	14.3	18.1	7	29	12.1	18.4	14.7	61.1	13
13	18.0	18.0	18.0	19.5	1	30	9.0	18.1	13.4	62.9	18
14	11.0	17.9	14.8	20.8	22	31	9.7	17.1	12.8	64.0	10
15	10.0	20.5	15.9	25.3	19	32	13.0	21.0	16.2	71.2	13
16	11.5	19.6	15.8	31.8	24	33	13.0	19.2	15.6	73.0	19
17	10.5	19.0	15.4	35.7	20	34	11.9	20.1	15.5	75.3	12

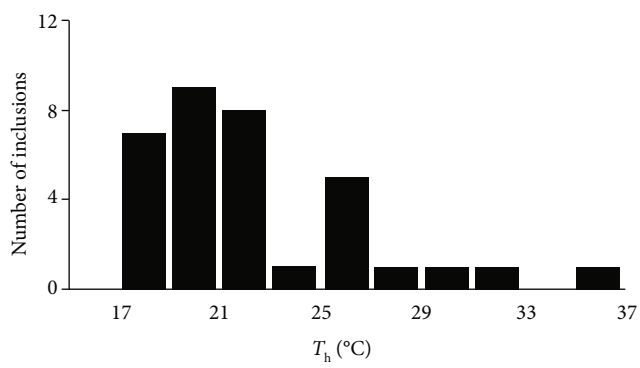

Figure 5: The T_{hMAX} distribution in the Kunteyi halite of borehole ZK3608.

Table 2: The samples without temperature data and K and Mg contents in halite about the same deposition stage.

Original no.	Freezing time (h)	Amount	Depth (m)	AVGρ(K) (g/l)	AVGρ(Mg) (g/l)
15	5.0	8	45.5	25.4	78.0
16	>5.0	0	44.5	17.8	82.4
17	>5.0	0	43.3	18.2	63.3
18	3.0	8	41.5	7.1	32.3
23	>5.0	0	30.5	8.0	46.6
24	>5.0	0	29.0	16.7	77.1
26	>5.0	0	24.9		
30	3.5	1	19.5	11.7	47.9
31	>4.3	0	19.2	12.5	48.4
32	4.0	7	18.1	15.7	47.9

conditions, especially K^+, will lead to the higher T_{hMAX} of halite fluid inclusions. As for whether the existence of K^+ and Mg^{2+} plasma affects the temperature measurement process and leads to high temperature, it needs further study, but it can be proven that the existence of K^+ and Mg^{2+} plasma does affect the T_h results under natural conditions. Combined with the chemical composition of ZK3608 halite fluid inclusions [57], the T_{hMAX} of 34 halites ranging from 17.1 to 35.5°C may be higher than the temperature in different historical periods in the study area. Although the specific height cannot be quantified at present, it can be determined that the actual brine temperature and polyhalite ore-formed temperature are a little lower than the tested T_{hMAX} in the study area since the late Middle Pleistocene.

4.2. Paleotemperature since the Late Middle Pleistocene of KSL

4.2.1. Brine Temperature in KSL and QB. In laboratory- and nature-grown halite crystals, the T_{hMAX} all matched the brine temperature [22, 29, 58]. The results showed that the T_{hMAX} ranges from 17.1 to 35.5°C with an average of 22.1 (major concentration 17-23°C) (Figure 5). Since the salt lakes in QB are the common characteristics of Quaternary modern salt lakes in nonmarine environment, our results can be compared with the previous brine temperature data in different geological ages in the basin. Reported temperatures for QB modern brine evaporites range from 17.9 to 38.2°C [26]. Salt lake brine temperatures in the Qarhan Salt Lake (southeast QB) range from 23 to 40°C [59]. Brine temperatures of the Chaka Salt Lake (southeast QB) generally range from 19 to 25°C but can reach 30°C in August [27]. The T_h of halite fluid inclusions in Yiliping Salt Lake reflects the temperature variation range of ancient brine from 21.4°C to 30.1°C [60]. The temperature of ancient brine in the northern area of Bieletan in Qarhan Salt Lake is mainly concentrated at 15-20°C, and some horizons can reach 28°C and

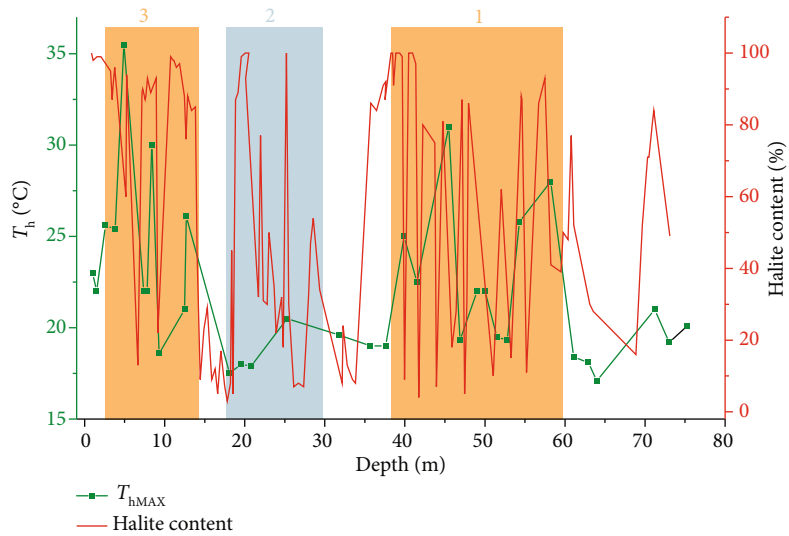

Figure 6: Relationship between halite content and ancient brine temperature in the ZK3608 core.

the high-temperature horizons promote the deposition of potassium salt [54]. Core SG-1 was located in Chahansilatu of northwest QB. Based on the study of Mg^{2+} isotopes of polyhalite and bloedite in core samples, it was suggested that there is existence of a warm dry climate in the QB, with brine temperature as high as ~70°C at 0.39 Ma, 0.36 Ma, and 0.12 Ma [61]. According to unpublished age data of ZK3608 ($y = 0.249x - 16.611$), 0.36 Ma and 0.12 Ma correspond to 73.0 m and 13.0 m of ZK3608, respectively, and the latest T_h of halite fluid inclusion results is 19.2°C (72.9 m) and 26.1°C(12.7 m), respectively. It reflects these two periods, and the temperature is relatively high. However, according to isotope results, it is questionable that there is a high temperature of 70°C.

The temperature are generally consistent with the brine temperature that halite precipitates, which can well reflect the brine temperature. Compared with the brine temperature of other salt lakes in the QB, the range of 17.1-35.5°C is reasonable, but the temperature is mainly concentrated at 17-23°C (Figure 5), which is generally lower than that of other salt lakes.

4.2.2. Halite Fluid Inclusion T_h with Mineral. Halite deposit is the most direct mineral reflecting the sedimentary evolution degree of salt lake, and halite is the mineral that has been running through since the salt formation of KSL. Therefore, through the remarkable sedimentary characteristics of halite, it shows that there are three main salt-forming periods since the Middle Pleistocene in Kunteyi Salt Lake (Figure 6). Combining the relationship between ancient brine temperature and main salt-forming periods, it can be clearly seen that the brine temperature is generally higher in the 1st (59.79-38.26 m) and 3rd (14.05-0 m) salt-forming periods, while the salt content in the 2nd salt-forming period (29.35-18.37 m) gradually increases, but the brine temperature is always at a lower level (Figure 6). The evaporation rocks in KSL were formed in dry, cold, and slightly acidic oxidation environment [39]. Temperature results show that KSL not only has salt formation in the cold period but also has salt formation in a relatively warm period, which is dominant. According to the systematic study of salt deposits in the arid salt-forming center areas in China since Quaternary (the salt lake areas in the west of the Qaidam Basin and the east of Tarim Basin), there are several cold-dry salt-forming periods and warm-dry salt-forming periods, while there is a strong cold-wet salt-forming period in 180-140 ka [62]. The salt-forming period of salt lakes in the Qaidam Basin responded to the Quaternary glacial period of Qinghai-Tibet Plateau to a certain extent, especially in the salt lakes in the western Qaidam Basin, where halite salt layers of the penultimate glacial period (MIS6) were widely developed [63, 64], while the second low-temperature salt-forming period (29.35-18.37 m) divided in this work can be seen from the ZK3608 age frame ($y = 0.249x - 16.611$) whose age span is 185-140.5 ka. Obviously, this low-temperature salt-forming period recorded this strong cold and wet event, and it was also a response to the salt-forming period of the penultimate glacial period. To some extent, it shows that the temperature trend of halite fluid inclusions is correct. The ancient brine temperature reflected by halite fluid inclusions shows that the brine and environment temperature in the main salt-forming periods (the first and third salt-forming periods) of KSL is higher, which belongs to a relatively warm and dry salt-forming mode, while the short salt-forming period in the second salt-forming stage belongs to cold and wet salt forming. These three salt-forming stages are the main sedimentary periods of polyhalite, among which the first and third relatively warm and dry salt-forming periods account for a large proportion. It shows that the ore-formed temperature of polyhalite in KSL is extensive. On the other hand, it shows that in KSL, a relatively dry and hot salt-forming model is dominant, which promotes the extensive production and deposition of polyhalite.

The phase diagrams of epsomite, hexahydrite, and kieserite under certain temperature and humidity conditions [65] are shown in Figure 7. In a certain range of humidity,

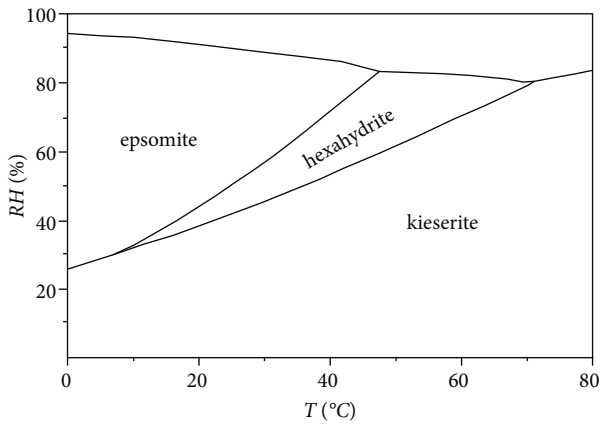

Figure 7: Diagram of existence conditions of epsomite, hexahydrite, and kieserite (modified from [65]).

with the increase in temperature, the phase area of salt discharge in hexahydrite increases slowly. According to [57], ZK3608 mineral was analyzed by X-ray powder diffractometry (XRD), and hexahydrite was scattered in the lithology. Comparing the hexahydrite content of ZK3608 with the T_{hMAX} of halite fluid inclusions (Figure 8), we can see that there is a high similarity between the hexahydrite content and the T_{hMAX}, and the hexahydrite is relatively high in the three main high-temperature stages, but almost no hexahydrite is released in the low-temperature stage. Although the distribution range of hexahydrite release is narrow in the high-temperature stage near the surface, it is a fact that more or less hexahydrite release is precipitated in the high-temperature stage of the core profile, and there is no or only a few hexahydrite release in the low-temperature stage. As far as magnesium sulfate salt is concerned, epsomite tends to be produced at low temperature and high humidity, kieserite tends to be produced at high temperature and moderate humidity, and hexahydrites sandwiched between them are easy to form at moderate temperature and humidity (Figure 8). Combined with the mineral phase diagram of magnesium sulfate double salt, in view of the actual geological background of drought and low temperature in the Kunteyi area, it is unrealistic for epsomite and kieserite to appear in the drill core profile, but it is reasonable for hexahydrite to appear. XRD results of ZK3608 mineral show that only hexahydrite does appear [13]. What is important is that the variation trend of hexahydrite content in the core profile is similar to the T_{hMAX}, which is in accord with the relationship between temperature and hexahydrite revealed by the phase diagram. It shows that the T_{h} of halite fluid inclusions reflects the actual temperature in the study area to a certain extent.

According to the sediment assemblage and its variation characteristics of KSL, it can be divided into 9 evaporite-clastic sedimentary cycles, and the closer to the surface, the thicker the halite layer [39, 57]. It shows that the climate change in the study area is generally characterized by oscillation and drying. The T_{hMAX} of ZK3608 halite fluid inclusions increases gradually from bottom to top and fluctuates on the way, which reflects the variation characteristics of paleoclimate in the study area.

Chlorite generally exists only in glacial areas and in the surface environment with weak chemical weathering, while illite shows that the climate is dry and cold and the leaching effect is weak. The clay mineral combination of chlorite and illite is considered to exist only in glacial areas [66, 67]. Muscovite is the main illite mineral, and there is a certain amount of chlorite and muscovite deposits in the ZK3608 clastic layer. Although the clay minerals in salt lakes reflect the climate characteristics of the source region more, the content of clay minerals is often low during the dominant period of chemical deposition [68]. Chlorite and muscovite, which should have been deposited in the clastic layer of salt lake, developed in great quantities in the second salt-forming period and deposited with evaporite at the same time, which corresponds to the low T_{hMAX} stage of halite fluid inclusions (Figure 8). Obviously, the lower temperature of ancient brine and the deposition of a large number of chlorite and muscovite in this period (Figure 8) are the environmental response to the strong cold and humidity during 180-140 ka [62]. The cold glacial climate environment resulted in a large number of chlorite and muscovite in the surrounding alpine provenance, which were transported to salt lake and deposited with evaporite at the same time due to the humid climate conditions. However, in the first relative dry-hot salt-forming period, chlorite and muscovite deposited in the clastic layer between evaporated rock layers and with the T_{hMAX} of halite fluid inclusions showed a flipped relationship (Figure 8), which confirmed the characteristics of this mineral deposited in the clastic layer. According to the analysis of sedimentary characteristics of minerals, including halite, hexahydrate, muscovite, and chlorite, it is confirmed that the T_{hMAX} of ZK3608 halite fluid inclusions truly reflects the temperature changes of ancient brine in KSL since the middle Pleistocene.

4.2.3. Temperature of Ancient Brine Response to Paleoclimate Variation in the Study Area. The T_{h} of primary halite fluid inclusions in shallow water can be used to indicate air temperature, indicating that paleotemperature is closely related to brine temperature. As mentioned earlier, the climate of KSL has been mainly dry and cold since the late Pleistocene. Deep borehole (SG-1) was located in Chahansilatu in western QB close to Kunteyi Playa, and research of stable isotopes of carbonates from the SG-1 core suggests that since 0.6 Ma, the climate in northwest China has been in a long-term dry and cold state, which is mainly affected by global cooling, especially cooling in the high latitudes of the Northern Hemisphere [69]. A 600 m deep core (SG-3) of lacustrine-playa deposits was obtained from the western Qaidam Basin, and sporopollen results show that from 0.6 Ma and 0.15 Ma to late Pliocene, Ephedraceae-dominated desert prevailed response to long-term global cooling [70]. As far as climate is concerned, both regional short-time scale climate characteristics and global long-time scale climate conditions have proven that the paleoclimate in the study area has been mainly dry and cold since the end of the late Pleistocene.

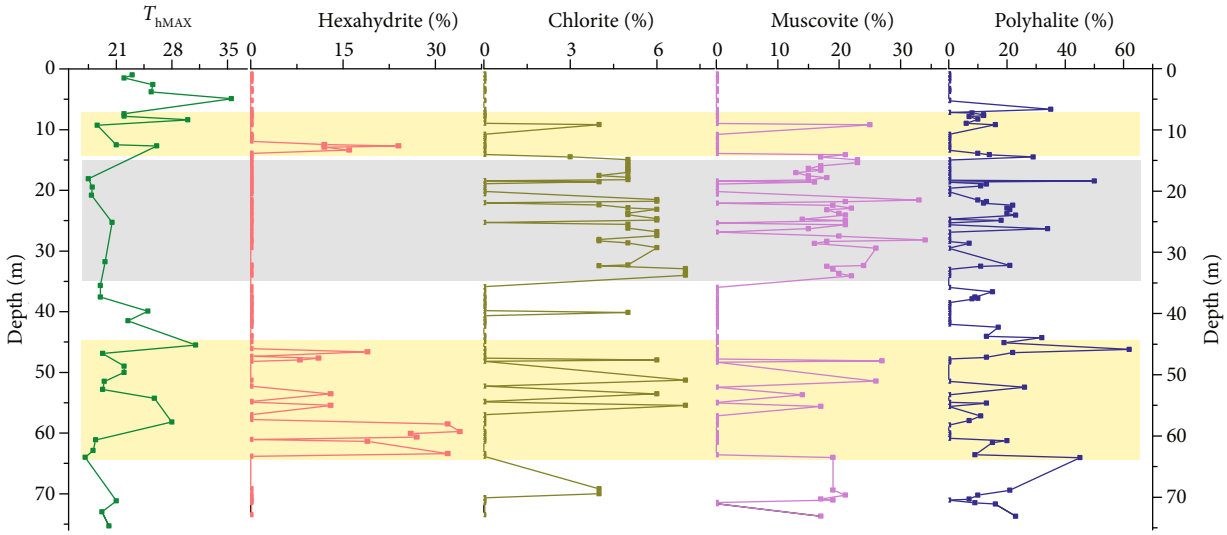

Figure 8: Plots showing concentrations of different minerals along the depth of the borehole and its relationship with T_{hMAX}.

Through the evidence of brine temperature of other salt lakes in QB, mineral sedimentary, and paleoclimate characteristics in the study area, it shows that the temperature range of 17.1-35.5°C, mainly concentrated at 17-23°C, faithfully reflects the ancient brine temperature characteristics of KSL since the late Middle Pleistocene.

4.3. Ore-Formed Temperature of Polyhalite in KSL. Salt minerals were divided into three types: cold phase, warm phase, and wide temperature phase, and polyhalite was identified as wide temperature-phase mineral [62]. The widespread existence of polyhalite in ancient and modern evaporite deposits [71], to a certain extent, explains the wide temperature range of polyhalite mineralization in nature. It can be seen from the phase diagram of the five-element system superimposed by calcium ions that the polyhalite phase area is very small when the temperature is less than 32.5°C, and the polyhalite phase area expands rapidly when the temperature is 55°C [72]. Polyhalite crystallisation slows down, when at lower temperatures [73]. Polyhalite can be synthesised under laboratory conditions by a reaction of gypsum with appropriate solutions in the ternary system K_2SO_4-$MgSO_4$-H_2O at temperatures above 70°C [74]. Through EQL/EVP hydrogeochemistry software, the Kunteyi polyhalite ore-forming fluid was simulated under different temperature conditions, and it was found that low temperature was not conducive to polyhalite mineral deposition, while polyhalite was easy to deposit under high-temperature conditions [75]. In Lop Nur western China, polyhalite has been deposited many times in a short time, which is considered to be mainly affected by climate fluctuations with high temperature [10]. The polyhalite microfabrics in an Alpine evaporite melange of Eastern Alps have a formation temperature of 61.4°C in the presence of halite [76]. As mentioned earlier, the salt lake brine temperature was at a high level during the formation of polyhalite in SG-1 drilling at Chahansilatu [61]. Whether it is the indoor experimental study of polyhalite or the exploration of the formation temperature of polyhalite in nature, it shows that polyhalite is more inclined to form at higher temperature.

Although paleoclimate research shows that the climate of KSL is relatively dry and cold in this period, through combining the relationship between evaporite and ancient brine temperature, it is found that brine and environment temperature was relatively high when the main evaporite was formed in KSL, while polyhalite was mainly formed in this relatively high-temperature salt formation process. In addition, polyhalite peaks at 46 m, and the temperature of ancient brine is relatively high. It is proven that the enrichment characteristics of polyhalite in KSL at relatively high temperature in this low-temperature environment are consistent with the conclusion that polyhalite is easier to develop at high temperature. At the same time, the polyhalite developed in the first and third relatively dry and hot salt-forming environments, while the polyhalite also developed in the second strongly cold and humid salt-forming environment (Figure 8), which indicated that the polyhalite in KSL has strong adaptability to temperature and is a mineral with a wide temperature phase. It also proves to some extent that temperature has a limited effect on the formation of polyhalite. Numerous evidences show that polyhalite tends to be deposited at high temperature, and the low temperature of brine in KSL during this period may be one of the reasons why polyhalite did not develop on a larger scale.

5. Summary and Conclusion

(1) Polyhalite is mostly formed in the relatively high-temperature stage in the low-temperature environment, and the relatively high-temperature conditions promote the formation of polyhalite in KSL

(2) Polyhalite has a strong adaptability to temperature and is a mineral with a wide temperature phase; while temperature has limited influence on

polyhalite formation, it is deposited at different temperatures

(3) In the evaporite geological environment, in sedimentary areas with high K^+ and Mg^{2+} content, especially in areas with high Mg^{2+} content, Mg^{2+} has an important influence on the freezing process of the cooling nucleation method of halite fluid inclusions. We according to the previous experimental research speculate that the actual ore-formed temperature of polyhalite in KSL is lower than the measured T_h

Data Availability

The data used to support the findings of this study are available from the corresponding authors upon request.

Conflicts of Interest

The authors declare that they have no conflicts of interest.

Acknowledgments

This research was supported by the National Key Research and Development Program of China (Grant No. 2018YFC0406605), National Natural Science Foundation of China (Grant Nos. 41672087 and 41402082), Foundation of Qinghai Science & Technology Department (2014-ZJ-704, 2019-ZJ-7004), and West Light Foundation of Chinese Academy of Sciences (Grant to YS Du).

References

[1] K. Pavuluri, Z. Malley, and M. K. Mzimbiri, "Evaluation of polyhalite in comparison to muriate of potash for corn grain yield in the Southem Highlands of Tanzaria," *International Scholars Journals*, vol. 5, no. 3, pp. 325–332, 2017.

[2] A. K. Sutradhar, D. E. Kaiser, and C. J. Rosen, "Evaluation of polyhalite as a source of potassium and sulfur for acorn-soybean rotation in Minnesota," *Proceedings of the 46th North Central Extension-Industry Soil Fertility Conference*, vol. 32, pp. 125–135, 2016.

[3] F. H. Stewart, "The mineralogy of the British Permian evaporites," *Mineralogical magazine and journal of the Mineralogical Society*, vol. 34, pp. 460–470, 1965.

[4] D. G. Harville and S. J. Fritz, "Modes of diagenesis responsible for observed succession of potash evaporites in the Salado Formation, Delaware Basin, New Mexico," *Journal of Sedimentary Petrology*, vol. Vol. 56, no. 5, pp. 648–656, 1986.

[5] H. Rahimpour-Bonab, Z. Shariatinia, and M. G. Siemann, "Origin and geochemistry of Miocene marine evaporites associated with red beds: Great Kavir Basin, Central Iran," *Geological Journal*, vol. 42, no. 1, pp. 37–54, 2007.

[6] X. Z. Huang, "The first polyhalite deposit of China," *Yunnan Geology*, vol. 15, no. 1, pp. 52–61, 1996.

[7] Y. T. Lin and J. Q. He, "The characters and genies meanings of shallow polyhalite potash deposit in Huayingshan, Sichuan," *Geology of Chemical Minerals*, vol. 26, no. 3, pp. 145–149, 2004.

[8] Y. J. Zhao, C. L. Liu, T. Ding et al., "Origin and depositional paleoenvironment of Triassic polyhalite in the Jialingjiang Formation, Sichuan Basin," *Carbonates and Evaporites*, vol. 35, no. 2, pp. 1–17, 2020.

[9] M. L. Wang, "The geological significance of polyhalite in depression Q," *Geological Review*, vol. 28, no. 1, pp. 29–37, 1982.

[10] C. L. Liu, M. L. Wang, P. C. Jiao et al., "Sedimentary characteristics and origin of polyhalite in Lop Nur salt lake, Xinjiang," *Mineral Deposits*, vol. 27, no. 6, pp. 705–713, 2008.

[11] D. J. Zhao, W. T. Han, K. Q. Cai, and J. H. Gao, "The study of polyhalite genesis and its significance of potash-finding in Dawenkou depression, Shandong Province," *Earth Science-Journal of Wuhan College of Geology*, vol. 12, no. 4, pp. 342–356, 1987.

[12] Z. Liu, D. L. Gao, X. L. Yuan, Y. Zhang, and B. L. Li, "Sedimentary characteristics and origin of polyhalite of Kunty salt lake mine in Qaidam Basin," *Journal of Salt Lake Research*, vol. 23, no. 1, pp. 30–37, 2015.

[13] X. Zhang, X. Y. Zhang, W. L. Miao et al., "Genesis of polyhalite in Kunteyi Salt Lake based on mineralogical analysis-taking ZK3608 borehole in Dayantan mining area as an example," *Journal of Salt Lake Research*, vol. 1, no. 28, pp. 45–51, 2020.

[14] Z. Y. Ai, Y. S. Li, Q. L. Tang et al., "Preliminary study on the source of formation-ore fluids of polyhalite in Kunty Playa based on hydrogeochemical simulation," *Journal of Salt Lake Research*, vol. 26, no. 4, pp. 44–50, 2018.

[15] H. W. Xu, X. F. Guo, and J. M. Bai, "Thermal behavior of polyhalite: a high-temperature synchrotron XRD study," *Physics and Chemistry of Minerals*, vol. 44, no. 2, pp. 125–135, 2017.

[16] H. D. Cheng, J. Li, Q. Y. Hai, J. G. Song, and X. H. Ma, "Raman and XRD study of polyhalite ore during calcinations," *Vibrational Spectroscopy*, vol. 102, pp. 63–70, 2019.

[17] L. P. Ogorodova, M. F. Vigasina, L. V. Mel'chakova, I. A. Bryzgalov, and D. A. Ksenofontov, "Enthalpy of formation of natural polyhalite," *Geochemistry International*, vol. 54, no. 7, pp. 645–649, 2016.

[18] L. Soliev, "Phase equilibria in the Na, K, Mg, Ca||SO_4,Cl-H_2O system at 50°C in the polyhalite crystallization region," *Russian Journal of Inorganic Chemistry*, vol. 61, no. 4, pp. 511–517, 2016.

[19] X. F. Guo and H. W. Xu, "Enthalpies of formation of polyhalite: a mineral relevant to salt repository," *The Journal of Chemical Thermodynamics*, vol. 114, pp. 44–47, 2017.

[20] S. M. Roberts and R. J. Spencer, "Paleotemperatures preserved in fluid inclusions in halite," *Geochimica et Cosmochimica Acta*, vol. 59, no. 19, pp. 3929–3942, 1995.

[21] E. Roedder, "The fluids in salt," *American Mineralogist*, vol. 69, pp. 413–439, 1984.

[22] T. K. Lowenstein, J. R. Li, and C. B. Brown, "Paleotemperatures from fluid inclusions in halite: method verification and a 100,000 year paleotemperature record, Death Valley, CA," *Chemical Geology*, vol. 150, no. 3-4, pp. 223–245, 1998.

[23] K. C. Benison and R. H. Goldstein, "Permian paleoclimate data from fluid inclusions in halite," *Chemical Geology*, vol. 154, no. 1-4, pp. 113–132, 1999.

[24] F. W. Meng, P. Ni, J. D. Schiffbauer et al., "Ediacaran seawater temperature: evidence from inclusions of Sinian halite," *Precambrian Research*, vol. 184, no. 1-4, pp. 63–69, 2011.

[25] J. J. Zambito and K. C. Benison, "Extremely high temperatures and paleoclimate trends recorded in Permian ephemeral lake halite," *Geology*, vol. 41, no. 5, pp. 587–590, 2013.

[26] Y. J. Zhao, C. L. Liu, H. Zhang, Z. Q. Li, T. Ding, and M. Q. Wang, "The controls of paleotemperature on potassium salt precipitation in ancient salt lakes," *Acta Petrologica Sinica*, vol. 31, no. 9, pp. 2751–2756, 2015.

[27] X. Q. Liu, P. Ni, H. L. Dong, and T. G. Wang, "Homogenization temperature and its significance for primary fluid inclusion in halite formed in Chaka salt lake, Qaidam basin," *Acta Petrologica Sinica*, vol. 23, no. 1, pp. 0113–0116, 2007.

[28] Y. J. Zhao, H. Zhang, C. L. Liu, B. K. Liu, L. C. Ma, and L. C. Wang, "Late Eocene to early Oligocene quantitative paleotemperature record: evidence from continental halite fluid inclusions," *Scientific Reports*, vol. 4, pp. 1–6, 2014.

[29] X. Y. Zhang, F. W. Meng, W. X. Li, Q. L. Tang, and P. Ni, "Reconstruction of Late Cretaceous coastal paleotemperature from halite deposits of the Late Cretaceous Nongbok Formation (Khorat Plateau, Laos)," *Palaeoworld*, vol. 25, no. 3, pp. 425–430, 2016.

[30] X. H. Sun, Y. J. Zhao, C. L. Liu, P. C. Jiao, H. Zhang, and C. H. Wu, "Paleoclimatic information recorded in fluid inclusions in halites from Lop Nur, Western China," *Scientific Reports*, vol. 7, no. 1, pp. 1–10, 2017.

[31] Y. Xu, C. L. Liu, Y. T. Cao, and H. Zhang, "Quantitative temperature recovery from middle Eocene halite fluid inclusions in the easternmost Tethys realm," *International Journal of Earth Sciences*, vol. 108, no. 1, pp. 173–182, 2019.

[32] M. H. Li, S. R. Sun, M. D. Yan et al., "Late Cretaceous paleoclimate reconstruction from halite in an evaporite deposit on the Khorat Plateau, Laos," *Cretaceous Research*, vol. 116, article 104589, 2020.

[33] P. X. Zhang, *Salt Lake in Qaidam Basin*, Science Press, Beijing, 1987.

[34] X. J. Wei and J. X. Jiang, "The evolution of the quaternary salt lake in the Qaidam Basin," *Acta Geologica Sinica*, vol. 67, no. 3, pp. 255–265, 1993.

[35] M. L. Wang, Z. C. Yang, C. L. Liu, Z. C. Xie, P. C. Jiao, and C. H. Li, *Salt Lake Potassium Deposit in Northern Qaidam Basin and Its Development Prospect*, Geology Press, Beijing, 1997.

[36] Z. L. Fan, J. N. Chen, Q. W. Dong, X. X. Liu, X. Yue, and X. D. Qiu, "An analysis of geological characteristics of Okubotan potassium deposit in Kunteyi potassium mine in Qinghai Province," *China's Manganese Industry*, vol. 36, no. 3, pp. 8–12, 2018.

[37] J. H. Zhang, J. R. Ren, and Z. G. Zhang, "Aquifers hydrogeological characteristics of Kunty salt lake," *Journal of Salt Lake Research*, vol. 19, no. 2, pp. 7–10, 2011.

[38] Z. S. Sheng, G. Cheng, and C. S. Le, *Division and Sedimentary Environment of Quaternary Salt-Bearing Strata in Qaidam Basin*, Geological Publishing Press, Beijing, 1991.

[39] F. Q. Han, Q. Huang, K. J. Wang, H. A. Wang, and L. Yuan, "Study of geochemical evolution and palaeoclimatic fluctuation of Kunteyi Salt Lake in the Qaidam Basin, Qinghai," *Oceanologia et Limnologia Sinica*, vol. 26, no. 5, pp. 502–508, 1995.

[40] S. J. Bao, *Detailed Investigation Report of Dayantan Potassium Deposit in Kunteyi Ore Field, Lenghu Town*, Bureau of Geological Exploration and Development of Qinghai Province, Xining, Qinghai Province, 2002.

[41] Z. Q. Sheng, G. B. Tong, J. P. Zhang, S. F. Yu, and Y. L. Li, "Geological environments since Pliocene and accumulation process of saline deposit in west Chaidamu Basin, Qinghai, China," *Marine Geology and Quaternary Geology*, vol. 10, no. 4, pp. 89–99, 1990.

[42] W. G. Liu, Y. K. Xiao, F. Q. Han, and Z. C. Peng, "Characteristics of chlorine isotopes in salt lakes of Kunteyi and their significance of plaeoclimate," *Oceanologia et Limnologia Sinica*, vol. 29, no. 4, pp. 431–435, 1998.

[43] Z. Yuan, *The Characteristics of Climate since Lake Pleistocene in Lenghu Area of Qaidam Basin and Its Response to Global Climate Change and Uplift of the Plateau*, China University of Geosciences, Hubei Province, 2015.

[44] L. A. Hardie, T. K. Lowenstein, and R. J. Spencer, "The problem of distinguishing between primary and secondary features in evaporites," *Sixth International Symposium on Salt*, vol. 1, pp. 11–39, 1983.

[45] T. K. Lowenstein and L. A. Hardie, "Criteria for the recognition of salt-pan evaporites," *Sedimentology*, vol. 32, no. 5, pp. 627–644, 1985.

[46] B. Z. Zhang, H. B. Fan, P. X. Zhang, T. K. Lowenstein, and R. J. Spencer, "Hydrogen and oxygen stable isotope analyses of fluid inclusions in halite in Qarhan salt lake with geochemical implications," *Acta Sedimentologica Sinica*, vol. 8, no. 1, pp. 3–17, 1990.

[47] X. Chen, *Characteristics of Salt-Bearing Series in Eastern Sichuan Basin and Research on Homogenization Temperature of the Fluid Inclusions in Salt*, Beijing, Chinese Academy of Geological Sciences, 2014.

[48] J. Li, H. D. Cheng, X. Y. Zhang et al., "Experimental studies of homogenization temperature of fluid inclusions of halite by isothermal evaporation at 25°C involving NaCl-X-H_2O (X=KCl, $MgCl_2$, $CaCl_2$, Na_2SO_4) system," *Mineral Deposits*, vol. 38, no. 1, pp. 1–9, 2019.

[49] M. WANG, Y. ZHAO, W. LI, and C. LIU, "Fluid inclusions in surface-temperature halite: sample preparation and application," *Acta Geologica Sinica*, vol. 92, no. 4, pp. 1592–1597, 2018.

[50] C. L. Wang, C. L. Liu, H. M. Xu, L. C. Wang, and L. B. Zhang, "Homogenization temperature study of salt inclusions from the upper section of Shashi Formation in Jiangling depression," *Acta Petrologica et Mineralogica*, vol. 32, no. 3, pp. 383–392, 2013.

[51] J. Dong, X. Gao, Q. F. Fang, Q. Peng, H. W. Ma, and G. Y. Liu, "The characteristics of halite inclusions in the Mengyejing potash deposit, Yunnan Province, and their palaeoenvironmental significance," *Acta Petrologica et Mineralogica*, vol. 34, no. 2, pp. 227–236, 2015.

[52] M. Q. Wang, Y. J. Zhao, C. L. Liu, and T. Ding, "Paleotemperature and significance of the evaporated seawater in salt-forming process of the forth member of Jialingjiang Formation in the eastern Sichuan Basin," *Acta Petrologica Sinica*, vol. 31, no. 9, pp. 2745–2750, 2015.

[53] F. J. Karmanocky and K. C. Benison, "A fluid inclusion record of magmatic/hydrothermal pulses in acid Salar Ignorado gypsum, northern Chile," *Geofluids*, vol. 16, no. 3, 506 pages, 2016.

[54] D. Wang, *Characteristics of Potash Sediment and Paleo Water Temperature in Bieletan Qarhan Salt Lake Qinghai Province*, China University of Geosciences, Beijing, 2020.

[55] J. L. X. Y. Zhang, X. Zhang, M. Y. Hu et al., "High-resolution mineralogical investigations on polyhalite-bearing strata in the Kunteyi Salt Lake, Qaidam Basin," *Acta Geologica Sinica*, vol. 95, no. 7, pp. 2138–2149, 2021.

[56] Y. J. Zhao, C. L. Liu, H. Zhang, and L. C. Wang, "Analytical method and paleoenvironmental interpretation of fluid inclusion homogenization temperature of ancient halite," *Acta Geoscientica Sinica*, vol. 34, no. 5, pp. 603–609, 2013.

[57] X. Zhang, *Study on Geochemical Characteristics of Paleobrine in Kunteyi Playa Based on Fluid Inclusions Hosted in Halite*, University of Chinese Academy of Sciences, Beijing, 2019.

[58] F. W. Meng, P. Ni, C. D. Ge et al., "Homogenization temperature of fluid inclusions in laboratory grown halite and its implication for paleotemperature reconstruction," *Acta Petrologica Sinica*, vol. 27, no. 5, pp. 1543–1547, 2011.

[59] E. Casas, T. K. Lowenstein, R. J. Spencer, and P. X. Zhang, "Carnallite mineralization in the nonmarine, Qaidam Basin, China: evidence for the early diagenetic origin of potash evaporites," *Journal of Sedimentary Petrology*, vol. 62, pp. 881–898, 1992.

[60] M. Q. Wang, *Origin of Lithium-Rich Brine in Yiliping Salt Lake*, Beijing, China University of Geosciences, Qaidam Basin, 2020.

[61] M. H. Li, X. M. Fang, A. Galy, H. L. Wang, X. S. Song, and X. X. Wang, "Hydrated sulfate minerals (bloedite and polyhalite): formation and paleoenvironmental implications," *Carbonates and Evaporites*, vol. 35, no. 4, pp. 1–12, 2020.

[62] M. P. Zheng, Y. Y. Zhao, and Y. J. Liu, "Quaternary saline Lake deposition and paleoclimate," *Quaternary Sciences*, vol. 4, pp. 297–307, 1998.

[63] A. D. Chen and M. P. Zheng, "Salt-forming periods in the Qaidam Basin and their correlation with Quaternary glaciations and tectonic movements on the Tibetan plateau," *Science & Technology Review*, vol. 35, no. 6, pp. 36–41, 2017.

[64] A. Chen, M. Zheng, G. Song et al., "Evaporite deposits in the Qaidam Basin and their response to Quaternary glacial climates since marine oxygen isotope stage 6 (MIS6)," *Geological Review*, vol. 66, no. 3, pp. 611–624, 2020.

[65] M. Steiger, K. Linnow, H. Juling et al., "Hydration of $MgSO4{\cdot}H_2O$ and generation of stress in porous materials," *Crystal Growth and Design*, vol. 8, no. 1, pp. 336–343, 2008.

[66] D. S. Zhao, P. He, H. X. Sun, H. P. Zheng, and Z. F. Lei, "Characteristics and evolution of the clay minerals in Qaidam Basin," *Acta Sedimentologica Sinica*, vol. 9, no. 1, pp. 66–70, 2001.

[67] Y. J. Tang, J. Y. Jia, and X. D. Xie, "Environment significance of clay minerals," *Earth Science Frontiers*, vol. 9, no. 2, pp. 337–344, 2002.

[68] X. Y. Zhang, H. Z. Ma, F. Q. Han, Z. Chen, G. C. Cao, and J. G. Wang, "Mineral assemblages and palaeoenvironmental changes of core DG03 of Gahai Lake in Delingha Basin," *Acta Sedimentologica Sinica*, vol. 25, no. 5, pp. 767–773, 2007.

[69] W. X. Han, X. M. Fang, C. C. Ye, X. H. Teng, and T. Zhang, "Tibet forcing Quaternary stepwise enhancement of westerly jet and central Asian aridification: carbonate isotope records from deep drilling in the Qaidam salt playa, NE Tibet," *Global and Planetary Change*, vol. 116, pp. 68–75, 2014.

[70] M. T. Cai, X. M. Fang, F. L. Wu, Y. F. Miao, and E. Appel, "Pliocene-Pleistocene stepwise drying of Central Asia: evidence from paleomagnetism and sporopollen record of the deep borehole SG-3 in the western Qaidam Basin, NE Tibetan Plateau," *Global and Planetary Change*, vol. 94-95, pp. 72–81, 2012.

[71] J. K. Warren, *Evaporites: Sediments, Resoureces and Hydrocarbons*, Springer Science and Business Media Press, Berlin, Germany, 2006.

[72] F. M. He, S. C. Liu, and C. Q. Bai, *Identification Method Manual of Saline Minerals*, Chemical Industry Press, Beijing, 1988.

[73] G. Wollmann, *Crystallization Fields of Polyhalite and Its Heavy Metal Analogues*, University Bergakademie Freiberg, Free State of Saxony, 2010.

[74] D. Freyer and W. Voigt, "Crystallization and phase stability of $CaSO_4$ and $CaSO_4$-based salts," *Monatshefte für Chemie*, vol. 134, no. 5, pp. 693–719, 2003.

[75] Z. Y. Ai, *Study on Formation Mechanism of Polyhalite in Kunteyi Playa Based on Hydrochemical Simulations*, University of Chinese Academy of Sciences, Beijing, 2018.

[76] A. Schorn, F. Neubauer, and M. Bernroider, "Polyhalite microfabrics in an Alpine evaporite melange: Hallstatt, Eastern Alps," *Journal of Structural Geology*, vol. 46, pp. 57–75, 2013.

Hindawi
Geofluids
Volume 2021, Article ID 5566757, 19 pages
https://doi.org/10.1155/2021/5566757

Research Article

The Metallogeny of the Tieling Cu-Mo Porphyry Deposit in Eastern Tianshan, NW China: New Insights from Zircon U-Pb, Fluid Inclusion, and H-O-S Stable Isotope Analyses

Ping Li,[1,2] **Ting Liang**,[1] **Fan Huang**,[3] **Tongyang Zhao**,[2] **Zhixin Zhu**,[2] **Yong Li**,[4] **Jing Feng**,[5] **and Lei He**[1]

[1]*College of Earth Science and Resources, Chang'an University, Xi'an, Shanxi 710054, China*
[2]*Geological Survey Academy of Xinjiang, Urumqi, Xinjiang 830000, China*
[3]*MNR Key Laboratory of Metallogeny and Mineral Assessment, Institute of Mineral Resources, CAGS, Beijing 100037, China*
[4]*Research Institute of Geology and Mineral Exploration of Xinjiang Nonferrous Geological Exploration Bureau, Urumqi, Xinjiang 830000, China*
[5]*Xinjiang Bureau of Geological Mineral Exploration and Development, Urumqi, Xinjiang 830000, China*

Correspondence should be addressed to Ting Liang; liangt@chd.edu.cn and Fan Huang; hfhymn@163.com

Received 26 January 2021; Revised 16 April 2021; Accepted 18 August 2021; Published 21 September 2021

Academic Editor: Paolo Fulignati

The eastern Tianshan metallogenic belt is an important molybdenum resource base in Xinjiang and is characterized by large-scale porphyry Mo deposits formed during the Triassic. The Tieling Cu-Mo porphyry deposit, which is situated in the western part of the eastern Tianshan metallogenic belt, was recently recognized as being related to Carboniferous granite porphyry. Three stages of hydrothermal mineralization were identified, including quartz+K-feldspar+pyrite±molybdenite±magnetite (stage I), quartz +molybdenite+pyrite+chalcopyrite (stage II), and quartz+pyrite±molybdenite±epidote (stage III). Fluid inclusion petrography and microthermometry analyses indicate the presence of gas-liquid inclusions with a H_2O-NaCl composition. The ore-forming fluids have a characteristic temperature ranging from 157 to 262°C under stage II and 135 to 173°C under stage III, which correspond to salinities of 7.2-17.2 wt% NaCl equiv. and 5.9 to 9.6 wt% NaCl equiv., respectively. The hydrogen and oxygen isotope data indicate that the ore-forming fluids of the Tieling deposit were originally derived from magmatic hydrothermal fluids and then mixed with meteoric water. The sulfur isotope compositions indicate that the ore-forming materials were mainly derived from the Late Carboniferous felsic magma. Furthermore, zircon U-Pb analysis of ore-bearing granite porphyry yields a concordant age of 298.4 ± 0.7 Ma, indicating that the Tieling Cu-Mo deposit formed during the Late Carboniferous and differed from that processed under pre-Early Carboniferous and Triassic mineralization in the eastern Tianshan metallogenic belt. These results also indicate that the Tieling porphyry deposit was formed in the transition condition between subduction-related accretion and postcollisional orogeny, and it should be given more attention in prospect evaluations.

1. Introduction

Porphyry deposits, as one of the most important types of Cu-Mo-Au deposits, have attracted extensive interest from the geologic community [1, 2]. Subduction-related magmatic arcs are considered to be closely related to porphyry deposits worldwide, especially that of porphyry Cu-Mo in the Circum-Pacific metallogenic belt [3–5]. Recent studies of metallogenic systems in China have shown that a postcollisional setting is favourable for the development of porphyry deposits [6–10], especially for porphyry Mo-only or Mo-dominated polymetallic deposits in the Dabie orogen [11–13].

The postcollision-type porphyry Mo deposits in eastern Tianshan are found within a Triassic formation [14, 15], and the subduction-type porphyry Cu-Mo deposits are characterized by a formation preceding the Early Carboniferous [16, 17]. However, the Tieling Cu-Mo deposit, which was

discovered by the Xinjiang Geological Survey Academy during a geochemical element anomaly survey, may be closely related to Late Carboniferous magmatism [18]. As an unexploited blind mineral system, the geological characteristics and metallogenic processes supporting its formation are still unclear. In this contribution, we first report new data, including the zircon U-Pb isotopic age of ore-bearing granite porphyry rocks, fluid inclusions, and H-O-S isotopes, to constrain the age of mineralization, determine the origin of the ore-forming fluids and material, and establish a metallogenic model of the Tieling deposit, which will be beneficial to enhance metallogenic theory and provide insights for the exploration of porphyry Cu-Mo mineralization in eastern Tianshan.

2. Geological Background

The Central Asian Orogenic Belt (CAOB), surrounded by North China, Tarim, European, and Siberian cratons (Figure 1(a)), is a typical accretionary orogenic belt [19, 20], which resulted from collision between the Siberian and Tarim plates (Figure 1(a)) that progressively closed eastwards from the Late Carboniferous to Early Triassic [21, 22]. Eastern Tianshan, located at the southern margin of the CAOB, is an important mineral resource base in China (Figure 1(b)). Many notable deposits have occurred, including the Huangtupo and Xiaorequanzi VMS Cu-(Zn) [23, 24], Tuwu and Yandong porphyry Cu [16], Baishan and Donggebi porphyry Mo [21, 25], Huangshan and Tulaergen magmatic sulfide Ni-Cu [26, 27], Kangguer and Shiyingtan orogenic Au [28], and Yamansu volcanic Fe [29] deposits.

Eastern Tianshan, as an important part of the CAOB, has been subdivided into four tectonic units from north to south, namely, the Dananhu–Tousuquan island arc, the Kanggur–Huangshan shear zone, the Aqishan–Yamansu belt, and the Central Tianshan massif, with a series of approximately east-west-trending faults defining the boundaries, including the Dacaotan, Kanggur, Yamansu, and Aqikekuduke faults (Figure 1(c)). The Dananhu–Tousuquan belt comprises Ordovician to Carboniferous volcanic and intrusive rocks that host a series of large porphyry Cu-(Mo) deposits, such as the Yudai [30], Tuwu, Yandong, Linglong [31], Chihu [32], Fuxing [33, 34], Yuhai [17], and Sanchakou deposits [35]. The Kanggur–Huangshan shear zone, located between the Yamansu and Kanggur faults, contains a set of tectonic slices, disordered strata, and intrusive rocks. Most strata-originating rocks with strong deformation and metamorphism host gold deposits in the west, including the Kangguer, Matoutan, and Shiyingtan deposits [28]. Most mafic-ultramafic rocks in the east host nickel-copper deposits, such as Huangshan, Huangshandong, Huangshannan, Hulu, and Tulargen deposits [26, 27]. Most notably, the Baishan and Donggebi superlarge porphyry Mo deposits formed in the Triassic are also found in the Kanggur–Huangshan shear zone [25, 36]. The Aqishan–Yamansu belt, located between the Aqikekuduke and Yamansu faults, consists of lavas, volcaniclastic rocks, and terrigenous clastic sedimentary rocks interbedded with bioclastic limestones. Carboniferous granitic intrusions are widely distributed and intrusively bedded by diabase walls [37]. A series of iron deposits related to volcanism have been recognized in this belt, including the Hongyuntan, Bailingshan, Duotoushan, Heijianshan, Chilongfeng, and Yamansu deposits [18, 29, 38, 39]. The Central Tianshan massif, bounded by the Aqikekuduke fault in the north, is an ancient block composed of calc-alkaline basaltic to andesitic volcanic and volcaniclastic rocks, slightly altered granites and granodiorites, and Precambrian basement rocks [34]. In addition to iron and nickel-copper deposits, there is also a skarn-type tungsten-molybdenum deposit (Xiaobaishitou, Li et al. [40]) in the eastern part of the belt.

3. Geology of the Tieling Ore District

The Tieling Cu-Mo deposit is situated southwest of the Bailingshan intrusion in the Aqishan–Yamansu arc belt (Figure 1(c)). The lithostratigraphic unit in the ore district is dominated by the Late Carboniferous Tugutubulake Formation, which consists of tuffaceous dacitic lava with an age of 324 Ma [41]. The intrusive rocks at Tieling mainly include granite porphyry, monzogranite, and granodiorite, with minor gabbroic and dioritic dikes (Figure 2). The monzogranite and granodiorite of the Bailingshan complex were emplaced early into the strata at 317–307 Ma [41], and the gabbroic and dioritic dikes were both emplaced in the Late Carboniferous (311 to 315 Ma, Long et al. [37]). The concealed granite porphyry, as an important ore-bearing rock, was emplaced into the granodiorite (Figure 3). The granite porphyry is characterized by a medium- or fine-grained porphyritic texture (Figure 4(a)) and mainly consists of K-feldspar (65%) and quartz (30%), with minor accessory minerals such as molybdenite, zircon, apatite, pyrite, and magnetite. The phenocryst content is approximately 15% and mainly includes K-feldspar with a particle size of approximately 0.5 mm (Figure 4(b)). Muscovite is distributed among the K-feldspar and quartz aggregates in sheet form (Figure 4(c)).

The iron orebodies in the NE direction on the surface, which were regarded as target ores, are mainly distributed in the northeastern ore district (Figure 2). Newly identified molybdenum mineralization is only found in the deep part of granite porphyry, forming a combination of "upper iron and lower copper-molybdenum" with the previously mined iron ores. The iron ores are composed of magnetite, haematite, and pyrite [42]. The metal sulfide minerals of Cu-Mo mineralization mainly include molybdenite, chalcopyrite, and pyrite, with disseminated, massive, and vein structures, while gangue minerals mainly include K-feldspar, quartz, epidote, and chlorite. Molybdenite occurs as coarse-grained clusters in quartz veins (Figures 4(d) and 4(e)) and as a disseminated mineral (Figure 4(a)) and veinlets in granite porphyry (Figure 4(f)). Molybdenite either exists as independent aggregates (Figures 4(d), 4(g), and 4(h)) or is associated with chalcopyrite and pyrite (Figures 4(e) and 4(i)). Wallrock alteration includes silicification, argillization, sericitization, chloritization, epidotization, and biotitization. Silicification and potassic feldspar are closely related to molybdenum mineralization. The alteration of the

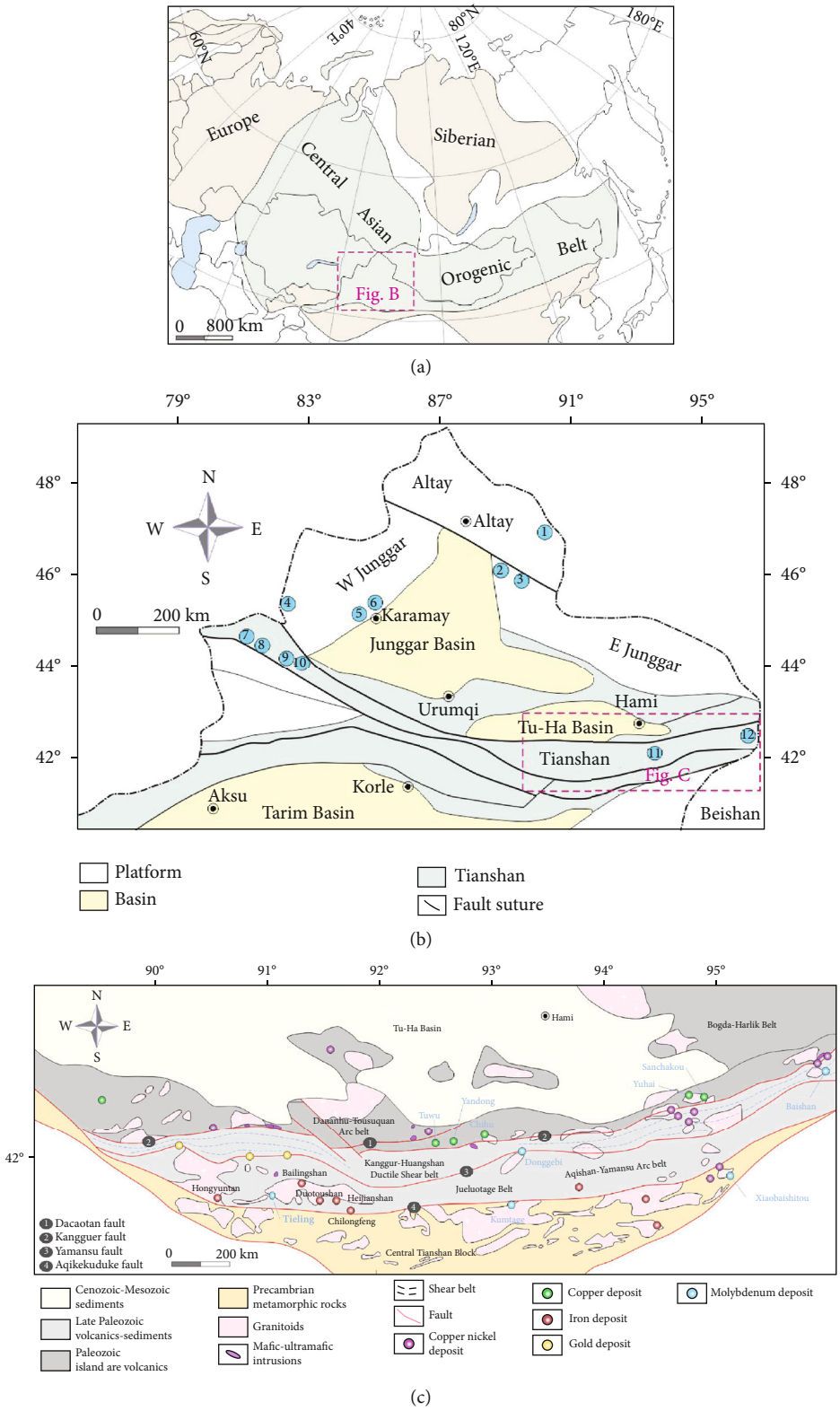

Figure 1: (a) Simplified map of the CAOB; (b) tectonic framework and representative deposits in northern Xinjiang; (c) simplified geological map of the eastern Tianshan showing the distribution of representative deposits (modified from Wang et al. [16]). 1: Asikaerte; 2: Suoerkuduke; 3: Yulekenhalasu; 4: Suyunhe; 5: Baogutu; 6: Hongyuan; 7: Dabate; 8: Kekesai; 9: Lailisigaoer; 10: Kendenggaoer; 11: Donggebi; 12: Baishan.

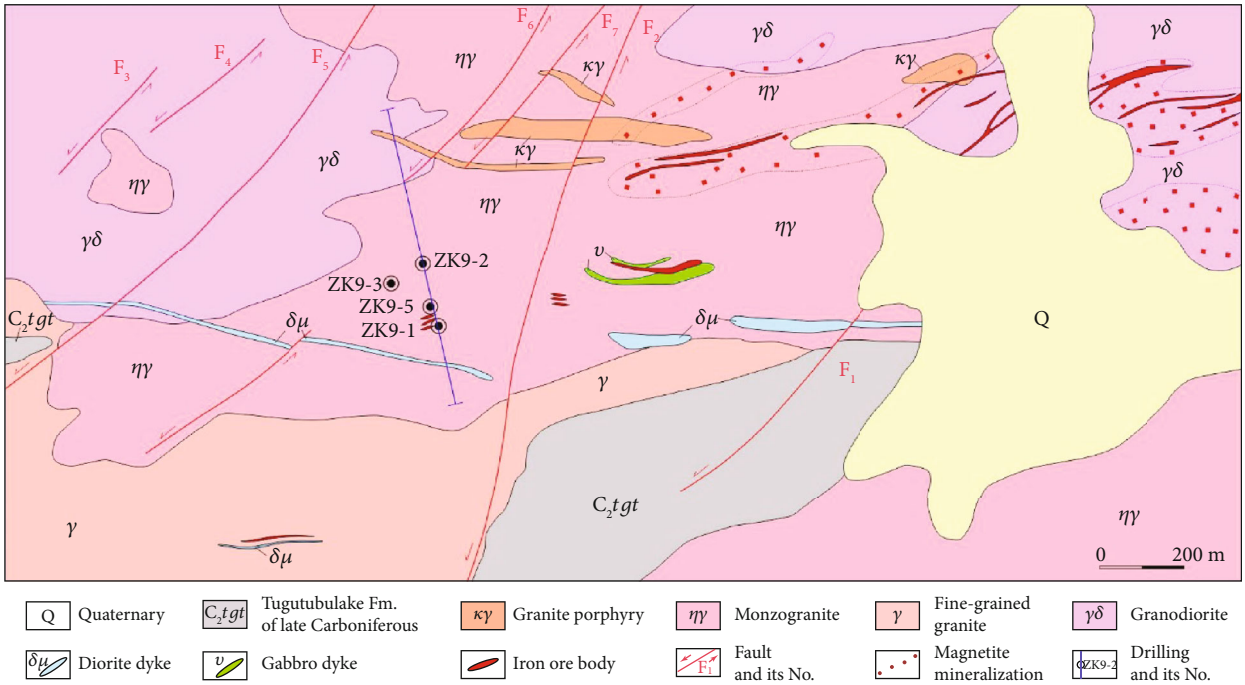

Figure 2: Simplified geological map of the Tieling Cu-Mo deposit (modified from Geological Survey Academy of Xinjiang, 2008).

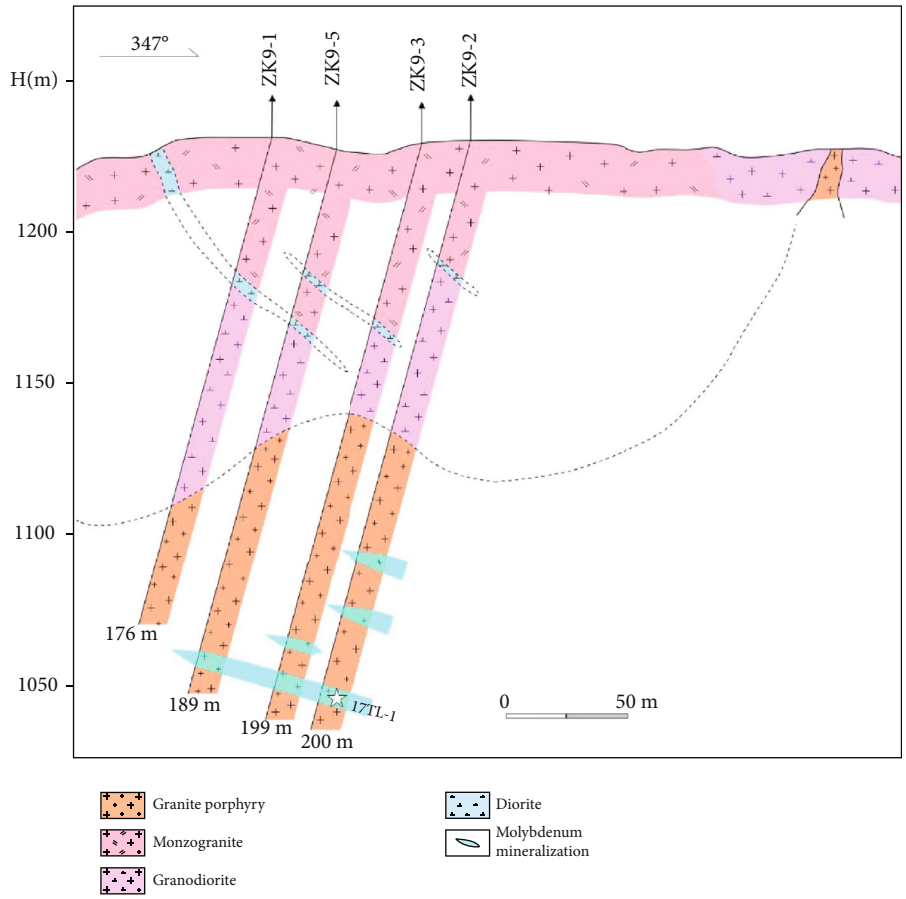

Figure 3: The geological section along the no. 9 exploration line on the map with lithologies and orebodies.

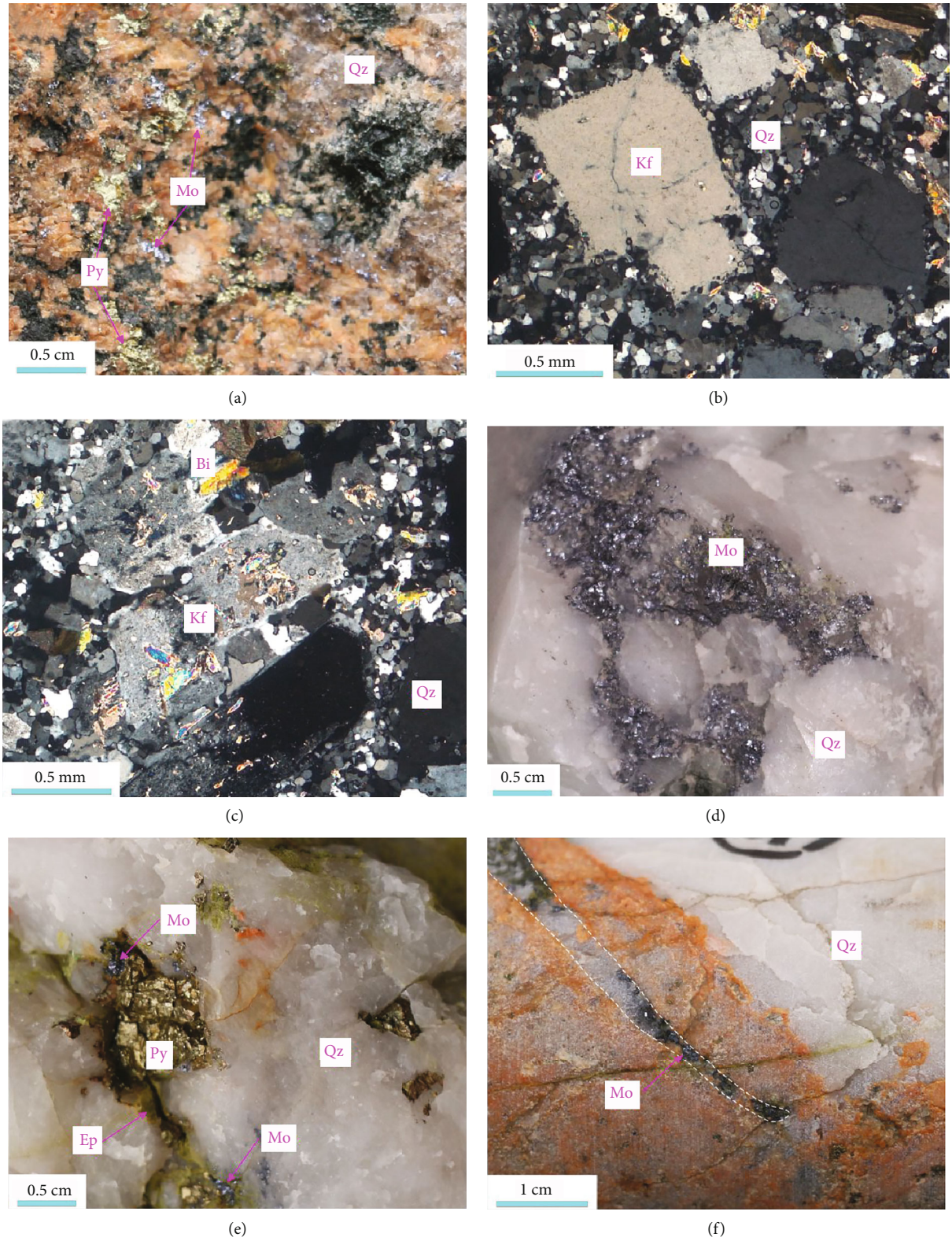

Figure 4: Continued.

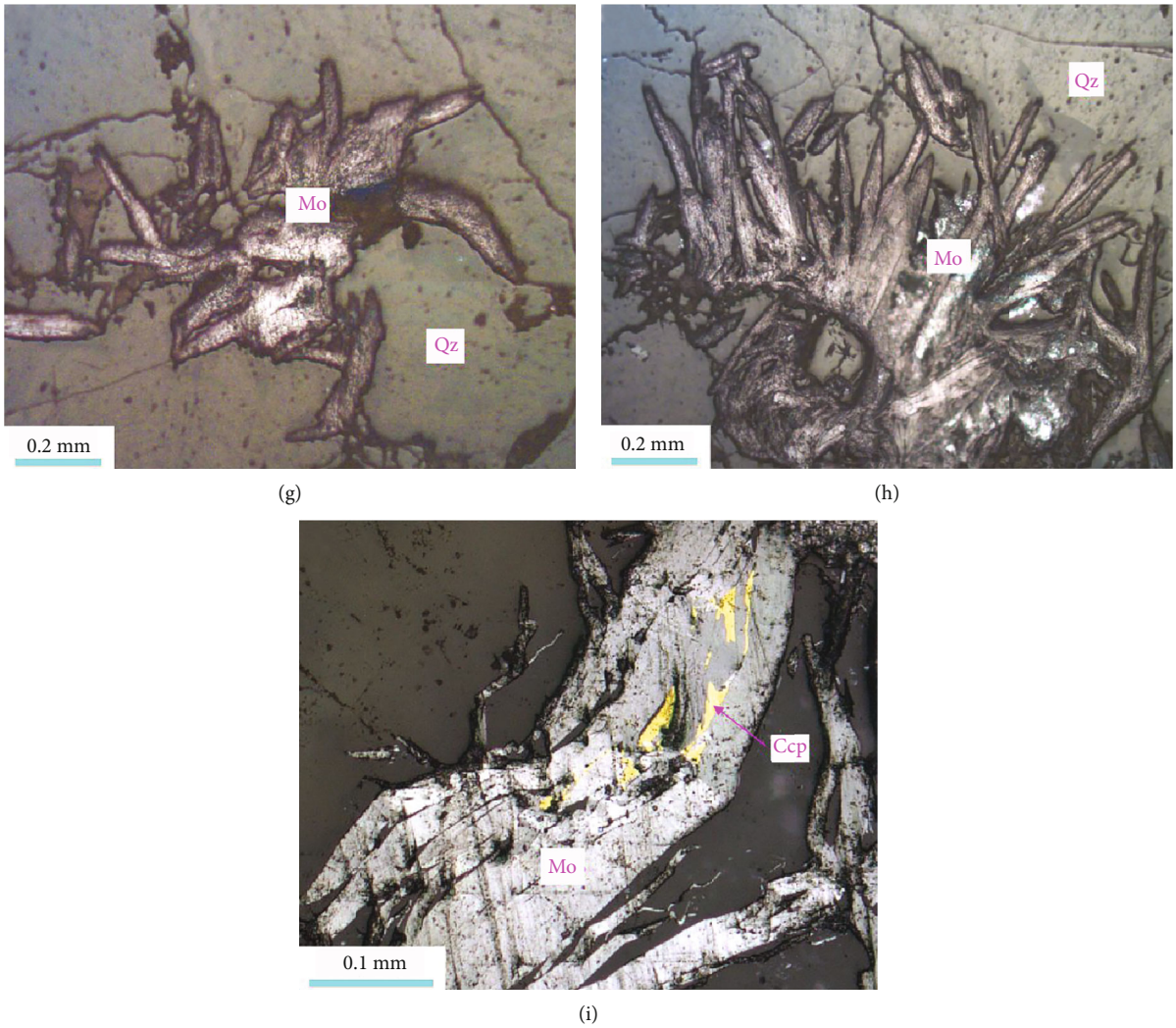

Figure 4: Characteristics of the rocks and ore minerals of the Tieling Cu-Mo deposit. (a) Disseminated molybdenite and pyrite in granite porphyry; (b) porphyritic texture of granite porphyry; (c) porphyritic texture of granite porphyry; (d) molybdenite in quartz vein; (e) molybdenite and pyrite coexisting in quartz vein and epidote fills in fissures; (f) veinlet molybdenite in granite porphyry; (g) molybdenite in quartz vein; (h) fascicular molybdenite in quartz vein; (i) molybdenite and chalcopyrite coexisting with quartz. Qz: quartz; Kf: K-feldspar; Ep: epidote; Bi: biotite; Mo: molybdenite; Py: pyrite; Ccp: chalcopyrite.

surrounding rock shows spatial zonation. From the granite porphyry to the surrounding rock, the alteration varies from a potassium silicate zone to a sericitization zone and finally a propylitization zone.

Based on field and microscopic observation of the mineralogy and the textural and paragenetic relationships of various hydrothermal minerals, three paragenetic stages of mineralization were identified in the Tieling deposit (Figure 5). These sequences are quartz+K-feldspar+pyrite +molybdenite±magnetite (stage I), quartz+molybdenite +pyrite+chalcopyrite (stage II), and quartz+pyrite+epidote ±molybdenite±chlorite (stage III).

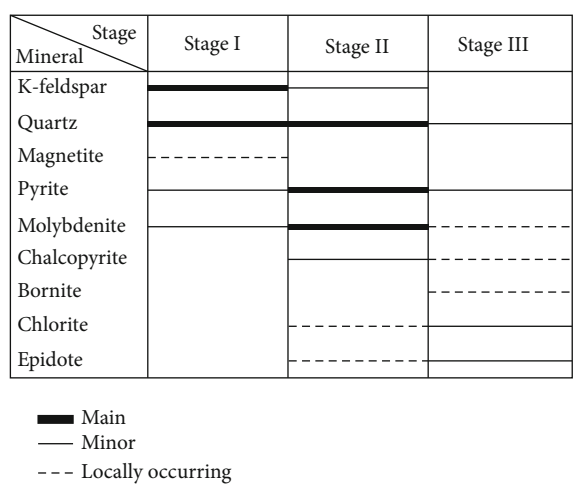

Figure 5: Paragenetic sequence of the Tieling Cu-Mo deposit.

4. Sampling and Analytical Methods

4.1. Zircon U-Pb Isotopes. The zircon U-Pb isotope samples were collected from bearing molybdenite granite porphyry at a depth of 188 m in drill hole no. ZK9-2. Zircon grains

were separated using heavy liquid and magnetic techniques, hand-picked under a binocular microscope, and mounted in epoxy resin. The internal texture of the zircons (including zoning, structures, and fractures) was characterized via cathodoluminescence (CL) imaging using a CAMECA electron microprobe at Yujin Technology Co., Ltd. U-Pb isotope analysis was performed at the State Key Laboratory of Mineral Deposits Research, Nanjing University, using an Agilent 7500a laser ablation system coupled with an iCAP RQ ICP-MS. The analytical spot size, laser frequency, and energy density were 32 mm, 5 Hz, and 6.5 J/cm^2, respectively. The analytical drift of the U-Th-Pb isotopic ratios was corrected using linear interpolation (with time) for every twelve analyses based on the signal variations of the zircon standard GJ1. Weighted mean age calculations and concordia diagrams were processed using ISOPLOT software [43].

4.2. Fluid Inclusion Microthermometry and Laser Raman Spectroscopy. The mineral assemblage and its paragenetic sequence were observed in the field and under the microscope for dividing three metallogenic stages. However, due to the low degree of exploration, we did not collect representative stage I samples for fluid inclusion study. Therefore, five samples comprising quartz veins of the stage II and stage III were selected, of which samples 20TL-3-78, 20TL-3-80, 20TL-3-83, and 20TL-3-87 were collected at depths of 78 m, 80 m, 83 m, and 87 m in drill hole no. ZK9-3, respectively. Sample 20TL-2-167 was collected at a depth of 167 m in drill hole no. ZK9-2.

Fluid inclusion analyses were carried out at the Laboratory of Mineralization and Dynamics, Chang'an University, Xi'an, China, using the fluid inclusion assemblage (FIA). Microthermometric measurements were conducted using a Linkam THMSG 600 heating-freezing stage mounted on a Leica DMR microscope. The estimated accuracies of the freezing and heating measurements were ±0.1°C from -100°C to 25°C, ±1°C from 25°C to 400°C, and ±2°C above 400°C. Heating and freezing rates were generally 0.2-5°C/min and were reduced to 0.2°C/min near the temperatures of phase change. The salinity of aqueous fluid inclusions was estimated using equations for the NaCl-H_2O system provided by Bodnar [44]. The density of the ore-forming fluid was estimated using data provided by Liu and Shen [45]. Volatile components of representative fluid inclusions were identified using a HORIBA HR Evolution 800 mm laser Raman spectrometer at the same institution. The laser wavelength was 532 nm, and the single spectrum collection time was 2 s. The Raman shift ranged from 100 cm^{-1} to 4000 cm^{-1}. The spectrum resolution was ±2 cm^{-1} with a beam size of 1 μm. The instrumental setting was kept constant during all analyses.

4.3. H-O-S Isotopic Systematics. Five quartz samples from stage II and stage III were analysed for O (quartz) and H (water from fluid inclusions) isotopes. Their acquisition location corresponds to that of the fluid inclusions. Seven pyrite samples and one chalcopyrite sample were analysed for S isotopes. Of these, samples 20TL-1-160 and 20TL-1-166 of stage I were collected from 160 m and 166 m drilling cores underground in drill hole no. ZK9-1, respectively. Samples 20TL-3-78, 20TL-3-87, 20TL-2-26, and 20TL-5-54 of stage II were collected from 78 m, 87 m, 26 m, and 54 m drilling cores underground in drill hole nos. ZK9-3, ZK9-2, and ZK9-5, respectively. Sample 20TL-2-167 was collected from a 167 m drilling core underground in drill hole no. ZK9-2. Samples 20TL-3-83 of stage III were collected from an 83 m drilling core underground in drill hole no. ZK9-3.

The δD values of water from fluid inclusions and the δ^{18}O values of their host minerals were measured at the Beijing Research Institute of Uranium Geology, China. The water contained in the fluid inclusions of the host minerals was released via thermal decrepitation at 400°C and then collected, frozen, and purified. Then, using reductive zinc, we replaced and released the hydrogen in the water to perform mass spectrometry. The analytical precision of the δD values was within ±2‰ (1σ) and that of the δ^{18}O values was within ±0.2‰ (2σ). The δ^{18}O values in quartz water ($\alpha_{\text{quartz water}}$) were calculated from the $\delta^{18}O_{\text{quartz}}$ values of the analysed quartz by using the fractionation equation $1000\text{In}\alpha_{\text{quartz water}} = (3.38 \times 10^6)T^{-2} - 3.40$, where T is the temperature in Kelvin [46], and the average corrected temperature of fluid inclusion was used to calculate the $\delta^{18}O_{\text{water}}$ value.

We separated the pyrite and chalcopyrite samples from the disseminations, veins, and crumb ores for sulfur isotope analysis. Sulfur isotopic analyses were carried out on a MAT253 mass spectrometer at the Beijing Research Institute of Uranium Geology, China. Seven pyrite samples and one chalcopyrite sample were converted to SO_2 under high-temperature vacuum conditions. The δ^{34}S values were measured on a DELTA V plus gas isotope mass spectrometer. Sulfur isotope values are reported in per mil relative following the Vienna Canyon Diablo Troilite (V-CDT) standard, and the analytical uncertainty was within ±0.2‰ for δ^{34}S. The equilibrium temperature of sulfur isotopes was calculated from symbiotic sulfides by using the fractionation equation $1000\text{In}\alpha_{\text{Py-Ccp}} = 0.45 \times 10^6/T^{-2}$, where T is the temperature in Kelvin [47].

5. Results

5.1. Zircon U-Pb Isotopes. The granite porphyry (TL1) was dated by zircon U-Pb analysis. LA-ICP-MS zircon U-Pb dating results are summarized in Table 1, and representative CL images of zircon grains from these rocks are shown in Figure 6. All the analysed zircons are prismatic, euhedral, and colourless, and most of them show oscillatory zoning patterns, which imply a magmatic origin. The analysed zircons have variable U (37-433 ppm) and Th (164-547 ppm) contents, with Th/U ratios ranging from 0.22 to 0.81 (mainly >0.1). Twenty-four zircon grains from the granite porphyry samples define a narrow range with ^{206}Pb/^{238}U ages of 296 to 298 Ma, yielding a concordant age of 298.4 ± 0.7 Ma (MSWD = 28; Figure 7(a)), with a weighted mean age of 297.0 ± 1.6 Ma (MSWD = 0.027; Figure 7(b)).

5.2. Fluid Inclusions. Based on phase characteristics at room temperature, phase transitions during heating and cooling,

Table 1: LA-ICP-MS U-Pb data of zircon grains from granite porphyry of the Tieling deposit.

Spot	Th (ppm)	U (ppm)	Th/U	$^{207}Pb/^{206}Pb$		$^{207}Pb/^{235}U$		$^{206}Pb/^{238}U$		$^{207}Pb/^{206}Pb$		$^{207}Pb/^{235}U$		$^{206}Pb/^{238}U$	
				Ratio	1σ	Ratio	1σ	Ratio	1σ	Age (Ma)	1σ	Age (Ma)	1σ	Age (Ma)	1σ
TL1-1	125	290	0.43	0.05308	0.00097	0.34501	0.00662	0.04715	0.00060	332	42	301	5	297	4
TL1-2	114	267	0.43	0.05142	0.00096	0.33475	0.00654	0.04723	0.00060	260	44	293	5	297	4
TL1-3	240	430	0.56	0.05241	0.00092	0.33954	0.00631	0.04699	0.00060	303	41	297	5	296	
TL1-4	131	314	0.42	0.05240	0.00094	0.33953	0.00645	0.04700	0.00060	303	42	297	5	296	
TL1-5	325	445	0.73	0.05252	0.00092	0.34024	0.00631	0.04699	0.00060	308	41	297	5	296	
TL1-6	120	286	0.42	0.05228	0.00097	0.34071	0.00661	0.04727	0.00060	298	43	298	5	298	4
TL1-7	118	283	0.42	0.05336	0.00106	0.34709	0.00715	0.04718	0.00061	344	46	303	5	297	4
TL1-8	87	222	0.39	0.05326	0.00103	0.34701	0.00703	0.04726	0.00061	340	45	302	5	298	4
TL1-9	433	543	0.80	0.05352	0.00089	0.34704	0.00624	0.04703	0.00061	351	38	302	5	296	
TL1-10	169	351	0.48	0.05321	0.00085	0.34663	0.00606	0.04725	0.00061	338	37	302	5	298	4
TL1-11	123	311	0.40	0.05453	0.00093	0.35556	0.00654	0.04729	0.00061	393	39	309	5	298	4
TL1-12	74	197	0.38	0.05334	0.00105	0.34691	0.00721	0.04718	0.00062	343	46	302	5	297	4
TL1-13	160	333	0.48	0.05445	0.00097	0.35422	0.00675	0.04719	0.00062	390	41	308	5	297	4
TL1-14	286	547	0.52	0.05375	0.00080	0.34948	0.00576	0.04716	0.00061	361	34	304	4	297	4
TL1-15	190	368	0.52	0.05497	0.00089	0.35743	0.00631	0.04716	0.00061	411	37	310	5	297	4
TL1-16	115	277	0.42	0.05524	0.00094	0.35890	0.00659	0.04713	0.00061	422	39	311	5	297	4
TL1-17	71	198	0.36	0.05304	0.00104	0.34557	0.00718	0.04726	0.00063	331	46	301	5	298	4
TL1-18	76	210	0.36	0.05192	0.00097	0.33791	0.00673	0.04721	0.00063	282	44	296	5	297	4
TL1-19	55	164	0.34	0.05330	0.00169	0.34612	0.00986	0.04709	0.00065	342	73	302	7	297	4
TL1-20	72	179	0.40	0.05386	0.00113	0.34990	0.00773	0.04712	0.00063	365	48	305	6	297	4
TL1-21	90	229	0.39	0.05264	0.00101	0.34278	0.00702	0.04723	0.00063	313	45	299	5	297	4
TL1-22	112	242	0.46	0.05449	0.00105	0.35444	0.00723	0.04718	0.00063	391	44	308	5	297	4
TL1-23	179	417	0.43	0.05491	0.00086	0.35730	0.00616	0.04720	0.00062	409	36	310	5	297	4
TL1-24	154	390	0.39	0.05225	0.00085	0.33868	0.00601	0.04702	0.00062	296	38	296	5	296	

and the results of laser Raman spectroscopy, fluid inclusions in the Tieling deposit mainly include liquid-rich inclusions (WL type). Fluid inclusions occurring as isolated inclusions, random distributions, or clusters are interpreted as primary features at various stages (Figure 8). Each cluster or group of fluid inclusions along growth zones was considered to represent an FIA. Fluid inclusions occurring in linear arrays along fractures or grain boundaries were considered to be secondary fluid inclusions, which were not analysed by microthermometry because they formed later with respect to mineralization. The inclusions are ovular, polygonal, and irregular, with diameters in the range of 3-18 μm, mainly 5-10 μm, and contain gas bubbles that account for 10-40% of the total volume. These inclusions homogenize to the liquid phase when heated.

The microthermometric results and fluid inclusion parameters are shown in Table 2. For the fluid inclusions in quartz of stage II, the final ice melting temperatures of WL-type fluid inclusions range from -13.8 to -4.5°C (with an average of -9.1°C), with corresponding salinities of 7.2 to 17.2 wt% NaCl equiv. (with an average of 12.9 wt% NaCl equiv.). The homogenization temperatures of fluid

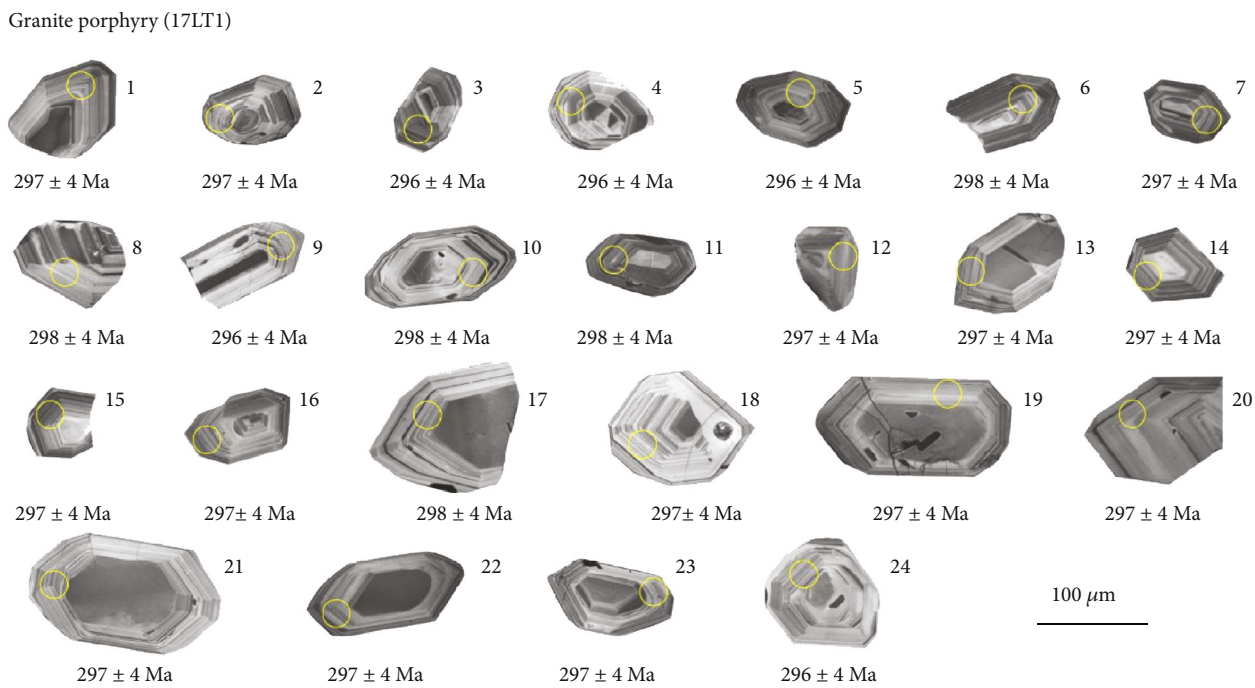

Figure 6: Cathodoluminescence (CL) images of representative zircons from granite porphyry in the Tieling deposit.

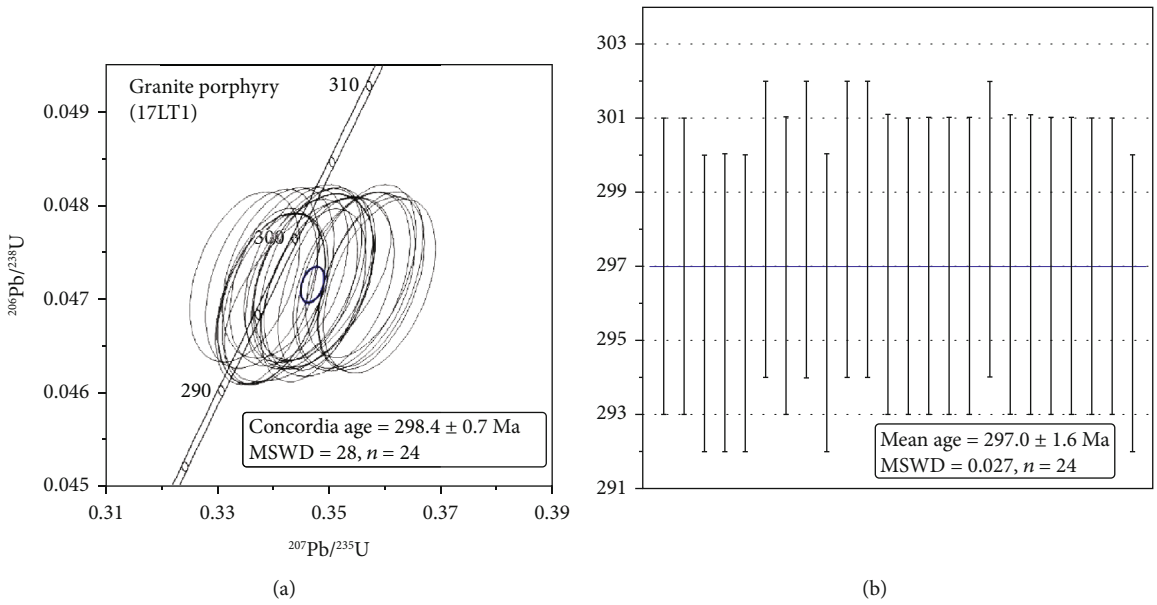

Figure 7: The U-Pb concordant diagram and the weighted average age of zircons from granite porphyry in the Tieling deposit.

inclusions range from 157 to 262°C (with an average of 193.1°C), and the fluid densities are 0.897 to 1.025 g/cm^3. For the fluid inclusions in quartz (samples 20TL-3-83) of stage III, the final ice melting temperature of WL-type fluid inclusions is -6.3 to -3.6°C (with an average of -5.0°C), the salinity is 5.9 to 9.6 wt% NaCl equiv. (with an average of 7.9 wt% NaCl equiv.), the homogenization temperatures of fluid inclusions range from 135 to 173°C (with an average of 154.2°C), and the fluid densities are 0.959 to 0.995 g/cm^3. Previous studies indicate that the emplacement depths for porphyry deposits are generally around 3-5 km [48]. Due to lack of pressure data for this deposit, we used the lithostatic pressure at 5 km to calculate the entrapment temperatures of the analysed fluid inclusions. The fluid lithostatic pressure of the Tieling deposit can be estimated to be 1350 bar. Then, the average ore-forming temperatures of stage II and stage III were corrected to range from 268°C to 225°C (Figure 9).

We conducted a laser Raman spectroscopic speak scan of the gas-phase components in the fluid inclusions of quartz from the Tieling deposit. The results of representative laser Raman spectroscopic analyses are shown in Figure 10. The

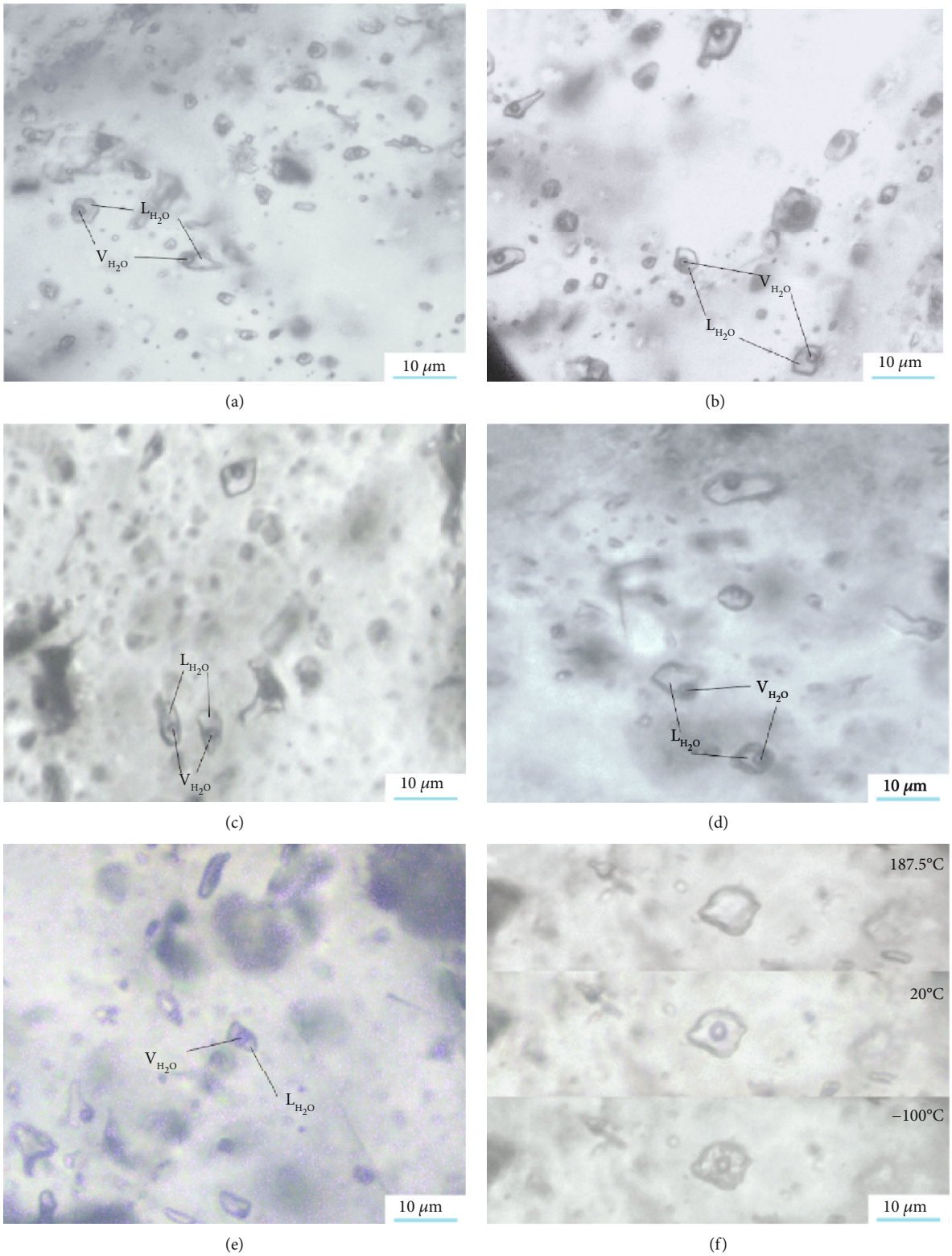

Figure 8: Photomicrographs of representative fluid inclusions in quartz crystals from the Tieling Cu-Mo deposit: (a) liquid-rich inclusions in quartz of stage II; (b) liquid-rich inclusions in quartz of stage II; (c) liquid-rich inclusions in quartz of stage II; (d) liquid-rich inclusions in quartz of stage II; (e) liquid-rich inclusions in quartz of stage III; and (f) morphology of liquid-rich inclusions in quartz at different temperatures. L_{H2O}: liquid-phase H_2O; V_{H2O}: vapor-phase H_2O.

Table 2: Microthermometry data and relative parameters of fluid inclusions in the Tieling deposit.

Sample no.	Location	Mineral	Type	Size(μm)	V (%)	No.	$T_{m\,(ice)}$ (°C)	T_h (°C)	T_c (°C)	Salinity (% NaCl equiv.)	Density (g/cm^3)
Quartz of stage II											
20TL-3-78	ZK9-3/78 m	Quartz+pyrite	WL	5-14	10-60	28	-13.2 to -6.7	182 to 262	251 to 355	10.1 to 17.2	0.897 to 1.013
20TL-3-80	ZK9-3/80 m	Quartz+pyrite +chalcopyrite	WL	6-15	10-45	16	-12.8 to -7.2	157 to 242	224 to 328	10.7 to 16.8	0.934 to 1.025
20TL-3-87	ZK9-3/87 m	Quartz+pyrite +molybdenite	WL	5-15	10-40	23	-13.8 to -4.5	168 to 222	237 to 301	7.2 to 17.1	0.922 to 1.019
20TL-2-167	ZK9-2/167 m	Quartz+molybdenite	WL	6-12	10-40	21	-12.8 to -6.1	165 to 250	232 to 340	9.3 to 16.8	0.906 to 0.999
Quartz of stage III											
20TL-3-83	ZK9-3/83 m	Quartz	WL	3-8	10-20	21	-6.3 to -3.6	135 to 173	201 to 246	5.9 to 9.6	0.959 to 0.995

$T_{m\,(ice)}$: final melting temperature of ice; T_h: total homogenization temperature; T_c: corrected temperature; V: percentage of bubble volume.

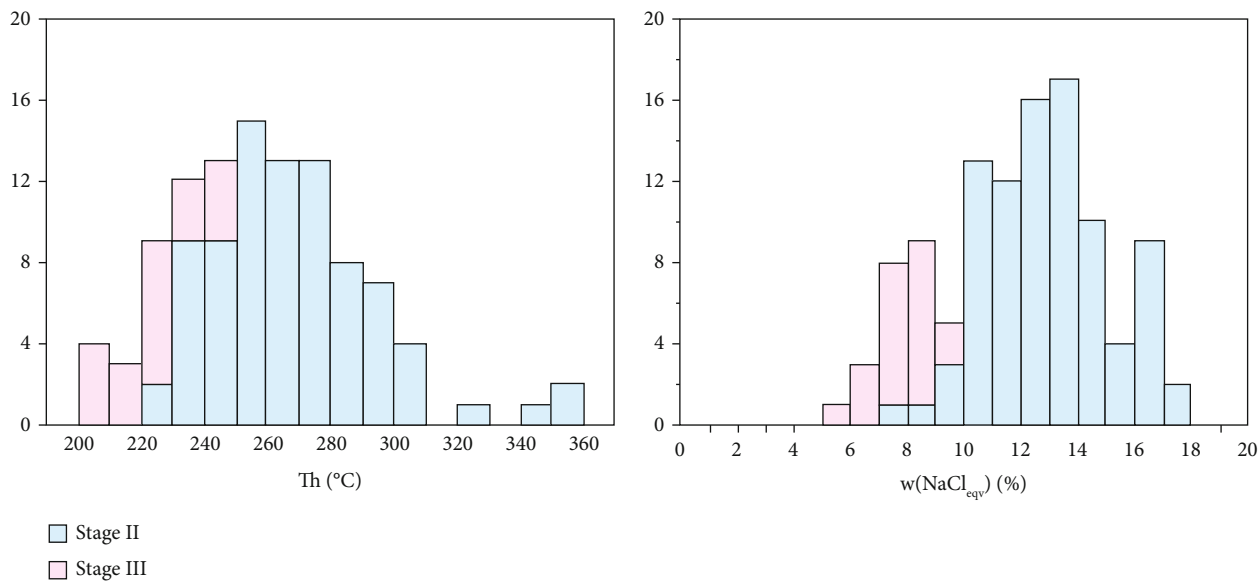

Figure 9: Histograms of homogenization temperatures and salinities of fluid inclusions in the Tieling Cu-Mo deposit. T_h: total homogenization temperature.

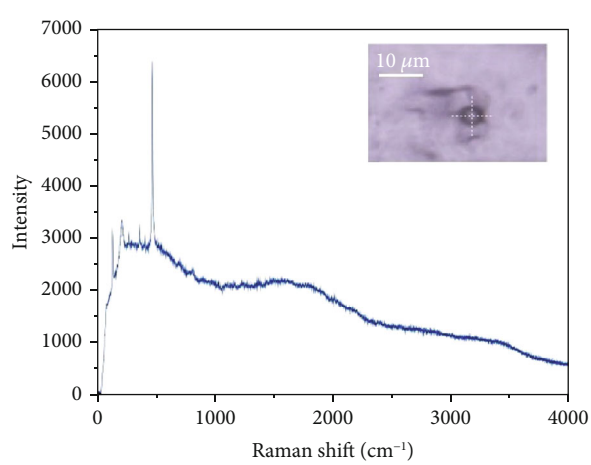

Figure 10: Laser Raman spectra of vapor-phase composition of WG-type fluid inclusions of the Tieling Cu-Mo deposit.

primary gas component of WL-type fluid inclusions in quartz veins is mainly H_2O.

5.3. H-O-S Isotopes. The hydrogen and oxygen isotope data of the host minerals and water from fluid inclusions are summarized in Table 3. The $\delta D_{H2O(V\text{-}SMOW)}$ values of quartz in four samples from stage II range from −79.5‰ to −63.3‰, the $\delta^{18}O_{Q(V\text{-}SMOW)}$ values of quartz range from 8.8‰ to 9.5‰, and the calculated $\delta^{18}O_{H2O(V\text{-}SMOW)}$ values of quartz range from 0.5‰ to 1.3‰. The $\delta D_{H2O(V\text{-}SMOW)}$ value of quartz in one sample from stage III is −67.6‰, the $\delta^{18}O_{Q(V\text{-}SMOW)}$ value is 9.1‰, and the calculated $\delta^{18}O_{H2O(V\text{-}SMOW)}$ value is 1.1‰.

Sulfur isotopic analysis on the Tieling deposit yielded pyrite and chalcopyrite. The sulfur isotopic compositions of seven pyrite samples and one chalcopyrite sample were analysed, and the corresponding measured $\delta^{34}S_{V\text{-}CDT}$ values

Table 3: Hydrogen, oxygen, and sulfur isotopic compositions of the Tieling Cu-Mo deposit.

Sample no.	Location	Stage	Mineral	$\delta^{18}O_Q$ (‰)	T_c (°C)	δD_{H2O} (‰)	$\delta^{18}O_{H2O}$ (‰)	$\delta^{34}S_{CDT}$ (‰)
20TL-1-160	ZK9-1/160 m	Stage I	Pyrite					-0.8
20TL-1-166	ZK9-1/166 m	Stage I	Pyrite					-1.1
20TL-3-78	ZK9-3/78 m	Stage II	Quartz	8.9	282	-63.9	1.3	
			Pyrite					0.2
20TL-3-80	ZK9-3/80 m	Stage II	Quartz	9.5	249	-63.3	0.5	
20TL-3-87	ZK9-3/87 m	Stage II	Quartz	8.8	266	-67.7	0.6	
			Pyrite					1.3
20TL-2-26	ZK9-2/26 m	Stage II	Pyrite					1.4
20TL-2-167	ZK9-2/167 m	Stage II	Quartz	9.3	267	-79.5	1.1	
20TL-5-54	ZK9-5/54 m	Stage II	Pyrite					-1.6
			Quartz	9.1	225	-67.6	-1.1	
20TL-3-83	ZK9-3/83 m	Stage III	Pyrite					1.4
			Chalcopyrite					-0.1
D443/2		Stage I	Pyrite					-1.5
D434/1		Stage I	Pyrrhotite					0.5
D436/1		Stage I	Pyrrhotite					0.1

of minerals are listed in Table 3. The eight $\delta^{34}S_{V\text{-}CDT}$ values of the samples vary narrowly from −1.6‰ to 1.4‰. The sulfur isotopic compositions of the disseminations, veins, and crumb ores are symmetrical and cluster near zero. The equilibrium temperature of symbiotic sulfides between the pyrite and chalcopyrite crystals was 275°C.

6. Discussion

6.1. Sources of Hydrothermal Fluid and Sulfur

6.1.1. Sources of Hydrothermal Fluid. The fluid inclusions show that the ore-forming fluid has the characteristics of a relatively medium-low temperature, medium-high salinity, and medium-high density and represents a NaCl-H_2O system. The average corrected mineralization temperatures of stage II and stage III range from 268°C to 225°C, which is consistent with the equilibrium temperature of sulfur isotopes (275°C) and indicates that the corrected mineralization temperature is within the acceptable error range. The $\delta^{18}O$ values of quartz in the Tieling deposit range from 8.8‰ to 9.5‰, with an average value of 9.1‰ (Table 2), which is consistent with those of crustal remelting granite (10.0–12.0‰ [49]), indicating that the formation of hydrothermal quartz was associated with Carboniferous felsic intrusive rocks and was derived from magmatic fluids. The δD values of the fluids in the Tieling deposit mostly range from −79.5‰ to −63.3‰ (Table 3) and approach those of magmatic water and meteoric water [50, 51]. The H-O isotope data of stages II and III plot between the primary magmatic water field and the meteoric water line (Figure 11), which is similar to other deposits in the same metallogenic belt [25, 52–57], indicating that the ore-forming fluids of the Tieling Cu-Mo deposit were derived from Carboniferous magmatic hydrothermal fluids and then mixed with meteoric water.

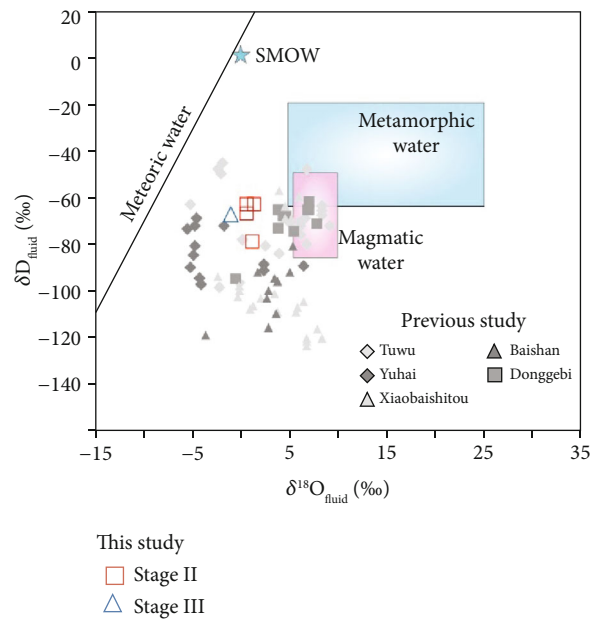

Figure 11: δD_{fluid} vs. $\delta^{18}O_{fluid}$ values from various stages in the Tieling Cu-Mo deposit. Fields for magmatic and metamorphic water are from Taylor [50] and Sheppard [51]. The data of previous studies were referenced from Zhang et al. [54], Zhang et al. [25], Liu et al. [55], Wang et al. [56], and Li et al. [57].

6.1.2. Sources of Sulfur. The sulfide assemblage in the Tieling deposit is dominated by molybdenite and pyrite with minor chalcopyrite, and no sulfate minerals have been detected. Therefore, the hydrothermal system during the ore-forming process in the Tieling deposit was dominated by H_2S. Molybdenite, pyrite, and chalcopyrite were formed under low-f_{O2} and low-pH conditions [58]. According to Table 3, the average $\delta^{34}S_{V\text{-}CDT}$ value for the seven pyrite samples collected from the Tieling deposit is 0.1‰, and

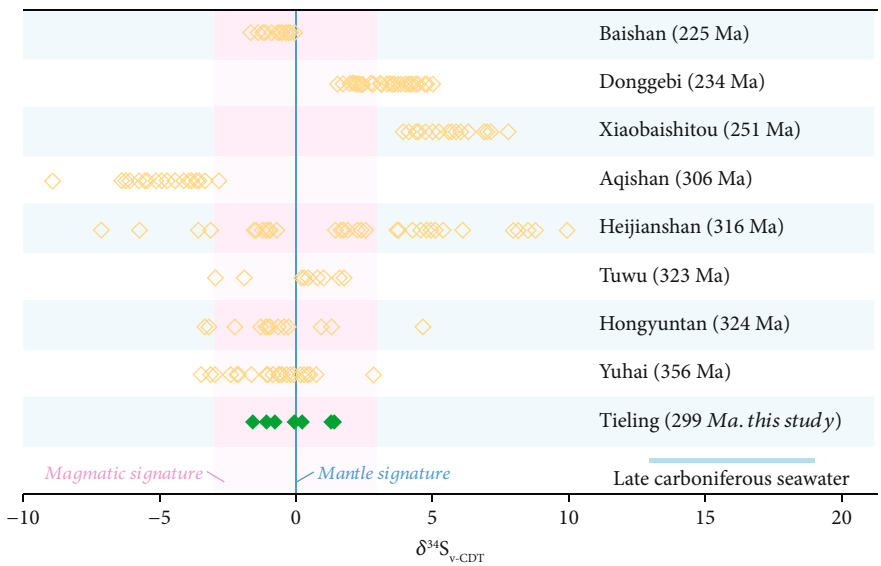

Figure 12: $\delta^{34}S_{V\text{-}CDT}$ values of ore-forming fluids at Tieling and other major deposits in eastern Tianshan. Sulfur isotopic compositions of global seawater in the Late Carboniferous were modified after Holser [63]. Sulfur isotopic compositions of representative deposits were modified after Han et al. [14], Wang et al. [16], Zhang et al. [25], Sun et al. [39], Zhang et al. [54], Wang et al. [56], Dai et al. [61], and Zhao et al. [62].

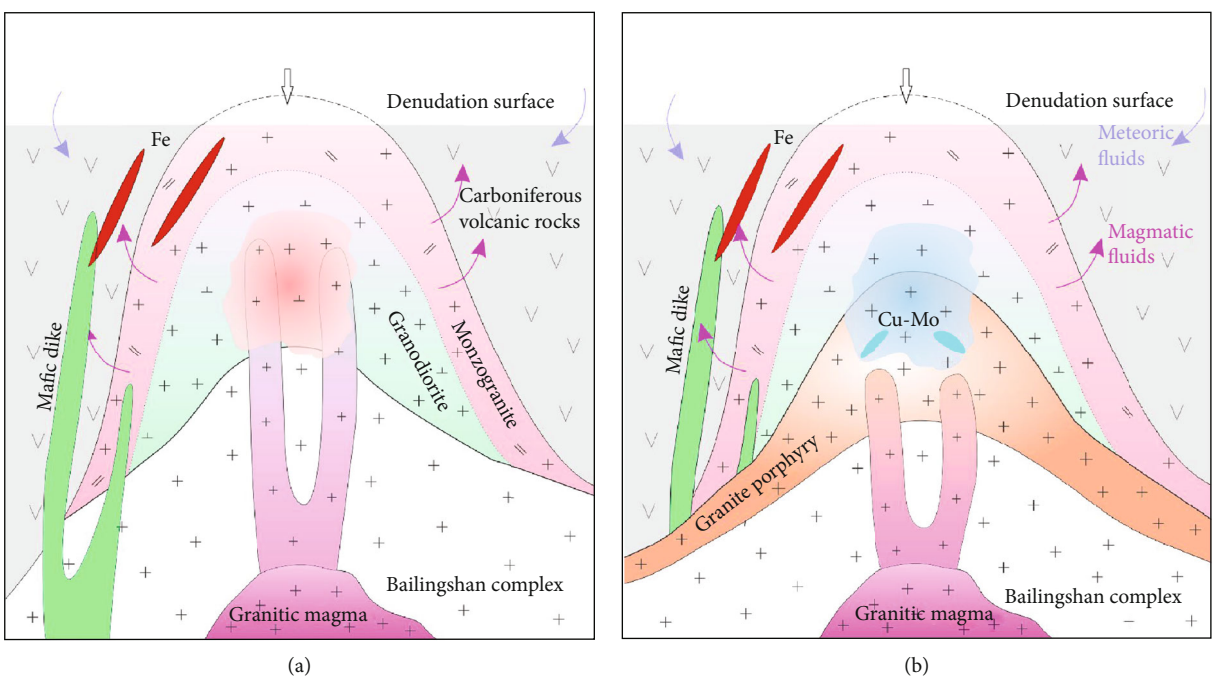

Figure 13: The metallogenic model of the Tieling copper-molybdenite deposit: (a) iron mineralization period in the early Late Carboniferous; (b) copper-molybdenum mineralization at the end of the Late Carboniferous.

the $\delta^{34}S_{V\text{-}CDT}$ value for one chalcopyrite sample is -0.1‰. The basic sequence is consistent with the $\delta^{34}S$ enrichment condition of $\delta^{34}S_{Py} > \delta^{34}S_{Ccp}$ at isotopic equilibrium, indicating that the mineral S isotopes had reached equilibrium [59]. Therefore, the S isotopic compositions of pyrite are close to the total S isotopic compositions of the hydrothermal system and can be used to trace S sources. The overall range of the $\delta^{34}S_{V\text{-}CDT}$ values of sulfides in the Tieling deposit is narrow, indicating that the S sources of sulfides deposited in the ore-forming hydrothermal fluids were undiversified. The $\delta^{34}S_{V\text{-}CDT}$ values are consistent with those of felsic magma [60] and other representative deposits related to magmatism [14, 16, 25, 39, 54, 56, 61, 62], indicating that the sulfur in the Tieling deposit was mainly derived from Late Carboniferous felsic magma (Figure 12).

Table 4: Molybdenite Re-Os isochron ages of Mo deposits in northern Xinjiang, NW China.

No.	Deposit	Type	Metal	Size	Method	Age (Ma)	Reference
Altay							
1	Asikaerte	Porphyry	Be, Mo	Large	Molybdenite Re-Os	218.6 ± 1.3 228.7 ± 7.1	Wang et al. [74] Liu et al. [75]
East Junggar							
2	Suoerkuduke	Skarn	Cu, Mo	Medium	Molybdenite Re-Os	317.1 ± 7.6 305 ± 7	Liu and Liu [82] Wan et al. [84]
3	Xilekuduke	Porphyry	Cu, Mo	Medium	Molybdenite Re-Os	327.1 ± 2.9	Long et al. [81]
4	Yulekenhalasu	Porphyry	Cu, Mo	Medium	Molybdenite Re-Os	331.5 ± 4.8 357.3 ± 5.2 376.9 ± 2.2	Xiang et al. [85] Xue et al. [86]
5	Mengxi	Porphyry	Cu, Mo		Molybdenite Re-Os	411.6 ± 3.2	Qu et al. [87]
West Junggar							
6	Suyunhe	Porphyry	Mo	Giant	Molybdenite Re-Os	294.4 ± 1.7	Zhong et al. [78]
7	Baogutu	Porphyry	Cu, Mo	Large	Molybdenite Re-Os	310 ± 3.6	Song et al. [89]
8	Hongyuan	Porphyry	Mo		Molybdenite Re-Os	294.6 ± 4.6 314.3 ± 1.9	Li [79] Yan et al. [80]
West Tianshan							
9	Dabate	Porphyry	Cu, Mo	Small	Molybdenite Re-Os	300.3 ± 2.1 301 ± 20	Li [92] Zhang et al. [91]
10	Lailisigaoer	Porphyry	Cu, Mo	Small	Molybdenite Re-Os	379.9 ± 8.3 359 ± 8	Zhu et al. [90] Li et al. [93]
11	Kendenggaoer	Skarn	Cu, Mo	Small	Molybdenite Re-Os	313.9 ± 2.5	Jia [88]
East Tianshan							
12	Tuwu-Yandong	Porphyry	Cu, Mo	Large	Molybdenite Re-Os	323 ± 2 343 ± 26	Rui et al. [65] Zhang et al. [66]
13	Donggebi	Porphyry	Mo	Giant	Molybdenite Re-Os	233.2 ± 2.2 231.1 ± 1.5 231.9 ± 6.5 234.3 ± 1.6	Wu et al. [72] Tu et al. [94] Wu et al. [76] Han et al. [14]
14	Kumutage	Skarn	Mo		Molybdenite Re-Os	319.1 ± 4.5	Zhang et al. [95]
15	Yuhai	Porphyry	Cu, Mo	Small	Molybdenite Re-Os	355.7 ± 2.4	Wang et al. [17]
16	Sanchakou	Porphyry	Cu, Mo		Molybdenite Re-Os	416 ± 6.4 358 ± 6.2	Lin et al. [64] Liao and Lv [35]
17	Xiaobaishitou	Skarn	W, Mo		Molybdenite Re-Os	239.7 ± 3.6 251.4 ± 3.6 251.1 ± 1.6	Deng et al. [96] Li et al. [57]
18	Baishan	Porphyry	Mo	Giant	Molybdenite Re-Os	224.8 ± 4.5 227 ± 4.3 223.2 ± 2.7	Zhang et al. [25] Zhang et al. [73] Tu et al. [15]
19	Tieling	Porphyry	Cu-Mo		Molybdenite Re-Os Zircon U-Pb	299.0 ± 7.7 298.4 ± 0.7	Unpublished This study

6.2. Mineralization Age and Ore-Forming Process. In the early Paleozoic, porphyry Cu-Mo-Au deposits formed under the northward subduction of the Kanggur ocean basin, such as Sanchakou [64], Sanchakouxi [35], and Yudai [30]. During the Early Carboniferous, porphyry Cu-Mo deposits in the northern Kanggur belt, such as Yuhai and Tuwu [65, 66], formed under the north-south bidirectional subduction of the Kanggur ocean basin. At the same time, a series of iron ores related to magmatism were formed in the southern Kanggur belt, including those of the Bailingshan [67], Hongyuntan [39], and Duotoushan [68]. The ductile shear gold deposits were formed in Late Carboniferous [69], followed by abundant magmatic sulfide Cu-Ni under the postcollisional extensional environment of the Early Permian [70, 71]. After approximately ca. 240 Ma, porphyry Mo deposits related to Triassic granite porphyry in a postcollisional environment were formed, including the Baishan and Donggebi deposits [72, 73]. The zircon U-Pb age from ore-bearing

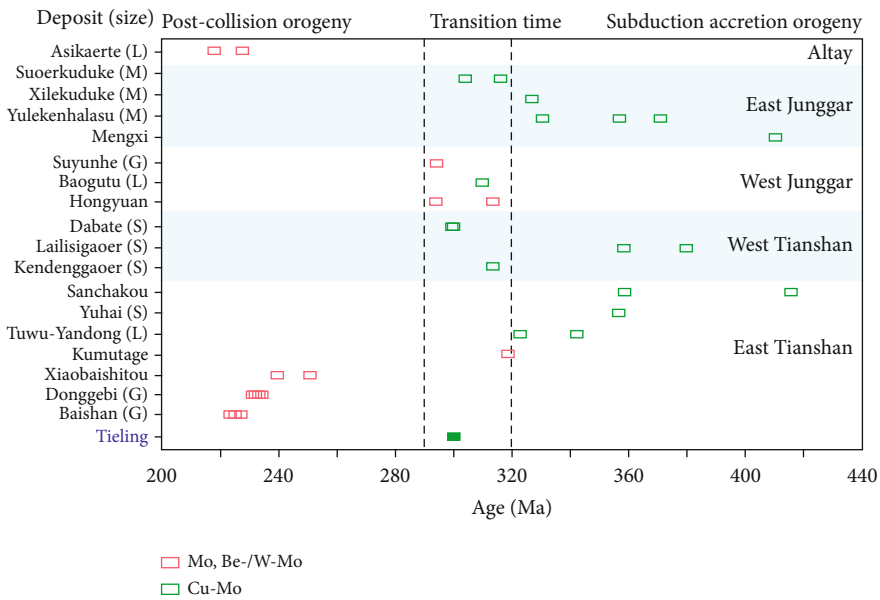

Figure 14: Re-Os isotopic ages from the Mo deposits in northern Xinjiang, NW China.

granite porphyry yields a concordant age of 298.4 ± 0.7 Ma, which is consistent with the molybdenite Re-Os isochron age (299.0 ± 7.7 Ma, in publishing). The chronology data of the two groups within error indicate that the Tieling Cu-Mo deposit was decidedly formed during the Late Carboniferous.

Previous studies have shown that the iron orebodies taking tabular or lensoid shapes of the Tieling deposit were hosted in monzogranite and granodiorite along fractures [42]. The formation of the iron orebodies was considered related to the Bailingshan complex generated by the southward subduction of the Kanggur oceanic plate beneath the Yili–Central Tianshan block during 324 to 303 Ma [42, 67], and Cu-Mo mineralization was supposed to have formed later than Fe mineralization. Therefore, the mineralization process of the Tieling deposit has been described as two distinct metallogenic periods, including Fe and Cu-Mo periods. The iron orebodies related to volcanic rocks were formed first in the strata during the subduction stage of the early Late Carboniferous [42]. With the emplacement of the Bailingshan complex, iron orebodies were formed in monzogranite and granodiorite and partially in the contact zone with skarnization (Figure 13(a)). Magnetite was found in the later basic dikes [37]. At the end of the Late Carboniferous, the hydrothermal fluids released from the ore-bearing granite porphyry in the late crystallization stage were mixed with meteoric water, resulting in precipitation mineralization in favourable structural positions (Figure 13(b)).

6.3. Geological Significance. The Mo deposits mainly include (W-/Be-) Mo and Cu-Mo types in northern Xinjiang on the southwestern margin of the CAOB (Table 4). The (W-/Be-) Mo-type deposits were formed in the Triassic period resulting from postcollisional orogeny and mainly distributed in Altay [74, 75] and eastern Tianshan [14, 25, 76, 77]. The (W-/Be-) Mo-type deposits distributed in West Junggar formed in the transition condition [78–80]. In addition, the Cu-Mo-type deposits formed before the Carboniferous were widely distributed in the northern region of Xinjiang [78–82]. All of them, including Suoerkuduke, Xilekuduke, Yulekenhalasu, and Mengxi in East Junggar [78, 79, 82–85]; Baogutu in West Junggar [86]; Dabate, Lailisigaoer, and Kendenggaoer in West Tianshan [87–91]; and Tuwu-Yandong, Yuhai, and Sanchakou in East Tianshan [17, 64–66], were related to subduction-related accretion orogeny. Notably, Mo mineralization in the eastern Tianshan was concentrated in the Triassic and before the Early Carboniferous, with the (W-/Be-) Mo type related to collisional orogeny and the Cu-Mo type related to subduction-related accretion orogeny (Figure 14). However, no significant Cu-Mo deposits were found in the transitional time between the Triassic and Early Carboniferous in eastern Tianshan. Perhaps more attention should be given to prospecting because there are abundant contemporaneous Cu-Mo deposits in West Junggar [86], East Junggar [79, 82], and West Tianshan [88, 89, 91, 92].

7. Conclusions

(1) The Tieling deposit is a porphyry system that exhibits three ore-forming stages, including quartz +K-feldspar+pyrite±molybdenite±magnetite (stage I), quartz+molybdenite+pyrite+chalcopyrite (stage II), and quartz+pyrite±molybdenite±epidote (stage III)

(2) The ore-forming fluids of the Tieling Cu-Mo deposit are characterized by medium-low temperatures (224 to 355°C in stage II and 201 to 246°C in stage III), medium-high salinities (7.2–17.2 wt% NaCl equiv. of stage II and 5.6 to 9.6 wt% NaCl equiv. of stage III), and a H_2O-NaCl composition

(3) The H-O-S isotopes indicate that the ore-forming fluids were derived from a mixture of magmatic hydrothermal water and meteoric water and the ore-forming materials were derived from Late Carboniferous felsic magma

(4) The zircon U-Pb of ore-bearing granite porphyry yields a concordant age of 298.4 ± 0.7 Ma, indicating that the Tieling Cu-Mo deposit was a rare metallogenic event in the Late Carboniferous of the eastern Tianshan, which should be given more attention for prospecting

Data Availability

The data used to support the findings of this study are available from the corresponding authors upon request.

Conflicts of Interest

The authors declare that there is no conflict of interest regarding the publication of this paper.

Acknowledgments

We thank Yonggang Feng and Wei Du from the Chang'an University for their help during fluid inclusion analyses, and we thank Senior Engineer Mu Liu from the Beijing Research Institute of Uranium Geology for her help during H-O-S isotope analyses. We also thank Wanzhi Yang, Ganggang Yang, Qiong Han, and Liuyuan Jin of the Xinjiang Geological Survey Academy for their support and assistance during the fieldwork. This work was financially supported by the Project of the China Geological Survey (Grant no. DD20190379), the Project of the Xinjiang Natural Science Youth Fund (Grant no. 2020D01B51), the National Key R&D Project of China (Grant No. 2018YFC0604001–04), and the Natural Science Basic Research Program of Shanxi (Grant no. 2020JQ-974).

References

[1] J. P. Richards, "Postsubduction porphyry Cu–Au and epithermal Au deposits: products of remelting of subduction-modified lithosphere," *Geology*, vol. 37, no. 3, pp. 247–250, 2009.

[2] F. Pirajno, R. E. Ernst, A. S. Borisenko, G. Fedoseev, and E. A. Naumov, "Intraplate magmatism in Central Asia and China and associated metallogeny," *Ore Geology Reviews*, vol. 35, no. 2, pp. 114–136, 2009.

[3] R. H. Sillitoe, "A plate tectonic model for the origin of porphyry copper deposits," *Economic Geology*, vol. 67, no. 2, pp. 184–197, 1972.

[4] C. R. Stern, M. A. Skewes, and A. Arevalo, "Magmatic evolution of the giant El Teniente Cu–Mo deposit, Central Chile," *Journal of Petrology*, vol. 52, no. 7-8, pp. 1591–1617, 2011.

[5] J. P. Richards, "High Sr/Y arc magmas and porphyry Cu ± Mo ± Au deposits: just add water," *Economic Geology*, vol. 106, no. 7, pp. 1075–1081, 2011.

[6] Z. Q. Hou, Z. M. Yang, X. M. Qu et al., "The Miocene Gangdese porphyry copper belt generated during post-collisional extension in the Tibetan orogen," *Ore Geology Reviews*, vol. 36, no. 1-3, pp. 25–51, 2009.

[7] Z. Q. Hou, H. R. Zhang, X. F. Pan, and Z. M. Yang, "Porphyry Cu (-Mo-Au) deposits related to melting of thickened mafic lower crust: examples from the eastern Tethyan metallogenic domain," *Ore Geology Reviews*, vol. 39, no. 1-2, pp. 21–45, 2011.

[8] J. P. Richards, "Magmatic to hydrothermal metal fluxes in convergent and collided margins," *Ore Geology Reviews*, vol. 40, no. 1, pp. 1–26, 2011.

[9] Y. J. Chen, "The development of continental collision metallogeny and its application," *Acta Petrologica Sinica*, vol. 29, no. 1, pp. 1–17, 2013.

[10] Y. J. Chen, P. Wang, N. Li, Y. F. Yang, and F. Pirajno, "The collision-type porphyry Mo deposits in Dabie Shan, China," *Ore Geology Reviews*, vol. 81, no. 2, pp. 405–430, 2017.

[11] P. Wang, Y. J. Chen, B. Fu, Y. F. Yang, M. Mi, and Z. L. Li, "Fluid inclusion and H–O–C isotope geochemistry of the Yaochong porphyry Mo deposit in Dabie Shan, China: a case study of porphyry systems in continental collision orogens," *International Journal of Earth Sciences*, vol. 103, no. 3, pp. 777–797, 2014.

[12] M. Mi, Y. J. Chen, Y. F. Yang et al., "Geochronology and geochemistry of the giant Qian'echong Mo deposit, Dabie Shan, eastern China: implications for ore genesis and tectonic setting," *Gondwana Research*, vol. 27, no. 3, pp. 1217–1235, 2015.

[13] Y. F. Yang, Y. J. Chen, F. Pirajno, N. Li, and N. Li, "Evolution of ore fluids in the Donggou giant porphyry Mo system, East Qinling, China, a new type of porphyry Mo deposit: evidence from fluid inclusion and H-O isotope systematics," *Ore Geology Reviews*, vol. 65, no. 1, pp. 148–164, 2015.

[14] C. M. Han, W. J. Xiao, G. C. Zhao, M. Sun, W. J. Qu, and A. D. Du, "Re–Os geochronology on molybdenites from the Donggebi Mo deposit in the eastern Tianshan of the Central Asia Orogenic Belt and its geological significance," *Resource Geology*, vol. 64, no. 2, pp. 136–148, 2014.

[15] Q. J. Tu, Y. S. Wang, and L. H. Dong, "Re-Os dating of molybdenite from the Baishan molybdenum deposit in the eastern Tianshan area of Xinjiang and its geological significance," *Xinjiang Geology*, vol. 32, no. 3, pp. 322–327, 2014.

[16] Y. H. Wang, C. J. Xue, J. J. Liu et al., "Early Carboniferous adakitic rocks in the area of the Tuwu deposit, eastern Tianshan, NW China: slab melting and implications for porphyry copper mineralization," *Journal of Asian Earth Sciences*, vol. 103, pp. 332–349, 2015.

[17] Y. H. Wang, F. F. Zhang, and J. J. Liu, "The genesis of the ores and intrusions at the Yuhai Cu-Mo deposit in eastern Tianshan, NW China: constraints from geology, geochronology, geochemistry, and Hf isotope systematics," *Ore Geology Reviews*, vol. 77, pp. 312–331, 2016.

[18] W. F. Zhang, H. Y. Chen, L. H. Peng et al., "Discriminating hydrothermal fluid sources using tourmaline boron isotopes: example from Bailingshan Fe deposit in the eastern Tianshan, NW China," *Ore Geology Reviews*, vol. 98, pp. 28–37, 2018.

[19] A. M. C. Sengör, B. A. Natal'In, and V. S. Burtman, "Evolution of the Altaid tectonic collage and Palaeozoic crustal growth in Eurasia," *Nature*, vol. 364, no. 6435, pp. 299–307, 1993.

[20] B. F. Windley, D. Alexeiev, W. J. Xiao, A. Kröner, and G. Badarch, "Tectonic models for accretion of the Central Asian Orogenic Belt," *Journal of the Geological Society, London*, vol. 164, no. 1, pp. 31–47, 2007.

[21] Y. S. Wu, K. F. Zhou, N. Li, and Y. J. Chen, "Zircon U-Pb dating and Sr-Nd-Pb-Hf isotopes of the ore-associated porphyry at the giant Donggebi Mo deposit, Eastern Tianshan, NW China," *Ore Geology Reviews*, vol. 81, pp. 794–807, 2017.

[22] W. J. Xiao, D. F. Song, B. F. Windley et al., "Accretionary processes and metallogenesis of the Central Asian Orogenic Belt: advances and perspectives," *Science China Earth Sciences*, vol. 63, no. 3, pp. 329–361, 2020.

[23] Q. G. Mao, J. B. Wang, M. J. Yu et al., "Re-Os and U-Pb geochronology for the Xiaorequanzi VMS deposit in the eastern Tianshan, NW China: constraints on the timing of mineralization and stratigraphy," *Ore Geology Reviews*, vol. 122, article 103473, 2020.

[24] X. H. Cheng, F. Q. Yang, R. Zhang, Q. F. Xu, and N. Li, "Metallogenesis and fluid evolution of the Huangtupo Cu-Zn deposit, East Tianshan, Xinjiang, NW China: constraints from ore geology, fluid inclusion geochemistry, H-O-S isotopes, and U-Pb zircon, Re-Os chalcopyrite geochronology," *Ore Geology Reviews*, vol. 121, article 103469, 2020.

[25] L. C. Zhang, W. J. Xiao, K. Z. Qin, W. J. Qu, and A. D. Du, "Re–Os isotopic dating of molybdenite and pyrite in the Baishan Mo–Re deposit, eastern Tianshan, NW China, and its geological significance," *Mineralium Deposita*, vol. 39, no. 8, pp. 960–969, 2005.

[26] Y. J. Mao, K. Z. Qin, D. M. Tang, H. Y. Feng, and S. C. Xue, "Crustal contamination and sulfide immiscibility history of the Permian Huangshannan magmatic Ni-Cu sulfide deposit, East Tianshan, NW China," *Journal of Asian Earth Sciences*, vol. 129, pp. 22–37, 2016.

[27] S. M. Wang, C. Z. Wu, M. N. Muhtar, R. X. Lei, and M. J. Brzozowski, "Mobilization of ore-forming metals during post-magmatic hydrothermal overprinting of the Huangshandong Ni–Cu sulfide deposit, Eastern Tianshan, NW China," *Ore Geology Reviews*, vol. 137, article 104315, 2021.

[28] M. N. Muhtar, C. Z. Wu, M. J. Brzozowski et al., "Sericite $^{40}Ar/^{39}Ar$ dating and S-Pb isotope composition of the Kanggur gold deposit: Implications for metallogenesis of late Paleozoic gold deposits in the Tianshan, central Asian Orogenic Belt," *Ore Geology Reviews*, vol. 131, article 104056, 2021.

[29] J. S. Han, H. Y. Chen, H. J. Jiang, L. D. Zhao, W. F. Zhang, and C. K. Lai, "Genesis of the Paleozoic Aqishan-Yamansu arc-basin system and Fe (-Cu) mineralization in the eastern Tianshan, NW China," *Ore Geology Reviews*, vol. 105, pp. 55–70, 2019.

[30] Y. Sun, J. B. Wang, Y. C. Li et al., "Recognition of Late Ordovician Yudai porphyry Cu (Au, Mo) mineralization in the Kalatag district, eastern Tianshan terrane, NW China: constraints from geology, geochronology, and petrology," *Ore Geology Reviews*, vol. 100, pp. 220–236, 2018.

[31] M. Sun, Y. H. Wang, F. F. Zhang et al., "Petrogenesis of Late Carboniferous intrusions in the Linglong area of Eastern Tianshan, NW China, and tectonic implications: geochronological, geochemical, and zircon Hf-O isotopic constraints," *Ore Geology Reviews*, vol. 120, article 103462, 2020.

[32] H. Wu, H. Q. Li, F. W. Chen et al., "Zircon SHRIMP U–Pb dating of plaglogranite porphyry in the Chihu molybdenum-copper district, Hami, east Tianshan," *Geological Bulletin of China*, vol. 25, pp. 549–552, 2006.

[33] Y. H. Wang, F. F. Zhang, J. J. Liu, and C. Y. Que, "Genesis of the Fuxing porphyry Cu deposit in Eastern Tianshan, China: evidence from fluid inclusions and C-H-O-S-Pb isotope systematics," *Ore Geology Reviews*, vol. 79, pp. 46–61, 2016.

[34] B. Xiao, H. Y. Chen, P. Hollings et al., "Magmatic evolution of the Tuwu-Yandong porphyry Cu belt, NW China: constraints from geochronology, geochemistry and Sr-Nd-Hf isotopes," *Gondwana Research*, vol. 43, pp. 74–91, 2017.

[35] K. L. Liao and C. L. Lv, "The geological significance of molybdenite Re-Os isotope dating result of Sanchakouxi Cu deposit in east Tianshan, Xinjiang," *Mineral Resources and Geology*, vol. 34, no. 3, pp. 471–476, 2020.

[36] C. M. Han, W. J. Xiao, B. X. Su et al., "Geology, Re-Os and U-Pb geochronology and sulfur isotope of the the Donggebi porphyry Mo deposit, Xinjiang, NW China, Central Asian Orogenic Belt," *Journal of Asian Earth Sciences*, vol. 165, pp. 270–284, 2018.

[37] X. P. Long, B. Wu, M. Sun, C. Yuan, W. J. Xiao, and R. Zuo, "Geochronology and geochemistry of Late Carboniferous dykes in the Aqishan-Yamansu belt, eastern Tianshan: evidence for a post-collisional slab breakoff," *Geoscience Frontiers*, vol. 11, no. 1, pp. 347–362, 2020.

[38] W. F. Zhang, H. Y. Chen, L. H. Peng et al., "Ore genesis of the Duotoushan Fe-Cu deposit, eastern Tianshan, NW China: constraints from ore geology, mineral geochemistry, fluid inclusion and stable isotopes," *Ore Geology Reviews*, vol. 100, pp. 401–421, 2018.

[39] Z. Y. Sun, L. L. Long, Y. W. Wang, Z. H. Luo, Q. T. Hu, and M. L. Wang, "Geology, chronology, fluid inclusions, and H-O-S isotopic compositions of the Hongyuntan magnetite deposit, eastern Tianshan, NW China," *Journal of Asian Earth Sciences*, vol. 172, pp. 328–345, 2019.

[40] N. Li, F. Q. Yang, Z. X. Zhang, and C. D. Yang, "Geochemistry and chronology of the biotite granite in the Xiaobaishitou W-(Mo) deposit, eastern Tianshan, China: petrogenesis and tectonic implications," *Ore Geology Reviews*, vol. 107, pp. 999–1019, 2019.

[41] W. F. Zhang, H. Y. Chen, J. S. Han et al., "Geochronology and geochemistry of igneous rocks in the Bailingshan area: implications for the tectonic setting of late Paleozoic magmatism and iron skarn mineralization in the eastern Tianshan, NW China," *Gondwana Research*, vol. 38, pp. 40–59, 2016.

[42] S. H. Fan, S. E. Chen, Y. B. Zhang, L. Zhang, L. Liu, and L. C. Yang, "The characteristics and geneses of iron deposits in the Bailingshan area, eastern Tianshan, Xinjiang, NW China," *Geological Journal*, vol. 53, pp. 319–328, 2018.

[43] K. R. Ludwig, *User's Manual for Isoplot/Ex. Version 3.00: a Geochronological Toolkit for Microsoft Excel*, Berkeley Geochronology Center Special Publication, Berkeley, 2003.

[44] R. J. Bodnar, "Revised equation and table for determining the freezing point depression of H_2O-NaCl solutions," *Geochimica et Cosmochimica Acta*, vol. 57, no. 3, pp. 683-684, 1993.

[45] B. Liu and K. Shen, *Thermodynamics of fluid inclusions*, Geological Publishing House, Beijing, 1999.

[46] R. N. Clayton, J. R. O'Neil, and T. K. Mayeda, "Oxygen isotope exchange between quartz and water," *Journal of Geophysical Reseach*, vol. 77, no. 17, pp. 3057–3067, 1972.

[47] Y. Kajiwara and H. R. Krouse, "Sulfur isotope partitioning in metallic sulfide systems," *Canadian Journal of Earth Sciences*, vol. 8, no. 11, pp. 1397–1408, 1971.

[48] R. H. Sillitoe, "Porphyry copper systems," *Economic Geology*, vol. 105, no. 1, pp. 3–41, 2010.

[49] Y. J. Chen, C. Li, J. Zhang, Z. Li, and H. H. Wang, "Sr and O isotopic characteristics of porphyries in the Qinling molybdenum deposit belt and their implication to genetic mechanism

and type," *Science in China Series D-Earth Sciences*, vol. 43, no. S1, pp. 82–94, 2000.

[50] H. P. Taylor, "Oxygen and hydrogen isotope relationships in hydrothermal mineral deposits," *Geochemistry of Hydrothermal Ore Deposits*, H. L. Barnes, Ed., pp. 236–277, Wiley, New York, NY, USA, 1997.

[51] S. M. F. Sheppard, "Characterization and isotopic variations in natural waters," *Reviews in Mineralogy*, vol. 16, pp. 165–183, 1986.

[52] Y. H. Wang, C. J. Xue, F. F. Zhang, J. J. Liu, J. B. Gao, and T. J. Qi, "SHRIMP zircon U-Pb geochronology, geochemistry and H-O-Si-S-Pb isotope systematics of the Kanggur gold deposit in Eastern Tianshan, NW China: implication for ore genesis," *Ore Geology Reviews*, vol. 68, pp. 1–13, 2015.

[53] L. D. Zhao, J. S. Han, W. J. Lu, P. Liang, and F. Jourdan, "The Middle Permian Hongshanliang Manto-type copper deposit in the East Tianshan: constraints from geology, geochronology, fluid inclusions and H-O-S isotopes," *Ore Geology Reviews*, vol. 124, article 103601, 2020.

[54] F. F. Zhang, Y. H. Wang, C. J. Xue, J. J. Liu, and W. Zhang, "Fluid inclusion and isotope evidence for magmatic-hydrothermal fluid evolution in the Tuwu porphyry copper deposit, Xinjiang, NW China," *Ore Geology Reviews*, vol. 113, article 103078, 2019.

[55] S. J. Liu, J. J. Yu, T. Z. Wang et al., "Fluid inclusions and stable isotope study of Yuhai copper-(molybdenum) deposit in eastern Tianshan Mountains, Xinjiang," *Mineral Deposits*, vol. 37, pp. 371–386, 2018.

[56] Y. H. Wang, F. F. Zhang, J. J. Liu, C. J. Xue, B. C. Li, and X. C. Xian, "Ore genesis and hydrothermal evolution of the Donggebi porphyry Mo deposit, Xinjiang, northwest China: evidence from isotopes (C, H, O, S, Pb), fluid inclusions, and molybdenite Re-Os dating," *Economic Geology*, vol. 113, no. 2, pp. 463–488, 2018.

[57] N. Li, F. Q. Yang, Z. X. Zhang, and C. Li, "Dating the Xiaobaishitou skarn W-(Mo) deposit, eastern Tianshan, NW China: constraints from zircon U-Pb, muscovite ^{40}Ar-^{39}Ar, and molybdenite Re-Os system," *Ore Geology Reviews*, vol. 124, article 103637, 2020.

[58] H. Ohmoto, "Systematics of sulfur and carbon isotopes in hydrothermal ore deposits," *Economic Geology*, vol. 67, no. 5, pp. 551–578, 1972.

[59] H. Ohmoto, "Stable isotope geochemistry of ore deposits," *Stable Isotopes in High Temperature Geological Processes. Review in Mineralogy*, J. W. Valley, H. P. Taylor, and J. R. O'Neil, Eds., vol. 16, pp. 460–491, 1986.

[60] H. Ohmoto and R. O. Rye, "Isotopes of sulfur and carbon," in *Geochemistry of Hydrothermal Ore Deposit*, H. L. Barnes, Ed., pp. 509–567, Wiley, New York, 1979.

[61] J. F. Dai, C. J. Xue, G. X. Chi et al., "Genesis of the Aqishan skarn Zn-Pb deposit in the eastern Tianshan, NW China: constraints from geology, geochronology and Hf-S-Pb isotopic geochemistry," *Ore Geology Reviews*, vol. 123, no. 103608, article 103608, 2020.

[62] L. D. Zhao, H. Y. Chen, L. Zhang, W. F. Zhang, J. T. Yang, and X. L. Yan, "The Late Paleozoic magmatic evolution of the Aqishan-Yamansu belt, eastern Tianshan: constraints from geochronology, geochemistry and Sr-Nd-Pb-Hf isotopes of igneous rocks," *Journal of Asian Earth Sciences*, vol. 153, pp. 170–192, 2018.

[63] W. T. Holser, "Catastrophic chemical events in history of the ocean," *Nature*, vol. 267, pp. 402–408, 1977.

[64] T. Lin, Y. F. Deng, W. J. Qu, T. F. Zhou, F. Yuan, and G. Deng, "The genesis, petrology, chronology and geochemical evidence of the Sanchakou copper deposit in the east Tianshan area, Xinjiang," *Journal of Mineral Petrology*, vol. 37, no. 4, pp. 47–61, 2017.

[65] Z. Y. Rui, R. J. Goldfarb, Y. M. Qiu et al., "Paleozoic-early Mesozoic gold deposits of the Xinjiang autonomous region, northwestern China," *Mineralium Deposita*, vol. 37, no. 3, pp. 393–418, 2002.

[66] L. C. Zhang, K. Z. Qin, and W. J. Xiao, "Multiple mineralization events in the eastern Tianshan district, NW China: isotopic geochronology and geological significance," *Journal of Asian Earth Sciences*, vol. 32, no. 2-4, pp. 236–246, 2008.

[67] L. D. Zhao, H. Y. Chen, P. Hollings, and J. S. Han, "Late Paleozoic magmatism and metallogenesis in the Aqishan-Yamansu belt, eastern Tianshan: constraints from the Bailingshan intrusive complex," *Gondwana Research*, vol. 65, pp. 68–85, 2019.

[68] W. F. Zhang, H. Y. Chen, H. J. Jiang et al., "Geochronology, geochemistry and petrogenesis of granitoids in the duotoushan Fe-Cu deposit, Eastern Tianshan, Xinjiang: implications on tectonic setting of late paleozoic magmatism," *Geotectonica et Metallogenia*, vol. 41, pp. 1171–1191, 2017.

[69] M. N. Muhtar, C. Z. Wu, M. J. Brzozowski et al., "Geochronology, geochemistry, and Sr-Nd-Pb-Hf-S isotopes of the wall rocks of the Kanggur gold polymetallic deposit, Chinese North Tianshan: implications for petrogenesis and sources of ore-forming materials," *Ore Geology Reviews*, vol. 125, article 103688, 2020.

[70] C. Z. Wu, S. W. Xie, L. X. Gu et al., "Shear zone-controlled post-magmatic ore formation in the Huangshandong Ni-Cu sulfide deposit, NW China," *Ore Geology Reviews*, vol. 100, pp. 545–560, 2018.

[71] P. Li, T. Liang, Y. G. Feng et al., "The metallogeny of the Lubei Ni–Cu–Co sulfide deposit in eastern Tianshan, NW China: insights from petrology and Sr-Nd-Hf isotopes," *Frontiers in Earth Science*, vol. 9, 2021.

[72] Y. S. Wu, N. Xiang, H. S. Tang, K. F. Zhou, and Y. F. Yang, "Molybdenite Re–Os isotope age of the Donggebi Mo deposit and the Indosinian metallogenic event in eastern Tianshan," *Acta Petrologica Sinica*, vol. 29, pp. 121–130, 2013.

[73] D. Y. Zhang, T. F. Zhou, F. Yuan, Y. Fan, S. Liu, and W. J. Qu, "A genetic analysis of Baishan molybdenum deposit in east Tianshan area, Xinjiang," *Mineral Deposits*, vol. 28, no. 5, pp. 663–672, 2009.

[74] C. L. Wang, K. Z. Qin, D. M. Tang et al., "Geochronology and Hf isotope of zircon for the Arskartor Be-Nb-Mo deposit in Altay and its geological implications," *Acta Petrologica Sinica*, vol. 31, pp. 2337–2352, 2015.

[75] W. Z. Liu, H. Zhang, H. F. Tang, Y. Tang, and Z. H. Lv, "Molybdenite Re–Os dating of the Asikaerte Be–Mo deposit in Xinjiang, China and its genetic implications," *Geochimica*, vol. 44, pp. 145–154, 2015.

[76] Y. H. Wu, X. L. Xiong, T. P. Zhao, Z. M. Zhu, and L. Li, "Zircon U-Pb age of the ore-bearing granite and molybdenite Re-Os isotopic age of the Donggebi Mo deposit, Xinjiang and their geological significance," *Geotectonica et Metallogenia*, vol. 37, no. 4, pp. 743–753, 2013.

[77] Y. S. Wu, Y. J. Chen, and K. F. Zhou, "Mo deposits in northwest China: geology, geochemistry, geochronology and tectonic setting," *Ore Geology Reviews*, vol. 81, pp. 641–671, 2017.

[78] S. H. Zhong, P. Shen, H. D. Pan, G. P. Zheng, Y. H. Yan, and J. Li, "The ore-forming fluid and geochronology of the Suyunhe Mo deposit, west Junggar, Xinjiang," *Acta Petrologica Sinica*, vol. 31, pp. 449–464, 2015.

[79] W. D. Li, *The geological characteristics and genesis of the Hongyuan porphyry Mo (Cu) deposit from west Junggar, [Ph.D. thesis]*, China University of Geosciences, Beijing, 2013.

[80] H. Y. Yan, P. Shen, H. D. Pan, J. N. Wang, S. H. Zhong, and X. G. Liu, "Research on the fluid inclusion and Re-Os dating of Hongyuan (Cu) Mo deposit and Tuketuke Mo-Cu deposit, west Junggar, Xinjiang," *Chinese Journal of Geology*, vol. 49, pp. 287–304, 2014.

[81] L. L. Long, Y. W. Wang, A. D. Du et al., "Molybdenite Re-Os age of Xilekuduke Cu–Mo deposit in Xinjiang and its geological significance," *Mineral Deposits*, vol. 30, pp. 635–644, 2011.

[82] X. J. Liu and W. Liu, "Re-Os dating of the Suoerkuduke Cu (Mo) deposit, Fuyun County, Xinjiang, and its geodynamic implications," *Journal of Earth Science*, vol. 24, no. 2, pp. 188–202, 2013.

[83] F. Q. Yang, F. M. Chai, Z. X. Zhang, X. X. Geng, and Q. Li, "Zircon U-Pb geochronology, geochemistry, and Sr-Nd-Hf isotopes of granitoids in the Yulekenhalasu copper ore district, northern Junggar, China: petrogenesis and tectonic implications," *Lithos*, vol. 190-191, pp. 85–103, 2014.

[84] B. Wan, W. J. Xiao, C. M. Han et al., "Re-Os molybdenite age of the Cu-Mo skarn ore deposit at Suoerkuduke in East Junggar, NW China and its geological significance," *Ore Geology Reviews*, vol. 56, pp. 541–548, 2014.

[85] P. Xiang, L. C. Zhang, X. W. Xu et al., "Geological characteristics and genesis of Yuleken-Halasu superimposed and tectonically reworked porphyry copper-gold (molybdenum) deposit in Qinghe, Xinjiang," *Acta Petrologica Sinica*, vol. 28, pp. 2369–2380, 2012.

[86] C. J. Xue, Z. F. Zhao, G. G. Wu et al., "The multiperiodic superimposed porphyry copper mineralization in central Asian tectonic region: a case study of geology, geochemistry and chronology of Halasu copper deposit, southeastern Altai, China," *Earth Science Frontiers*, vol. 17, pp. 53–82, 2010.

[87] X. Qu, X. W. Xu, G. L. Liang et al., "Geological and geochemical characteristics of the Mengxi Cu–Mo deposit and its constraint to tectonic setting of the Qiongheba magmatic arc in eastern Junggar, Xinjiang," *Acta Petrologica Sinica*, vol. 25, pp. 765–776, 2009.

[88] Z. Y. Jia, *Study on the magmatic processes and Cu–Mo mineralization in the Lailigaoer-Kengdenggaoer region, western Tianshan, Xinjiang, China, (master thesis)*, China University of Geosciences, Beijing, 2011.

[89] H. X. Song, Y. L. Liu, W. J. Qu, B. Song, R. Zhang, and Y. Cheng, "Geological characters of Baogutu porphyry copper deposit in Xinjiang, NW China," *Acta Petrologica Sinica*, vol. 23, pp. 1981–1988, 2007.

[90] M. T. Zhu, G. Wu, H. J. Xie et al., "Re-Os isotopic geochronology and fluid inclusion study of the Lailisigao'er porphyry Cu–Mo deposit in western Tianshan, Xinjiang, NW China," *Acta Petrologica Sinica*, vol. 26, pp. 3667–3682, 2010.

[91] Z. H. Zhang, J. W. Mao, Z. L. Wang, A. D. Du, and G. C. Zuo, "Geology and metallogenetic epoch of the Dabate porphyry copper deposit in west Tianshan Mountains, Xinjiang," *Geological Review*, vol. 52, pp. 683–689, 2006.

[92] Y. Li, *Geological and geochemical characteristics and genesis of Dabate Cu–Mo deposit, western Tianshan, Xinjiang, [Ph.D. thesis]*, China University of Geosciences, Beijing, 2012.

[93] H. Q. Li, D. H. Wang, Y. Wan et al., "Isotopic geochronology study and its significance of the Lailisigaoer Mo deposit, Xinjiang," *Acta Petrologica Sinica*, vol. 22, pp. 437–2443, 2006.

[94] Q. J. Tu, L. H. Dong, and K. Z. Wang, "Molybdenite Re-Os dating and its geological implication for the east Gebi molybdenum deposit of the eastern Tianshan mountain in Xinjiang," *Xinjiang Geology*, vol. 30, no. 3, pp. 272–276, 2012.

[95] C. Q. Zhang, D. B. Lou, K. Y. Xiao et al., "Geological characteristics and molybdenite Re–Os isotopic dating of Kumutage Mo deposit, in Hami area, Xinjiang, China," *Geological Bulletin of China*, vol. 29, pp. 1586–1593, 2010.

[96] X. H. Deng, Y. J. Chen, M. Santosh et al., "U-Pb zircon, Re-Os molybdenite geochronology and Rb-Sr geochemistry from the Xiaobaishitou W (-Mo) deposit: implications for Triassic tectonic setting in eastern Tianshan, NW China," *Ore Geology Reviews*, vol. 80, pp. 332–351, 2017.

Hindawi
Geofluids
Volume 2021, Article ID 9365364, 17 pages
https://doi.org/10.1155/2021/9365364

Research Article

The Accumulation Characteristics of the Paleozoic Reservoir in the Central-Southern Ordos Basin Recorded by Organic Inclusions

Ruijing Zhu,[1,2] **Rongxi Li**,[1] **Xiaoli Wu**,[1] **Xiaoli Qin**,[1] **Bangsheng Zhao**,[1] **Futian Liu**,[1] **and Di Zhao**[1]

[1]*School of Earth Science and Resources, Chang'an University, Xi'an, Shaanxi 710054, China*
[2]*Shanxi Institute of Engineering Technology, Yangquan, Shanxi 045000, China*

Correspondence should be addressed to Rongxi Li; rongxi99@163.com

Received 22 May 2021; Revised 22 July 2021; Accepted 24 August 2021; Published 16 September 2021

Academic Editor: Giovanni Mongelli

The Permian tight clastic reservoir and Ordovician carbonate reservoir were developed in the central-southern Ordos Basin. This study investigated the fluid inclusion petrography, diagenetic fluid characteristics, formation process of natural gas reservoir, source rock characteristics, and reservoir accumulation characteristics of these Paleozoic strata by petrographic observations, scanning electron microscope imaging, fluid inclusion homogenization temperature, salinity, laser Raman spectrum, and gas chromatograph analyses. The results have suggested two phases of fluid inclusions in both the Permian sandstone and the Ordovician Majiagou Formation dolomite reservoirs, and the fluid inclusions recorded the history from the early thermal evolution of hydrocarbon generation to the formation, migration, and accumulation of natural gas. The early-phase inclusions show weak yellow fluorescence and recorded the early formation of liquid hydrocarbons, while the late-phase inclusions are nonfluorescent natural gas inclusions distributed in the late tectonic fractures and recorded the late accumulation of natural gas. The brine systems of the Permian and Ordovician fluid inclusions are, respectively, dominated by $CaCl_2$-H_2O and $MgCl_2$-NaCl-H_2O. The diagenetic fluids were in the ranges of medium-low temperature and moderate-low salinity. The natural gas hydrocarbon source rocks in the Ordos Basin include both the Permian coal-bearing rocks and the Ordovician carbonates. The process of the early-phase liquid hydrocarbon formation and migration into the reservoir corresponded to 220 Ma (Late Triassic). The late large-scale migration and accumulation of natural gas occurred at 100 Ma (early Late Cretaceous), which was close to the inclusion Rb/Sr isochron age of 89.18 Ma, indicating that the natural gas accumulation was related to the Yanshanian tectonic movement.

1. Introduction

The Ordos Basin is one of the most important natural gas resource exploration and development bases in China. At present, most discovered natural gas are stored in the Upper Paleozoic Permian clastic rock reservoir and the Lower Paleozoic Ordovician carbonate reservoir, and their natural gas accumulation theories have been established based on a large number of studies. In the Upper Paleozoic, the extensive hydrocarbon generation and continuous charging of coal source rocks provided high-quality gas source conditions. The large-scale delta distributary channel sand bodies, spreading from north to south and stacking vertically, comprise the reservoirs. Natural gas migration and accumulation in a close range formed the large tight gas reservoirs [1–3]. The Lower Paleozoic Ordovician natural gas reservoirs are mainly karst cavernous reservoirs and dolomite reservoirs, and the gas accumulation was mainly controlled by karst paleogeomorphology [4–6].

However, both the Permian tight gas reservoirs and the Ordovician carbonate gas reservoirs discovered in the Ordos Basin are mainly distributed in the northern part of the basin, while the exploration progress in the vast southern area is relatively slow. Previous studies on the southern part

of the basin mainly focused on the characteristics and evaluation of hydrocarbon source rocks, the genesis and source of natural gas, clastic rock reservoirs, karst paleogeomorphology, characteristics, accumulation, and evolution of the carbonate reservoirs [7–17]. Some scholars [18–20] believe that the natural gas in the northern part of the Ordos Basin originated from the southern region, and the natural gas migrated and accumulated on a large scale from south to north. The natural gas in the early Paleozoic gathered around the old central uplift in the form of liquid hydrocarbons, which then became gaseous due to thermal cracking. These gaseous hydrocarbons then migrated northeastward from the central uplift and accumulated in the northern reservoirs. Wang [12] proposed three stages of oil and gas filling in the Shanxi Formation of the Lower Paleozoic at the end of Triassic, middle and late Jurassic, and the end of Early Cretaceous, respectively. Wang [13] believed that the "self-generation-self-storage" and the "lower-generation-upper-storage" were the main types of source-reservoir-cap assemblages, and the regional uplift movement around the end of the Early Cretaceous was the key period for the large-scale migration and accumulation of oil and coal gas in this area. Wang et al. [14] argued that the oil generated from the Pingliang Formation hydrocarbon source rocks accumulated in the weathering layer of the Lower Paleozoic at the central paleo-uplift, which was then transformed into a gas reservoir. Despite the abundant studies, many problems still remain unsolved concerning the Paleozoic gas reservoirs in the southern Ordos Basin, such as the diagenetic evolution of reservoirs, gas accumulation phases, and the diagenetic fluid characteristics.

This study investigated core samples from exploration wells by petrographic observation, scanning electron microscope imaging, fluid inclusion homogenization temperature, salinity, laser Raman spectrum, and gas chromatograph analyses. The investigation will not only better characterize the petrography of the fluid inclusions but also reveal the source rock characteristics, diagenetic fluid characteristics, isotopic dating, the natural gas components, gas accumulation characteristics, and phases.

2. Geological Setting

The Ordos Basin is one of the most important fossil-fuel energy basins in west-central China and contains large reserves of coal, oil, natural gas, and coalbed methane [21–23]. It is a large intracontinental, superimposed, and residual basin in the North China block [24–26] and is composed of six subtectonic units, including the Yimeng uplift, Western thrust zone, Tianhuan syncline, Yishan monocline, Jinxi fold belt, and Weibei uplift [27, 28]. The main target strata of this study are the Upper Paleozoic Permian and Lower Paleozoic Ordovician Majiagou Formation. Late Carboniferous and Permian strata experienced a transition from an epeiric sea to an inland lake basin. Sediments were mainly developed in shallow shelves, shallow deltas, rivers, and lakes [29]. The Majiagou Formation mainly contains limestone and dolomite that were formed in a carbonate platform environment [30].

As a large sedimentary basin in the west of the North China block, the Ordos Basin has gone through five tectono-sedimentary stages, i.e., the Middle-Late Proterozoic aulacogen stage, the Early Paleozoic shallow marine platform stage, the Late Paleozoic littoral plain stage, the Mesozoic hinterland basin stage, and the Cenozoic peripheral faulted basin stage [31–33]. From the Middle-Late Proterozoic to Early Paleozoic, stable carbonate rocks of several kilometers' thick were deposited. During the early Ordovician, the uplift and depression patterns were formed in the Ordos Basin. The central paleo-uplift extended from Qingyang to the southeast (Figure 1). The depressions on both sides of the central paleo-uplift were characterized by an evaporative saline lake system with thick argillaceous dolomite, which was considered as the potential hydrocarbon source rock [34]. The slope belts on both sides of the central paleo-uplift were broad areas of tidal flat dolomite. Affected by the Caledonian tectonic movement, the Ordos Basin uplifted together with the North China block in the Middle-Late Ordovician, resulted in weathering and erosion at the top of Middle-Late Ordovician for 150 million years with well-developed dissolution pores and good reservoir performance. It is therefore the most favorable layer of a gas field and one of the main gas reservoirs found in the Ordos Basin. This tectonic movement caused the absence of the Late Ordovician-Early Carboniferous sediments in the Ordos Basin and even the whole North China block. It was not until the Middle-Late Carboniferous that the Ordos Basin and the North China block began to subside again. The seawater invaded from northeast to southwest, and the Ordos Basin and the vast areas of North China block as a whole exhibited a paleogeographic pattern of coexisted epeiric sea and delta, forming the coal-bearing deposits mixed with carbonate rocks and terrigenous clastics. In the regressive environment, the Permian sediments gradually evolved into lacustrine delta with thick deposition of dark organic-rich mudstone and coal-bearing sediments. These deposits are good natural gas source rocks and clastic reservoirs, which are the most important natural gas reservoirs that have been discovered by exploration so far [1].

During Triassic, the Ordos Basin became a large-scale depression basin dominated by river-lake delta deposits, which constituted the major low-permeability oil and gas system in the Ordos Basin. At the end of the Late Triassic, due to the Indosinian movement, the collision between the North and South China blocks formed the Qinling Central Orogenic Belt, resulting in the uplift of the North China block. Hence, the Upper Triassic strata in the Ordos area experienced a long period of erosion, forming a wide range of valleys filled with Jurassic glutenite. The Yanshan movement at the end of the Jurassic led to the formation of large-scale nappes and thrust uplifts in the western and eastern margins of the basin. The main body of the basin formed an asymmetric east-west compressive syncline. The northern Ordos Basin remained as an uplift for a long time and was higher than the southern Ordos Basin. At the same time, the southern margin and eastern part of the basin uplifted as a whole. From the Cenozoic, the Paleozoic strata at the edge of the basin were exposed to the surface, while the fault

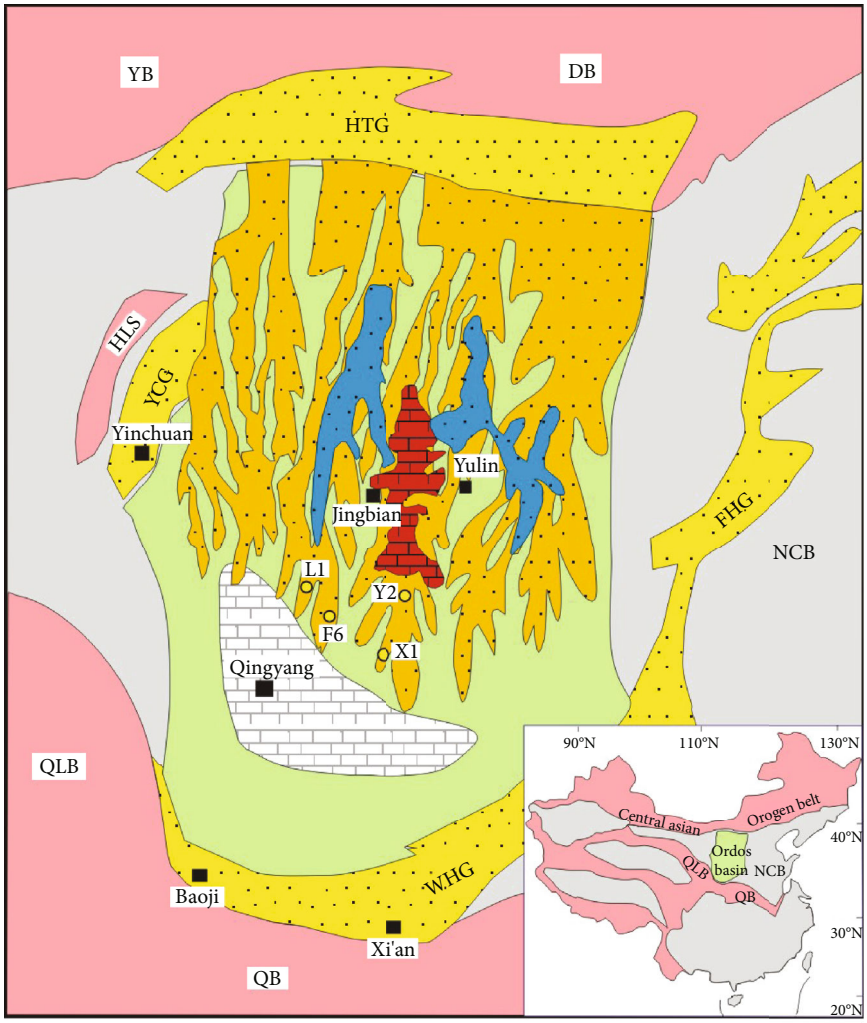

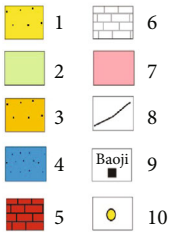

1. Cenozoic depression; 2 Ordos basin; 3. Upper paleozoic fluvial sand bodies; 4. Upper paleozoic sandstone gas reservoir; 5. The dolomite gas reservoir of Ordovician Majiagou Formation; 6. Central palaeo-uplift; 7. Orogenic belt; 8. Boundary line; 9. City; 10. Exploratory well

YB-Yinshan orogenic Belt DB-Daqingshen orogenic Belt HTG-He Tao Graben
HLS-HeLan Shan YCG-YinChuan Grabe QLB-QiLian orogenic Belt
QB-Qinling orogenic Belt WHG-WeiHe Graben FHG-FenHe Graben
NCB-North Chine Block

(a)

Figure 1: Continued.

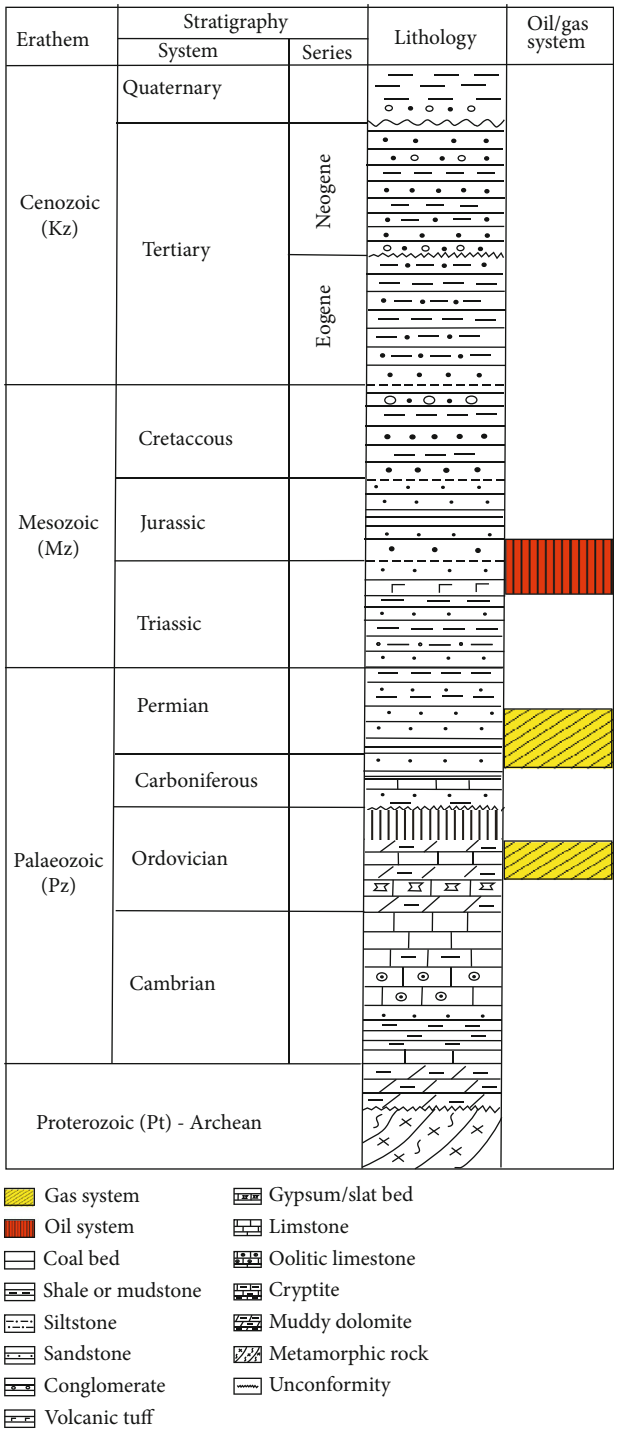

(b)

Figure 1: Structure and gas reservoir distribution of the Ordos Basin.

depressions around the basin formed a series of fault basins, in which the thickness of the Cenozoic strata exceeds 5000 m.

There are two sets of gas-bearing layers in the middle and southern part of the Ordos Basin, namely, the oil-type gas system of the Lower Paleozoic Ordovician marine carbonate rocks and the typical coal-derived gas system of the Permian mudstone and coal seam. The Upper Paleozoic coal-bearing source rocks have diverse material sources and kerogen types. Generally, the coal seam has organic carbon content of 70.8%-83.2% and chloroform bitumen "A" content of 0.61%-0.80%, while the dark mudstone has organic carbon abundance of 2%-3% and chloroform bitumen "A" content 0.037%-0.120%. Most hydrocarbon source rocks were in the high/over mature stage with Ro > 1.5%.

The Lower Paleozoic Ordovician hydrocarbon source rocks belong to type I and type II organic matter types, with moderate to good abundances and Ro > 2.0%. The Ordovician system mainly consists of weathering crust type, dolomite type, and karst fracture-cavity type reservoirs, which can be divided into three major gas accumulation assemblages, the Ordovician weathering crust, the dolomite on the east of the paleo-uplift, and the karst fracture-cave type gas reservoir on the west of the paleo-uplift. The effective hydrocarbon source rocks in the Upper and Lower Paleozoic strata provided rich gas sources for the karst fracture-cavity traps and formed a good source-reservoir configuration.

3. Samples and Experiments

In this study, more than 50 sandstone core samples of the He 8 section and Shan 1 section were collected from several exploratory wells in the central paleo-uplift of the Ordos Basin (L1 well, Xt 1 well, Yt 1 well, U1 well, F1 well, F2 well, F3 well, Y2 well, S139 well, and S15 well). A total of 50 representative Paleozoic core samples around the central paleo-uplift of the basin were selected for analysis of fluid inclusions, including the core samples of the Permian sandstone reservoir and the Ordovician Majiagou Formation reservoir [35]. Firstly, the samples were made into 50 polished double-sided rock slices. A Leitz microscope was used to observe the petrographic characteristics of fluid inclusions, including color, size, occurrence, host minerals, and the gas-liquid ratio of fluid inclusions, with a lens combination of 10 times eyepiece and 50 times objective lens under the laboratory temperature of 26°C. The brine composition types of fluid inclusions were determined by measuring the initial melting temperatures of the inclusions. The fluid inclusions were placed on a heating and freezing stage until frozen and then slowly heated to record the initial melting temperature at the appearance of the first drop of the liquid phase. The initial melting temperature is related to the chemical properties of the saline system of the inclusion fluid and thus could reflect the properties of the ancient fluid. Different brine systems have different initial melting temperatures. The initial melting temperatures of the common $NaCl$-H_2O system, $CaCl_2$-H_2O system, and $MgCl_2$-H_2O system are −20.8°C, −49.8°C, and −33.6°C, respectively. Secondly, laser Raman spectrometry analyses on fluid inclusions were conducted using a Ramnor-u1000 laser Raman molecular microprobe manufactured by Jobin-Yvon Instruments, France. The experiment used an Ar+ laser with a wavelength of 514.5 nm and a power of 300 mW. The double monochromator slit was 450 μm, and the dispersion was 9.3 cm^{-1}/mm. The high voltage of the photomultiplier tube was 1530 V. The laboratory temperature was 22°C, and the humidity was 65%.

The compositions of natural gas in hydrocarbon-bearing inclusions of Permian sandstone and Ordovician carbonate rock samples were analyzed by a thermal explosion method. Firstly, the samples were crushed through 100-80 mesh sieves and cleaned repeatedly with alcohol and benzene-methanol mixed solution to remove surface-adsorbed hydrocarbons. After drying, the samples were put into a quartz furnace and vacuumed and heated to 300°C causing the explosion of the inclusions and the release of the gas in the inclusions. The compositions and relative content of natural gas were analyzed by an HP 5890 GC gas chromatograph, and they were compared against the natural gas compositions obtained by gas logging. At the same time, CH_4 was separated, and $\delta^{13}C_1$ carbon and δD were, respectively, determined, which were compared with the isotopes of natural gas collected from the natural gas layer. The compositions and source characteristics of natural gas in the inclusions were therefore determined.

4. Results

4.1. Fluid Inclusions

4.1.1. Inclusion Types. Through microscopic petrographic observation, fluid inclusions in both the Permian sandstone and Ordovician Majiagou Formation dolomite reservoirs can be divided into two phases. The early-phase inclusions are gas-liquid two-phase inclusions containing liquid hydrocarbon and showing fluoresce, indicating that petroleum entered the reservoir in the early stage of the reservoir formation. The late-phase inclusions are gas-liquid two-phase inclusions containing gaseous hydrocarbons, recording gaseous hydrocarbon entering the reservoir in the late stage of reservoir formation. In the Permian sandstone reservoir, the early-phase gas-liquid two-phase inclusions containing liquid hydrocarbons are small and distributed along the early fractures of clastic particles and in the irregular dissolution pores at the edge of particles. In addition, many gas-liquid two-phase inclusions containing liquid hydrocarbon are in the dissolution pores of quartz particles. The liquid hydrocarbon phase emits weak yellow-green fluorescence under the fluorescence microscope (Figures 2(a), 2(b), 2(d), and 2(e)), but the gaseous phase does not emit fluorescence (Figures 2(c) and 2(f)). The late-phase gas-liquid two-phase inclusions containing gaseous hydrocarbons are distributed in a bead-like direction along the late-diagenetic fractures that cut through the particle boundary. The gaseous bubbles are grayish-black, and the gas/liquid ratios are generally about 20%. These inclusions do not emit fluorescence (Figures 2(c) and 2(f)).

The early-phase inclusions in the dolomite of the Middle Ordovician Majiagou Formation are gas-liquid two-phase inclusions containing liquid hydrocarbons and distributed in the dissolution pores of dolomite. The sizes of the inclusions are mostly 3-5 μm, and the gas/liquid ratios are 5%-10%. There is no fluorescence in the bubble center, whereas the liquid hydrocarbon phase distributed around the inclusions shows weak yellow-green fluorescence (Figures 3(a) and 3(b)). The late-phase inclusions are gas-liquid two-phase inclusions containing gaseous hydrocarbons and distributed in sparry calcite filled with dissolution pores. The bubbles of the inclusions are light gray, and the inclusions are large with sizes of 10-30 μm. These inclusions have varied gas/liquid ratios and do not emit fluorescence. Inclusions filled the cleavages of the calcite and showed angular shapes (Figures 3(c)–3(f)).

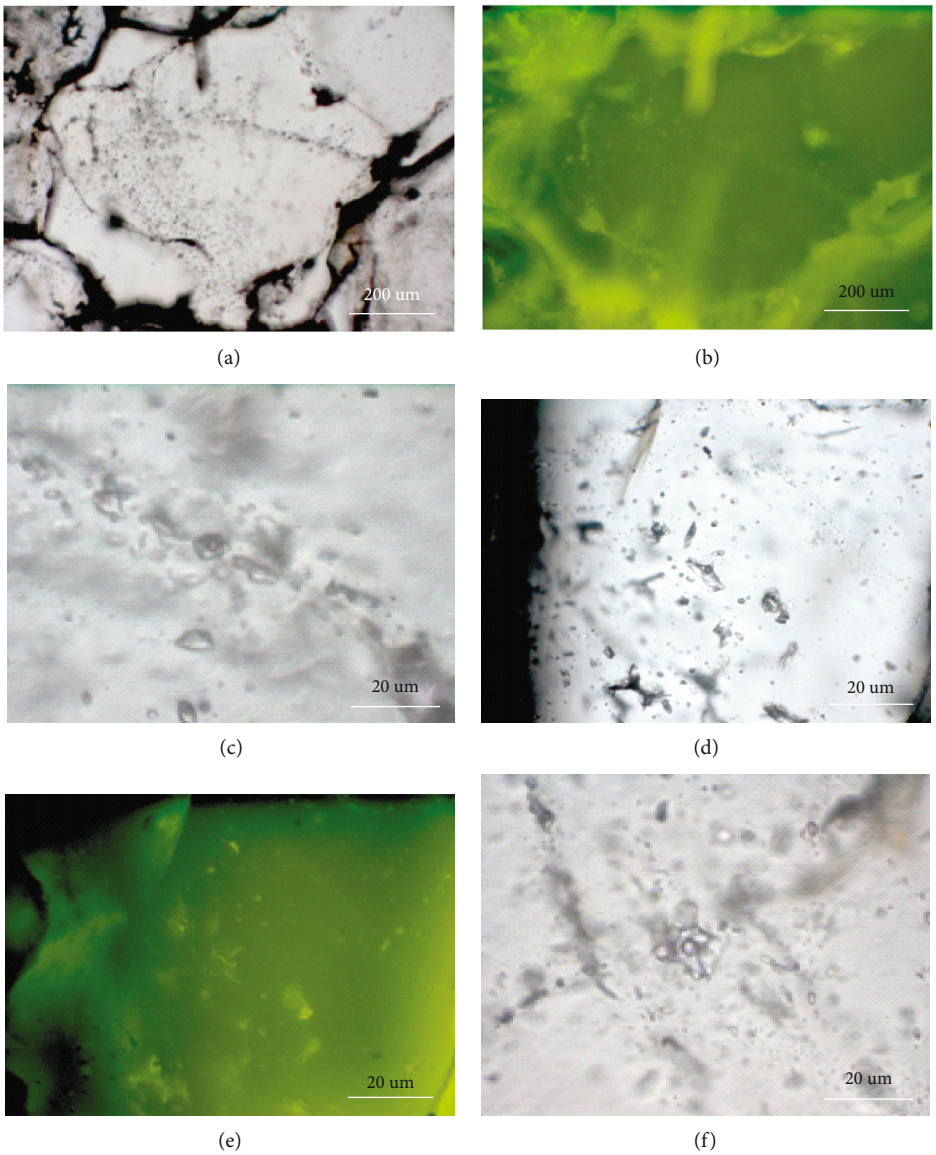

Figure 2: Microscopic photographs of Early and Late Paleozoic Permian sandstone inclusions. (a) Liquid hydrocarbon inclusions in early fractures and enlarged edges of quartz grains, F3 well, 2958.61 m, P_2, (-); (b) the same field of view as (a), fluorescence; (c) gaseous hydrocarbon inclusions in late fractures of quartz grains, F2 well, 2753.87 m, P_2, (-); (d) quartz particle dissolution pore fractures contain liquid hydrocarbon inclusions, F1 well, 2708.4 m, P_2, (-); (e) the same field of view as (d), fluorescence; (f) gaseous hydrocarbon inclusions in late fractures of quartz particles, F2 well, 2753.87 m, P_2, (-).

4.1.2. Inclusions Homogenization Temperature and Salinity. Homogenization temperature and other parameters of fluid inclusions in the central-southern basin were measured by a heating and freezing stage. Both the Permian sandstone inclusions and Ordovician Majiagou Formation dolomite inclusions have two peak ranges of homogenization temperatures. The homogenization temperature peak ranges of the Permian sandstone inclusions vary from 110°C to 120°C and from 160°C to 170°C. The homogenization temperature peak ranges of the Ordovician dolomite inclusions are 120°C-130°C and 170°C-180°C (Figure 4), slightly higher than those of the Permian sandstone. Through microscopic observation, the low-temperature inclusions from either the Permian sandstone or the Ordovician carbonate rocks are mostly early-phase liquid hydrocarbon inclusions with fluorescence, corresponding to the early formation of liquid hydrocarbon and migration into the reservoir. The high-temperature inclusions are mostly late-phase gaseous hydrocarbon inclusions without fluorescence, formed during the large-scale migration of natural gas into the reservoir.

The fluid salinity of fluid inclusions was then calculated. The salinity of fluid inclusions in the Permian sandstone varies from 0.2 wt% to 15.0 wt% but is generally low and concentrated in the range of 0.0–5.0 wt% (Figure 5). The salinity is generally low, and relatively few are higher than 5.0 wt%. The salinity of dolomite fluid inclusions in the Ordovician Majiagou Formation ranges from 1.0 wt% to 20.0 wt% with the peak interval from 1.0 wt% to 11.0 wt%,

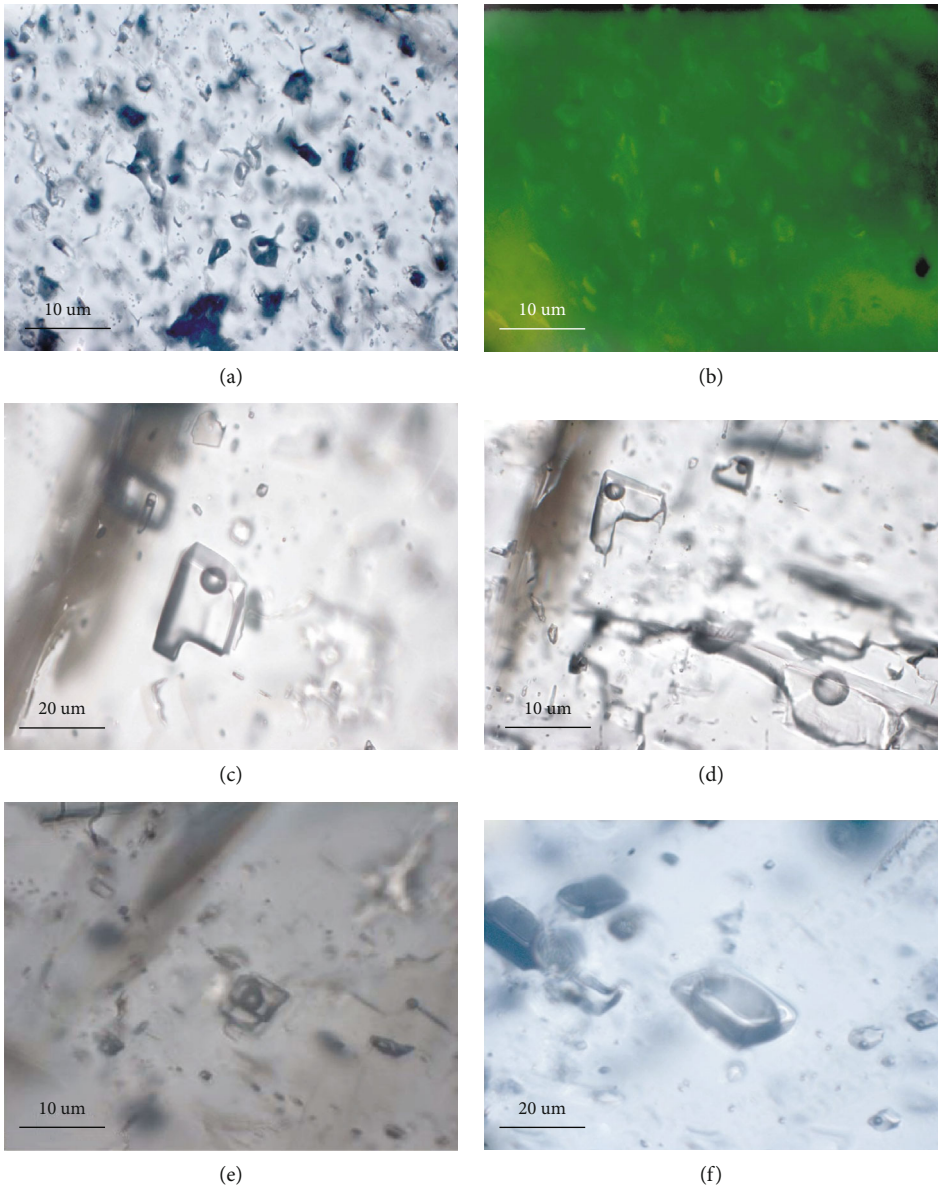

Figure 3: Microscopic photographs of early and late-stage inclusions in Ordovician Majiagou Formation dolomite. (a) Liquid hydrocarbon inclusions in dolomite dissolution pores, F6 well, 2770.9 m, O_2, (+); (b) the same field of view as (a), fluorescence microscope; (c, d) gaseous hydrocarbon inclusions in late bright crystal calcite filled with dissolution pores, Xt 1 well, 3297.5 m, O_2, (+); (e) gaseous hydrocarbon inclusions in late-stage calcite filled with dissolution pores, Y2 well, 2528.7 m, O_2; (f) methane-rich gas inclusions in bright crystal calcite, F6 well, 2770.9 m, O_2, (+).

which is generally higher than that of the Permian sandstone fluid inclusions. Combined with the petrographic observation, most fluid inclusions with high salinity are early-phase liquid hydrocarbon fluid inclusions, while most late-phase gaseous hydrocarbon fluid inclusions have relatively lower salinity.

4.1.3. Inclusions Composition. Through laser Raman microprobe analyses of fluid inclusions from the Permian and Ordovician Majiagou Formation, the contents of H_2O are generally between 50% and 70% in liquid inclusions and from 0% to 30% in gas inclusions, with CH_4, CO_2, H_2S, and other trace hydrocarbons. CH_4 content is the highest among all hydrocarbon gases, and its content in the gas phase is obviously higher than that in the liquid phase. A comparison shows that the CH_4 contents and the CH_4/total hydrocarbon ($\sum$CH) ratios in the late-phase inclusions are significantly higher than those in the early-phase inclusions, indicating that the late-phase inclusions mainly recorded the organic matter composition during the main period of organic fluid migration. CH_4 contents in the gas phase of late-phase inclusions account for more than 92% of the total hydrocarbons, indicating that late-phase inclusions recorded fluid composition during the main accumulation period (Figure 6). The gas and liquid phases of the early and late inclusions of the Ordovician Majiagou Formation contain a certain amount of H_2S. The CH_4 contents in gas and liquid

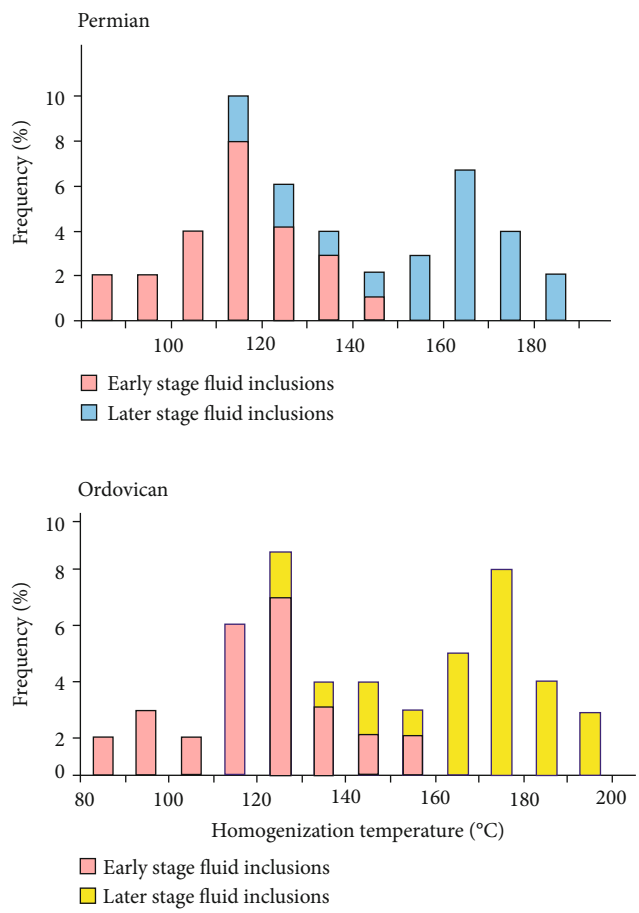

Figure 4: Uniform temperature distribution of inclusions.

phases show a positive correlation with the total hydrocarbon contents in the inclusions. With the increase of total hydrocarbon contents, the content of CH_4 also increases accordingly (Figure 7). It also proves that hydrocarbon-bearing inclusions are signs and records of hydrocarbon fluid migration.

The hydrocarbon components of the fluid inclusions were examined by thermal explosion of the fluid inclusions, and the results are shown in Table 1. The CH_4 contents in the hydrocarbon gases of the inclusions in the three carbonate samples of the Majiagou Formation are between 65.79% and 84.66%, while those in the two Permian sandstone samples are between 49.15% and 73.31%. In general, the characteristics of gaseous hydrocarbon compositions and contents in the inclusion samples analyzed by this method are generally consistent with those of individual inclusions analyzed by laser Raman (Figure 7), i.e., the methane content is the highest in all gaseous hydrocarbons.

4.1.4. Inclusions Isotopic Characteristics. The inclusions were opened to analyze the carbon and hydrogen isotopes of the wrapped methane, and the results are shown in Table 1. The methane gas $\delta^{13}C_1$ and δD_{SMOW} of the inclusions in the Permian sandstone reservoir are significantly lower than those of the dolomite inclusions in the Majiagou Formation. The methane gas $\delta^{13}C_1$ of the inclusions in the Permian sandstone reservoir is between −30.22‰ and −29.63‰, and the corresponding δD_{SMOW} varies from −96.37‰ to −102.78‰. The $\delta^{13}C_1$ of methane gas in dolomite inclusions of Majiagou Formation ranges from -33.29‰ to −37.76‰, and the corresponding δD_{SMOW} is between −128.3‰ and −132.19‰.

4.1.5. Comparison of Gas Composition between Inclusions and Natural Gas in the Natural Gas Layer. The natural gas found in the Ordos Basin is mainly composed of methane (CH_4), and the content of heavy hydrocarbon (C_{2+}) is generally low, with a small amount of carbon dioxide, nitrogen and trace hydrogen [36, 37]. The Lower Paleozoic generally contains trace hydrogen sulfide gas. The methane (CH_4) content of natural gas in the Permian reservoir is between 85.619% and 98.62%, concentrating from 92% to 96% with an average of 93.82%. The methane content in the Ordovician Majiagou Formation is between 87.38% and 98.37%, mainly from 92% to 97% with an average of 94.39% [36, 37].

Since natural gas inclusions were captured during the large-scale migration and accumulation of natural gas, the gaseous hydrocarbon components in these inclusions should be similar to those in the natural gas reservoirs. This study analyzed and compared the gas composition of the gas layer of the Ordovician Majiagou Formation in the F6 well, the gas composition obtained by gas logging in this gas-bearing interval (2770.07–2770.89 m), and the gas composition of inclusions in this layer obtained by thermal explosion method (Table 2). The results show that the main hydrocarbon gas composition of the three is CH_4, and the content of heavy hydrocarbon gas is very low (Figure 8). The natural gas layer has the highest (>94%) CH_4 content. The CH_4 contents of natural gas measured by gas logging and of the same-layer inclusions are relatively low (less than 80%), and heavy hydrocarbon gas is more than 20%. These indicate that the compositions of natural gas in the inclusions are different from those in the natural gas layer. The reason is the natural gas compositions captured in the inclusions represent the compositions of the original natural gas during the large-scale migration and accumulation period, in which the gas-moisture differentiation was incomplete and the inclusion compositions remained unchanged after being captured. Comparatively, natural gas in the gas layer experienced complex changes in the later period, including secondary differentiation of gas and water after accumulation.

5. Discussion

5.1. Analysis of Natural Gas Source Rock. The hydrocarbon source rocks and genesis of the natural gas in the Ordos Basin are controversial. It is generally believed that the coal-bearing rocks in the Upper Paleozoic are the main hydrocarbon source rocks [29, 36]. Natural gas exploration has been carried out around coal-bearing rocks for a long time, and several large natural gas fields have been found around the hydrocarbon generation center of the Upper Paleozoic coal-bearing rocks in the northern basin. In recent years, many scholars have noticed the contribution of Ordovician marine rocks to hydrocarbon generation. Through the study on the distribution of Ordovician marine rocks,

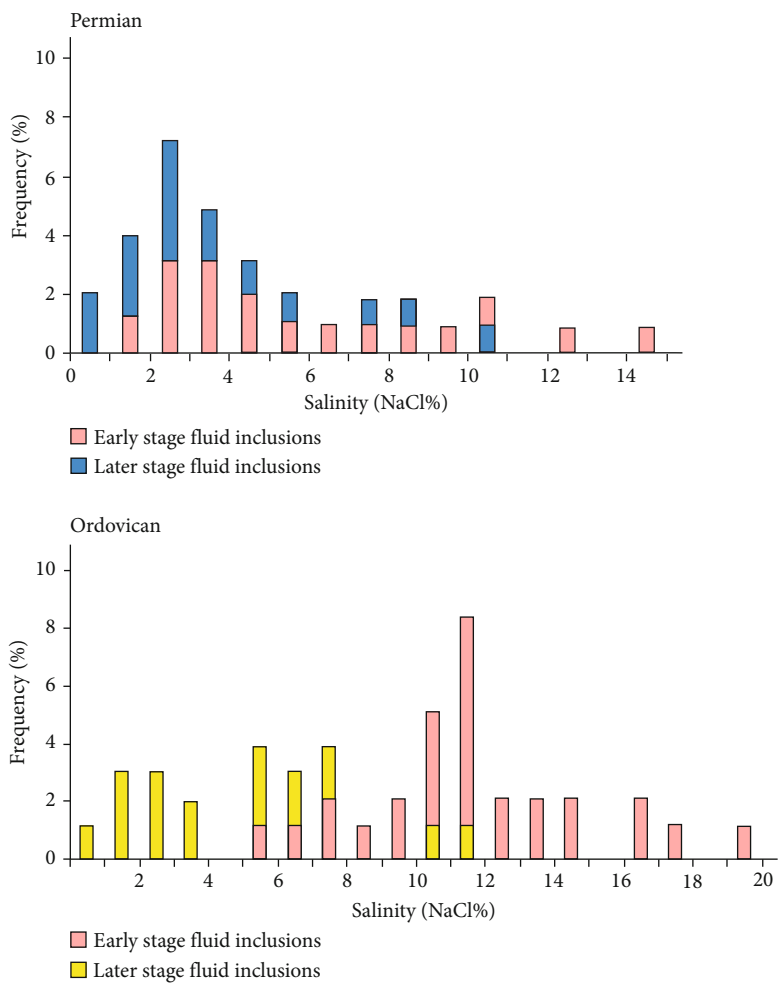

Figure 5: Salinity components of fluid inclusion.

organic geochemistry of rocks, natural gas composition, and isotope geochemistry, it is considered that the dark stratiform mudstone, dolomitic mudstone, and argillaceous dolomite of the Ordovician Majiagou Formation are also effective hydrocarbon source rocks [38].

The carbon and hydrogen isotopes of methane in natural gas inclusions in different layers are different. Methane isotopes of natural gas inclusions in different layers in Table 1 show the methane $\delta^{13}C_1$ in the inclusions of the Permian sandstones varies from −30.22‰ to −29.63‰, and the methane $\delta^{13}C_1$ in the inclusions of the Ordovician Majiagou Formation dolomite ranges from −33.29‰ to −37.76‰. Compared with the methane $\delta^{13}C_1$ in the natural gas, the gas layer of weathering crust, and the gas layer beneath the weathering crust of the Ordos Basin (Table 3) summarized by Dai et al. [39], the methane $\delta^{13}C_1$ in the inclusions of the Permian Shanxi Formation sandstone is consistent with that in the Carboniferous-Permian gas layer of the Ordos Basin, while the methane $\delta^{13}C_1$ in the Ordovician Majiagou Formation is consistent with that in the gas layer of weathering crust in Ordos Basin.

The natural gas $\delta^{13}C_1$ of the inclusion from Majiagou Formation dolomite in F6 well is much closer to that of the Majiagou Formation compared to that of other different gas layers in the well area (Table 4), indicating that the inclusions recorded the characteristics of the natural gas accumulation.

On the genetic discrimination diagram of natural gas $\delta^{13}C_1$-δD of Schoell [40] (Figure 9), the natural gas inclusions from different wells and different layers plot in different genetic fields but all in the dry gas field, corresponding to a thermal evolution degree with Ro greater than 2.0%, which is consistent with that of the natural gas hydrocarbon source rocks in this region. Inclusions in the Permian sandstone of the Shanxi Formation are located in the dry gas area of humic pyrolysis, indicating the natural gas wrapped in the sandstone was derived from the Carboniferous-Permian coal-bearing strata. Inclusions in the Ordovician dolomite fall in the mixed dry gas area, suggesting the natural gas was derived from the Upper Paleozoic coal-bearing strata and the Lower Paleozoic carbonate rocks. Therefore, the inclusion isotopes show natural gas originated from both Permian coal-bearing rocks and Ordovician carbonate rocks.

5.2. Fluid Characteristics. Fluid inclusions are widely distributed in petroliferous basins. The fluid system in inclusions is used to trace the ancient fluid migration as it is the only observable primary fluid sample for hydrocarbon migration

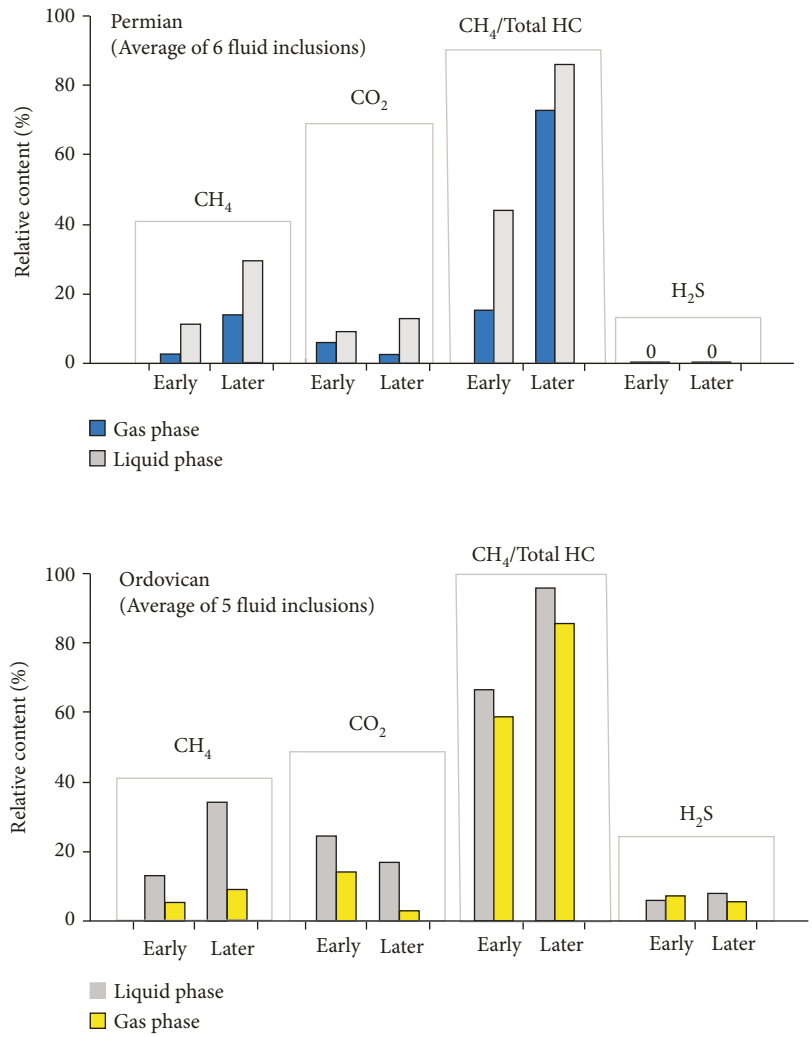

Figure 6: Comparison of mean values of main components in gas and liquid phases of inclusions by laser Raman spectroscopy.

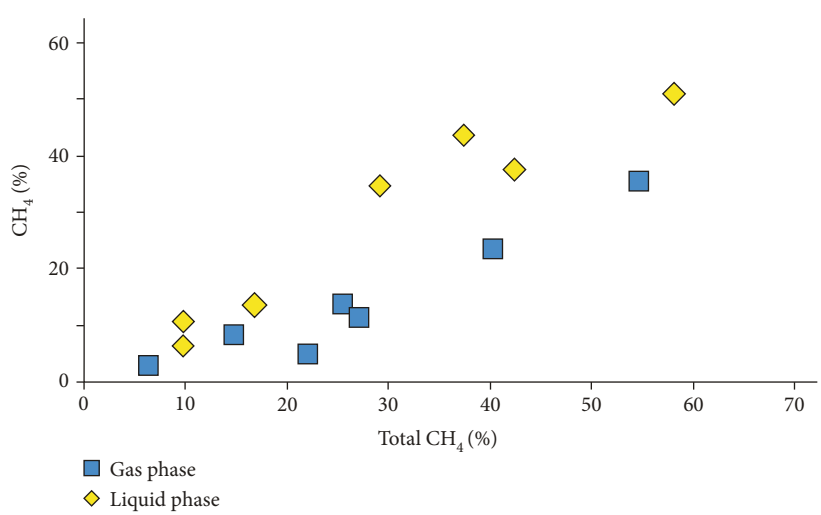

Figure 7: Relationship between the content of gas, liquid methane in inclusions, and total hydrocarbon in laser Raman analysis.

Table 1: Results of gaseous hydrocarbon composition and methane isotope analysis of inclusions analyzed by inclusion opening method.

Sample	Lithology	Stratum/depth	Composition	C_1	C_2	C_3	C_4	C_5	$\sum C_i$	$\delta^{13}C_1$	δD_{SMOW}
L1 well	Sandstone	Shanxi Formation/3424.08	a	0.8132	0.4051	0.2071	0.143	0.086	1.6544	-29.63	-102.78
			b	49.15	24.49	12.52	8.64	5.20	100		
	Dolomite	Majiagou Formation/3563.50	a	1.9616	0.6461	0.1664	0.1172	0.0905	2.9818	-33.29	-128.3
			b	65.79	21.67	5.58	3.93	3.04	100		
Xt 1 well	Dolomite	Majiagou/	a	1.8946	0.1947	0.1007	0.0568	0.0118	2.2586	-37.76	-132.19
			b	83.88	8.62	4.46	2.51	0.52	100		
Y2 well	Sandstone	Benxi Formation/2503.1	a	2.0206	0.4514	0.1621	0.1074	0.0146	2.7561	-30.22	-96.37
			b	73.31	16.38	5.88	3.90	0.53	100		
F6 well	Dolomite	Majiagou Formation/2770.9	a	1.8991	0.2191	0.1434	0.0861	0.041	2.3887	-33.35	-111.03
			b	79.51	9.17	6.01	3.60	1.72	100		
		2770.17-2770.89	c	77.49	21.77	0.37	0.37	0.00	100	——	——

Note: a: gas content, unit: m^3/t rock; b: relative content, Ci/Ci (×100%); c: relative gas content, %, obtained from gas logging in well section 2770.17-2770.89 m.

Table 2: Comparison of hydrocarbon composition (%) of natural gas inclusions and gas logging in Majiagou Formation of F6 well.

Gas layer	Depth (m) 2770.07-2770.89	Composition (%)	C_1 94.26	C_2 3.57	C_3 1.74	C_4 0.43	C_5 0	$\sum C_i$ 100
Dolomite inclusions	2770.9	Gas content (m^3/rock)	1.8991	0.2191	0.1434	0.0861	0.041	2.3887
		Relative content (%)	79.51	9.17	6.01	3.60	1.72	100
Gas logging	2770.07-2770.89	Content (%)	1.121	0.126	0.055	0.002	0.002	1.326
		Relative content (%)	77.49	21.77	0.37	0.37	0.00	100

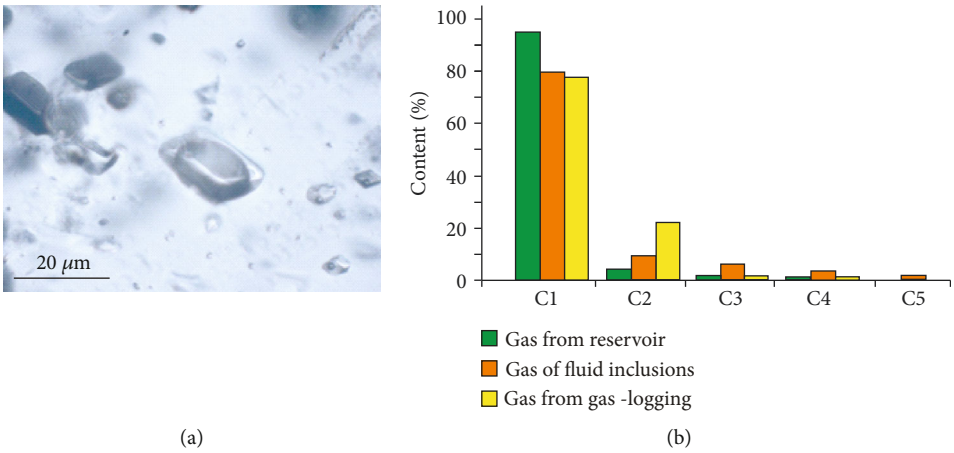

Figure 8: Comparison of gas compositions among Majiagou Formation gas layer, gas logging, and the same-layer fluid inclusions.

and accumulation. The common fluid inclusion brine systems are $NaHCO_3$ type water, $CaCl_2$ type water, Na_2SO_4 type water, $MgCl_2$ type water, and NaCl type water. $NaHCO_3$ type water is a common type of semiclosed oilfield water, and it is a direct sign of oil when the total salinity of the water is high and Cl^- and HCO^{3-} are dominant in water. $CaCl_2$ type water is also common in oilfield water. Generally, in a reservoir with a stable geological structure of good sealing and interlayer separation, $CaCl_2$ type water is dominant and directly signifies oil. Na_2SO_4 type water is rare in oilfield water, and the oil-bearing prospect is not ideal. In the gas field, Na_2SO_4 type water is hardly seen and $NaHCO_3$ type water is predominant. $MgCl_2$ type water has marine geochemical characteristics and is not an oil-bearing marker under normal conditions. NaCl type water is widely distributed in oilfield.

Fluid inclusion analysis shows that the peak homogenization temperatures of the Permian sandstone inclusions are 110°C-120°C and 160°C-170°C, while those of the Ordovician dolomite inclusions are 120°C-130°C and 170°C-180°C. The peak salinity of fluid inclusions in the Permian sandstone is from 0.0 wt% to 5.0 wt %, and that of the fluid inclusions in the Ordovician Majiagou Formation dolomite is between 1.0 wt% and 11.0 wt%. The diagenetic fluid is in

Table 3: Statistical values of natural gas methane isotopes in different layers of the Ordos Basin [39].

Stratum	$\delta^{13}C_1$ (‰)	
	Range	Average value (amount)
Carboniferous-Permian gas layer	-37.3~-25.5	-33.4 (44)
Gas layer of weathering crust	-36.9~-29.0	-33.6 (90)
The gas layer beneath the weathering crust	-40.8~-37.2	-38.9 (7)

Table 4: Comparison of carbon isotopes of inclusions in Fugu 6 well in different gas layers in the well area.

Sample	Stratum/depth (m)	$\delta^{13}C_1$ (‰)
Dolomite inclusions	Majiagou Formation/2770.9	-33.35
Gas	Shanxi Formation	-31.8
Gas	Majiagou Formation	-34.4

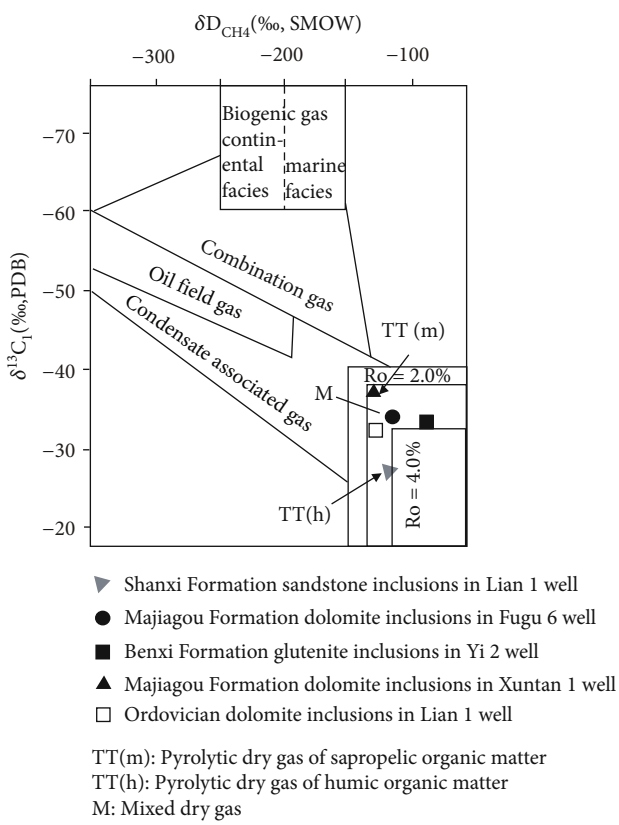

Figure 9: Genetic map of natural gas inclusions in the study area.

the range of medium-low temperature and moderate-low salinity [41]. According to the varying characteristics of fluid inclusion brine systems in the Permian and Ordovician strata of different wells in the study area (Figures 10 and 11), the fluid inclusion brine system in the Permian sandstones is mainly $MgCl_2$-NaCl-H_2O and subordinate $CaCl_2$-H_2O. The brine system of fluid inclusions in the Ordovician dolomite is mainly $CaCl_2$-NaCl-H_2O, followed by the $CaCl_2$-H_2O brine system, and rare $MgCl_2$-H_2O system. In short, the brine system of fluid inclusions in the Ordovician is mainly a $CaCl_2$ brine system, indicating the hydrogeological stagnant conditions of the Ordovician were conducive to the existence of oil and gas. The brine of fluid inclusions in the Permian is mainly $MgCl_2$-NaCl-H_2O, which was not conducive to the existence of oil and gas. The formation and migration conditions of natural gas in the Lower Paleozoic were better than those in the Upper Paleozoic.

5.3. Accumulation Characteristics. The process of hydrocarbon accumulation is the formation and continuous injection of oil and gas fluid into the reservoir, displacing the primary pore water in the reservoir and finally accumulating [35]. Before oil and gas were injected into the reservoir, the reservoir pores were mainly occupied by the primary formation water. With the formation and entry of oil and gas into the reservoir, the primary fluid in the reservoir pores was displaced and replaced by oil and gas fluid. The fluid inclusions formed during this process contained oil and gas. Meanwhile, there was a coexistence of brine inclusions and liquid hydrocarbon inclusions [35, 42, 43]. Previous studies have shown the Upper Paleozoic coal-bearing hydrocarbon source rocks in the Ordos Basin produced mainly natural gas but no liquid hydrocarbons [44, 45]. This study has found that the early-phase inclusions in the Permian and Ordovician reservoirs contain liquid hydrocarbons with weak fluorescence, confirming the natural gas in the Ordos Basin experienced a liquid hydrocarbon formation stage [18]. It is consistent with the thermal evolution process of kerogen hydrocarbon generation of hydrocarbon source rocks. Liu et al. [29] and other studies have also found liquid hydrocarbon inclusions in the Paleozoic of the Ordos Basin and proposed that the formation of natural gas in the Ordos Basin experienced a process from liquid hydrocarbon to gaseous hydrocarbon. They believed the central-southern regions of the basin entered the oil generation stage in the Middle-Late Triassic, and the crude oil filled the central region in the early Middle Jurassic, forming liquid hydrocarbon inclusions with blue fluorescence and minor yellow fluorescence. However, at this time, industrial reservoirs were not formed. A large number of natural gas was generated in the middle of the Early Cretaceous and filled from south to the northern part of the Yishan slope and continued to form large-scale reservoirs before the uplift in the late Early Cretaceous. In this study, the inclusion lithofacies and compositional analysis have further proved that the natural gas reservoirs in Ordos Basin experienced an early liquid hydrocarbon formation stage, and the large-scale migration of natural gas was related to the development of late tectonic fractures.

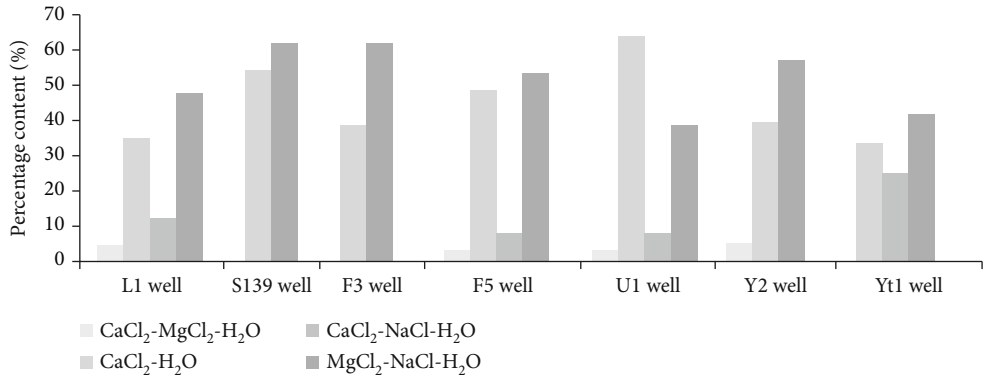

Figure 10: Characteristics of brine system of Upper Paleozoic inclusions.

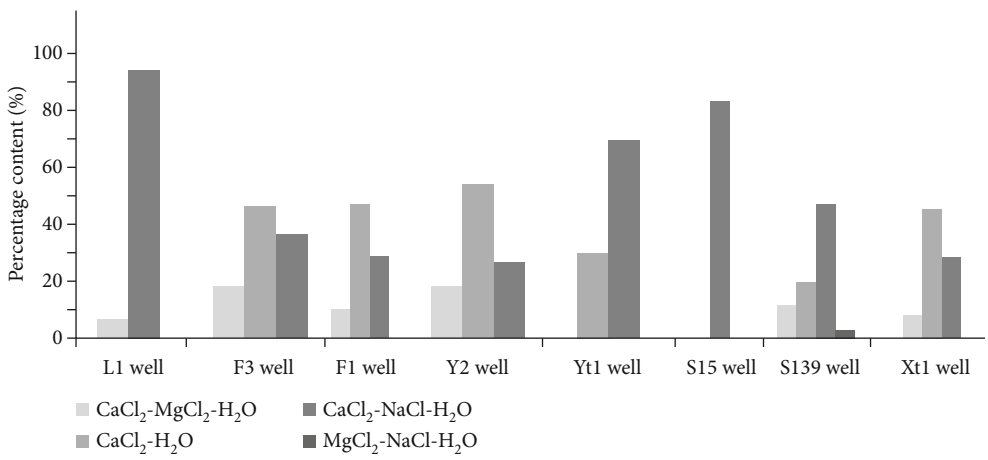

Figure 11: Characteristics of brine system of Lower Paleozoic inclusions.

Table 5: Rb/Sr isotope ratio analysis of the Permian fluid inclusions in F1 well.

Position	Depth (m)	Sample	Rb (μg/g)	Sr (μg/g)	$^{87}Rb/^{86}Sr$	$^{87}Sr/^{86}Sr$	Precision
Upper Shihezi Formation	2708.40	F2-1	0.008	0.122	0.1896	0.7154	±0.000027
Upper Shihezi Formation	2711.20	F2-2	0.005	0.081	0.17834	0.71275	±0.000034
Upper Shihezi Formation	2712.13	F2-3	0.005	0.075	0.18457	0.71454	±0.000015
Shanxi Formation	3016.86	F2-4	0.006	0.168	0.17371	0.71266	±0.000023
Shanxi Formation	3017.11	F2-5	0.006	0.08	0.19474	0.71593	±0.000043

The Rb/Sr isotope method was used to date the age of fluid inclusions. The hydrocarbonaceous inclusions in the Permian sandstone of the F1 well are well-developed and dominated by the late gaseous hydrocarbon inclusions filled in fractures. The Rb-Sr isochron age of fluid inclusions represents the isotopic homogenization age of fluid and surrounding rock when the inclusions were formed, that is, the formation age of inclusions. To determine the age of fluid inclusions by Rb/Sr dating, the prerequisite is synchronous inclusions with the initial Sr isotopes reaching complete homogenization. In other words, the fluid in a group of fluid inclusion samples is homologous and synchronous. After the formation of fluid inclusions, the Rb/Sr isotope system should remain closed. The Rb/Sr ratios in a group of fluid inclusions that meet the prerequisite should be consistent and will plot on the same line in the Rb/Sr coordinates. The slope of the line represents the change of the Rb/Sr ratio, which can determine the reliable formation age of fluid inclusion. The Rb/Sr isochron age of fluid inclusions was analyzed by selecting the mineral fluid inclusions developed in late-phase gas inclusions at different depths of the Permian strata in the F1 well. The results show the Rb/Sr isotope ratios of the five samples are relatively uniform (Table 5) with a good linear relationship (Figure 12), indicating the Sr isotopes of fluid inclusions in the selected samples reached homogenization and the Rb/Sr isotope system maintained a good sealing after the formation of fluid inclusions. The age of the determined fluid inclusions is 89.18 Ma, which represents the timing of the inclusions capturing the gas-bearing hydrocarbon fluids, namely, the age of natural gas accumulation.

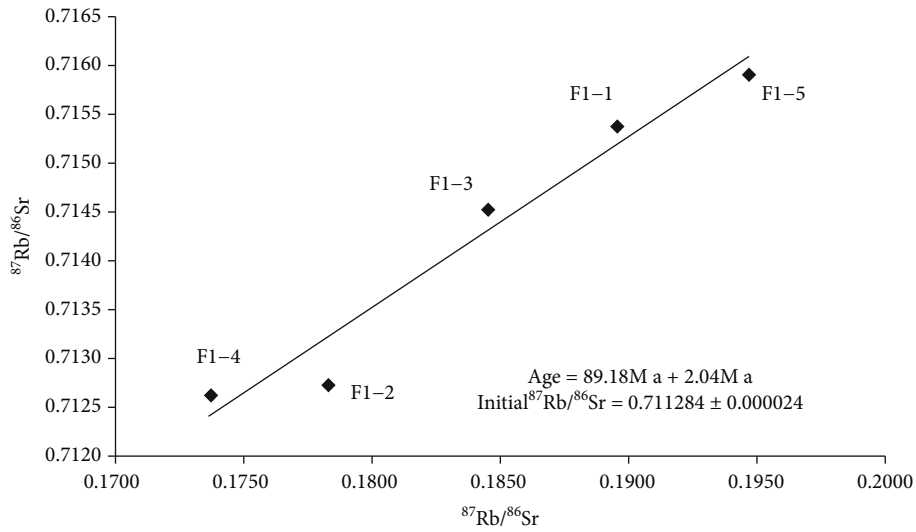

Figure 12: Rb/Sr isochron ages of fluid inclusions.

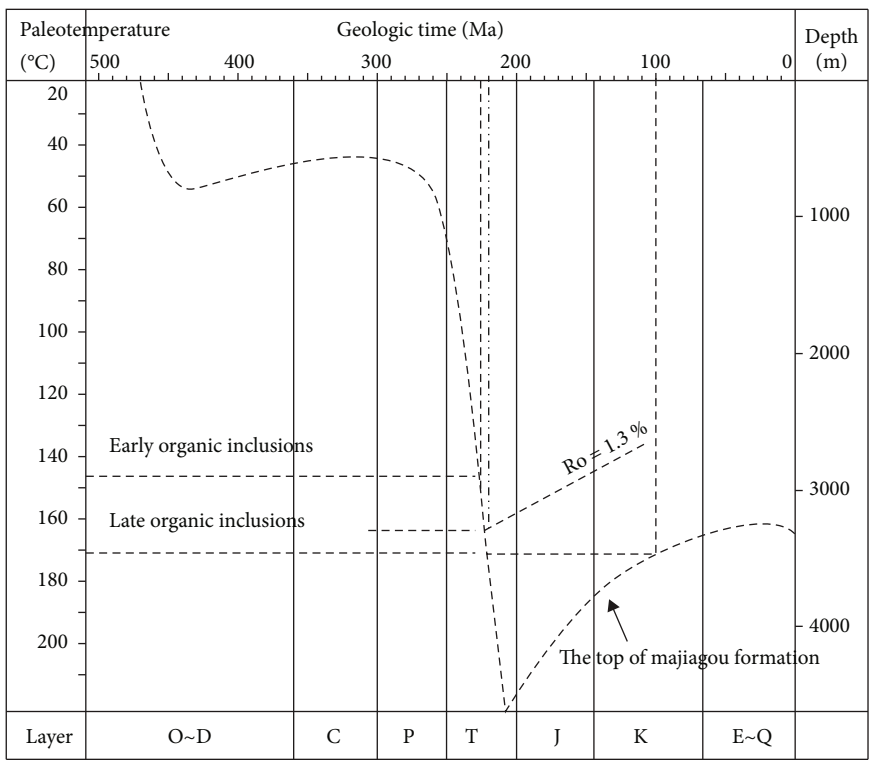

Figure 13: Gas accumulation time of Majiagou Formation of Xt 1 well in the Ordos Basin.

According to the homogenization temperatures of fluid inclusions, combined with the paleogeothermal and sedimentary tectonic evolution history of the basin, the formation time of inclusions can be determined, and then the formation time of natural gas reservoirs can be determined. This method is also called the "fluid inclusion method" for determining oil and gas accumulation [46–49]. According to the tectonic evolution history of the Ordos Basin, the representative Xt 1 well with complete stratigraphic data was selected to establish the burial depth-thermal evolution curve of the Permian and Ordovician in the study area (Figure 13). The homogenization temperature method of inclusions was used to determine the time of natural gas migration and accumulation. Stratigraphic stratification of the Xt 1 well was based on the stratification data from the Changqing Oilfield Research Institute, and the strata erosion thickness and paleogeothermal gradient are based on references [50].

The inclusions in the temperature range of 145°C–155°C are the early-phase gas-liquid two-phase inclusions containing

liquid hydrocarbons, indicating the thermal evolution of the hydrocarbon source rocks was in the stage of liquid hydrocarbon generation. At this time, the thermal evolution was below the gas generation window (Ro = 1.3%) (Figure 13). The inclusions in this stage recorded the early filling of liquid hydrocarbon-containing organic fluid into the reservoir. The homogenization temperature of the inclusions in this period intersects the burial section of the burial depth-thermal evolution curve of the Permian strata at the Late Triassic (220 Ma), when the fluid containing liquid hydrocarbon formed and began to enter the reservoir. The inclusions in the high-temperature range of 160°C-170°C are gaseous hydrocarbon inclusions. At this time, the thermal evolution of hydrocarbon source rocks entered the gas generation window (Figure 13). The inclusions in this period were formed during the large-scale migration and accumulation of natural gas and were distributed in the late structural fractures. The homogenization temperature of these inclusions intersects the uplift section of the burial depth-thermal evolution curve of the Ordovician strata at the early Late Cretaceous (100 Ma), which is the time of natural gas accumulation in the Ordovician.

Combined with the burial thermal evolution history of the Xt 1 well (Figure 13), the gas accumulation process of the Majiagou Formation in the Ordos Basin was analyzed. Sedimentation occurred in the Middle and Late Ordovician, and then the carbonate rocks of the Lower Ordovician Majiagou Formation experienced a long period of weathering and erosion for about 150 Ma. Hence, the weathering crust reservoirs were formed [14]. Subsidence started in the Permian and lasted till the Late Triassic, with the burial depth increase of about 3900 m and the paleogeotemperature up to 145°C–150°C. During this period (220 Ma), the hydrocarbon source rocks of Majiagou Formation entered the oil generation window and began to discharge hydrocarbons. The generated oil migrated along the weathering surface. The Ro reached the lower limit of the gas generation window of 1.3%, and thus, the oil began to transform into natural gas. At about 210 Ma, the paleogeotemperature of the strata reached 220°C, and a large quantity of oil and gas were accumulated. Due to the Yanshan movement, the strata were uplifted and resulted in a large number of structural fractures, which served as channels for oil and gas migration and accumulation space. After that, the strata were eroded due to the Himalayan movement. Till the Cenozoic, the burial depth of the strata was about 3300 meters. During this period, the formed oil and gas escaped along fractures, and the hydrocarbon generation gradually weakened to the end. The karst paleogeomorphology reservoirs of the Lower Ordovician Majiagou Formation in central Ordos Basin provided a good space for natural gas accumulation.

6. Conclusion

(1) There are early- and late-phase organic fluid inclusions in the Upper Paleozoic Permian sandstone and the Lower Paleozoic Ordovician Majiagou Formation dolomite reservoirs. The early-phase inclusions are gas-liquid two-phase inclusions containing liquid hydrocarbons with fluorescence, recording the petroleum entering the reservoir in the early stage of the reservoir formation. Late-phase inclusions are gas-liquid two-phase inclusions containing gaseous hydrocarbons, recording gaseous hydrocarbon migrating into the reservoir in the late stage of accumulation. Methane is the most abundant gaseous hydrocarbon in the inclusion

(2) The Upper Paleozoic sandstone inclusions have peak homogenization temperature ranges of 110-120°C and 160-170°C, and the salinity peak range is 0.0-5.0 wt%, while the lower Paleozoic dolomite inclusions have peak homogenization temperature ranges of 120-130°C and 170-180°C and the peak salinity range of 1.0-11.0 wt%. The diagenetic fluid was in the range of medium-low temperature and medium-low salinity. The brine system of Ordovician fluid inclusions was dominated by $CaCl_2$-H_2O, and the brine system of Permian fluid inclusions was mainly $MgCl_2$-NaCl-H_2O. The conditions for the formation and migration of natural gas in the Ordovician were better than those in the Permian

(3) Methane is the most abundant gaseous hydrocarbon in the inclusion. The formation of natural gas experienced a process from liquid hydrocarbon to gaseous hydrocarbon. The large-scale migration of natural gas was related to the development of late tectonic fractures. Both the coal-bearing rocks of the Permian and the carbonate rocks of the Ordovician were hydrocarbon source rocks for natural gas in the Ordos Basin

(4) The time of accumulation was determined by Rb/Sr isotopic dating and the inclusion homogenization temperature method. The analysis of the gas formation process indicates that the process of the early-phase liquid hydrocarbon formation and migration into the reservoir corresponded to 220 Ma (Late Triassic). The late large-scale migration and accumulation of natural gas occurred at 100 Ma (early Late Cretaceous), which was close to the inclusion Rb/Sr isochron age of 89.18 Ma, indicating that the natural gas accumulation was related to the Yanshanian tectonic movement

Data Availability

Fluid inclusion homogenization temperature, salinity data, laser Raman spectroscopy analysis data, and gas chromatograph analyses used to support the findings of this study are included within the article.

Conflicts of Interest

The authors declare that they have no conflicts of interest.

Acknowledgments

This study was supported by the National Natural Science Foundation of China (number: 41772118) and the Fundamental Research Funds for the Central Universities, Chang'an University (No. 300102279106).

References

[1] H. Yang, X. S. Liu, and X. X. Yan, "Tectonic-sedimentary evolution and tight sandstone gas accumulation in Ordos Basin since Late Paleozoic," *Earth Science Frontiers*, vol. 22, no. 3, pp. 174–183, 2015.

[2] H. Yang, J. H. Fu, and X. S. Wei, "Characteristics of natural gas accumulation in Ordos Basin," *Natural Gas Industry*, vol. 25, no. 4, pp. 5–8, 2005.

[3] H. Yang, J. H. Fu, X. S. Liu, and P. L. Mei, "Accumulation conditions and exploration and development of Upper Paleozoic tight gas in Ordos Basin," *Petroleum Exploration and Development*, vol. 39, no. 3, pp. 295–303, 2012.

[4] H. Yang, X. S. Liu, and D. F. Zhang, "Main controlling factors and exploration progress of natural gas accumulation in Ordovician marine carbonate rocks in Ordos Basin," *Natural Gas Industry*, vol. 33, no. 5, pp. 1–12, 2013.

[5] J. H. Fu, H. F. Bai, L. Y. Sun, and Z. R. Ma, "Types and characteristics of Ordovician carbonate reservoirs in Ordos Basin," *Acta Petrolei Sinica*, vol. 33, no. 2, pp. 110–117, 2012.

[6] X. S. Liu, Y. L. Jiang, Y. D. Hou et al., "Genesis of combinatorial natural gas and its main controlling factors in Ordovician in Jingxi area of Ordos Basin," *Natural Gas Industry*, vol. 36, no. 4, pp. 16–26, 2016.

[7] X. Li, *Study on the Characteristics and Thermal Evolution History of Paleozoic Source Rocks in Southeastern Ordos Basin, [M.S. thesis]*, Chang'an University, 2007.

[8] D. Liu, W. Z. Zhang, Q. F. Kong, Z. Q. Fen, C. C. Fang, and W. L. Peng, "The source rocks of Lower Paleozoic and natural gas causes in the Ordos Basin," *Petroleum Exploration and Development*, vol. 43, no. 4, pp. 540–549, 2016.

[9] Z. J. Wang and X. S. Xu, "Discussion on gas source of Lower Paleozoic reservoir gas in Ordos Basin," *Sedimentary Geology and Tethyan Geology*, vol. 23, no. 4, pp. 84–90, 2003.

[10] H. X. Cao, H. Y. Wu, X. M. Ren, Y. Wu, Q. S. Liang, and M. B. Tong, "The Ordovician karst paleomorphology and reservoir distribution in the southeast of Ordos Basin," *China Petroleum Exploration*, vol. 25, no. 3, pp. 146–155, 2020.

[11] J. Duan, *Characteristics of Carbonate Reservoir in the Lower Paleozoic in the Southern Margin of Ordos Basin, [M.S. thesis]*, Chengdu University of Technology, 2009.

[12] Z. L. Wang, L. Wei, X. Z. Wang et al., "The process and mechanism of natural gas accumulation of Lower Paleozoic in Yan'an area Ordos Basin," *Acta Petrolei Sinica*, vol. 37, no. 1, pp. 99–110, 2016.

[13] J. H. Wang, *Study on the Lower Paleozoic Reservoir Formation in the Southern Margin of Ordos Basin, [M.S. thesis]*, Chengdu University of Technology, 2009.

[14] C. G. Wang, Y. Wang, H. Z. Xu, Y. P. Sun, W. L. Yang, and T. H. Wu, "The characteristics of hydrocarbon accumulation and evolution of Lower Paleozoic source rocks in Ordos Basin," *Acta Petrolei Sinica*, vol. 30, no. 1, pp. 38–50, 2009.

[15] Y. Li, A. P. Fan, R. C. Yang, Y. P. Sun, and N. Lenhardt, "Sedimentary facies control on sandstone reservoir properties: a case study from the permian shanxi formation in the southern ordos basin, central China," *Marine and Petroleum Geology*, vol. 129, pp. 1–16, 2021.

[16] W. X. Han, S. Z. Tao, W. J. Ma, Y. Li, and G. X. Ou, "Reasons for carbon isotope rollover in the Yan'an gas field of the southern Ordos Basin, China: evidence from the geochemical comparison of gas from fluid inclusions with wells," *International Journal of Coal Geology*, vol. 234, pp. 1–11, 2021.

[17] C. Y. Wang, Z. C. Wang, J. L. Wang, Y. Bao, and X. M. Hu, "Reconstruction of paleo river systems and distribution of sedimentary facies of Shanxi and lower Shihezi formations in southern Ordos Basin," *Journal of China University of Mining and Technology*, vol. 18, no. 2, pp. 241–244, 2008.

[18] Z. X. An, "The formation of northern Shaanxi gas area and the central paleo-uplift, China Offshore Oil and Gas," vol. 12, no. 3, pp. 150–153, 1998.

[19] H. J. Gan, J. K. Mi, and X. M. Xiao, "Research on natural gas source and migration and accumulation of the gas field in the Upper Paleozoic in the north-central Ordos Basin," *Journal of Oil and Gas Technology*, vol. 29, no. 1, pp. 16–22, 2007.

[20] L. Zhao, X. X. Xia, and J. X. Dai, "Migration and accumulation of natural gas in the Upper Paleozoic in the Ordos Basin," *Earth and Environment*, vol. 28, no. 3, pp. 48–53, 2000.

[21] S. Wang, "Ordos Basin superposed evolution and structural controls of coal forming activities," *Earth Science Frontiers*, vol. 24, no. 2, pp. 54–63, 2017.

[22] Y. Yao, D. Liu, and T. Yan, "Geological and hydrogeological controls on the accumulation of coalbed methane in the Weibei field, southeastern Ordos Basin," *International Journal of Coal Geology*, vol. 121, pp. 148–159, 2014.

[23] C. Guo, Y. C. Xia, D. M. Ma et al., "Geological conditions of coaled methane accumulation in the Hancheng area, southeastern Ordos Basin, China: implications for coalbed methane high-yield potential," *Energy Exploration and Exploitation*, vol. 37, no. 3, pp. 922–944, 2019.

[24] Z. X. He, *Evolution and Oil Gas of the Ordos Basin*, Petroleum Industry Press, Beijing, China, 2003.

[25] H. Zhang, Z. P. Meng, and Z. L. He, "Study on the tectonic stress fields in the Ordos Coal Basin," *Journal of China Coal Society*, vol. 25, pp. 1–5, 2000.

[26] Y. K. Zhang, L. F. Zhou, B. Dang, and W. Sun, "Relationship between the Mesozoic and Cenozoic tectonic stress fields and the hydrocarbon accumulation in the Ordos Basin," *Petroleum Geology & Experiment*, vol. 28, no. 3, pp. 215–219, 2006a.

[27] L. L. Wang, B. Jiang, J. L. Wang, Z. H. Qu, and R. Chen, "Structural controls on joint development in the southeastern margin of the Ordos Basin," *Arabian Journal of Geosciences*, vol. 9, no. 5, p. 352, 2016.

[28] H. Xu, D. Z. Tang, J. L. Zhao, S. Tao, S. Li, and Y. Fang, "Geologic controls of the production of coalbed methane in the Hancheng area, southeastern Ordos Basin," *Journal of Natural Gas Science and Engineering*, vol. 26, no. 26, pp. 156–162, 2015.

[29] J. L. Liu, K. Y. Liu, and L. L. Gui, "Characteristics of fluid inclusions and hydrocarbon charging history of the Upper Paleozoic in the central Ordos Basin," *Journal of China University of Petroleum*, vol. 43, no. 2, pp. 13–25, 2019.

[30] T. Lei, H. C. Deng, D. Wu et al., "Depositional model of the lower-middle Ordovician Majiagou Formation in Daniudi Gas Field, Ordos Basin," *Journal of Palaeogeography*, vol. 22, no. 3, pp. 523–538, 2020.

[31] J. L. Liu, K. Y. Liu, and X. Huang, "Effect of sedimentary heterogeneities on hydrocarbon accumulations in the Permian Shanxi Formation, Ordos Basin, China: insight from an integrated stratigraphic forward and petroleum system modelling," *Marine and Petroleum Geology*, vol. 76, pp. 412–431, 2016.

[32] J. Yang and X. Pei, *Geology of Natural Gas in China, v. 4(Ordos Basin)*, Petroleum Industry Press (in Chinese), 1996.

[33] Y. Yang, W. Li, and L. Ma, "Tectonic and stratigraphic controls of hydrocarbon systems in the Ordos Basin: a multicycle cratonic basin in central China," *AAPG Bulletin*, vol. 89, no. 2, pp. 255–269, 2005.

[34] W. Z. Zhang, H. Yang, C. L. Zan, and Q. F. Kong, "Study on the geochemistry of natural gas in Paleozoic in the high thermal evolution area located the central - southern Yishan Slope, Ordos Basin," *Geochimica*, vol. 45, no. 6, pp. 614–622, 2016.

[35] D. Middleton, J. Parnell, P. Carey, and G. Xu, "Reconstruction of fluid migration history of Northwest Ireland using fluid inclusion studies," *Journal of Geochemical Exploration*, no. 69, pp. 633–677, 2000.

[36] J. Li, J. Z. Zhao, D. X. Wang et al., "Origin and source of natural gas in the Ordovician middle assemblage on the east side of the central paleo-uplift of the Ordos Basin," *Acta Petrolei Sinica*, vol. 37, no. 7, pp. 821–831, 2016.

[37] X. Sun, J. Wang, C. Tao et al., "Geochemical characteristics and source of Paleozoic natural gas in Daniudi, Ordos Basin," *Acta Petrolei Sinica*, vol. 43, no. 2, pp. 307–314, 2021.

[38] J. Q. Tu, Y. G. Dong, B. Z. Zhang et al., "Discovery of large-scale effective source rocks of Ordovician Majiagou Formation in Ordos Basin and its geological significance," *Natural Gas Industry*, vol. 36, no. 5, pp. 15–24, 2016.

[39] J. X. Dai, X. Y. Xia, S. F. Qin, and J. Z. Zhao, "Causes of carbon isotope series reverse of organic alkane gas in China," *Oil & Gas Geology*, vol. 24, no. 1, pp. 1–6, 2003.

[40] M. Schoell, "Genetic characterization of natural gases," *AAPG Bulletin*, vol. 67, no. 12, pp. 2225–2238, 1983.

[41] L. Li, H. M. Tang, X. Wang et al., "Evolution of diagenetic fluid of ultra-deep Cretaceous Bashijiqike Formation in Kuqa depression," *Journal of Central South University*, vol. 25, no. 10, pp. 2472–2495, 2018.

[42] J. Kelly, J. Parnell, and H. C. Chen, "Application of fluid inclusions to studies of fractured sandstone reservoirs," *Journal of Geochemical Exploration*, vol. 69-70, pp. 705–709, 2000.

[43] A. M. Ingrid, "Petroleum inclusions in sedimentary basins: systematics, analytical methods and applications," *Lithos*, vol. 55, no. 1–4, pp. 195–212, 2001.

[44] Q. Cao, J. Z. Zhao, J. H. Fu et al., "Gas source conditions of quasi-continuous gas reservoirs in the Upper Paleozoic of Ordos Basin," *Oil & Gas Geology*, vol. 34, no. 5, pp. 584–591, 2013.

[45] J. H. Fu, X. S. Wei, S. S. Luo et al., "Discovery and geological understanding of Qingyang deep coal-derived gas field," *Petroleum Exploration and Development*, vol. 46, no. 6, pp. 1047–1061, 2019.

[46] J. Z. Zhao, "Analysis of application examples of oil and gas inclusions in the study of accumulation chronology," *Earth and Environment*, vol. 30, no. 2, pp. 83–89, 2002.

[47] X. M. Xiao, Z. F. Liu, and D. H. Liu, "Using reservoir fluid inclusion information to study the accumulation time of natural gas reservoirs," *Chinese Science Bulletin*, vol. 47, no. 12, pp. 957–960, 2002.

[48] D. L. Liu, S. Z. Tao, and B. M. Zhang, "Application of inclusions in determining the age of accumulation and problems needing attention," *Natural Gas Geoscience*, vol. 16, no. 1, pp. 16–19, 2005.

[49] R. X. Li, S. L. Xi, and L. J. Di, "Using reservoir oil and gas inclusion petrography to determine the period of oil and gas accumulation-taking Longdong oilfield in Ordos Basin as an example," *Oil & Gas Geology*, vol. 27, no. 2, pp. 194–199, 2006.

[50] Z. L. Ren, S. Zhang, S. L. Gao, J. P. Cui, Y. Y. Xiao, and H. Xiao, "The tectonic thermal evolution history of Ordos Basin and its significance of accumulation and mineralization," *Scientia Sinica (Terrae)*, vol. 37, no. S1, pp. 23–32, 2007.

Hindawi
Geofluids
Volume 2021, Article ID 5541540, 20 pages
https://doi.org/10.1155/2021/5541540

Research Article

The Evolution of Diagenetic Fluids and Accumulation Characteristics of Tight Sandstone Reservoir in Upper Paleozoic, Southwestern Ordos Basin

Ruijing Zhu,[1,2] **Rongxi Li**,[1] **Xiaoli Wu**,[1] **Xiaoli Qin**,[1] **Bangsheng Zhao**,[1] **and Futian Liu**[1]

[1]*School of Earth Science and Resources, Chang'an University, Xi'an, Shaanxi 710054, China*
[2]*Shanxi Institute of Engineering Technology, Yangquan, Shanxi 045000, China*

Correspondence should be addressed to Rongxi Li; rongxi99@163.com

Received 19 January 2021; Accepted 4 May 2021; Published 15 June 2021

Academic Editor: Basim Abu-Jdayil

The Upper Paleozoic in the southwestern Ordos Basin has significant potential for natural gas exploration. This study investigated the diagenetic fluid evolution and hydrocarbon accumulation characteristics of He 8 section from Permian Lower Shihezi formation and Shan 1 section from Shanxi formation tight sandstone reservoirs by petrographic observation, scanning electron microscope imaging, fluid inclusion study, and laser Raman spectrum analysis. The results show that He 8 section and Shan 1 section reservoirs are mainly composed of quartz sandstone, subordinate arkose quartz sandstone, and lithic quartz sandstone, with minor lithic sandstone and lithic arkose sandstone. The major pores are intergranular dissolved pores. The main diagenetic minerals include quartz overgrowth, siliceous cement, carbonate cement, illite, montmorillonite, and mixed-layer clay minerals. The overall diagenetic features show strong compaction, multistage siliceous and calcareous cements, and abundant clay minerals, strong dissolution, and well-developed fractures. Two stages of fluid inclusions developed in the He 8 and Shan 1 sections recorded the migration and accumulation of the early-stage and late-stage natural gas, respectively. The reservoir in the study area experienced early and late diagenetic stages, and its formation was simultaneous with or after its densification. The diagenetic environment changed from alkaline to acidic and again into alkaline. There are two stages of fluid activities in the study area, namely, the early diagenetic stage corresponding to hydrocarbon generation and migration and the late diagenetic stage corresponding to hydrocarbon accumulation. This study suggests that Upper Paleozoic natural gas migrated into the reservoir in Weibei Uplift, Yishan Slope, and Tianhuan Depression tectonic units during 220-197 Ma, and the large-scale migration and accumulation occurred in these tectonic units at different times. No natural gas was generated in the west margin of the basin because the temperatures of the hydrocarbon source rocks in the Upper Paleozoic were below the gas window.

1. Introduction

Fluid-rock interaction, throughout the basin formation and evolution, generally controls the diagenesis and mineralization in the basin and is closely related to hydrocarbon accumulation and occurrence [1]. Fluid inclusions are independent closed systems formed by fluids sealed in crystallographic defects of minerals [2], and they commonly record plenty of information on temperature, salinity, pressure, and composition related to the oil and gas migration processes and geological events [3–9]. Therefore, the study of fluid inclusions can be used to reverse the formation and evolution history of oil and gas reservoirs [10–13], and it has become an important and mature method for hydrocarbon accumulation research.

Exploration practice has revealed that the Upper Paleozoic of the Ordos Basin gas field is rich in oil and gas resources, with several large and medium-sized gas fields discovered successively in Yulin, Sulige, Wushenqi, Shenmu, Daniudi, and Zizhou have been proved successively in Upper Paleozoic [14–23]. Previous studies have been mainly focused in the central, western, northern, eastern, and southeastern parts of the basin. Recently, in the southwest of the basin, some exploration wells have obtained industrial gas

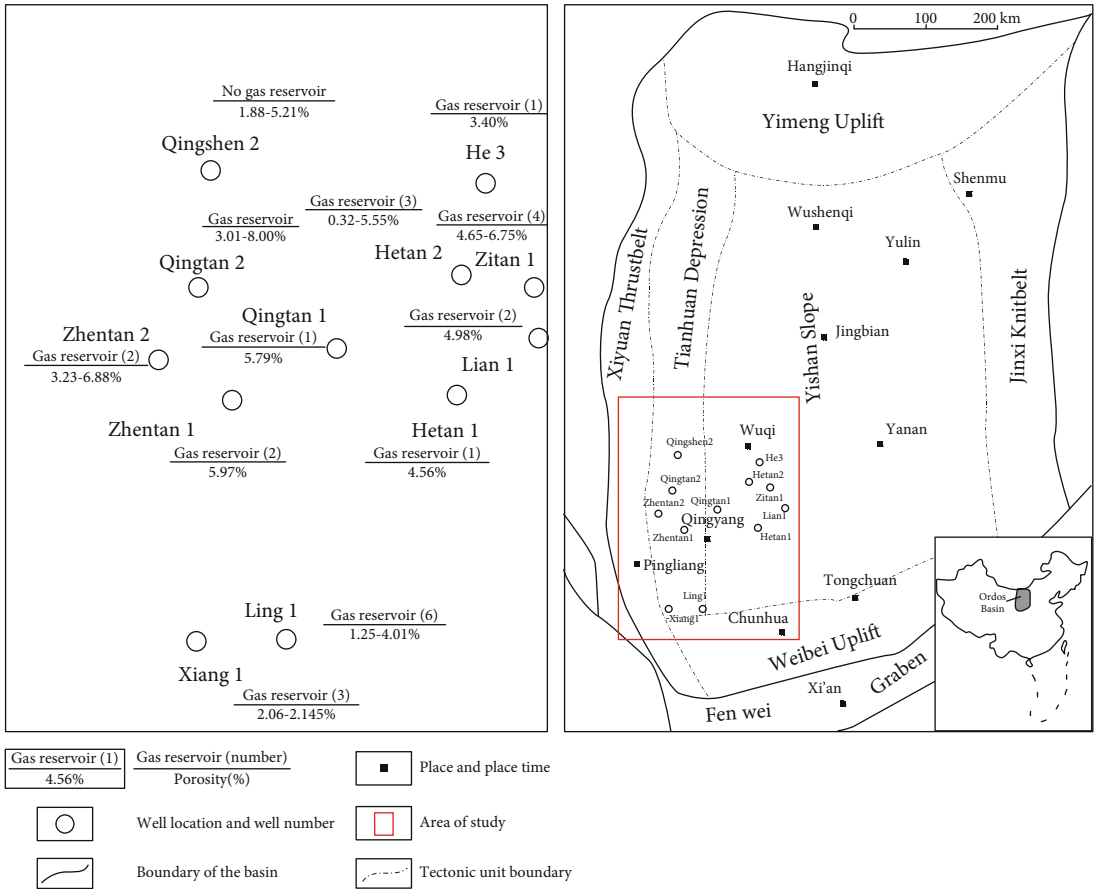

Figure 1: Locations of wells and regional structural location map in the study area.

flow [24], such as the open airflow of 6.62×10^4 m^3/d from Qingtan 1 well in the Shanxi formation, indicating a good prospect for natural gas exploration in the Upper Paleozoic in the southwestern basin. However, the study on the Upper Paleozoic in the southwestern basin is limited with controversial opinions. Zhang et al. [24] believed that the late Cretaceous oil and gas filling in this area was around the paleostructure of the Shan 1 section in the late Jurassic, and it is a near-source or in situ accumulation, whereas Cao et al. [25] suggested that the migration and accumulation of natural gas in the Upper Paleozoic in the southwest part of the basin was a relatively long and continuous process, with the main filling period during the Early Cretaceous (155-100 Ma). Liao et al. [26] argued that a primary natural gas charging occurred in the northern part of this area and the filling and accumulation lasted from late Jurassic to early Cretaceous (J_3-K_1). Hu et al. [27] believed that the hydrocarbon generation started from the Late Triassic (T_3) and ended at the end of the Early Cretaceous (K_1). Moreover, the properties of the gas reservoirs in the southwestern basin are strongly disputed, such as the timing of natural gas accumulation, the types and stages of diagenesis, the processes of gas migration and accumulation, and the diagenetic fluids.

This study investigated core samples from the exploration wells by petrographic examinations, scanning electron microscope imaging, measurement of fluid inclusion homogenization temperature, and laser Raman spectroscopy analysis. The findings will not only better characterize the reservoirs and the fluid inclusions, but also help reveal the diagenetic setting and evolution and the timing of gas accumulation and reservoir densification.

2. Geological Setting

The Ordos Basin, the second-largest petroliferous basin in China, is one of the most important basins abundant in oil and gases in China [28, 29]. It consists of six secondary structural units, namely, the Yimeng Uplift, the Yishan Slope, the Tianhuan Depression, the Weibei Uplift, the Jin-West Knitbelt, and the Xiyuan Thrust belt (Figure 1). The study area, with an area of 3.8×10^4 km^2, situates in the southwestern part of the basin (Figure 1) involving four tectonic units [30], i.e., the Yishan Slope, Weibei Uplift, Tianhuan Depression, and Western Thrust belt. The strata are generally flat with small-scale faults developed in the Xiyuan Thrust belt.

As a large sedimentary basin in the west of the North China block, The Ordos Basin has experienced multistage tectonic evolution, including the Middle-Late Proterozoic Craton valley stage, the Early Paleozoic submarine platform, Late Paleozoic coastal plain, Mesozoic foreland basin, and Cenozoic peripheral fault-depression [31–33]. The main target strata of this study are the He 8 section of Xiashihezi Formation and Shan 1 section of Shanxi Group. The basin was an inland lake setting during the sedimentation of the He 8

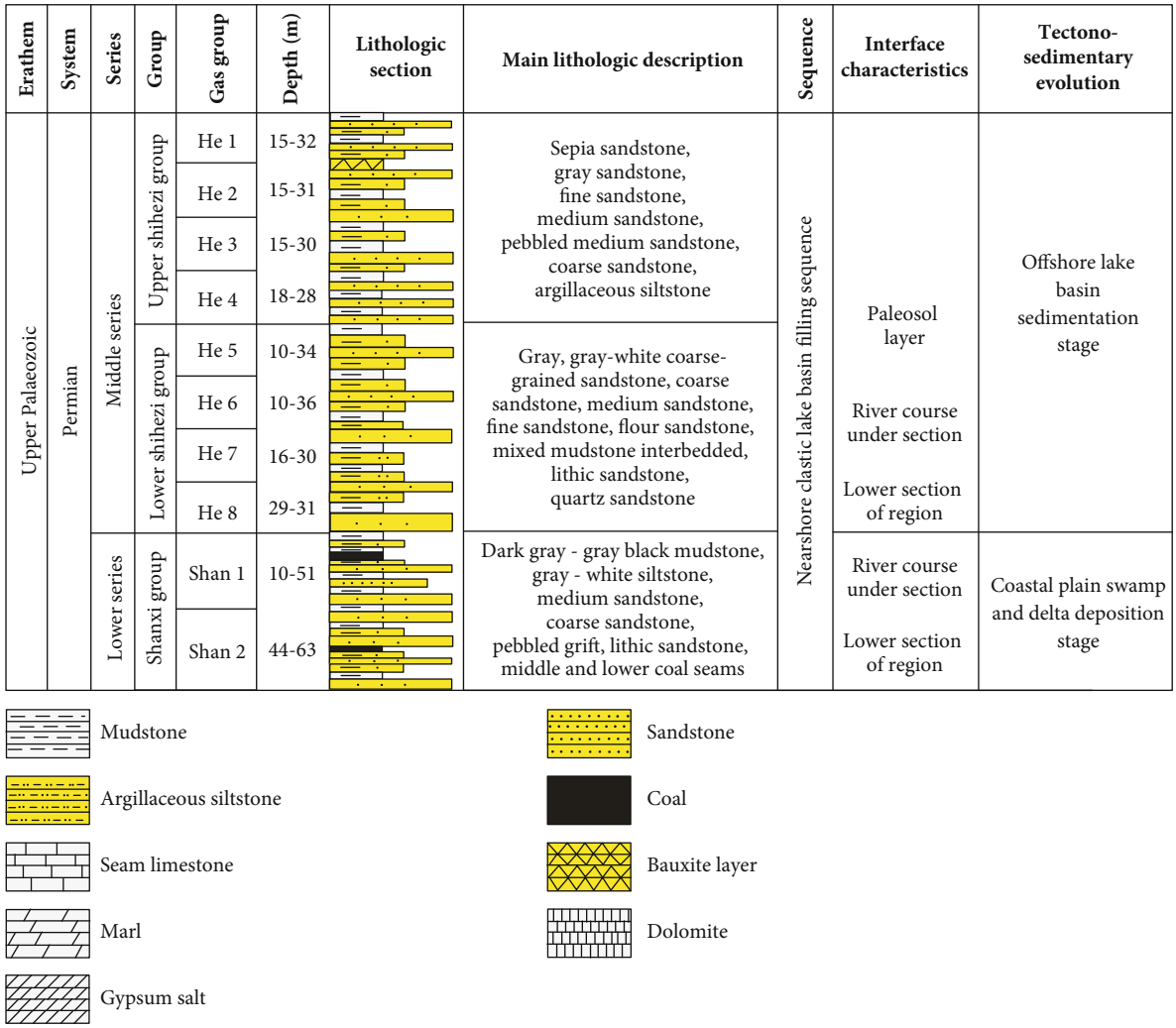

Figure 2: Lithological histogram of Shihezi Group and Shanxi Group in the study area [24].

section, while it changed to offshore plain swamp and delta setting during the sedimentation of the Shan 1 sections (Figure 2).

The strata in the Ordos Basin, from bottom to top, include the Proterozoic, Paleozoic, Mesozoic, and Cenozoic sandstone, mudstone, limestone, and siltstone, with the absence of the Silurian and Devonian [32]. The basement is composed of Archean and Early Proterozoic metamorphic rocks. Due to the Caledonian Orogeny, the Upper Paleozoic strata in the studied area were subjected to uplift and erosion and then began to sink as a whole during the Middle-Late Carboniferous. These strata include the Carboniferous Benxi Group, the Permian Taiyuan, Shanxi, Upper Shihezi, Lower Shihezi, and Shiqianfeng formations [34]. The coal and dark mudstone of the Lower Shihezi formation in the He 8 section and the Shanxi formation in the Shan 1 section are the main source rocks for the Upper Paleozoic gas deposits. The sandstone in these two formations can be reservoirs, and the overlying marine limestone of the Taiyuan Formation, the argillaceous rocks of the Shiqianfeng, and the Upper Shihezi formations can be stable cap layers [17, 35]. These strata form a favorable source-reservoir-cap system in the Upper Paleozoic. The He 8 section distributes as north-south strips with multiphase superposition in the longitudinal direction [36–38]. The sand body of the He 8 section has a thickness of 10-30 m, up to 60 m locally, and width of 10-30 km and extends up to more than 200 km. Sand and mudstone are interbedded in the He 8 section and Shan 1 section. Various sedimentary structures are developed in sandstone sections, such as parallel bedding and cross-bedding. The strong interlayer heterogeneity and the above characteristics are favorable conditions for the formation of tight sandstone with low porosity and low permeability.

3. Samples and Experiments

In this study, more than 50 sandstone core samples of the He 8 section and Shan 1 section were collected from 12 exploratory wells in the southwest of the Ordos Basin. Among the samples, 30 chip samples were selected for petrographic observation from different depths of the Xiang 1 well, Qingshen 2 well, He 3 well, Zitan 1 well, Ling 1 well, and Lian 1 well. Some thin sections were impregnated with red-dyed resin to identify diagenetic minerals and analyze their

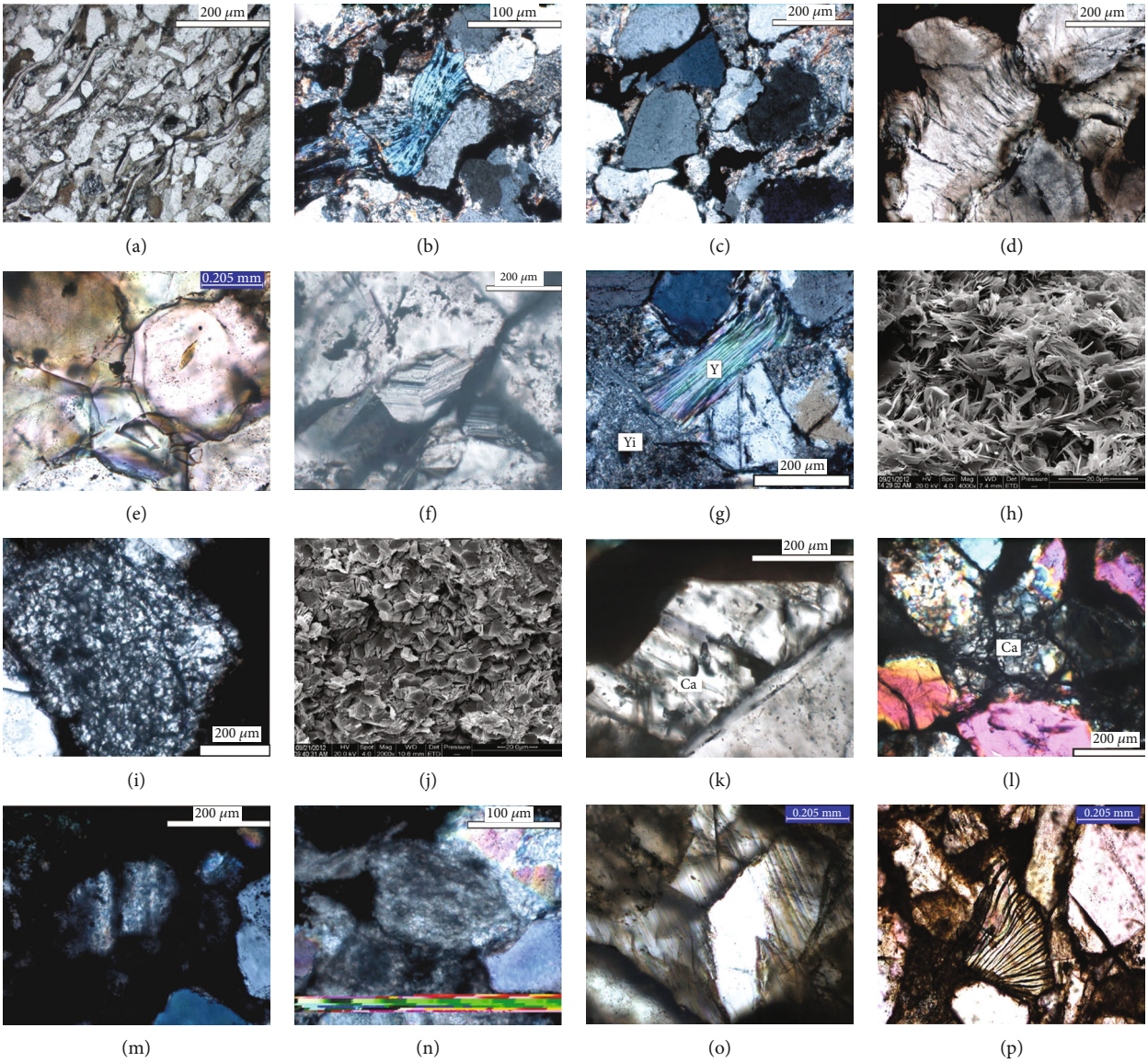

Figure 3: Continued.

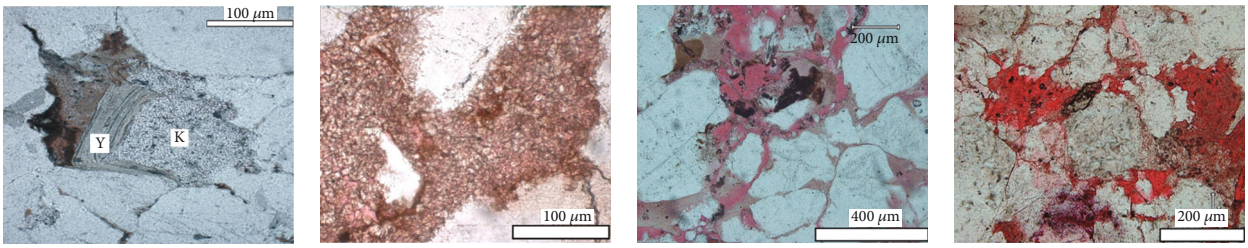

(q) (r) (s) (t)

Figure 3: The typical diagenetic characteristics of sandstone reservoirs under microscope in the southwestern Ordos Basin. (a) Oriented mica and clastic particles and primary pores, Qingshen 2 well, Shan 1 section, 4733 m, (-); (b) bending deformation of clay minerals, Zitan 1 well, He 8 section, 3740.51 m, (+); (c) linear contact and concave-convex contacts between particles, He 3 well, Shan 1 section, 4146.16 m, (+); (d) concave-convex contacts of particles, He 3 well, He 8 section, 4079.88 m, (+); (e) quartz overgrowths and siliceous cements, Qingtan 2 well, Shan 1 section, 4705.68 m, (+); (f) authigenic quartz microcrystal, Zhentan 1 well, Shan 1 section, 4381.13 m, (-); (g) scaly illite aggregates filling intergranular pores, Qingshen 2 well, Shan 1 section, microscope; (h) flaky illite filling intergranular pores, Qingshen 2 well, Shan 1 section, SEM; (i) kaolinite microcrystalline aggregates filling pores, preserving morphology of feldspar and other clastic particle. Zhentan 1 well, Shan 1 section, microscope; (j) vermicular kaolinite filling intergranular pores, Zhentan1 well, Shan 1 section, SEM; (k) calcite cement, Ling 1 well, Shan 1 section, 3698.60 m, (+); (l) micrite calcite cement, He 3 well, Xiashihezi section, 4081.68 m, (+); (m) feldspar metasomatized by micrite with remnant twining, Zhentan 1 well, Shan 1 section, 4379.07 m, (+); (n) metasomatic micrite and clay minerals with the morphology of lithic particles, Lian 1 well, Shan 1 section, 3469.69 m, (+); (o) quartz metasomatized by sparry calcite cement, He 3 well, Shan 1 section, 4146.62 m (+); (p) lithic particles metasomatized by flaky illite, He 3 well, Shan 1 section, 4146.62 m (+); (q) kaolinite altered from volcanic materials (K) and illite (Y), Lian 1 well, Shan 1 section, 3470.03 m, (-); (r) kaolinization altered from volcanic materials, He 3 well, Shan 1 section, 4146.23 m, (-); (s) dissolution pores of the clay and calcareous cements, Zhentan 1 well, Shan 1 section, 4387.7 m; (t) dissolution pores of cement, Chuntan 1 well, He 8 section, 1723.73 m. All photomicrographs were under microscope unless otherwise specified. Mineral abbreviations: Y: foliated illite; Yi: scaly illite; Ca: calcite cement; K: volcanic material.

distribution under the optical microscope. Ten samples were selected for scanning electron microscopy (SEM) analyses, six samples for X-ray diffraction (XRD) analyses, and seven samples for electron probe microanalysis (EPMA).

A total of 20 samples that are mainly quartz sandstone and lithic sandstone from 7 representative wells (Lian 1 well, Ling 1 well, He 3 well, Zitan 1 Well, Qingtan 2 well, Qingtan 1 well, and Zhentan 2 well) were selected for microscope petrographic observation. We observed the color, size, and occurrence of inclusions under transmitted light and fluorescence and identified different types and stages of inclusions. All analyses were performed at the Xi'an Institute of Geology and Mineral Resources, China. Compositional analyses were conducted on 15 samples by ramnor-U1000 laser Raman molecular microprobe (Jobin-Yvon Instrumentation, France) under the conditions of 22°C and 65% humidity. The laser was operated at a wavelength of 514 nm with a laser exposure time of 15 s, a laser-beam spot size of approximately 1 μm, a spectral resolution of 0.14 cm^{-1}, and output power of 22 mW. The fluid inclusion homogenization temperatures of these 15 samples were determined by THMS600 heating and cooling stage (Linkam Scientific Instruments, UK), calibrated by standards to obtain an error of 0.1°C for temperatures below 100°C and no higher than 0.5°C for temperatures above 100°C [39].

4. Results

4.1. Reservoir Characteristics

4.1.1. Reservoir Rock Types. The Upper Paleozoic clastic rocks of the Xiashihezi Formation in the study area mainly comprise quartz sandstone, arkose quartz sandstone, lithic quartz sandstone, and lithic arkose sandstone, with minor lithic sandstone and arkose sandstone. The debris grains show close contact dominated by linear and concave-convex boundaries. These sandstones are subangular to subrounded and moderately to poorly sorted (Figure 3(d)), suggesting a moderate textural maturity of the Xiashihezi Formation. The Shan 1 section is mainly composed of quartz sandstone, with minor lithic quartz sandstone, lithic sandstone, and arkose sandstone (Figure 4), and most of the arkoses have been kaolinized. The clastic particles in tight sandstone are mainly subangular to subrounded and moderately to poorly sorted. Their contacts are dominated by linear boundaries with a few points or suture contacts (Figure 3(c)). These features suggest grain-supported cementation. Petrographic observations on all thin sections show the pore space in the studied area/samples includes primary intergranular pore, intergranular dissolution pore, intragranular dissolution pore, and autogenous mineral intergranular pore (Figure 5).

4.1.2. Diagenesis. Diagenesis has been regarded as the controlling factor of reservoir densification [40–49]. Based on comprehensive analyses through petrographic observation, SEM analysis, cathodoluminescence imaging, XRD analysis, and EPMA, the Upper Paleozoic in the southwestern Ordos Basin has undergone compaction, cementation, metasomatism, dissolution, and fracturing [50], of which compaction and cementation are important factors to form a dense reservoir in the study area [51–55]. Under a microscope, compaction is represented by bent plastic grains such as mica, broken rigid grains, linear or concave-convex interparticle contacts, and "pressure cracks" in quartz (Figures 3(a)–3(d)). Cements

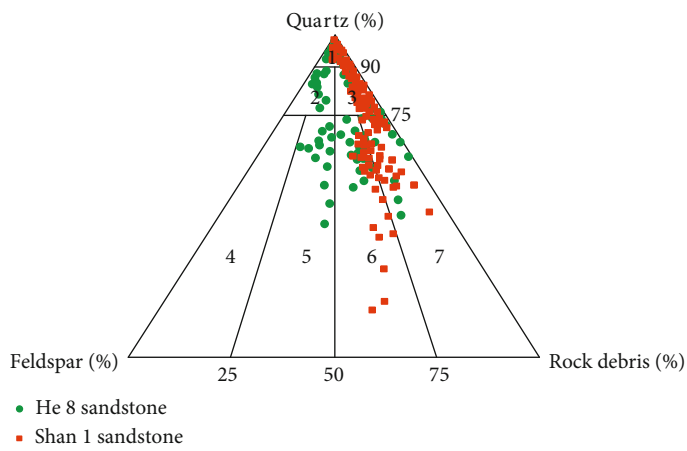

1: Quartz sandstone 2: Fieldspathic quartz sandstone 3: Lithic quartz sandstone
4: Arkose sandstone 5: Fielspar lithic sandstone 6: Lithic feldspar sandstone 7: Lithic sandstone

Figure 4: Lithologic triangle map of Upper Paleozoic in the study area.

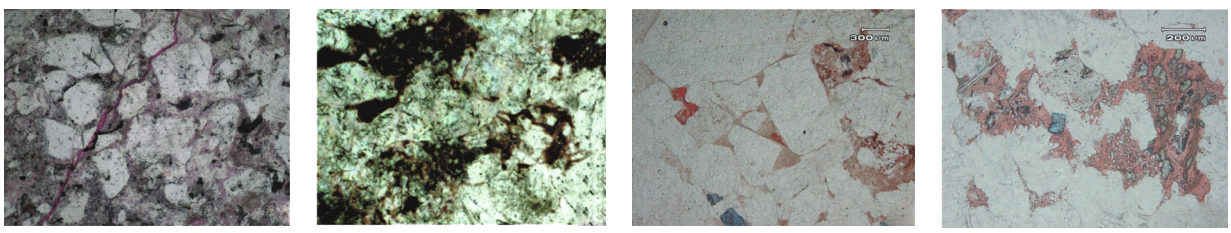

(a) (b) (c) (d)

Figure 5: Characteristics of pore types in the Upper Paleozoic Erathem sandstone of the study area. (a) Intergranular pores and fractures, Zitan 1 well, He 8 section, 3736.19 m; (b) intergranular pores and intragranular pores, Zhentan 2 well, Shan 1 section, 2893.10 m; (c) residual intergranular pores and intergranular dissolution pores, Ling 1 well, Shan 1 section, 3469.69 m; (d) intergranular pores and intragranular pores, Qingtan 2 well, Shan 1 section, 4723.68 m.

include multistage siliceous and calcareous cements, illite, kaolinite, and mixed-clay minerals (Figures 3(e)–3(o)). Metasomatism and dissolution can improve the physical properties of reservoirs [56–59]. The metasomatism of quartz, feldspar, and lithics by carbonate and clay minerals and the dissolution of volcanic materials, clastic particles, and cements (Figures 3(p)–3(t)) formed illite, kaolinite, and secondary overgrowth of quartz [60]. In summary, the tight reservoir in the study area is strongly compacted with multistage siliceous and calcareous cements, a large number of clay minerals, strong dissolution, and well-developed fractures and fissures (Figures 3(a)–3(d)).

4.1.3. Diagenetic Mineral Characteristics. Diagenetic minerals mainly include siliceous cements, carbonate cements, authigenic illite, kaolinite, and mixed-layer clay minerals. The siliceous cements include mainly different forms of siliceous cements among the particles, secondary quartz overgrowth around particles, and authigenic microcrystalline quartz (Figures 3(e) and 3(f)). Under a microscope, the secondary quartz overgrowths are clean and transparent with few inclusions, and it can be divided into early and late diagenetic stages. Clay films/rings are common at the rims of the overgrowths.

Carbonate cementation is another main cementation in the reservoir, and it can block the pores of sandstone. Early carbonate cementation weakens or prevents compaction, providing favorable conditions for later dissolution to form secondary pores. Later, after carbonate corrosion, the reservoir's physical properties become better. In this study, two stages of calcareous cementation have been observed in this study under the microscope (Figures 3(k) and 3(l)): The early stage was dominated by micrite and iron-bearing calcite, most of which are irregular fine grains and micrite. Due to dissolution, they are in patchy shapes and filled the pores. The calcite content is relatively low and less than 3%. The late stage was dominated by sparry calcite, with a relatively high calcite content of 8% on average, which distributed in intergranular pores in forms of granular or poikilitic cementation. Based on EPMA and XRD data (Tables 1 and 2), iron-bearing dolomite is also a calcareous cement in this study area.

Illite is the most abundant clay mineral in the study area. Under the microscope, illite is mainly an altered product or cement in various forms such as fish scales, hairs, fibers, and flakes (Figure 3(g)). Under SEM, most illite appears as pore liners and fillings forms of network or bridge, while honeycomb aggregates occur as flakes or filamentous growth

Table 1: Whole-rock X-ray diffraction analysis of sandstone and clay in the Upper Paleozoic of the study area.

Well number	Depth (m)	Stratum	Sample number	Whole-rock X-ray diffraction analysis of mineral relative content (%)							Clay mineral relative content (%)	
				Amount of clay	Quartz	Ankerite	Graphite	Siderite	Anatase	Not detected	Illite	Kaolinite
Xiang 1 well	2554.77	Zhifang Formation	1	31	52	11		5	1	0	61.06	38.94
Qingtan 2 well	4731.5	Shan 1	2	26	65	5		2	1	1	67.00	33.00
He 3 well	4146.62	Shan 2	3	15	61	18	1	2	2	1	87.89	12.11
Zitan 1 well	3742.50	He 8	4	21	49	23		5	1	1	58.41	41.59
Ling 1 well	3697.14	Shan 1	5	37	44	14		2	1	2	66.55	33.45
Lian 1 well	3470.03	Shan 1	6	39	54	2		2	2	1	56.08	43.92
Average				28.3	54.2	12.2		3.0	1.3	1.0	66.17	33.83

Table 2: Electron probe microanalysis of the compositions of sandstone cements in the Upper Paleozoic Erathem in the southwest of study area.

Well number	Depth (m)	Stratum	Sample number	Na_2O	P_2O_5	MnO	MgO	K_2O	Cr_2O_3	Al_2O_3	CaO	TiO_2	SiO_2	FeO	NiO	Mineral type
Qingtan 2 well	4731.5	Shan 1	1		0.023	0.535	20.66	0.02		0.088	49.84	0.071		28.75	0.002	Ankerite
He 3 well	4146.62	Shan 2	2		0.004		0.032	0.024	0.002				99.89	0.044		Quartz
Zitan 1 well	3742.50	He 8	3		0.014			0.012				0.026	99.87	0.012	0.058	Quartz
Ling 1 well	3697.14	Shan 1	4	0.026	0.018				0.038		0.011		99.87		0.028	Quartz
Lian 1 well	3470.03	Shan 1	5			0.11	3.14	3.3		33.6	0.19		45.7	11.4		Mixed-layer clay
Qingtan 2 well	4731.5	Shan 1	6				0.015	0.42		37.4	0.066	0.142	48.46			Kaolinite
He 3 well	4146.62	Shan 2	7				0.057	3.98		33.74		0.062	50.29	1.163		Kaolinite

on particle surface or in the pores (Figure 3(h)). Illite in this area is either authigenic or altered products formed by the dissolution of feldspar and volcanic materials. Generally, the transition of diagenetic fluid from acid to neutral is favorable for the formation of illite.

Kaolinite is a common clay mineral in the study area. It occurs in vermicular and leave-like shapes under SEM (Figure 3(j)), and some appear as microcrystalline aggregates under a microscope (Figure 3(i)). Kaolinite is usually formed by feldspar corrosion during water-rock interaction in an acid environment, and it also has a positive correlation with the secondary porosity. Thus kaolinite with well-developed intracrystalline pores as important reservoir space can indicate the formation of favorable reservoirs [61–64].

The mixed-layer/clay minerals in the study area are mainly illite-smectite, which is the middle product of the transformation of montmorillonite to illite. This transformation could only occur when the temperature reaches 60-100°C in an alkaline fluid environment with a large number of K^+ and Al^{3+}. Mixed-layer clay mineral contents in this area are not high, second to illite and kaolinite.

4.2. Fluid Inclusions

4.2.1. Inclusion Types. Through the microscopic observation of fluid inclusion distribution and occurrence, combined with diagenetic characteristics of the research area, fluid inclusions can be divided into two phases. The early phase inclusions are distributed in the pores and fissures and were produced by dissolution and fracturing, consisting mainly of gas-liquid organic inclusions and brine inclusions (Figures 6(a)–6(c)). The early cracks, where organic inclusions distributed along the fissures as a string of beads, did not cut the overgrowths of detrital particles. Single inclusions are nearly circular or elliptic. Inclusions in the fissures are generally larger, and their long axes are consistent with the orientation of the fissures (Figures 6(b)–6(d)). Under the fluorescence microscope, liquid hydrocarbon in the early organic inclusions emitted weak bright yellow fluorescence (Figures 6(e)–6(h)) but gaseous hydrocarbon did not fluoresce, suggesting liquid and gaseous hydrocarbon have occurred in the early diagenetic stage, and the gas/liquid ratios of early organic inclusions were 10% or so. Oil and

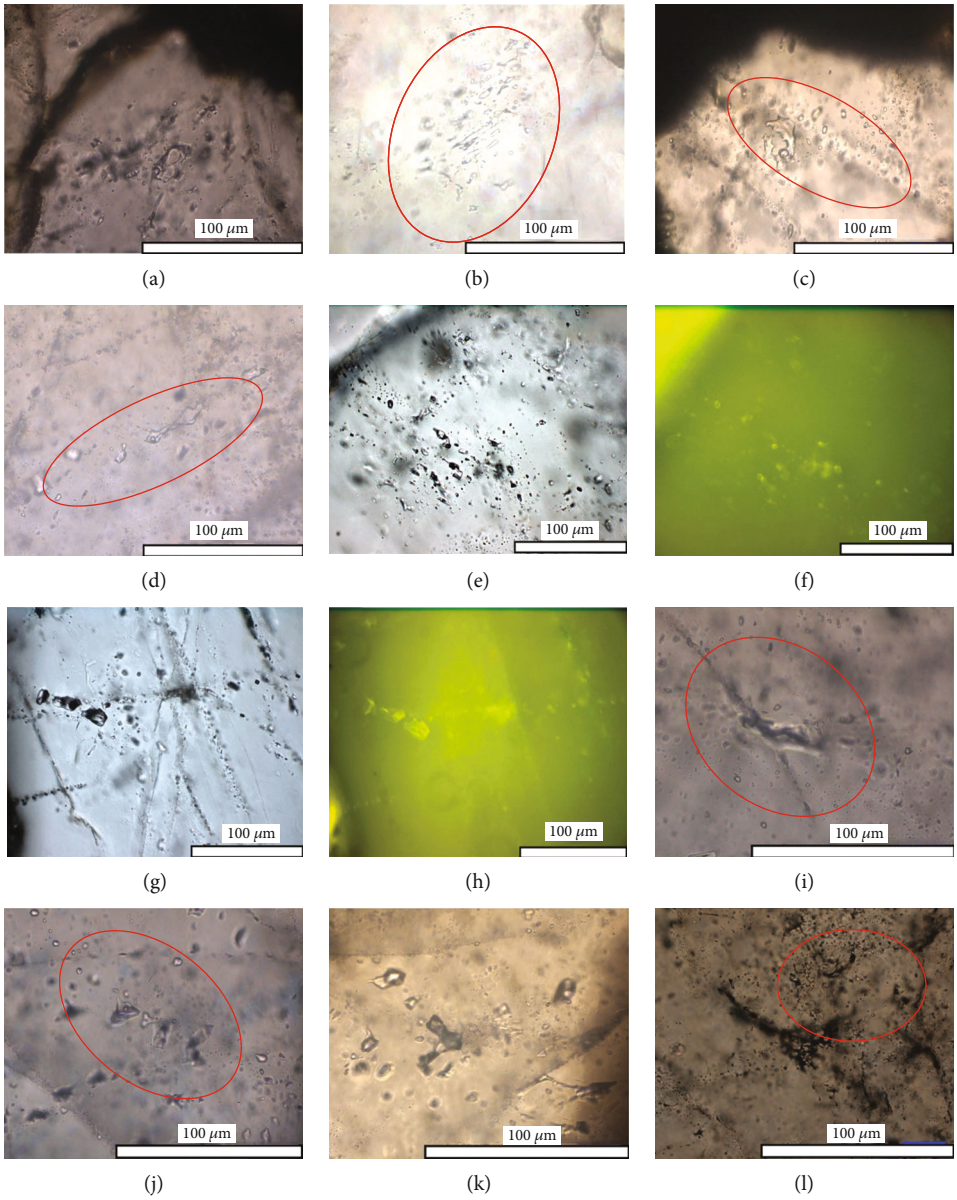

Figure 6: Microscopic characteristics of fluid inclusions in the sandstone reservoir of the study area. (a) Gas-liquid two-phase inclusions in dissolution pores, He 3 well, Shan 1 section, 4146.16 m; (b) oriented gas-liquid two-phase inclusions in fissures in early stage, Lian 1 well, Shan 1 section, 3467.72 m; (c) gas-liquid two-phase inclusions in dissolution pores, Lian 1 well, Shan 1 section, 3424.26 m; (d) oriented gas-liquid two-phase inclusions in fissures in early stage, Qingshen 2 well, Shan 1 section, 4732.6 m; (e) dark-colored hydrocarbon gas-liquid two-phase inclusions in the dissolution pores, He 3 well, Shan 1 section, 4146.62 m; (f) same view field of (e) under the fluorescence microscope; (g) dark hydrocarbon gas-liquid two-phase inclusions in early fissures, Lian 1 well, Shan 1 section, 3424.26 m; (h) same view field of G under the fluorescence microscope; (i) gas-liquid two-phase inclusions along late fissues, He 3 well, He 8 section, 4081.68 m; (j) gas-liquid two-phase inclusions with beaded fractures and directional distribution, Qingshen 2 well, Shan 1 section, 4722.8 m; (k) late dark gas-rich inclusions, Lian 1 well, Shan 1 section, 3424.26 m; (l) gas-rich inclusions with fracture distribution in late stage, Qingshen 2 well, 4730.14 m.

gas filling strength was weak and distributed and migrated along the dissolution pores and fissures.

The late inclusions are distributed in dissolution pores and fissures and formed in the late diagenetic stage. Most late inclusions are gas-liquid inclusions with a few pure gas-phase inclusions. They are elongated and distributed along the crack extension or as a string of beads along the fissure (Figures 6(i)–6(l)). The gas/liquid ratios of gas-liquid organic inclusions were generally greater than 20%, suggesting that the strength of the gas filling was high and reached the hydrocarbon generation peak. A large amount of natural gas has migrated and accumulated in favorable locations.

4.2.2. Inclusions Composition. Laser Raman microprobe analyses of inclusions from the Xiashihezi and Shanxi Groups in the southwestern Ordos Basin have revealed both organic and inorganic components (Figure 7). In the different phases of inclusions (Tables 3 and 4), gas-phase inclusions have

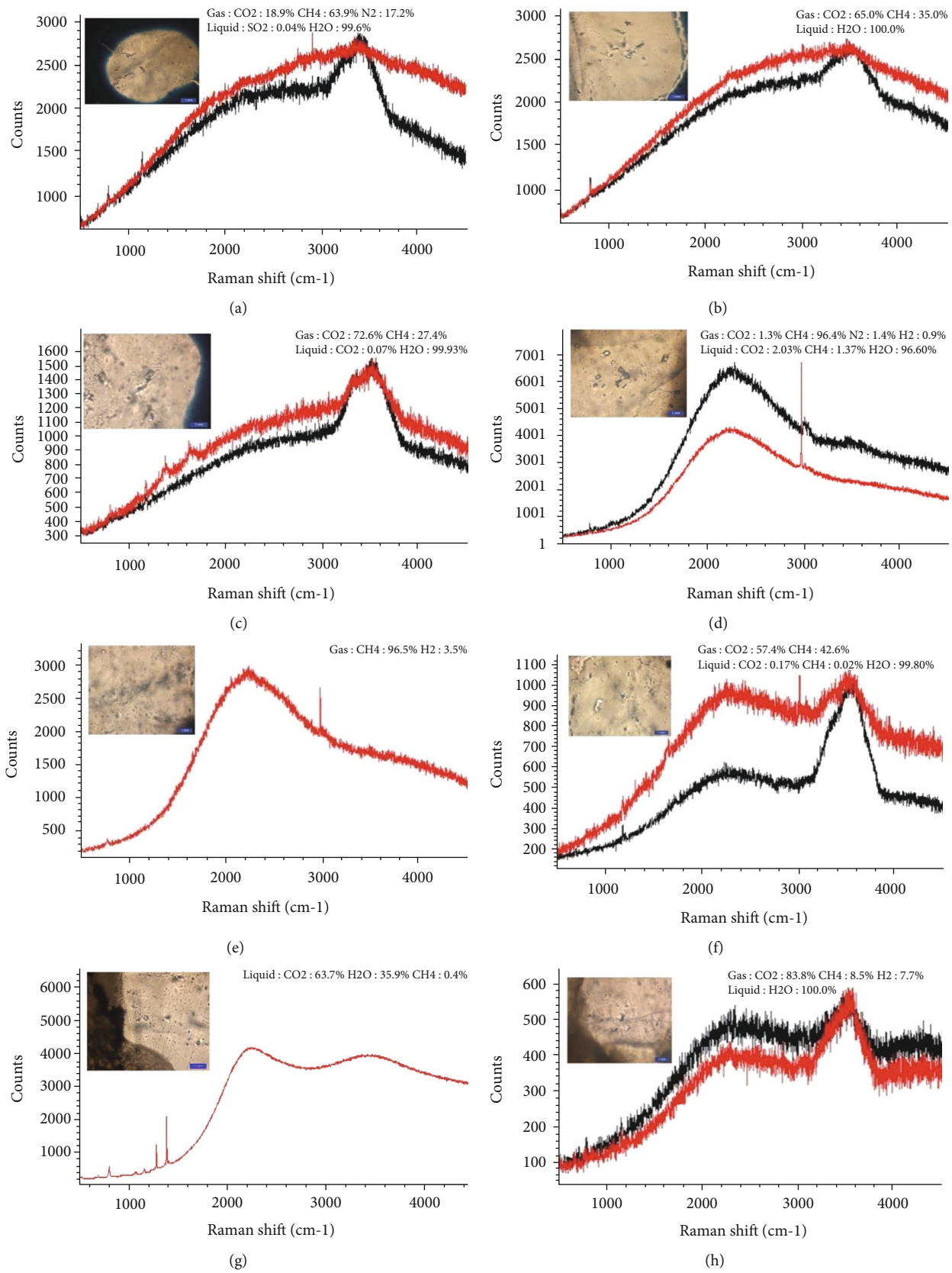

Figure 7: Continued.

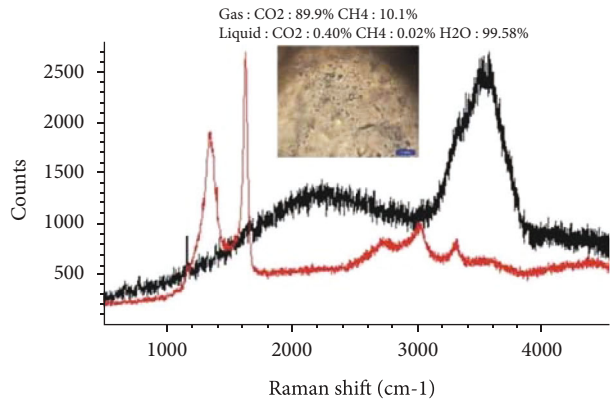

(i)

Figure 7: Laser Raman spectrogram of fluid inclusions in sandstone reservoir in the study area. (a) Qingtan 2 well, Shanxi Group, 4722.80 m; (b) Qingtan 2 well, Shanxi Group, 4722.80 m; (c) Qingtan 2 well, Shanxi Group, 4728.08 m; (d) Lian 1 well, Shihezi Group, 3424.26 m; (e) Lian1 well, Shihezi Group, 3424.26 m; (f) He 3 well, Shihezi Group, 4073.09 m; (g) He 3 well, He 8 section, 4081.68 m; (h) Zitan 1 well, Shihezi Group, 3736.19 m; (i) Zitan 1 well, Shihezi Group, 3740.51 m.

major organic ingredients of CH_4 and inorganic components of CO_2 in addition to H_2S and N_2, with H_2O contents varying in a wide range. In liquid phase inclusions, H_2O content is greater than 95% but CO_2 content is less than 2%, whereas CH_4 is the only organic component. However, in this area, no hydrocarbon gas components such as C_2H_4, C_2H_6, H_2S, C_2H_2, and C_4H_6 were detected in the organic inclusions, indicating that the natural gas had a high degree of thermal evolution in the hydrocarbon generation, reflecting the feature of "dry gas" [65].

Comparing the early and late organic inclusions of sandstone reservoirs in Upper Paleozoic in the study area (Figure 8), the CO_2 and CH_4 contents of gas-phase organic inclusions were higher than those of liquid-phase inclusions, whereas the individual contents of CO_2 and CH_4 were a trade-off. Thus, the early inclusions were rich in CO_2 and low in CH_4, but the late inclusions were rich in CH_4 and low in CO_2. Different stages of inclusions captured in the same sample have different CO_2 and CH_4 contents, indicating that the degree of thermal evolution of the hydrocarbon gas was relatively low in the early diagenetic stage but higher in the late diagenetic stage.

The homogenization temperatures of inclusions in the early stage of the He 8 and Shan 1 sections vary from 80°C to 200°C in distinct ranges (Figure 9). In the He 8 section, the homogenization temperatures of the early inclusions range from 80°C to 140°C with the peak from 120°C to 130°C. In the Shan 1 section, the homogenization temperatures of late inclusions range from 110°C to 200°C with the peak from 150°C to 160°C. The uniform continuous distribution of the homogenization temperature of the two stages of fluid inclusions in the He 8 and Shan 1 sections indicates that the oil and gas generation, migration, and accumulation was a continuous filling process. The early inclusions recorded the natural gas generation and migration into the reservoir, while the late inclusions witnessed the accumulation in the reservoir. Based on the freezing temperature, the salinity of the fluid inclusions was calculated. The results show consistent salinity distribution of fluid inclusions in the He 8 and Shan 1 sections between 0 and 17 wt%. The peaks of 4 wt% NaCl and 8 wt% NaCl in the two major peak ranges correspond to the homogenization temperature analysis, confirming the existence of two stages of fluid inclusions. Besides, the salinity of the early inclusions is relatively higher than that of the late inclusions, indicating that the reservoir had better sealing during the formation of the early inclusions as opposed to the formation of late inclusions.

5. Discussion

5.1. Diagenetic Events and Characteristics. On the basis of authigenic minerals, the relationship of metasomatism and dissolution-filling of different cements, features of fluid inclusions, and uniform homogenization temperature distribution, the He 8 section and Shan 1 section experienced early and late diagenetic stages and are currently in the late diagenetic stage. Combined with burial history from the study area and its adjacent regions [22, 66–68], the diagenetic evolution of reservoirs in the He 8 and Shan 1 sections has been further studied. During the burial process, the diagenesis in the study area was dominated by mechanical compaction due to the increased burial depth and overlying sediments. Clastic particle contacts are close, and plastic minerals were squeezed due to deformation while rigid minerals were dissolved and ruptured (Figures 3(b) and 3(c)). The compression of mudstone released Ca^{2+} and HCO_3^- in the early stage, forming alkaline diagenetic fluids that were favorable for the formation of early siliceous and calcareous cements [67]. With the increase of burial depth, temperature, and pressure increased, when mica reacted with pore water [69], potassium ions were released and entered the pore solution. Hydrolysis of volcanic tuffaceous resulted in the release of alkali metal ions such as Na^+ and K^+. All of those led to increased pH values of the pore fluids, promoting a more alkaline diagenetic environment [41], in which authigenic illite gradually precipitated (Figures 3(g) and 3(h)). At this time, organic matter was immature and the temperature

Table 3: Results of laser Raman analysis of gas phase composition of Paleozoic inclusions in southwestern Ordos Basin (molar relative content %).

Well number	Sample number	Description	Depth (m)	Stratum/lithology	Gas phases%																		
					CO_2	H_2S	CH_4	SO_2	H_2O	Cl_2	O_2	CO	F_2	N_2	H_2	C_2H_2	C_2H_4	C_2H_6	C_3H_6	C_3H_8	C_4H_6	C_6H_6	Total
Qingtan 2 well	5-1	Late stage	4722.8	Shanxi formation/purplish red medium-coarse quartz sandstone	18.9		63.9							17.2									100.0
	5-2	Early stage			65.0		35.0																100.0
	29	Early stage	4728.1	Shanxi formation/gray-white medium-coarse quartz sandstone	72.6		27.4																100.0
	35-1	Early stage	4729.4		67.5		17.8							14.7									100.0
	35-2	Late stage			57.8		42.2																100.0
	47	Late stage	4732.0	Shanxi formation/gray-white pebbled medium-coarse quartz sandstone			100																100.0
Lian 1 well	Li98-1	Early stage	3467.7	Shanxi formation/gray-white pebbled medium-coarse quartz sandstone	69.4		30.6																100.0
	Li98-2	Late stage			19.2	3.7	75.3							1.8									100.0
	Li93-1	Late stage	3423.3	Shanxi formation/gray-white pebbled medium-coarse quartz sandstone	1.3		96.4							1.4	0.9								100.0
	Li93-2	Late stage					96.5								3.5								100.0
Zitan 1 well	TZ1,116-2	Early stage	3736.2	Shihezi group/gray-white medium-fine sandstone	83.8		8.5								7.7								100.0
	TZ1,136-2	Early stage	3740.5		89.9		10.1																100.0
He 3 well	132-1	Late stage	4073.1	Shihezi group/gray-white medium-fine lithic sandstone	57.4		42.6																100.0
	132-2	Early stage	4073.1		99.3		0.1							0.3	0.3								100.0
	138-1	Early stage	4081.7		20.2	4.2	75.6																100.0

Table 4: Results of laser Raman analysis of liquid phase composition of Paleozoic inclusions in southwestern Ordos Basin (molar relative content %).

Well number	Sample number	Description	Depth(m)	Stratum/lithology	Gas phases%																		
					CO_2	H_2S	CH_4	SO_2	H_2O	Cl_2	O_2	CO	F_2	N_2	H_2	C_2H_2	C_2H_4	C_2H_6	C_3H_6	C_3H_8	C_4H_6	C_6H_6	Total
Qingtan 2 well	5-1	Late stage	4722.8	Shanxi formation/magenta medium-coarse quartz sandstone				0.04	99.96														100.0
	5-2	Early stage	4722.8						100.00														100.0
	29	Early stage	4728.1	Shanxi formation/gray-white medium-coarse quartz sandstone	0.07				99.93														100.0
	35-1	Early stage	4729.4	Shanxi formation/gray-white medium-coarse quartz sandstone	0.12				99.88														100.0
	35-2	Late stage	4729.4						100.00														100.0
	47	Late stage	4732.0	Shanxi formation/grayish-white gravel medium-coarse quartz sandstone			0.04		99.96														100.0
Lian 1 well	Li98-1	Early stage	3467.7	Shanxi formation/gray-black fine sandstone					100.00														100.0
	Li98-2	Late stage			0.07				99.93														100.0
	Li93-1	Late stage	3423.3	Shanxi formation/gray-white medium-fine-grained sandstone	2.03		1.37		96.60														100.0
	Li93-2	Late stage			Dark single gas phase																		100.0
Zitan 1 well	TZ1,116-2	Early stage	3736.2	Shihezi Group/gray-white fine sandstone					100.00														100.0
He 3 well	132-1	Late stage	4073.1	Shihezi Group/gray-white medium-fine lithic sandstone	0.17		0.02		99.80														100.0
	132-2	Early stage	4073.1		Dark single gas phase																		100.0
	138-1	Early stage	4081.7				0.06		99.94														100.0

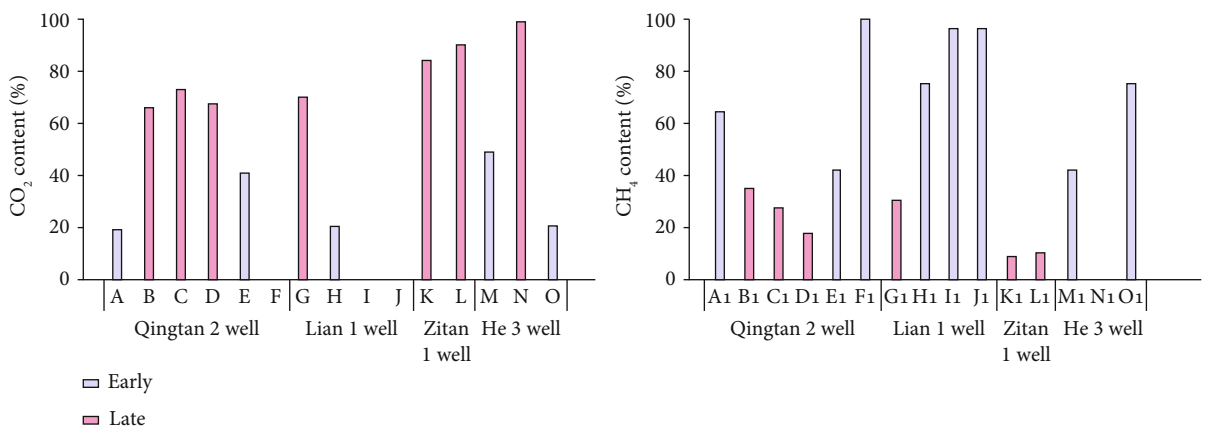

Figure 8: Comparison of gas-phase CO_2 and CH_4 contents compositions of early and late organic inclusions between He 8 section and Shan 1 section sandstone reservoir in the study area.

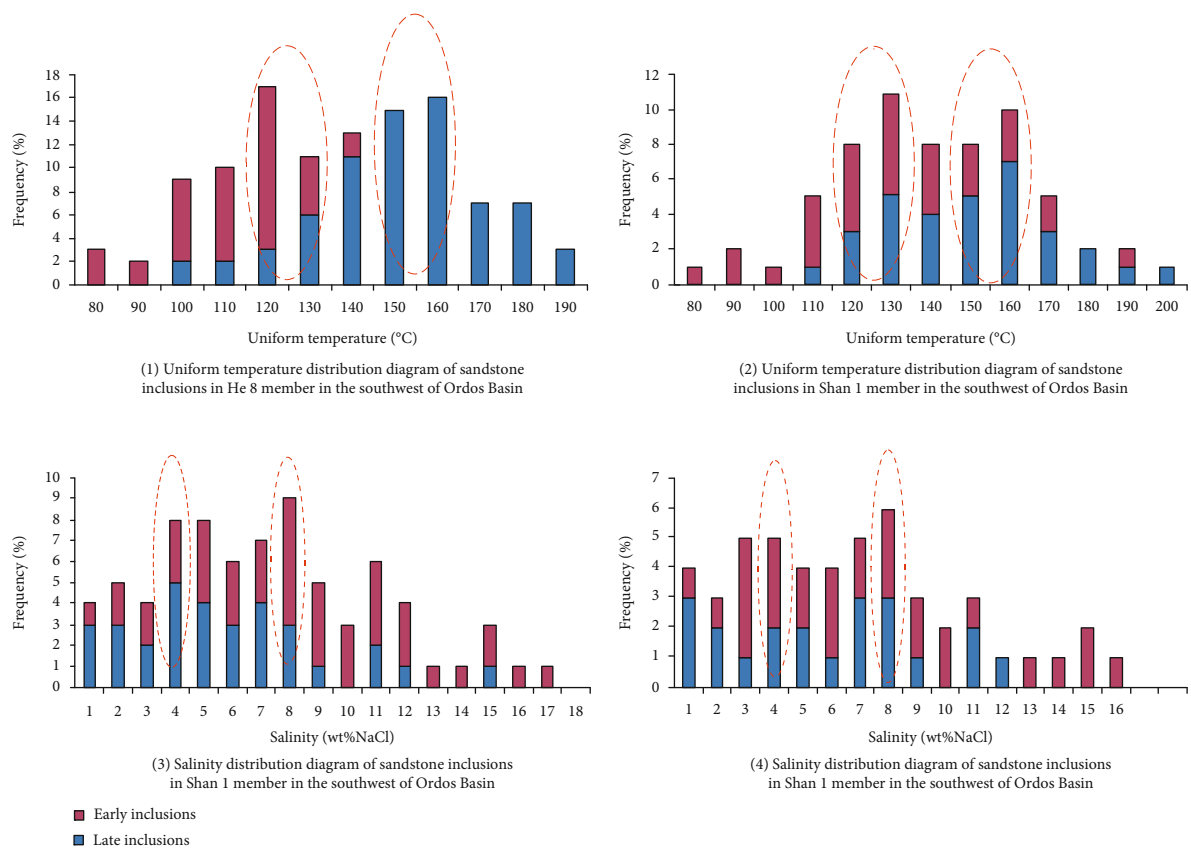

Figure 9: Homogenization temperature and salinity distribution profiles of sandstone inclusions in the Upper Paleozoic Erathem in the study area.

was less than 80°C, further confirming that the diagenetic fluid was alkaline [67].

In the late period of the early diagenetic stage, organic matter matured and gas production began, resulting the fluid environment gradually became less alkaline but more acidic. The acidic fluids led to metasomatism of feldspar, lithic, volcanic, and calcareous cements as well as the dissolution of feldspar (Figure 3(n)) and volcanic materials, forming kaolinite and quartz secondary overgrowth. The dissolution pores of feldspar were filled with organic inclusions (Figures 6(a) and 6(b)), indicating that the acid dissolution was ahead of early oil and gas filling. Under appropriate conditions, SiO_2 dissolved from feldspar in an acidic environment formed quartz secondary overgrowth around debris particles. The pure gas phase of the second phase fluid inclusions (Figures 6(k) and 6(l)) and the laser Raman spectroscopy analysis results, as well as the vitrinite reflectance (Ro) greater than 1.0% in Permian mudstone, all together

suggest a high degree of thermal evolution (Figure 7). In the study area, micritic calcite and sparry calcite replaced/metasomatized quartz, feldspar, and other debris particles (Figures 3(n)–3(p)), some of which were early phase quartz overgrowth and dissolved feldspar. This relationship suggests that calcite cementation was after feldspar dissolution and quartz overgrowth and also later than oil and gas filling. The fissures with late inclusions cut quartz edge but not the late cements that formed at the late diagenetic stage without inclusions, suggesting that large-scale migration and accumulation of gas happened before reservoir cementation. In Upper Paleozoic, gas accumulation time was not later than the time of reservoir densification, meaning that the gas was accumulated simultaneously with or after the reservoir densification.

In conclusion, the reservoir diagenetic evolution sequence can be summarized in the following order: (1) compaction/early siliceous and calcareous cement; (2) formation of authigenic clay minerals and organic acid; (3) start of natural gas filling; (4) early dissolution and metasomatism including dissolution of carbonate, particle, feldspar, and volcanic debris and formation of illite and kaolinite and quartz secondary overgrowth; (5) a large amount of natural gas filling; (6) dissolution of late-stage feldspar and calcareous cement; (7) late-stage calcite metasomatizing clay minerals, quartz, and feldspar (Figure 10).

5.2. Evolutionary Sequence of Diagenetic Fluids

5.2.1. Fluid Evolution of Early Diagenetic Stage. Based on Petromod 1D and related simulation parameters of The Ordos Basin [70], the tectonic burial history of the Qingtan 1 well was established (Figure 10). The early Permian strata underwent early burial diagenesis until the late Jurassic period (145 Ma) which belonged to the early diagenetic stage (288 Ma–211 Ma). During this period, compaction was predominant and the intergranular contacts vary from linear to concave-convex. Some early siliceous and calcareous cements began, reducing the pore space greatly. The organics of mudstone were immature in the alkaline diagenetic fluid environment. As the strata continued subsiding with the rise of temperature and pressure, the pore fluid gradually changed from alkaline to acidic. When buried depth was over 2500 m, the strata entered the late diagenesis stage (211 Ma–145 Ma). At this time, the thermal evolution of strata reached a mature stage and began to produce gas. Oil and gas began filling and migrating, and the organic acids and methane gas made the pore fluid acidic. During this stage, diagenesis was given priority to dissolution and metasomatism. The dissolution of feldspar and rock debris, volcanic materials, and early carbonate cements produced secondary porosity such as dissolution pores, which consequently improved the reservoir's physical properties. The formation of illite and kaolinite and quartz overgrowth at particle edges reduced the porosity of the reservoir, leading to the reservoir densification.

5.2.2. Fluid Evolution of Late Diagenetic Stage. The early Cretaceous late diagenetic stage (145 Ma-48 Ma) can be further divided into two phases, 145 Ma-95 Ma and 95 Ma-48 Ma. From Late Jurassic to Early Cretaceous, a regional thermal anomaly event occurred in the Ordos Basin [71–73], resulting the Upper Paleozoic source rocks reached the highest degree of thermal evolution. The source rocks reached the peak of gas generation while oil and gas filling continued and accumulated in the reservoir. The concurrent diagenetic environment was acidic, and the diagenesis was characterized by the dissolution of feldspar and calcareous cements, which increased the secondary porosity. The second phase from 95 Ma to 48 Ma was dominated by strata uplift and erosion caused by the Yanshanian movement, during which the geothermal gradient and strata temperature decreased. The burial depth of gas source rocks became shallow and the organic became less acidic. The release of internal pressure produced fractures and cracks, which may become the channels of gas migration and places of accumulation. The diagenetic environment during this phase was weak alkaline. The main diagenesis included cementation and metasomatism, which severely lowered the reservoir's physical properties, and thus, the reservoir was further densified.

In Paleogene from 48 Ma to 30 Ma, the strata were uplifted due to the Himalayan movement, and the hydrocarbon generation gradually weakened. The concurrent diagenetic environment was alkaline. During this period, quartz and feldspar particles were metasomatized by late calcite, leading to the reduction of reservoir pore flow channels and worse physical properties, and hence further densified reservoir.

Based on the diagenesis and accumulation characteristics of different periods in the study area, the diagenetic environment was transitional from alkaline to acidic and then to alkaline. This corresponds well with the diagenetic evolution sequence concluded above.

5.3. Investigation of Fluid Characteristics. Fluid plays an important role in the formation of sedimentary basins and the formation, migration, and accumulation of hydrocarbon gases. It participates in diagenesis and improves reservoir performance. Through the analyses of fluid inclusions, diagenetic fluid evolution, and diagenesis, we can further understand the fluid properties and the characteristics of active stage. The results indicate the two generations of paleofluid flows corresponding to the early and late diagenetic stages. The first generation of paleo-fluid flows is represented by fluid inclusions filling in the pores and fractures of the early diagenetic sandstone, recording the generation and migration of early oil and gas. The second generation of paleo-fluid flows filled in the late diagenetic sandstone pores and fractures, recording the late hydrocarbon accumulation.

Fluid inclusion analysis shows their homogenization temperatures (80-200°C) and salinities (0-17 wt%) are continuously distributed over wide ranges. The homogenization temperature peak of the early fluid is 120-130°C, and the salinity peak is 4 wt% NaCl. The homogenization temperature peak of the late fluid is 150-160°C, and the salinity peak is 8 wt% NaCl. These data suggest the diagenetic fluid is in the range of medium-low temperature and moderate-low salinity [39], which is dominated by strata water. According to the initial melting temperature of the inclusions, the

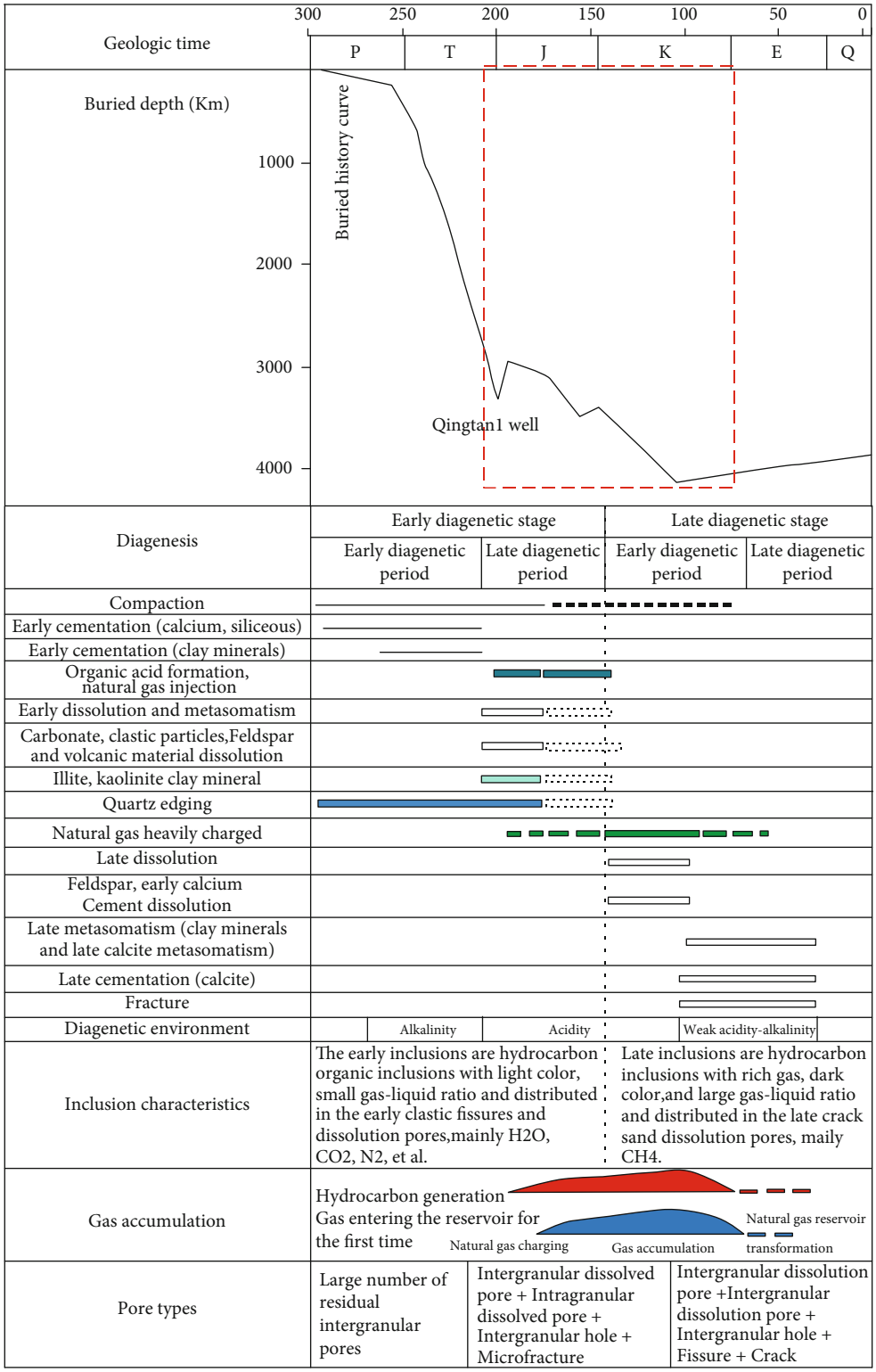

Figure 10: The diagenetic evolution sequence and accumulation history of the sandstone reservoir in the Upper Paleozoic Erathem of the Qingtan 1 drilling well.

paleo-fluid properties recorded by the Upper Paleozoic fluid inclusions can be determined. There are four types of brine systems in the southwestern part of the basin: (1) $CaCl_2$-H_2O system, (2) $CaCl_2$-NaCl-H_2O system, (3) $CaCl_2$-$MgCl_2$-H_2O system, and (4) $MgCl_2$-NaCl-H_2O system, of which the $CaCl_2$-H_2O and $MgCl_2$-NaCl-H_2O systems are dominant. It is considered that the formation environment and migration and storage conditions of Upper Paleozoic

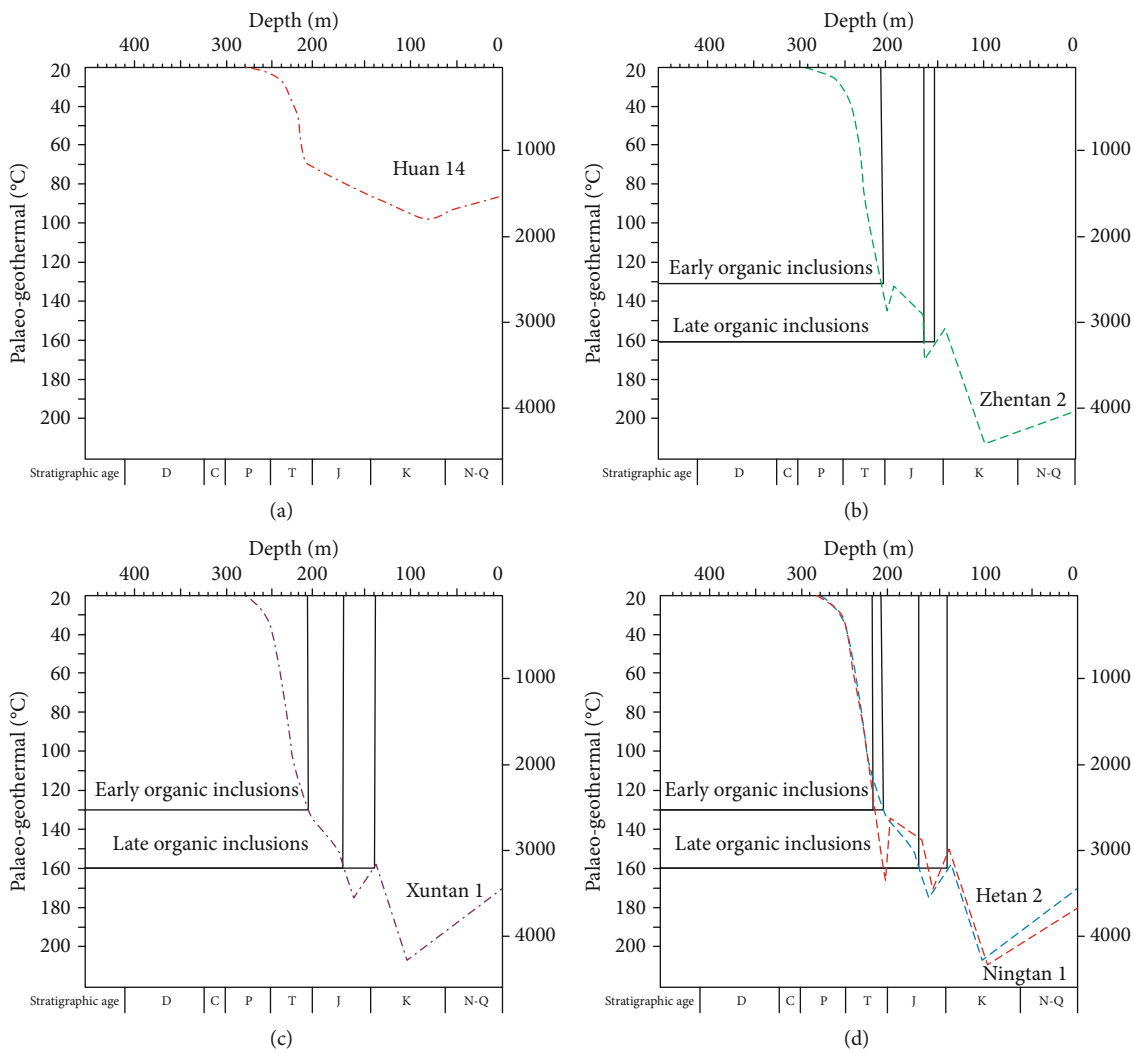

Figure 11: Natural gas accumulation time of the Upper Paleozoic in the study area recorded by fluid inclusions.

natural gas in the study area are medium. Based on the analysis of diagenesis and diagenetic fluid evolution in different periods of the study area, the diagenetic environment of the study area has experienced the transition from alkaline through acidic to alkaline.

5.4. Accumulation Time. Accumulation stages can be determined through the study of natural gas inclusions, which are the key evidence for the process of oil and gas migration or accumulation [74]. In this study, based on the diagenesis and inclusion petrography, the natural gas accumulation in the study area is divided into natural gas formation and migration stage and massive accumulation stage.

The specific time of natural gas migration and accumulation represented by inclusions can be determined by comparing the inclusion homogenization temperatures (Tt) against the burial history curves of exploratory wells in different secondary tectonic units across the Ordos basin. In detail, the Xuntan 1 well represents the Weibei Uplift, the Ningtan 1 well and Hetan 1 well represent the Yishan Slope, the Huan 14 well represents the Xiyuan Thrust belt, and the Zhentan 2 well represents the Tianhuan Depression (Figure 11).

According to the results of inclusion homogenization temperatures, the low temperature (120°C -130°C) inclusions are the first-stage inclusions, which are distributed in the early fissures or dissolution pores. They belong to hydrocarbon inclusions in the initial gas migration to the reservoir, and some inclusions have fluorescence. The high-temperature inclusions (150°C-160°C) are the second-stage inclusions, belonging to the nonfluorescent natural gas inclusions formed during the massive gas migration and accumulation in the tectonic uplift stage. Considering the gas "window" is Ro = 1.30% for the Upper Paleozoic source rocks in the southwest of Ordos Basin, large-scale gas generation could only occur when the paleogeothermal temperature was higher than 170°C. However, the paleogeothermal temperature of the Upper Paleozoic in the Huan 14 well did not reach this temperature (Figure 11(a)), so the thermal evolution of the Upper Paleozoic in the Huan 14 well did not enter the gas production stage. In other tectonic units, the paleogeothermal temperatures all reached the hydrocarbon generation windows, and hence, the intersections of early inclusion homogenization temperatures and the burial curves represent the formation time of hydrocarbon source rocks in the Upper Paleozoic.

The intersection of the late inclusion homogenization temperature curve and the uplift section of the well burial history curve (rather than the descending stage) represent the formation time of the inclusion/hydrocarbon source rocks. Following the same principle, natural gas in the Weibei uplift migrated into the reservoir at 205 Ma (late Triassic) and accumulated during 170-136 Ma as represented by the Xuntan 1 well (Figure 11(c)). The gas migration time within the Yishan Slope (Hetan 2 well and Ningtan 1 well) was 220–210 Ma (Figure 11(d)), and the accumulation time was during 170–142 Ma. Natural gas in the Tianhuan Depression (Zhentan 2 well) migrated into the reservoir at 197 Ma and accumulated during 164–152 Ma (Figure 11(b)). In conclusion, the gas migration time of the Upper Paleozoic reservoir in Weibei Uplift, Yishan Slope, and Tianhuan Depression tectonic units were 220-197 Ma, but the large-scale migration and accumulation time in these tectonic units varied.

6. Conclusion

(1) In the southwest of the Ordos Basin, the He 8 section and Shan 1 section of the Upper Paleozoic reservoir consist mainly of quartz sandstone, arkose quartz sandstone, and lithic quartz sandstone. The diagenesis includes compaction, cementation, metasomatism and dissolution, and fissure, among which compaction and cementation are important factors for reservoir densification. The diagenetic process of the reservoir is featured by strong compaction, development of multistage siliceous and calcareous cements and abundant clay minerals, strong dissolution, and relatively well-developed fractures and fissures

(2) The He 8 and Shan 1 sections of reservoirs both have two stages of inclusions. Both early and late inclusions of the He 8 section and Shan 1 section show similar peak temperatures that are between 120-130°C and 150-160°C, respectively. The early inclusions recorded the natural gas generation and migration into the reservoir, while the late inclusions witnessed the accumulation in the reservoir. The salinity of fluid inclusions in He 8 and Shan 1 sections ranged from 0 to 17 wt%, with the two main peak values of 4 wt% NaCl and 8 wt% NaCl

(3) Diagenetic evolution of the He 8 and Shan 1 sections of the reservoir has gone through early and late diagenetic stages and is currently in the late diagenetic stage. The reservoir diagenetic evolution sequence can be summarized in order as follows: (1) compaction/early siliceous and calcareous cement; (2) formation of authigenic clay minerals and organic acid; (3) start of natural gas filling; (4) early dissolution and metasomatism including dissolution of carbonate, particle, feldspar, and volcanic debris and formation of illite and kaolinite and quartz secondary overgrowth; (5) a large amount of natural gas filling; (6) dissolution of late-stage feldspar and calcareous cement; (7) late-stage calcite metasomatizing clay minerals, quartz, and feldspar. The diagenetic environment was transitional from alkaline through acidic and then to alkaline

(4) Two periods of oil and gas filling occurred in the reservoir in the study area. The densification of the reservoir was simultaneous with or after the reservoir densification. There are two stages of fluid activity in the study area, namely, early diagenetic stage corresponding to hydrocarbon generation and migration and late diagenetic stage corresponding to hydrocarbon accumulation

(5) The natural gas accumulation in the study area is divided into natural gas formation and migration stage and massive accumulation stage. The gas migration time of the Upper Paleozoic reservoir in Yishan Slope, Weibei Uplift, and Tianhuan Depression tectonic units was during 220–197 Ma, but the gas accumulation time in different tectonic units varied. However, in the western margin of the basin, no natural gas was generated because the hydrocarbon source rocks of the Upper Paleozoic in the western margin of the basin did not reach the gas "window."

Data Availability

The X-ray diffraction (XRD) analyses, electron probe microanalysis (EPMA), fluid inclusion homogenization temperature, etc. data, and laser Raman spectroscopy analysis data used to support the findings of this study are included within the article.

Conflicts of Interest

The authors declare that they have no conflicts of interest.

Acknowledgments

This study was funded by the National Natural Science Foundation of China (number: 41772118) and the Fundamental Research Funds for the Central Universities, Chang'an University (No. 300102279106).

References

[1] K. X. Sun, X. Q. Li, Q. Wei et al., "Study on Paleo-fluid earth characteristics of tight sandstone reservoirs Cretaceous in Keshen gas field of Kuche Depression," *Geoscience*, vol. 33, no. 6, pp. 1220–1228, 2019.

[2] R. H. Goldstein, T. J. Reynolds, and R. James, *Fluid Inclusions in Metallogenic Minerals*, Petroleum Industry Press, Beijing, 2015.

[3] D. H. Liu, H. Z. Lu, and X. M. Xiao, *Oil and gas inclusions and their applications in petroleum exploration and development*, Guangdong Science and Technology Press, Guangzhou, 2007.

[4] D. Middleton, J. Parnell, P. Carey, and G. Xu, "Reconstruction of fluid migration history in Northwest Ireland using fluid inclusion studies," *Journal of Geochemical Exploration*, vol. 69-70, pp. 673–677, 2000.

[5] J. Kelly, J. Parnell, and H. H. Chen, "Application of fluid inclusions to studies of fractured sandstone reservoirs,"

Journal of Geochemical Exploration, vol. 69-70, pp. 705–709, 2000.

[6] J. Parnell, "Potential of palaeofluid analysis for understanding oil charge history," *Geofluids*, vol. 10, no. 1, p. 82, 2010.

[7] R. K. Mclimans, "The application of fluid inclusions to migration of oil and diagenesis in petroleum reservoirs(in Geochemistry of Waters in Deep Sedimentary Basins;selected contributions from the Penrose conference)," *Applied Geochemistry*, vol. 2, no. 5-6, pp. 585–603, 1987.

[8] S. D. Burley, J. Mullis, and A. Matter, "Timing diagenesis in the Tartan Reservoir (UK North Sea): constraints from combined cathodoluminescence microscopy and fluid inclusion studies," *Marine and Petroleum Geology*, vol. 6, no. 2, pp. 98–120, 1989.

[9] A. C. Aplin, S. R. Larter, M. A. Bigge, G. Macleod, R. E. Swarbrick, and D. Grunberger, "PVTX history of the North Sea's Judy Oilfield," *Journal of Geochemical Exploration*, vol. 69-70, pp. 641–644, 2000.

[10] I. A. Munz, "Petroleum inclusions in sedimentary basins: systematics, analytical methods and applications," *Lithos*, vol. 55, no. 1-4, pp. 195–212, 2001.

[11] P. John, M. David, H. H. Chen, and H. Don, "The use of integrated fluid inclusion studies in constraining oil charge history and reservoir compartmentation: examples from the Jeanne d'Arc Basin, offshore Newfoundland," *Marine and Petroleum Geology*, vol. 43, no. 3, pp. 175–549, 2002.

[12] J. Bourdet, J. Pironon, G. Levresse, and J. Tritlla, "Petroleum type determination through homogenization temperature and vapour volume fraction measurements in fluid inclusions," *Geofluids*, vol. 8, no. 1, p. 59, 2008.

[13] H. H. Chen, C. Q. Li, X. M. Zhang, H. C. Chen, and Z. M. Lin, "Determination of hydrocarbon accumulation stages and main hydrocarbon accumulation stages in Tahe oilfield by fluid inclusion," *Earth Science Frontiers*, vol. 10, no. 1, p. 190, 2003.

[14] L. Zhao, X. Y. Xia, J. X. Dai, and F. Hong, "Major controlling factors of natural gas enrichment in upper Paleozoic in Ordos basin," *Experimental Petroleum Geology*, vol. 22, no. 2, pp. 136–139, 2000.

[15] Q. Min, J. H. Fu, S. L. Xi et al., "Characteristics of migration and accumulation of natural gas in upper Paleozoic in Ordos basin," *Petroleum Exploration and Development*, vol. 27, no. 4, pp. 26–29, 2000.

[16] X. Q. Li, G. Y. Hu, J. Li, B. Xiong, J. K. Mi, and Y. J. T, "Fluid inclusion characteristics of Ordovician carbonate reservoirs in the central Ordos Basin and its significance to natural gas accumulation," *Natural Gas Geoscience*, vol. 15, no. 2, pp. 120–124, 2004.

[17] J. H. Fu, X. S. Wei, J. F. Ren, and H. S. Zhou, "The situation and development prospect of natural gas exploration in Ordos basin," *Acta Petrolei Sinica*, vol. 27, no. 6, pp. 1–4, 2006.

[18] H. Yang, J. H. Fu, X. S. Liu, and L. Y. Fan, "Formation conditions and exploration techniques of Sulige large tight sandstone gas reservoir," *Acta Ecologica Sinica*, vol. 33, no. 1, pp. 27–36, 2012.

[19] S. M. Hao, K. Y. Hui, and L. Li, "Reservoir forming characteristics and exploration and development technology of Daniudi large low permeability gas field in Ordos Basin," *Oil and Gas Geology*, vol. 27, no. 6, pp. 2–9, 2006.

[20] J. Z. Zhao, W. Z. Zhang, J. Li, Q. Cao, and Y. F. Fan, "Genesis of tight sand gas in the Ordos Basin, China," *Organic Geochemistry*, vol. 74, pp. 76–84, 2014.

[21] Y. Li, J. Yang, Z. Pan, S. Meng, K. Wang, and X. Niu, "Unconventional natural gas accumulations in stacked deposits: a discussion of Upper Paleozoic coal-bearing strata in the east margin of the Ordos Basin, China," *Acta Geologica Sinica (English Edition)*, vol. 93, no. 1, pp. 111–129, 2019.

[22] Y. Li, X. D. Gao, S. Z. Meng et al., "Diagenetic sequences of continuously deposited tight sandstones in various environments: a case study from upper Paleozoic sandstones in the Linxing area, eastern Ordos basin, China," *AAPG Bulletin*, vol. 103, no. 11, pp. 2757–2783, 2019.

[23] Y. Li, W. K. Xu, P. Wu, and S. Z. Meng, "Dissolution versus cementation and its role in determining tight sandstone quality: a case study from the Upper Paleozoic in northeastern Ordos Basin, China," *Journal of Natural Gas Science and Engineering*, vol. 78, no. 2020, p. 103324, 2020.

[24] Y. H. Zhang, J. Z. Zhao, Y. W. Wang, T. Liu, W. Q. Wang, and W. Tang, "Paleotectonic characteristics of the first member of the Shanxi Formation of the Upper Paleozoic in the southwest of Ordos Basin and its controlling effect on oil and gas," *Petroleum and Gas Geology*, vol. 39, no. 1, pp. 54–65, 2018.

[25] Q. Cao, J. M. Gao, L. Y. Fan, C. X. Pang, and J. Z. Yu, "Characteristics and significance of fluid inclusions in the upper Paleozoic in the southwest of Ordos basin," *Natural Gas Geoscience*, vol. 26, no. 12, pp. 2245–2253, 2015.

[26] M. G. Liao, X. W. Xiao, J. L. Yao, J. J. Liao, J. X. Nan, and D. Lin, "Study on fluid inclusion characteristics and accumulation period of He 8 section in Longdong area," *Geological Journal of China Universities*, vol. 23, no. 2, pp. 315–323, 2017.

[27] W. Q. Hu, J. Z. Zhao, J. Li, L. Li, J. Zheng, and X. H. Jing, "Characteristics of hydrocarbon source rocks in the upper Paleozoic in the southwest of Ordos Basin and their control on the formation and distribution of natural gas reservoirs," *Natural Gas Geoscience*, vol. 26, no. 6, pp. 1068–1075, 2016.

[28] Z. X. He, J. H. Fu, S. L. Xi, S. T. Fu, and H. P. Bao, "Geologic features of reservoir formation Sulige Gas Field," *Acta Petrolei Sinaca*, vol. 24, no. 2, pp. 6–12, 2003.

[29] Y. T. Yang, W. Li, and L. Ma, "Tectonic and stratigraphic controls of hydrocarbon systems in the Ordos Basin: a multicycle cratonic basin in central China," *American Association of Petroleum Geologists Bulletin*, vol. 89, no. 2, pp. 255–269, 2005.

[30] R. J. Zhu, *Study on the Characteristics of Upper Paleozoic Natural Gas Reservoirs in the Southwest of Ordos Basin, [M.S. thesis]*, Chang 'an University, 2014.

[31] S. M. Wang, "Tectonic evolution and tectonic coal control in the Ordos Basin," *Geological Bulletin of China*, vol. 30, no. 4, pp. 544–552, 2011.

[32] S. Z. Yang, W. H. Jin, and Z. H. Li, "Formation and evolution of the Ordos polycyclic superposition basin," *Natural Gas Geoscience*, vol. 17, no. 4, pp. 494–498, 2006.

[33] J. Yan and X. Pei, *Geology of Natural Gas in China, v.4 (Ordos Basin)*, Petroleum Industry Press (in Chinese), 1996.

[34] J. L. Liu, K. Y. Liu, and X. Huang, "Effect of sedimentary heterogeneities on hydrocarbon accumulations in the Permian Shanxi Formation, Ordos Basin, China: insight from an integrated stratigraphic forward and petroleum system modelling," *Marine and Petroleum Geology*, vol. 76, pp. 412–431, 2016.

[35] Z. D. Li, S. M. Hao, and L. Li, "Pressure storage tank and natural gas enrichment law of Upper Paleozoic in Ordos Basin," *Oil and Gas Geology*, vol. 28, no. 4, pp. 466–472, 2007.

[36] C. L. Zhang, J. Li, and R. E. Liu, "Microscopic characteristics and formation mechanism of tight sandstone gas reservoirs in He 8 section of Ordos basin," *China Petroleum Exploration*, vol. 24, no. 4, pp. 476–484, 2019.

[37] J. C. Tian, Q. Wu, F. Wang, X. B. Lin, J. Q. Zhang, and T. S. Cao, "The reservoir sand body developmental control factors and sedimentary models of He 8 of lower Shihzi formation in Ordos Basin," *Acta Petrologica Sinica*, vol. 27, no. 8, pp. 2403–2412, 2011.

[38] W. H. Wang, J. C. Tian, and J. Q. Zhang, "The sedimentary characteristics study of Permian He 8 section in Ordos Basin," *Journal of Chengdu University of technology:(Science & Technology Edition)*, vol. 43, no. 2, pp. 224–232, 2016.

[39] L. Li, H. M. Tang, X. Wang et al., "Evolution of diagenetic fluid of ultra-deep Cretaceous Bashijiqike Formation in Kuqa depression," *Journal of Central South University*, vol. 25, no. 10, pp. 2472–2495, 2018.

[40] H. Li, Y. Q. Liu, and L. Y. Liu, "Diagenesis of Yanchang section chang8^1 low permeability reservoir in Xifeng Oilfield, Ordos Basin," *Oil and Gas Geology*, vol. 27, no. 2, pp. 209–217, 2006.

[41] D. K. Zhong, L. J. Zhou, H. T. Sun, J. L. Yao, S. Y. Ma, and H. H. Zhu, "Effects of petrological characteristics of reservoirs on diagenesis and pore development: a case study of the Triassic Yanchang Formation in Longdong area, Ordos Basin," *Oil and Gas Geology*, vol. 33, no. 6, pp. 890–899, 2012.

[42] C. B. Che, Y. S. Zhu, X. J. Chen et al., "Sedimentary diagenesis of Yan Chang formation chang8^2 reservoir in Jiyuan area, Ordos Basin," *Oil and Gas Geology*, vol. 34, no. 5, pp. 685–693, 2013.

[43] F. Wang, R. Chen, J. C. Tian, M. R. Li, H. R. Zhang, and X. Liu, "Diagenesis and diagenetic facies of tight sandstone reservoirs in the Chang^{4+5} oil formation in Longdong area, Ordos Basin," *Oil and Gas Geology*, vol. 35, no. 2, pp. 199–206, 2014.

[44] X. Gong, X. Y. Hu, W. H. Li, and W. X. Shen, "The difference and quantitative expression of the influence of diagenesis on reservoir densification – a case study of tight sandstone in Su 77 block of Sulige Gas Field," *Acta Sedimentologica Sinica*, vol. 38, no. 6, pp. 1–13, 2020.

[45] R. C. Yang, Z. Z. Han, Z. X. Li, A. P. Fan, and Z. Z. han, "Base-level cycles and episodic coal accumulation–case study of Dongsheng Coalfield in Ordos Basin," *Journal of China University of Mining and Technology*, vol. 16, no. 4, pp. 439–442, 2006.

[46] A. Fan, R. Yang, J. Li, Z. Zhao, and A. J. T. van Loon, "Siliceous cementation of chlorite coated grains in the Permian sandstone gas reservoirs, Ordos basin," *Acta Geologica Sinica(English Edition)*, vol. 91, no. 3, pp. 1147-1148, 2017.

[47] Z. D. Li, K. Y. Hui, L. Li, W. Zhou, and M. Guo, "Analysis of characteristics of gas migration and reservoir forming in the upper Paleozoic of northern Ordos basin," *Mineralogy and Petrology*, vol. 28, pp. 77–83, 2008.

[48] S. J. Huang, K. K. Huang, W. L. Feng, H. P. Tong, L. H. Liu, and X. H. Zhang, "Mass exchanges among feldspar, kaolinite and illite and their influences on secondary porosity formation in clastic diagenesis — a case study on the Upper paleozoic, Ordos basin and Xujiahe formation, Western Sichuan depression," *Geochimica*, vol. 38, no. 5, pp. 498–506, 2009.

[49] R. Yang, A. Fan, A. J. van Loon, Z. Han, and X. Wang, "Depositional and diagenetic controls on sandstone reservoirs with low porosity and low permeability in the eastern Sulige gas field, China," *Acta Geologica Sinica(English Edition)*, vol. 88, no. 5, pp. 1513–1534, 2014.

[50] J. L. Luo, X. S. Liu, X. Y. Fu, M. Li, R. Kang, and Y. N. Jia, "Effects of petrological composition and diagenetic evolution on quality and productivity of tight sandstone reservoirs: a case study of upper Paleozoic He 8 section natural gas reservoir in Ordos Basin," *Earth Science*, vol. 39, no. 5, pp. 537–545, 2014.

[51] D. W. Houseknecht, "Assessing the relative importance of compaction processes and cementation to reduction of porosity in sandstones," *International Journal of Rock Mechanics and Mining Sciences and Geomechanics Abstracts*, vol. 25, no. 2, p. 53, 1988.

[52] J. Gluyas and C. A. Cade, "Prediction of Porosity in Compacted Sands," in *Reservoir Quality Prediction in Sandstones and Carbonates*, J. A. Kupecz, J. Gluyas, and S. Bloch, Eds., vol. 69, pp. 19–27, AAPG, 1997.

[53] J. Shou, H. Zhang, C. Si, X. Wang, Z. Chen, and S. Wang, *Sandstone Dynamic Diagenesis*, Petroleum Industry Press (in Chinese), 2005.

[54] S. Stricker, S. J. Jones, and N. T. Grant, "Importance of vertical effective stress for reservoir quality in the Skagerrak formation, central Graben, North Sea," *Marine and Petroleum Geology*, vol. 78, pp. 895–909, 2016.

[55] K. L. Xi, Y. C. Cao, K. Y. Liu et al., "Diagenesis of tight sandstone reservoirs in the upper Triassic Yanchang formation, southwestern Ordos Basin, China," *Marine and Petroleum Geology*, vol. 99, pp. 548–562, 2019.

[56] M. C. Hou, W. T. Dou, H. D. Chen, and G. Y. Dong, "Study on diagenesis of the He 8 member and Shan1 member in north of the Sulige gas field, Ordos Basin," *Mineralogy and Petrology*, vol. 29, no. 4, pp. 66–74, 2009.

[57] F. Wang, J. C. Tian, F. J. Li, J. X. Zhao, and M. R. Li, "Diagenesis of reservoirs in the Upper Paleozoic member 8 formation in the Sulige area," *Journal of Lanzhou University(Natural Sciences)*, vol. 45, no. 4, pp. 18–29, 2005.

[58] M. L. Zhang, S. P. Da, and T. S. Chen, "Diageneses and pore evolution of $P_1h_1^8$ reservoir in Sulige gas field," *Natural Gas Industry*, vol. 22, no. 6, pp. 13–16, 2002.

[59] X. M. Zhu, C. Sun, C. L. Liu, D. K. Zhong, and Q. T. Yan, "Reservoir diagenesis and flfluid-rock interaction simulation of the Sulige gas field in the Ordos Basin," *Geology in China*, vol. 34, no. 2, pp. 276–282, 2007.

[60] J. Shi, W. H. Huang, Y. Z. Wang, Y. T. Wang, and C. Lu, "Characteristics and genesis of secondary porosity of sandstone in the western part of Ordos Basin from He 8 - Shan 1 section," *Journal of Coal Science*, vol. 43, no. 12, pp. 3461–3470, 2008.

[61] L. Xu, X. H. Yu, Y. Yang, S. L. Li, Q. Q. Tian, and Y. Zhou, "Diagenesis and diagenetic facies division of tight sandstone reservoirs in He 8 section in the southern Sulige area," *Natural Gas Industry*, vol. 32, no. 7, pp. 15–20, 2012.

[62] L. W. Qiu, S. J. Mu, H. Li, J. Zhang, Y. P. Qiao, and S. B. Zhou, "The influence of diagenesis on pore development of tight sandstone reservoirs in lower Shihezi formation in Hangjinqi area," *Petroleum Geology and Recovery Efficiency*, vol. 26, no. 2, pp. 42–50, 2019.

[63] M. M. Cui, J. B. Li, Z. X. Wang et al., "Characteristics of tight sandstone reservoirs in the leading edge of Braid-shaped River Delta and factors controlling high-quality reservoirs – a case study of He 8 formation in Shihezi section in the southwest of Sulige Gas Field," *Acta Petrolei Sinica*, vol. 40, no. 3, pp. 279–293, 2019.

[64] S. C. Haddad, R. H. Worden, D. J. Prior, and P. C. Smalley, "Quartz cement in the Fontainebleau sandstone,Paris Basin, France:crystallography and implications for mechanisms of cement growth," *Journal of Sedimentary Research*, vol. 76, no. 2, pp. 244–256, 2006.

[65] W. Q. Hu, *Geochemical Characteristics of Upper Paleozoic Natural Gas Reservoirs in the Southwest of Ordos Basin, [M.S. thesis]*, Xi 'an Petroleum University, 2015.

[66] T. He, F. Wang, and H. H. Song, "Reservoir diagenesis and pore evolution in He.8 reservoir in southern Sulige gas field," *Journal of Oil and Gas Technology*, vol. 35, no. 2, pp. 31–35, 2013.

[67] H. M. Tang, M. Wang, F. Zhao, S. Liu, H. G. Guo, and S. Xu, "Quantitative analysis of main controlling factors of reservoir compaction in Shan 2 member of eastern section, Sulige gas field," *Reservoir Evaluation and Development*, vol. 7, no. 3, pp. 7–14, 2017.

[68] N. L. Sun, J. H. Zhong, S. G. Liu et al., "Diagenesis and physical evolution of tight reservoirs with gravity flow in the Yanchang Formation in the southern Ordos Basin," *Earth Science*, vol. 42, no. 10, pp. 1802–1816, 2017.

[69] H. H. Zhu, D. K. Zhong, J. L. Yao et al., "Diagenesis in alkaline environment and its effect on reservoir pores - a case study of tight sandstone in Chang 7 member of Ordos Basin," *Petroleum Exploration and Development*, vol. 42, no. 1, pp. 51–59, 2015.

[70] Q. Yu, Z. L. Ren, Z. W. Zhu, N. Tao, B. J. Wang, and C. C. Li, "Exhumation, cooling and erosion history of Triassic oil shale since Late Cretaceous, Binxian-Tongchuan area of Ordos Basin," *Earth Science*, vol. 43, no. 6, pp. 1839–1849, 2018.

[71] Z. L. Ren, S. Zhang, S. L. Gao, J. P. Cui, and X. S. Liu, "Discussion on the distribution area and formation period of thermal evolution degree anomaly in the Ordos Basin," *Acta Geologica Sinica*, vol. 80, no. 5, pp. 674–684, 2006.

[72] Q. Yu, Z. Ren, R. Li et al., "Meso-Cenozoic tectonothermal history of Permian strata, Southwestern Weibei Uplift: insights from thermochronology and geothermometry," *Acta Geologica Sinica (English Edition)*, vol. 93, no. 6, pp. 1647–1661, 2019.

[73] Q. Yu, Z. L. Ren, R. X. Li, B. J. Wang, X. L. Qin, and N. Tao, "Paleogeotemperature and maturity evolutionary history of the source rocks in the Ordos Basin," *Geological Journal*, vol. 52, no. S.1, pp. 97–118, 2017.

[74] X. M. Xiao, Z. F. Liu, D. H. Liu, J. K. Mi, J. G. Shen, and Z. G. Song, "Application of reservoir fluid inclusion information to study the formation time of natural gas reservoirs," *Chinese Science Bulletin*, vol. 47, no. 12, pp. 957–960, 2002.

Hindawi
Geofluids
Volume 2021, Article ID 5513490, 14 pages
https://doi.org/10.1155/2021/5513490

Research Article

Metal Flux from Dissolution of Iron Oxide Grain Coatings in Sandstones

J. Parnell,[1] **X. Wang**,[2] **A. Raab**,[2] **J. Feldmann**,[2,3] **C. Brolly**,[1] **R. Michie**,[1] **and J. Armstrong**[1]

[1]*School of Geosciences, University of Aberdeen, Aberdeen AB24 3UE, UK*
[2]*Trace Element Speciation Laboratory (TESLA), Department of Chemistry, University of Aberdeen, Aberdeen AB24 3UE, UK*
[3]*Environmental Analytical Chemistry, Institute of Chemistry, University of Graz, Graz, Austria*

Correspondence should be addressed to J. Parnell; j.parnell@abdn.ac.uk

Received 28 January 2021; Revised 11 March 2021; Accepted 20 April 2021; Published 18 May 2021

Academic Editor: Guo Xiang Chi

Iron oxide grain coatings in red sandstones contain trace metals that are released upon dissolution of the coatings. Analyses by ICP-MS following acid leaching of the grain coatings show that the dissolved metals can constitute an ore-forming fluid, as hypothesized in models for sandstone-hosted ore deposits. Median compositions of 37 samples, mostly of Triassic to Devonian age, from across Britain and Ireland are 6.3 ppm copper, 2.4 ppm cobalt, 10.1 ppm vanadium, and 0.3 ppm uranium. These contents at the basin scale are adequate to form the observed range of ore deposits in red beds. The migration of hydrocarbons or brines can cause the dissolution of grain coatings and contributes to controlling the distribution of ore deposits. Future measurements should test red beds derived from uplifted, mineralized plate margins, in which sandstones may be preloaded with ore metals.

1. Introduction

The mineralization of sedimentary basins has made an important contribution to the planet's resources of metals [1]. Mineralization in basins requires processes that concentrate metals beyond their normal abundance by several orders of magnitude. Examples include the concentration of redox-sensitive elements by reduction sites, such as black shales, and the release of metals from clays during diagenesis. In continental basins, one of the most widespread of processes is the formation of iron oxide coatings around sand grains during early diagenesis [2]. The iron oxide derives from the alteration of mineralogically immature grains such as ferromagnesian minerals. The coatings are what make many sandstones red, when the iron oxide becomes the mineral haematite. Iron oxides are particularly significant to diagenesis because of their capacity to adsorb a wide variety of trace elements from groundwaters [3]. As diagenesis proceeds, and the volume of secondary iron oxides increases, the proportion of trace elements resident in the oxides also increases. However, the grain coatings are also susceptible to removal by dissolution into acidic pore fluids, including oilfield brines [4]. For example, dissolution is evident from the bleaching of red beds following hydrocarbon migration (e.g., [5]) and from CO_2-rich brines [6, 7], but these fluids are not always evident. The combination of trace metal uptake and dissolution is a potential pathway to produce a mineralizing fluid [8–12]. This possibility has been invoked to explain moderate- to large-scale ore deposits in sandstones, such as copper and silver in Kazakhstan [13, 14], copper and silver in Iran [15], uranium in Australia [16], copper in Argentina [17, 18], vanadium in Argentina [19], copper in Arctic Canada [20], copper in Newfoundland [21], lead-zinc in China [22], and uranium in China [23]. The occurrence of red sandstones does not, however, necessarily explain mineralization, as other sources such as underlying basement may contribute more metal in certain hydrological regimes [24].

The high abundance of red beds, in space and time [25], implicates their potential importance to the mineralization of continental basins. Traces of mineralization occur in red beds

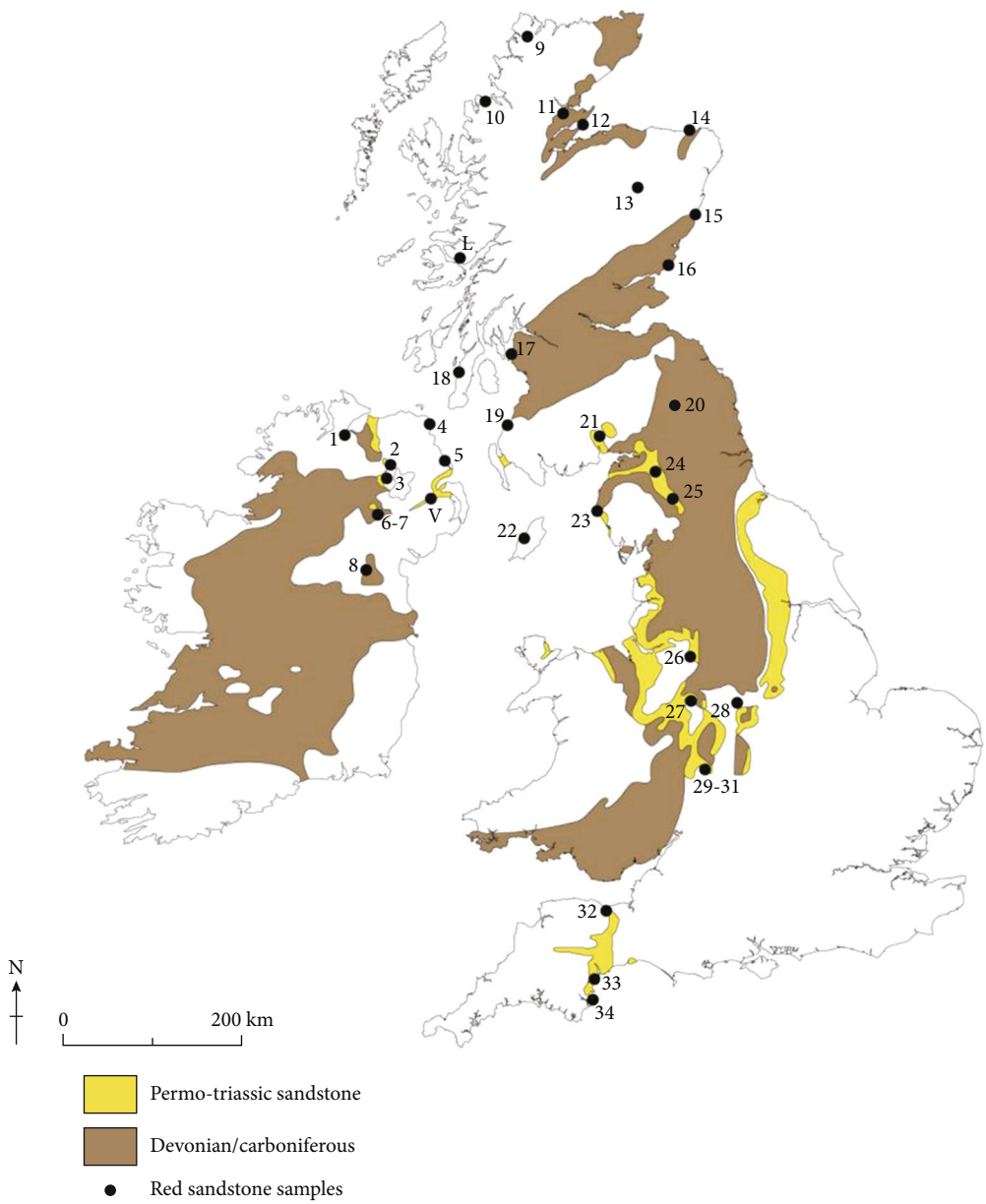

Figure 1: Locations for red sandstone samples, Britain and Ireland. Numbered localities were sampled for red sandstones (Table 1). L: Lochaline quartz sandstone procedural blank. V: Lagan Valley borehole 4B sandstone used for LA-ICP-MS map.

dated at least back to the Mesoproterozoic [26]. However, there are only very limited data for the trace element compositions of the iron oxide coatings that are central to the process. This study reports the compositions of grain coatings from numerous different localities and ages.

The objectives are specifically:

(i) Measurement of a data base of compositions of grain coatings. Data were collected for vanadium (V), cobalt (Co), copper (Cu), selenium (Se), uranium (U), arsenic (As), and lead (Pb) in iron- (Fe-) rich grain coatings. These elements represent those which commonly occur in red bed ore deposits

(ii) Assessment of whether the composition of grain coatings is related to their relative abundance, i.e., quantity of iron oxide

(iii) Assessing the typical range of metal fluxes that might be expected from their dissolution

2. Methods

The data set was measured from samples in Britain and Ireland, where a relatively limited area includes red sandstones from a range of stratigraphic ages, and the samples represent both first-cycle and multicycle erosion. Hence, they are a

Figure 2: Sandstone exposure, Engine Vein, Alderley Edge copper mines. Bleached sandstone (B) overlies red sandstone (R) and passes into the copper-rich region (C).

varied assemblage of sandstones suitable to best assess the chemistry of typical red grain coatings, rather than sandstones that are all associated with ore deposits. Samples were collected from 34 localities in Britain and Ireland (Figure 1), predominantly from red sandstones of Devonian, Permian, and Triassic age and deposited in fluvial or aeolian environments. Single samples of Neoproterozoic and Silurian red sandstone were collected. In addition, a sample of Carboniferous sandstone was collected, in which reddening had occurred at a relatively late stage, below the sub-Permian unconformity which caused widespread deep oxidation [27]. Red sandstone in dykes cutting down through the same unconformity [28] was collected at Berry Head, Torquay, England. A sample of Triassic sandstone at Maghera, Ireland, was chosen because it appeared to be enriched in iron by recent "iron pan" soil mineralization. Samples of red and bleached sandstone were collected for comparison from Alderley Edge, England (Figure 2), where bleaching is implicated in copper mineralization [29, 30]. Three red sandstone samples from other parts of the world (China, Australia, USA) were analysed to test if the main data base is typical of other regions. Samples were chosen that could be disaggregated readily and were not cemented by minerals that sealed in the iron oxide and prevented dissolution. Disaggregated samples were sieved to isolate the sub-500 micron or sub-250 micron fraction, depending on the predominant grain size. Sandstone from Gardenstown, Scotland, was separated into three size fractions, 500-250 micron, 250-125 micron, and sub-125 micron, to test if this factor might influence the compositions. Finally, a pure quartz sandstone with no iron oxide grain coatings (Cretaceous Lochaline Sandstone, Scotland) was analysed as a procedural blank.

Samples for acid leaching were added in weighed amounts of about 150 mg to 4 mL aqua regia (3 : 1 HCl:HNO_3, both analytical grade for trace elements) and boiled for 30 minutes at 95°C in a microwave. The liquid was then centrifuged, and the residue was subjected to a repeat of the procedure if any iron oxide remained undissolved (optical appearance). Only up to 20 wt.% of each sample was dissolved by this procedure, leaving more than 80 wt.% residue. The liquids from centrifuging were combined, and V, Co, Cu, Se, U, As, and Pb were measured by Triple Quad ICP-MS Agilent 8800 (Agilent Technologies), in the Trace Element Speciation Laboratory (TESLA), Department of Chemistry, at the Aberdeen University, UK. 10 μg/kg Rh in 2% HNO_3 was used as an internal standard. The total leached element masses were determined (to an accuracy of 0.001 g) and converted to concentrations of the original rock. Measurements were also taken from certified reference materials PACS-2 and BCSS-1 (marine sediments), and NIST2711a and NIST2709a (soils), and an absolute blank. Our data for V, Co, Cu, and Se for the NIST2711a and NIST2709a soils are consistent with the certificated data for the "acid-extractable" fraction. For the two sediments PACS-2 and BCSS-1, there is no certificated data for the "acid-extractable" fraction but only for the "whole rock" fraction, which also is in agreement with our data for Co, Cu, and Se, but show a higher value for V. Our acid leachable uranium, which had a recovery of 31-50% from certified totals, shows up to 70% totals from other ICPMS methods using PACS-2, and NIST SRM 2711a, 2709a [31, 32]. This indicates that the reported acid leachable uranium values most likely underestimate the content of uranium in the grain coatings.

Bulk analyses of Fe contents in all samples, and V and Cu in a subset of ten Permian and Triassic sandstone samples (available from another project that did not include the other samples), were made after multiacid digestion (perchloric, nitric, hydrofluoric, and hydrochloric acids) by ICP-MS.

Thin sections of a red sandstone from the Triassic of Northern Ireland (Lagan Valley borehole 4B, depth 30.7 m) were mapped by laser ablation-ICP-MS. Elements were analysed using a LSX-213 G2+ laser ablation system (equipped with a Fast Washout 2-Volume HelEx II Cell and Aerosol Rapid Introduction System (ARIS), Teledyne CETAC Technologies) attached to a Triple Quad ICP-MS Agilent 8800 (Agilent Technologies), in TESLA at the Aberdeen University, UK. V (m/z 51, 0.01 s), Fe (m/z 57, 0.01 s), Co (m/z 59, 0.01 s), Cu (m/z 63, 0.01 s), Se (m/z 78, 0.1 s), and U (m/z 238, 0.1 s) were measured (integration time). Analyses were performed in a helium atmosphere, at a repetition rate of 20 Hz, a laser power of 6.02 J/cm^2, a spot diameter of 25 μm, and an ablation speed of 50 μm/sec. Each line analysis

Table 1: Composition of grain coatings on red sandstones.

Map no.	Locality	Age		Lab code	*n*	Fe (%)	V (ppm)	Co (ppm)	Cu (ppm)	As (ppm)	Se (ppm)	Pb (ppm)	U (ppm)	V/Fe	Co/Fe	Cu/Fe	As/Fe	Se/Fe	Pb/Fe	U/Fe
Britain, Ireland																				
1	Londonderry	Triassic		TS-TL d	3	1.91	19.20	4.60	11.01	1.01	0.06	4.92	0.65	10.05	2.41	5.77	0.53	0.03	2.58	0.34
3	Moneymore	Triassic		RS-TM	3	0.23	4.09	1.08	6.66	0.70	0.02	0.74	0.10	17.76	4.71	28.94	3.05	0.08	3.22	0.43
4	Arched Mine	Carboniferous		RS-CA	3	0.35	2.30	2.43	25.72	0.22	0.04	0.59	0.09	6.57	6.95	73.48	0.62	0.11	1.69	0.27
5	Larne	Triassic		RS-TLa	3	0.17	4.29	0.46	5.88	1.01	0.00	1.55	0.11	25.22	2.71	34.61	5.97	0.00	9.09	0.64
6	Bonds Mill Bridge	Triassic		RS-BMB	3	1.43	12.90	5.02	3.55	1.48	0.06	3.92	0.25	9.02	3.51	2.48	1.03	0.04	2.74	0.18
7	Dree Hill	Triassic		RS-TOH	3	1.3	14.12	5.36	9.23	2.05	0.09	3.82	0.28	10.86	4.12	7.10	1.58	0.07	2.94	0.21
8	Kingscourt	Triassic		RS-TK	3	1.05	12.28	4.77	3.97	2.16	0.08	3.66	0.35	11.69	4.55	3.78	2.06	0.07	3.48	0.33
9	Gualin	Neoproterozoic		RS-PrG	3	1.41	13.23	1.40	3.92	0.11	0.03	4.68	0.62	9.39	1.00	2.78	0.07	0.02	3.32	0.44
10	Laide	Triassic		RS-TL	3	0.45	8.20	1.34	20.47	1.10	0.06	3.29	0.18	18.22	2.98	45.48	2.44	0.14	7.31	0.40
11	Redburn	Devonian		RS-DR	3	1.14	12.14	3.98	43.33	0.68	0.05	4.70	0.17	10.65	3.49	38.01	0.60	0.04	4.13	0.15
12	Nigg Bay	Devonian		RS-NB	3	1.28	9.63	1.89	1.78	1.09	0.07	2.71	0.35	7.52	1.48	1.39	0.85	0.06	2.12	0.28
13	Tomintoul	Devonian		RS-DT	3	4.74	18.49	7.86	6.18	2.23	0.19	10.74	0.63	3.90	1.66	1.30	0.47	0.04	2.27	0.13
14a	Gardenstown	Devonian	<125	RS-DG125	3	3.81	18.31	2.27	4.46	0.75	0.13	15.69	1.20	4.81	0.60	1.17	0.20	0.04	4.12	0.31
14b	Gardenstown	Devonian	125-250	RS-DG250	3	2.3	10.31	1.37	1.26	0.44	0.08	8.36	0.51	4.48	0.60	0.55	0.19	0.03	3.63	0.22
14c	Gardenstown	Devonian	250-500	RS-DG500	3	2.8	11.13	1.54	1.65	0.45	0.08	8.96	0.54	3.97	0.55	0.59	0.16	0.03	3.20	0.19
15	Cowie Harbour	Silurian		RS-SC	3	3.01	30.32	5.05	135.63	6.57	0.10	9.08	0.90	10.07	1.68	45.06	2.18	0.03	3.02	0.30
16	Arbroath	Devonian		RS-DA	3	3.12	64.70	6.76	14.24	9.53	0.09	14.71	0.62	20.74	2.17	4.56	3.06	0.03	4.72	0.20
17	Sheriff's Port	Devonian		RS-DS	4	0.83	12.30	7.06	2.50	2.98	0.05	3.10	0.22	14.82	8.51	3.01	3.59	0.06	3.73	0.26
18	Killean	Permian		RS-PK	3	0.81	9.09	1.52	2.66	2.08	0.05	1.90	0.17	11.22	1.88	3.28	2.57	0.06	2.35	0.21
19	Bennane Lea	Permian		RS-PBL	3	1.07	5.61	1.30	13.46	1.82	0.06	1.98	0.29	5.24	1.22	12.58	1.70	0.05	1.85	0.27
20	Jedburgh	Devonian		RS-DJ	3	1.66	17.59	6.54	9.88	2.15	0.07	10.50	0.44	10.60	3.94	5.95	1.29	0.04	6.33	0.26
21	Locharbriggs	Permian		TS-PLo	3	0.45	2.81	0.29	2.51	0.10	0.00	2.79	0.12	6.24	0.64	5.58	0.23	0.00	6.19	0.26
22	Peel	Devonian		RS-CP	3	1.38	9.84	3.21	35.90	3.07	0.13	6.50	0.69	7.13	2.32	26.01	2.22	0.09	4.71	0.50
23	St. Bees Head	Permian		RS-PBH	3	1.18	10.72	2.53	2.32	1.64	0.07	2.02	0.45	9.09	2.14	1.97	1.39	0.06	1.71	0.38
24	Lazonby	Permian		RS-PL	3	0.19	5.07	0.27	6.41	0.65	0.06	8.92	0.09	26.66	1.40	33.73	3.45	0.33	46.97	0.50

Table 1: Continued.

Map no.	Locality	Age		Lab code	*n*	Fe (%)	V (ppm)	Co (ppm)	Cu (ppm)	As (ppm)	Se (ppm)	Pb (ppm)	U (ppm)	V/Fe	Co/Fe	Cu/Fe	As/Fe	Se/Fe	Pb/Fe	U/Fe
25	Appleby	Permian		RS-PA	3	0.78	5.98	1.22	3.16	0.80	0.05	1.89	0.21	7.67	1.56	4.05	1.03	0.06	2.42	0.28
27	Park Hall	Triassic		RS-TP	3	1.02	7.64	2.98	18.85	1.21	0.06	1.61	0.45	7.49	2.93	18.48	1.18	0.06	1.58	0.44
28	Cotgrave	Triassic		RS-TC	2	1.49	15.68	6.99	10.70	3.91	0.08	4.03	0.50	10.52	4.69	7.18	2.63	0.05	2.71	0.34
29	Bromsgrove bypass	Triassic		RS-BP2	3	1.93	18.55	6.61	37.93	5.60	0.17	3.59	0.77	9.61	3.43	19.66	2.90	0.09	1.86	0.40
30	Burcot Lane	Triassic		RS-BL	2	0.47	4.02	0.67	0.86	0.82	0.07	2.53	0.17	8.56	1.43	1.83	1.74	0.15	5.38	0.37
31	Park Gate	Triassic		RS-PG	2	0.55	5.50	1.42	4.97	2.14	0.02	2.27	0.15	10.00	2.58	9.03	3.90	0.04	4.12	0.27
32	Old Cleeve	Triassic		RS-TOC	3	0.31	5.79	0.88	8.83	3.77	0.05	1.56	0.17	18.66	2.83	28.48	12.16	0.16	5.02	0.54
33	Dawlish	Permian		RS-PD	3	0.44	4.61	2.71	13.44	1.74	0.10	6.73	0.27	10.47	6.16	30.55	3.96	0.22	15.31	0.61
34	Berry Head	Permian		RS-PBR	3	0.35	2.23	0.66	2.89	1.81	0.00	10.35	0.05	6.37	1.88	8.25	5.18	0.00	29.57	0.16
Mean						1.34	12.02	3.06	14.01	2.00	0.07	5.13	0.38	9.00	2.29	10.49	1.49	0.05	3.84	0.28
Median						1.11	10.07	2.35	6.29	1.56	0.06	3.74	0.28	9.11	2.13	5.69	1.41	0.06	3.38	0.26
World																				
W1	Tumblagooda	Ordovician		RS-OT	3	0.37	3.09	0.11	0.84	0.31	0.09	1.45	0.09	8.35	0.29	2.26	0.83	0.24	3.92	0.24
W2	Min Chang	Jurassic		RS-JM	3	0.56	4.35	1.57	11.01	1.71	0.03	4.67	0.15	7.77	2.81	19.67	3.06	0.06	8.34	0.27
W3	Castle Valley	Jurassic		RS-JCV	3	0.52	7.08	2.23	13.33	1.46	0.01	1.29	0.17	13.62	4.28	25.63	2.81	0.03	2.49	0.32
Mineralized, procedural blank																				
L (blank)	Lochaline	Cretaceous		RS-CL2	3	0.01	0.20	0.07	0.40	0.00	0.00	0.14	0.01	19.88	7.44	40.00	0.00	0.00	14.05	0.60
2	Maghera	Triassic		RS-TMa	3	3.48	104.48	23.63	46.68	1.66	0.21	14.37	0.89	30.02	6.79	13.41	0.48	0.06	4.13	0.26
26a	Alderley Edge	Triassic	Red	RS-TAR-A	3	1.24	28.00	41.00	170.97	9.44	0.07	890.33	0.28	22.58	33.06	137.88	7.61	0.05	718.01	0.23
26b	Alderley Edge	Triassic	Red	RS-TAR-B	3	0.53	6.36	16.25	113.68	4.28	0.08	155.24	0.14	12.00	30.66	214.49	8.08	0.15	292.91	0.27
26c	Alderley Edge	Triassic	Bleached	RS-TAB-A	3	0.33	3.33	13.49	733.31	703.57	0.06	5627.42	0.36	10.10	40.89	2222.15	2132.04	0.17	17052.80	1.08
26d	Alderley Edge	Triassic	Bleached	RS-TAB-B	3	0.3	3.65	12.28	988.51	638.30	0.07	5426.67	0.27	12.17	40.95	3295.03	2127.66	0.23	18088.90	0.91

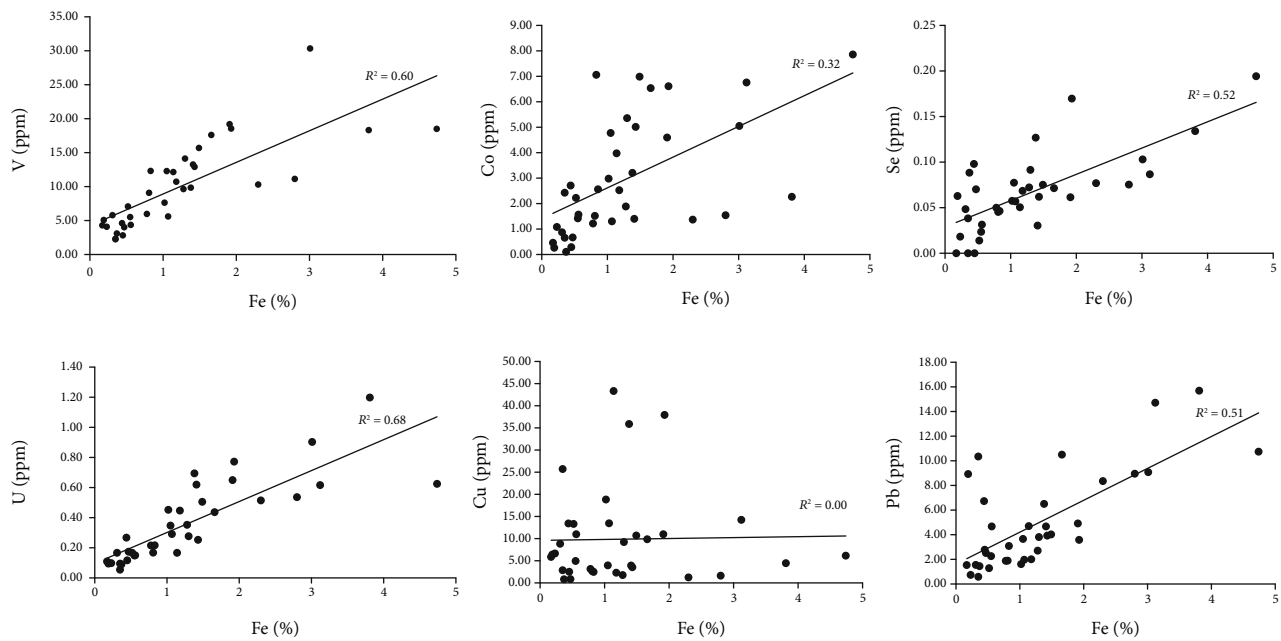

Figure 3: Cross-plots for whole rock Fe content against content of trace elements measured by acid extraction. Single samples omitted from cross-plots against V (locality 16) and Cu (locality 15) where they are distinct outliers. Five of six plots show positive correlation, while plot against Cu shows no correlation.

included 11 s background analysis followed by 20-30 s laser ablation time. Hydrogen was used in the collision reaction cell of ICP-MS/MS with a flow of 3.5 L/min to remove polyatomic interferences. Argon was used as dilution and carrier gas in ICP-MS/MS. The instrument was optimized for minimal molecular oxide species (i.e., $^{232}Th^{16}O/^{232}Th < 0.3\%$). Optimization of the instrument was performed by ablating the glass reference NIST612. Two reference materials of MRM MASS-1 from USGS and UQAC-FeS-1 from SLIM were used as calibration standards only.

3. Results

Each of the red sandstone samples processed by acid removal of grain coatings was leached, indicating liberation of iron and associated trace elements to solution. Analysis of the solutions, converted to concentrations of whole rock, confirmed that trace elements had been liberated (Table 1). The absolute blank and procedural blank yielded negligible contents (Table 1). Data for certified reference materials and all standard deviations are given in the Supplementary Information (Table S1). SEM observations confirmed that while iron oxides were removed by acid leaching, the substrate grains remained unaffected. Ranges of elements determined included 0.8 to 135.6 ppm Cu (mean 14.0 ppm, median 6.3 ppm, $n = 37$), 2.2 to 64.7 ppm V (mean 12.0 ppm, median 10.1 ppm, $n = 37$), 0.05 to 1.2 ppm U (mean 0.4 ppm, median 0.3 ppm, $n = 37$), and 0.3 to 7.9 ppm Co (mean 3.1 ppm, median 2.4 ppm, $n = 37$), excluding the copper-mineralized locality at Alderley Edge and the locality at Maghera influenced by soil mineralization. The small set of samples from other countries gave values comparable with those from Britain and Ireland.

The bleached sandstone from Alderley Edge yielded mean acid leach values higher than the red sandstones there. All the values for Cu, Co, and Pb at Alderley Edge are much higher than in other samples. The sandstone from Maghera enriched by soil mineralization contains relatively high levels of V, Co, Cu, Pb, and U. Comparison of the grain size fractions from Gardenstown showed that the composition of the two coarser fractions that were purely sand size was similar, but the finer size fraction that included mud had higher contents of trace elements.

The subset of Permian and Triassic samples measured for both whole rock composition and grain coating leach composition have mean compositions of 11 ppm V and 7.6 ppm V and 6.1 ppm Cu and 5.2 ppm Cu, respectively.

Whole rock Fe contents range up to 4.74%. The contents of V, Co, Se, U, and Pb show moderate positive correlation with Fe content (R^2 values 0.32 to 0.69; Figure 3). There is no correlation between Fe and Cu. Distributions of values within the data set show a bias towards lower values, but in the case of Cu, there is an additional group of higher values (Figure 4).

The LA-ICP-MS maps of a quartz grain with surrounding iron oxide coating in the thin section of red sandstone show a clear contrast between sand grain and grain coating (Figure 5). The grains exhibit negligible (less than 1 ppm) concentrations of V and Co, while the surrounding iron oxide shows V and Co at up to 120 ppm and 60 ppm, respectively.

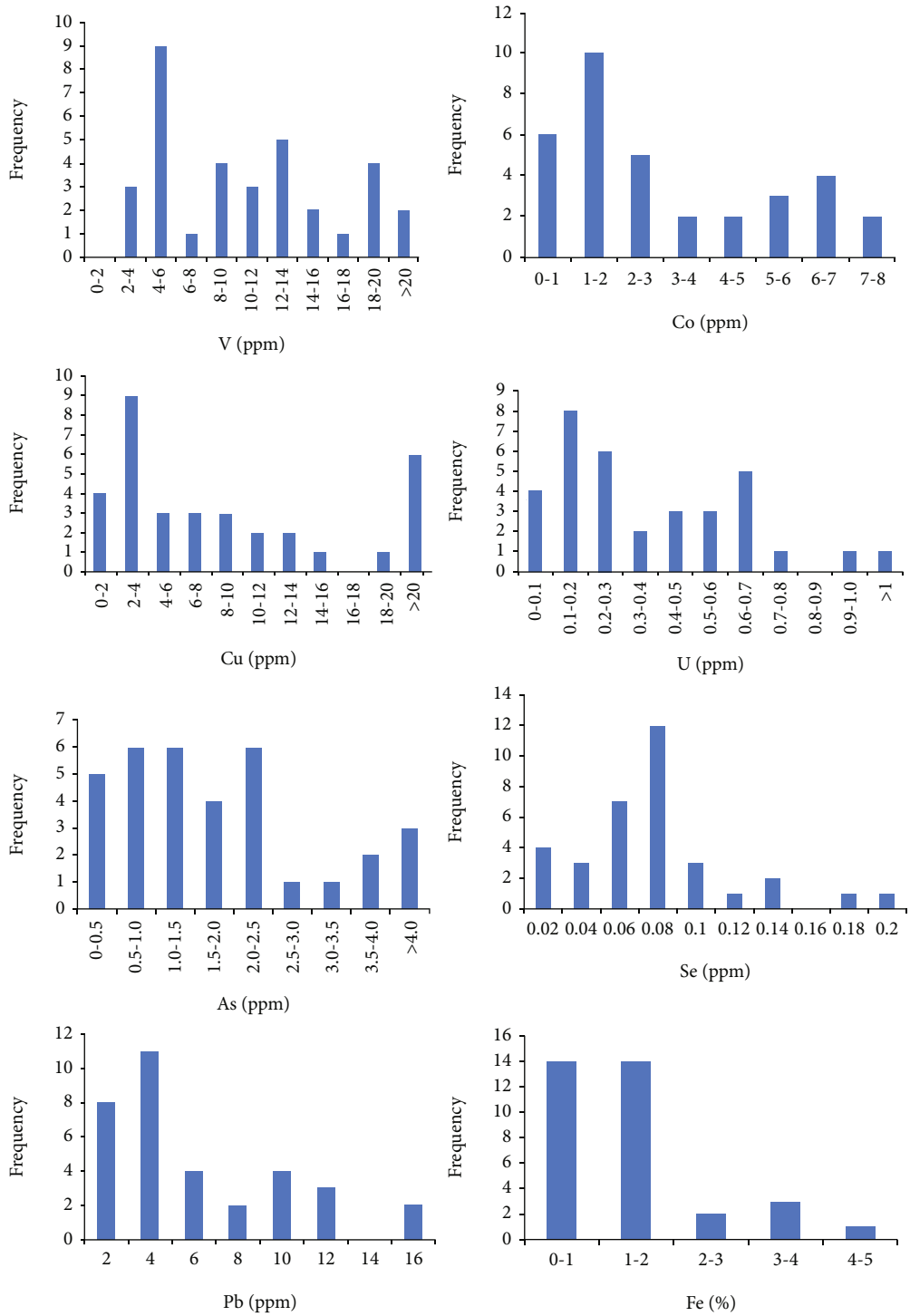

Figure 4: Distribution of values for trace elements and Fe within data set.

4. Discussion

4.1. Compositions of Grain Coatings. Previous proposals of a model of mineralization from leached grain coatings are based on the circumstantial occurrence of bleached sandstones in ore fields [14, 17, 18], distal reprecipitation of leached metals [6, 7], or whole rock data [11]. Measurements of some trace elements in iron oxide grain coatings were made by [33], including U and V and rare earth elements but not Cu, Co, or Se. The data set reported here for grain coatings is more comprehensive than hitherto. Variations in compositions of grain coatings are assessed here in terms of the iron content and the stratigraphic age.

The relatively high values of several metals within the soil-influenced sample from Maghera indicate that enrichment in iron oxides can occur on a geologically short time

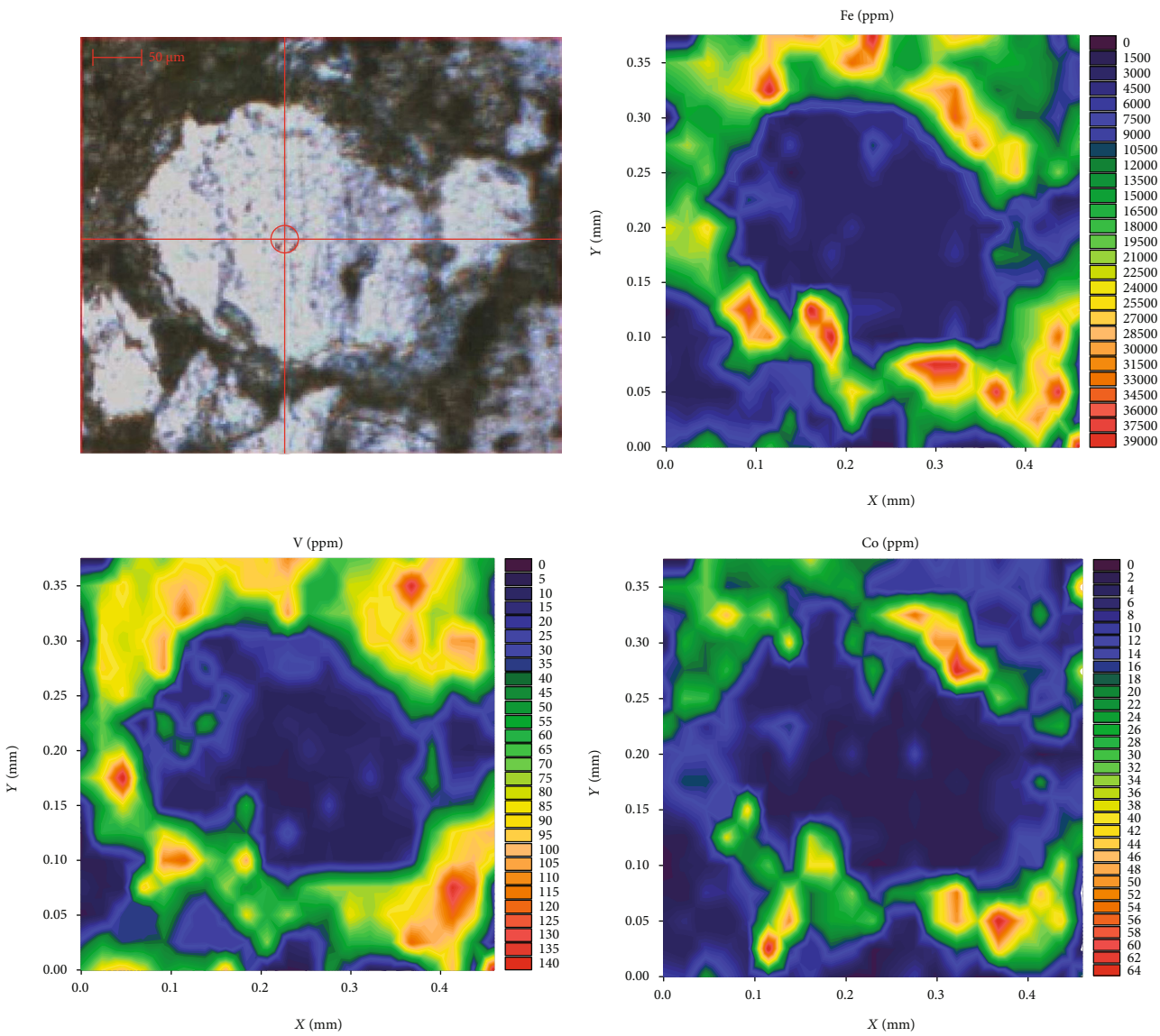

Figure 5: LA-ICP-MS maps for Fe, V, and Co, Triassic sandstone, Lagan Valley borehole 4B, oxide grain coating, marked by very high Fe levels, shows up to 120 ppm V and 60 ppm Co, but negligible contents in the grain.

scale. Similar enrichment at the surface is the basis of mineral exploration using metal anomalies in iron oxide precipitates in the surface environment [34, 35]. The early incorporation of trace elements is consistent with the model for metal release by mineral alteration during early diagenesis [2, 9].

Most sandstones have Fe contents in the range of 0.17 to 4.74% (mean 1.27%). The mean concentrations of aqua regia leachable elements from the unmineralized red sandstones are 14.0 ppm Cu, 12.0 ppm V, 0.4 ppm U, and 3.1 ppm Co. The median values are comparable, except in the case of copper which has a much lower median value of 6.3 ppm. In contrast, the pure quartz sandstone contains negligible contents of iron or trace elements (less than 1% of the mean values). The broad correlation of iron and other metals in the whole rock data (Figure 3) suggests that the residence for much of the trace metal is within the iron oxide grain coatings. This is consistent with the LA-ICP-MS maps, which show trace elements only in the grain coatings and not in the substrate grains. The lack of correlation between Cu and Fe (Figure 3) may reflect the incorporation of Cu into other phases such as aluminosilicates, as observed elsewhere in red sandstones [17, 36].

The measurements made are of metal that is readily leachable from the sandstone, rather than the total metal content of the sandstones. Some metal within detrital grains may not be readily accessible to the leaching fluids, whereas the metal in iron oxide grain coatings is amenable to leaching. However, a comparison of whole rock data and grain coating leach data for a subset of ten red sandstone samples analysed for V and Cu showed that over 70% and 85%, respectively, of the trace elements reside in the grain coatings and is leachable. Notably, the mean values of metals in the grain coatings are not anomalously high compared to typical rock compositions, but the occurrence of the metals in abundant thin coatings makes them relatively available.

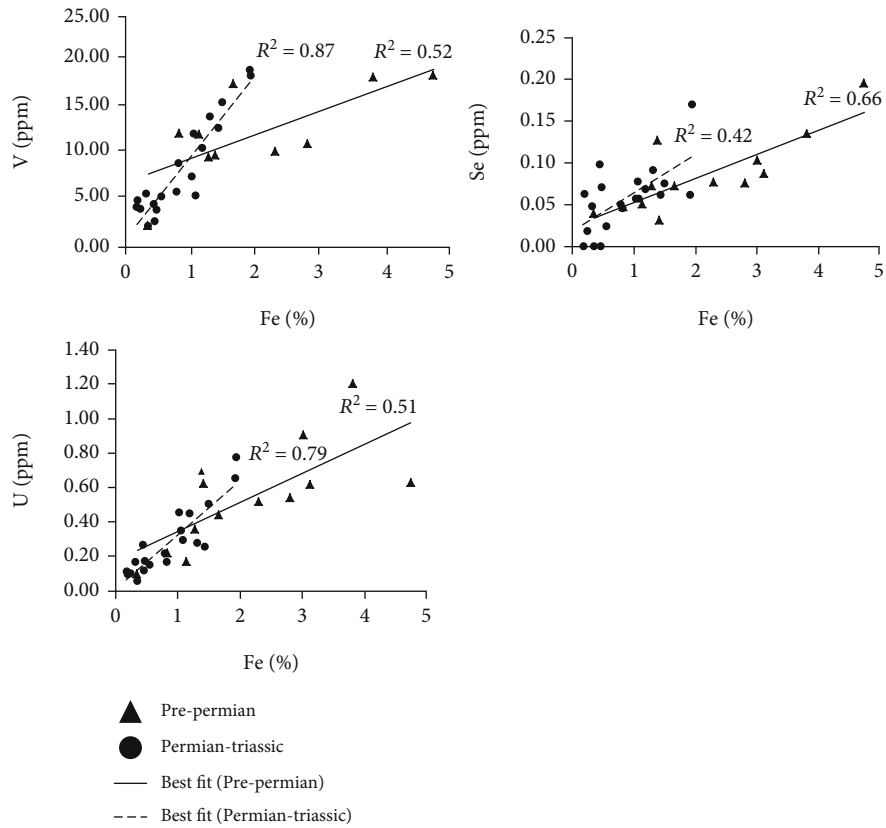

Figure 6: Comparison of acid leach compositions for red sandstones of pre-Permian age and Permian-Triassic age. Higher V values occur in pre-Permian samples. Data for other elements do not show a relationship with stratigraphy. Mineralized samples were omitted.

The aqua regia used to remove the iron oxide grain coatings is a more acidic and oxidizing solvent than would occur in nature, and the dissolution temperature (95°C) in the laboratory is higher, so shows the total potential that can be released, rather than what might be released during a single fluid flow event. Nevertheless, given that ore deposits may form over a period of millions of years (Brown, 2009), the total potential is an appropriate value to measure. Red bed sandstones commonly exhibit zones that are completely bleached, indicating that the iron oxide grain coating is completely removed over time.

Comparison of metal values with stratigraphic age shows that values of V and U are higher in the red sandstones of pre-Permian age than in those of Permian and Triassic age (Figures 6 and 7). The mean values for V are 17.7 ppm ($n = 13$) and 6.7 ($n = 21$), respectively. The mean values for U are 0.54 and 0.28, respectively. In contrast, values for the other elements show no relationship with stratigraphic age. The range of pre-Permian values for Cu is greater than for Permo-Triassic values, but the mean values are similar (Figure 7). The pre-Permian samples are mostly from northern Britain, where the provenance is in the Caledonide basement and sandstones represent first cycle erosion. They are therefore more likely to contain mineralogically immature grains than the Permo-Triassic sandstones which are commonly derived from multiple cycles of erosion, especially the aeolian Permian sandstones. The immature grains would have yielded trace metals during diagenetic alteration, whereas quartz-rich sandstones have much less potential. However, the higher contents in pre-Permian sandstones also reflect higher Fe contents (Figure 6). In fact, the V/Fe, Se/Fe, and U/Fe ratios are lower in the pre-Permian samples. The lower ratios in older sandstones could indicate that some of the trace elements have been released from the grain coatings, at a higher thermal maturity than in the younger sandstones. With thermal maturation, the crystallinity of haematite increases [37], and the capacity to adsorb trace metals would decrease with recrystallization [38], although changes in surface area during alteration could complicate the effect on adsorption. The contrast with age may be more evident in the case of V, Se, and U because of very ready redox-controlled mobility [39, 40], which is also evident in the predominance of these elements in diagenetic reduction spheroids [41, 42]. On the other hand, vanadian haematite containing percent level V is identified in some ore deposits, so this can occur as a stable phase [43, 44].

4.2. Ore Fluids. These measurements allow us to calculate the volume of rock required to supply metal to a large ore deposit (Table 2). For a sandstone of density $2.5.10^3$ kgm^{-3} (values typically range from 2.2 to $2.8.10^3$ kgm^{-3}), a metal availability of 10 ppm equates to 1 kg of metal from 40 m^3 (1 Mt from 40 km^3) or 2.5 kg of metal from 100 m^3 (2.5. 10^4 tonnes from 1 km^3) rock. Aquifer volumes for Triassic red beds, measured for potential CO_2 storage, range from hundreds to thousands of km^3 [45–47]. For 10 ppm metal availability, an aquifer of

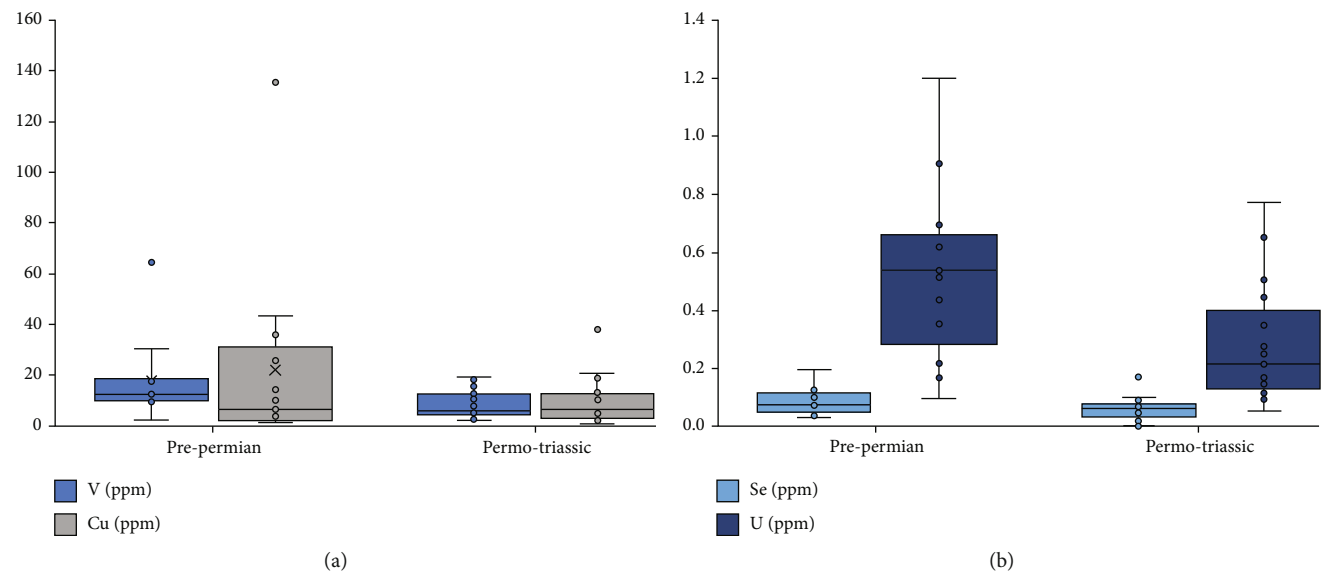

Figure 7: Box-and-whisker plots for V, Cu, Se, and U values in pre-Permian and Permo-Triassic values. Data show higher Permian samples.

Table 2: Metal availability from grain coatings relative to requirements for ore deposits.

Element	Median available (ppm)	Size most sandstone-hosted ore deposits	Available metal in 10^3 km^3	% of available metal in 10^3 km^3 needed for ore deposits	Aquifer volume needed for ore deposits
Cu	6.29	Mean 22 Mt; many 1 Mt	15.73 Mt	140% for 22 Mt 6% for 1 Mt	1399 km^3 for 22 Mt 64 km^3 for 1 Mt
U	0.28	0.1 to 10 kt	0.7 Mt	0.01 to 1.4%	0.1 to 14 km^3
V	10.07	1 to 100 kt	25.2 Mt	0.004 to 0.4%	0.04 to 4 km^3
Co	2.35	5 to 500 kt (all ores)	5.88 Mt	0.09 to 8.5%	0.9 to 85 km^3

10^3 km^3 would yield 25 Mt metal. The measured median 6.3 ppm Cu available would yield 15.7 Mt in 10^3 km^3. To put these values in context, the Cu resources in the world-class Chu-Sarysa Basin, Kazakhstan, consist of a huge 22 Mt deposit and smaller deposits of about 1 Mt [14]. The mean size of sediment-hosted Cu deposits is also 22 Mt [48], equivalent to 140% of the Cu available in 10^3 km^3. Previous calculations for the Triassic red beds of central England concluded that 1 ppm Cu from 340 km^3 could yield over 0.8 Mt Cu [49], and 2 ppm Cu from 3300 km^3 Triassic sandstone could yield 15 Mt Cu [50].

Most sandstone-hosted U deposits contain 0.1 to 10 kt U [51]. This represents 0.01 to 1.4% of the U available from 10^3 km^3 (Table 2). Most sandstone-hosted V deposits contain 1 to 100 kt V [52], which would require 0.004 to 0.4% of the V available from 10^3 km^3 (Table 2). Most types of Co deposit contain 5 to 500 kt Co [53], requiring 0.09 to 8.5% of the Co that could be released in 10^3 km^3.

The data for red and bleached sandstones at Alderley Edge, where Cu mineralization is attributed to the dissolution of grain coatings by reducing brines including hydrocarbons [30, 50], show variable patterns for different elements. The bleached sandstones have lower values of V and Co, but much higher values of Cu, As, and Pb. However, the high Cu values in the bleached sandstones indicate that the Cu was not exported from the system and has another residence. The bleached sandstones have a lower iron content, but they contain a range of secondary Cu minerals [29]. The lower values of V, at least, might reflect uptake by migrating hydrocarbons.

Multiple factors will control metal release, including pH, Eh, temperature, and pore fluid chemistry [10]. The model considered here envisages the dissolution of grain coatings by acidic fluids, particularly migrating oil and gas. Large-scale hydrocarbon migration, evidenced by widespread oil residues, therefore, contributes to the exploration for sandstone-hosted ore deposits [16, 17]. Most oil is generated <130°C, and it is likely that related removal of iron oxide grain coatings occurs at shallower depths and lower temperatures. This implies the removal of coatings and liberation of trace metals at depths of less than 4 km. At these depths, there is still adequate porosity (typically up to 10%) to allow intergranular fluid flow through sandstones and export of diagenetic alteration products.

The compositions of the grain coatings measured here are unexceptional, because the sandstones did not have a known provenance in preexisting metalliferous ore deposits. If the sand and/or grain coating was derived from a metal-rich source, red beds could be preloaded with metal that could more readily be leached to form an ore deposit. This is most likely where sand was eroded from an orogenic belt, in which metalliferous phases had been unroofed following

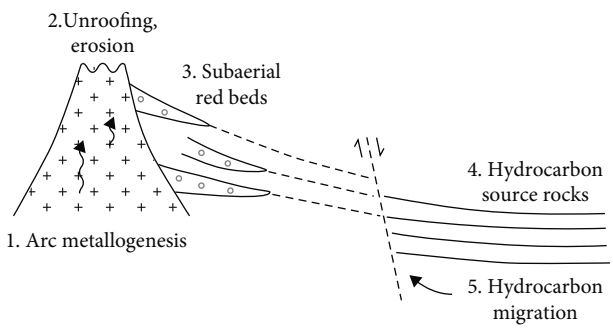

Figure 8: Schematic evolution of red bed ore deposit by erosion of magmatic arc rocks into red beds, followed by hydrocarbon migration through red beds to concentrate metals from metal-bearing grain coatings.

uplift. In this way, arc-based deposits such as Cu porphyries, V-rich magnetite, and Se-rich volcanic soils could be recycled into sandstone ore feedstock. A mineralized plate margin mountain chain with subaerial erosion products (red beds) and a foreland basin (potential hydrocarbon source rocks) could provide a scenario where hydrocarbons strip enriched grain coatings from the red beds to create an ore fluid (Figure 8). For example, in the Tethyan region (Iran, Iraq, and adjacent areas), where red bed-hosted copper deposits are widespread [15], the Zagros and other orogenic mountain chains are fringed by red beds and hydrocarbon sources. In the Andes, copper mineralization in red beds has been attributed to the unroofing of arc volcanics [54]. Examples like these could be tested by mass balance studies of metals in source regions and ore deposits. In particular, the alteration of titanomagnetite is a suggested source of metals in red bed deposits [55], and there is evidence of such alteration in mineralized red beds [54, 56] which could be quantified. In the Andes, the magnetite in volcanic rocks is rich in vanadium [57], altered magnetite in the volcanic rocks shows the release of vanadium [58], and red beds are rich in magnetite grains [59], suggesting that this region would make a good case study. While the vanadium in titanomagnetite ores can be processed and reprecipitated by microbes in the soil zone (e.g., [60, 61]), the contribution of microbial activity in the whole mineralization cycle has yet to be evaluated.

4.3. Limitations to Leaching Model. This study focused on red sandstones, as sandstones are potential aquifers for fluid flow and diagenetic reactions including dissolution of grain coatings. Red mudstones may contain higher contents of iron oxides and associated trace metals [50], as shown by the data from different grain size fractions at Gardenstown. Some trace metals in mudstones would be released into compactional brines, but they are not commonly pathways for the hydrocarbon migration envisaged to leach iron oxides from red sandstones. An exception is in mudstones which show evidence for overpressuring, which allows the flow of brines and hydrocarbons along bedding planes, a circumstance that may be promoted by impermeable evaporite beds that occur in some red bed sequences.

Leaching data reported by [8] are based largely on very young mudrocks of Holocene-Pliocene age in which the iron oxide crystallinity was not fully developed and allowed element liberation more readily than from fully crystalline oxides. Their data are nonetheless interesting in indicating a relative ease of leaching in which Co > Cu > Fe > U > V. The relatively high availability of Cu recorded in the present study and by [8] may partially reflect the high adsorption (log K values) of copper onto iron oxides [62, 63]. V and U (and Se) might be harder to desorb if initially adsorbed as oxyanions [63]. A calculation based on leaching data for zinc in the red mudrocks concluded a volume of $6.10^4\,km^3$ rock was required to source a sedex deposit [8, 64], at least an order of magnitude more than the volume required to source a large copper deposit. The contrast in volumes required may reflect differential adsorption of the elements onto iron oxide [62, 63], whereby copper outcompetes zinc for adsorption, and consequently, desorption occurs at greater rates and possibly under different pH conditions.

Bleached sandstones at Alderley Edge locally contain secondary Cu minerals, indicating that leached metals are not necessarily exported from the system but may be reprecipitated by variable redox conditions. This is borne out by the high Cu contents in the bleached samples at Alderley Edge. This difference in mobility may also contribute to the poor correlation of Cu and Fe contents. Copper accumulation in bleached facies has similarly been observed in the Kupferschiefer [65], and it is evident as metal-enriched cores in reduction spheroids in many red beds [42]. The potential for leaching to create an ore-forming fluid clearly requires a sedimentary basin scale and fluid flow system that are large enough to allow continued, cumulative transport of metals.

5. Conclusions

Measurement of trace elements resident in iron oxide grain coatings in red sandstones confirmed that they are a source of metals during diagenetic dissolution. In particular

(i) They represent a significant proportion of the metals available from the sandstones to ore-forming fluids

(ii) The quantities of metal in the grain coatings are adequate to form sandstone-hosted ore bodies. Only small proportions of available metal would be required to form U, V, and Co deposits, but the available Cu is still adequate to form moderate-size ore bodies if the process is efficient

(iii) A broad correlation between Fe content and the content of most trace metals confirms the predominant residence of the trace elements in the grain coatings, and hence, their availability to ore fluids

Future research should explore basins where red sandstones have a provenance which includes anomalous metal concentrations, for example, sandstones containing erosion products of mineralized granites or arc volcanics.

Data Availability

The manuscript is a data self-contained article, whose results were obtained from the laboratory analysis, and the entire data are presented within the article. However, if any additional information is required, these are available from the corresponding author upon request to the e-mail j.parnell@abdn.ac.uk.

Conflicts of Interest

The authors declare that they have no known competing financial interests or personal relationships that could have appeared to influence the work reported in this paper.

Acknowledgments

The paper benefitted from constructive reviews by anonymous referees, for which we are very grateful. Sandstone samples were kindly contributed by the Geological Survey of Northern Ireland, D. Halbert, R. Starkey, and L. Bullock. This work was partly supported by NERC grants NE/M010953/1 and NE/T003677/1. Electron Microscopy was performed with the help of J. Still in the ACEMAC Facility at the University of Aberdeen. We thank Teledyne-CETAC for the loan of the laser ablation system LSX-213 and support during the measurements.

Supplementary Materials

Table S1: compositions of grain coatings, with standard deviations, and data for certified reference materials. *(Supplementary Materials)*

References

[1] I. McDonald, A. J. Boyce, and I. B. Butler, *Mineral Deposits and Earth Evolution*, Geological Society of London, 2005.

[2] T. R. Walker, B. Waugh, and A. J. Crone, "Diagenesis in first-cycle desert alluvium of Cenozoic age, southwestern United States and northwestern Mexico," *Geological Society of America Bulletin*, vol. 89, no. 1, pp. 19–32, 1978.

[3] M. M. Benjamin, R. S. Sletten, R. P. Bailey, and T. Bennett, "Sorption and filtration of metals using iron-oxide-coated sand," *Water Research*, vol. 30, no. 11, pp. 2609–2620, 1996.

[4] R. C. Surdam, Z. S. Jiao, and D. B. MacGowan, "Redox reactions involving hydrocarbons and mineral oxidants: a mechanism for significant porosity enhancement in sandstones," *AAPG Bulletin*, vol. 77, pp. 1509–1518, 1993.

[5] W. T. Parry, M. A. Chan, and B. P. Nash, "Diagenetic characteristics of the Jurassic Navajo sandstone in the covenant oil field, Central Utah thrust belt," *American Association of Petroleum Geologists Bulletin*, vol. 93, no. 8, pp. 1039–1061, 2009.

[6] M. Wigley, N. Kampman, B. Dubacq, and M. Bickle, "Fluid-mineral reactions and trace metal mobilization in an exhumed natural CO2 reservoir, Green River, Utah," *Geology*, vol. 40, no. 6, pp. 555–558, 2012.

[7] M. Wigley, N. Kampman, H. J. Chapman, B. Dubacq, and M. J. Bickle, "In situ redeposition of trace metals mobilized by CO2-charged brines," *Geochemistry Geophysics Geosystems*, vol. 14, no. 5, pp. 1321–1332, 2013.

[8] R. A. Zielinkski, S. Bloch, and T. R. Walker, "The mobility and distribution of heavy metals during the formation of first cycle red beds," *Economic Geology*, vol. 78, no. 8, pp. 1574–1589, 1983.

[9] T. R. Walker, "Application of diagenetic alterations in red beds to the origin of copper in stratiform copper deposits," *Geological Association of Canada Special Paper*, vol. 36, pp. 85–96, 1989.

[10] A. W. Rose and G. C. Bianchi-Mosquera, "Adsorption of Cu, Pb, Zn, Co, Ni, and Ag on goethite and hematite: a control on metal mobilization from red beds into stratiform copper deposits," *Economic Geology*, vol. 88, no. 5, pp. 1226–1236, 1993.

[11] R. Metcalfe, C. A. Rochelle, D. Savage, and J. W. Higgo, "Fluid-rock interactions during continental red bed diagenesis: implications for theoretical models of mineralization in sedimentary basins," *Geological Society, London, Special Publications*, vol. 78, no. 1, pp. 301–324, 1994.

[12] A. C. Brown, "A process-based approach to estimating the copper derived from red beds in the sediment-hosted stratiform copper deposit model," *Economic Geology*, vol. 104, no. 6, pp. 857–868, 2009.

[13] P. M. Cossette, A. A. Bookstrom, T. S. Hayes, G. R. Robinson, J. C. Wallis, and M. L. Zientek, *Sandstone Copper Assessment of the Teniz Basin, Kazakhstan*, United States Geological Survey Scientific Investigations Report, 2010.

[14] S. E. Box, B. Syusyura, R. Seltmann, R. A. Creaser, A. Dolgopolova, and M. L. Zientek, "Dzhezkazgan and associated sandstone copper deposits of the Chu-Sarysa Basin, Central Kazakhstan," *Society of Economic Geologists Special Publication*, vol. 16, pp. 303–328, 2012.

[15] S. Maghfouri, E. Rastad, G. Borg et al., "Metallogeny and temporal–spatial distribution of sediment-hosted stratabound copper (SSC-type) deposits in Iran; implications for future exploration," *Ore Geology Reviews*, vol. 127, p. 103834, 2020.

[16] S. Jaireth, A. McKay, and I. Lambert, "Association of large sandstone uranium deposits with hydrocarbons," *AusGeo News*, vol. 89, no. 6, pp. 1–6, 2008.

[17] A. L. Rainoldi, M. Franchini, D. Beaufort et al., "Large-scale bleaching of red beds related to upward migration of hydrocarbons: Los Chihuidos High, Neuquen Basin, Argentina," *Journal of Sedimentary Research*, vol. 84, no. 5, pp. 373–393, 2014.

[18] A. L. Rainoldi, M. B. Franchini, A. J. Boyce et al., "Stable isotope and fluid inclusion study of sediment-hosted stratiform copper deposits from the Neuquén Basin, Argentina," *Mineralium Deposita*, vol. 54, no. 3, pp. 415–436, 2019.

[19] A. L. Rainoldi, D. Beaufort, P. Patrier, A. Giusiano, M. J. Pons, and N. Cesaretti, "Vanadium mineralization at Los Chihuidos sediment-hosted stratiform Cu deposit," in *Proceedings of the 15th Quadrennial IAGOD Symposium*, pp. 355-356, Salta, Argentina, 2018.

[20] J. Mathieu, E. C. Turner, D. J. Kontak, M. Fayek, and R. Mathur, "Atypical Cu mineralisation in the Cornwallis carbonate-hosted Zn district: storm copper deposit, Arctic Canada," *Ore Geology Reviews*, vol. 99, pp. 86–115, 2018.

[21] J. G. Hinchey, "Neoproterozoic sedimentary-hosted 'stratiform' copper mineralization – Bonavista Peninsula, Avalon Zone, Newfoundland: initial field and petrographic observations," *Current Research. Newfoundland and Labrador Department of Natural Resources, Geological Survey*, vol. 2010, pp. 1–21, 2010.

[22] R. Gao, C. Xue, X. Zhao, X. Chen, Z. Li, and D. Symons, "Source and possible leaching process of ore metals in the Uragen sandstone- hosted Zn-Pb deposit, Xinjiang, China: Constraints from lead isotopes and rare earth elements geochemistry," *Ore Geology Reviews*, vol. 106, pp. 56–78, 2019.

[23] B. Wu, G. Zheng, A. Zhang et al., "The different characteristics and geological significance of reduction alteration of sandstone-type uranium deposits in northwest region of China," *Energy Exploration & Exploitation*, vol. 27, no. 4, pp. 261–275, 2009.

[24] H. Chu, G. Chi, S. Bosman, and C. Card, "Diagenetic and geochemical studies of sandstones from drill core DV10-001 in the Athabasca basin, Canada, and implications for uranium mineralization," *Journal of Geochemical Exploration*, vol. 148, pp. 206–230, 2015.

[25] P. Turner, *Continental Red Beds*, Elsevier, Amsterdam, UK, 1980.

[26] J. Parnell, S. Spinks, and C. Brolly, "Tellurium and selenium in Mesoproterozoic red beds," *Precambrian Research*, vol. 305, pp. 145–150, 2018.

[27] W. H. Wang, "Origin of reddening and secondary porosity in Carboniferous sandstones, Northern Ireland," *Geological Society Special Publication*, vol. 62, no. 1, pp. 243–254, 1992.

[28] D. Richter, "On the new red sandstone neptunian dykes of the Tor Bay Area (Devonshire)," *Proceedings of the Geologists Association*, vol. 77, no. 2, pp. 173–IN3, 1966.

[29] R. A. Ixer and D. J. Vaughan, "The primary ore mineralogy of the Alderley Edge deposit, Cheshire," *Mineralogical Magazine*, vol. 46, no. 341, pp. 485–492, 1982.

[30] J. Rowe and S. D. Burley, "Faulting and porosity modification in the Sherwood Sandstone at Alderley Edge, northeastern Cheshire: an exhumed example of fault-related diagenesis," *Geological Society Special Publication*, vol. 124, no. 1, pp. 325–352, 1997.

[31] J.-H. Choi, J.-S. Ryu, H. S. Shin, J. Kim, and C.-s. Cheong, "Reevaluation of Th and U concentrations in marine sediment reference materials using isotope dilution MC-ICP-MS: towards the analytical improvements in dose rate estimation for luminescence dating," *Geosciences Journal*, vol. 17, no. 2, pp. 123–127, 2013.

[32] H. L. Byers, L. J. McHenry, and T. J. Grundl, "Forty-nine major and trace element concentrations measured in soil reference materials NIST SRM 2586, 2587, 2709a, 2710a and 2711a using ICP-MS and wavelength dispersive-XRF," *Geostandards and Geoanalytical Research*, vol. 40, pp. 443–455, 2016.

[33] M. R. Cave and K. Harmon, "Determination of trace metal distributions in the iron oxide phases of red bed sandstones by chemometric analysis of whole rock and selective leachate data," *Analyst*, vol. 122, no. 6, pp. 501–512, 1997.

[34] S. R. Huelin, H. P. Longerich, D. H. C. Wilton, and B. J. Fryer, "The determination of trace elements in Fe-Mn oxide coatings on pebbles using LA-ICP-MS," *Journal of Geochemical Exploration*, vol. 91, no. 1-3, pp. 110–124, 2006.

[35] A. Schmidt Mumm, R. C. Dart, and P. Say, "Hematite/maghemite trace element geochemistry in base metal exploration," *Journal of Geochemical Exploration*, vol. 124, pp. 239–251, 2013.

[36] M. B. Goldhaber, R. L. Reynolds, J. A. Campbell, R. B. Wanty, R. I. Grauch, and R. Northrop, "Mechanism of ore and gangue mineral formation at the interface between brine and meteoric water," *Economic Geology*, vol. 85, pp. 236–250, 1990.

[37] W. R. Fischer and U. Schwertmann, "The formation of hematite from amorphous iron (III) hydroxide," *Clays and Clay Minerals*, vol. 23, no. 1, pp. 33–37, 1975.

[38] A. J. Frierdich, Y. Luo, and J. G. Catalano, "Trace element cycling through iron oxide minerals during redox-driven dynamic recrystallization," *Geology*, vol. 39, no. 11, pp. 1083–1086, 2011.

[39] T. Schirmer, A. Koschinsky, and M. Bau, "The ratio of tellurium and selenium in geological material as a possible paleoredox proxy," *Chemical Geology*, vol. 376, pp. 44–51, 2014.

[40] J. P. Gustafsson, "Vanadium geochemistry in the biogeosphere – speciation, solid-solution interactions, and ecotoxicity," *Applied Geochemistry*, vol. 102, pp. 1–25, 2019.

[41] M. Van Panhuys-Sigler, N. H. Trewin, and J. Still, "Roscoelite associated with reduction spots in Devonian red beds, Gamrie Bay, Banffshire," *Scottish Journal of Geology*, vol. 32, no. 2, pp. 127–132, 1996.

[42] J. Parnell, S. Spinks, and D. Bellis, "Low-temperature concentration of tellurium and gold in continental red bed successions," *Terra Nova*, vol. 28, no. 3, pp. 221–227, 2016.

[43] A. J. Urban, B. F. Hoskins, and I. E. Grey, "Characterization of V-Sb-W-bearing rutile from the Hemlo gold deposit, Ontario," *Canadian Mineralogist*, vol. 30, pp. 319–326, 1992.

[44] A. V. Boitsov, "The mineral composition and the ore types of the uranium-vanadium deposit Srednaya Padma (Onega Region, Russian Federation)," in *Technical Committee Meeting on Changes and Events in Uranium Deposit Development, Exploration, Resources, Production and the World Supply-Demand Relationship*, pp. 259–269, IANA, Veinna, Austria, 1997.

[45] D. J. Noy, S. Holloway, R. A. Chadwick, J. D. O. Williams, S. A. Hannis, and R. W. Lahann, "Modelling large-scale carbon dioxide injection into the Bunter Sandstone in the UK Southern North Sea," *International Journal of Greenhouse Gas Control*, vol. 9, pp. 220–233, 2012.

[46] J. D. O. Williams, M. Bentham, M. Jin et al., "The effect of geological structure and heterogeneity on CO2 storage in simple 4-way dip structures; a modeling study from the UK Southern North Sea," *Energy Procedia*, vol. 37, pp. 3980–3988, 2013.

[47] S. Thibeau, S. Bachu, J. Birkholzer, S. Holloway, F. Neele, and Q. Zhou, "Using pressure and volumetric approaches to estimate CO2 storage capacity in deep saline aquifers," *Energy Procedia*, vol. 63, pp. 5294–5304, 2014.

[48] D. L. Mosier, D. A. Singer, and D. P. Cox, "Grade and tonnage model of sediment-hosted Cu," in *Mineral Deposit Models*, D. P. Cox and D. A. Singer, Eds., vol. 1693, pp. 206–208, U.S. Geological Survey Bulletin, 1992.

[49] I. Holmes, A. D. Chambers, R. D. Ixer, P. Turner, and D. J. Vaughan, "Diagenetic processes and the mineralization in the Triassic of Central England," *Mineralium Deposita*, vol. 18, pp. 365–377, 1983.

[50] J. A. Plant, D. G. Jones, and H. W. Haslam, *The Cheshire Basin – Basin Evolution, Fluid Movement and Mineral Resources in a Permo-Triassic Rift Setting*, British Geological Survey, Keyworth, UK, 2000.

[51] S. Thakur, B. Chudasama, and A. Porwal, "Global grade-and-tonnage modeling of uranium deposits," in *Quantitative and Spatial Evaluations of Undiscovered Uranium Resources (IAEA-TECDOC-1861)*, pp. 226–272, International Atomic Energy Agency, Vienna, Austria, 2018.

[52] K. D. Kelley, C. T. Scott, D. E. Polyak, and B. E. Kimball, "Vanadium," in *Critical Mineral Resources of the United States – Economic and Environmental Geology and Prospects for Future Supply*, K. J. Schulz, J. H. DeYoung, R. R. Seal, and D. C. Bradley, Eds., pp. U1–U36, U.S. Geological Survey Professional Paper, 2017.

[53] J. F. Slack, B. E. Kimball, and K. B. Shedd, *Cobalt*, United State Geological Survey Professional Paper, 2017.

[54] S. Flint, H. Clemmey, and P. Turner, "Conglomerate-hosted copper mineralization in cretaceous Andean molasse: the Coloso Formation of northern Chile," *Geological Magazine*, vol. 123, no. 5, pp. 525–536, 1986.

[55] R. L. Reynolds and M. B. Goldhaber, "Origin of a South Texas roll-type uranium deposit: I. Alteration of iron-titanium oxide minerals," *Economic Geology*, vol. 73, no. 8, pp. 1677–1689, 1978.

[56] R. Weibel and H. Friis, "Opaque minerals as keys for distinguishing oxidising and reducing diagenetic conditions in the Lower Triassic Bunter Sandstone, North German Basin," *Sedimentary Geology*, vol. 169, no. 3-4, pp. 129–149, 2004.

[57] S. A. S. Dare, S.-J. Barnes, G. Beaudoin, J. Méric, E. Boutroy, and C. Potvin-Doucet, "Trace elements in magnetite as petrogenetic indicators," *Mineralium Deposita*, vol. 49, no. 7, pp. 785–796, 2014.

[58] K. Uchida, "Minor elements of magnetite in unaltered and altered host rocks of Michiquillay porphyry copper deposit," *Peru. Mining Geology*, vol. 26, pp. 153–163, 1976.

[59] P. Roperch, C. Arriagada, A. Chauvin, and V. Carlotto, *Tectonic Imprint in Magnetic Fabrics in Sediments from the Central Andes*, AGU Spring Meeting Abstracts, 2009.

[60] L. Hao, B. Zhang, C. Feng et al., "Microbial vanadium (V) reduction in groundwater with different soils from vanadium ore mining areas," *Chemosphere*, vol. 202, pp. 272–279, 2018.

[61] B. Zhang, S. Wang, M. Diao et al., "Microbial community responses to vanadium distributions in mining geological environments and bioremediation assessment," *Journal of Geophysical Research: Biogeosciences*, vol. 124, no. 3, pp. 601–615, 2019.

[62] D. A. Dzombak and F. M. M. Morel, *Surface Complexation Modeling: Hydrous Ferric Oxide*, John Wiley & Sons, New York, NY, USA, 1990.

[63] S. S. Mathur and D. A. Dzombak, "Surface complexation modeling: goethite," in *Surface Complexation Modeling*, J. Lützenkirchen, Ed., pp. 443–468, Elsevier, Amsterdam, UK, 2006.

[64] P. Emsbo, R. R. Seal, G. N. Breit, S. F. Diehl, and A. K. Shah, *Sedimentary Exhalative (sedex) Zinc-Lead-Silver Deposit Model*, pp. 1–57, U.S. Geological Survey, Scientific Investigations Report 2010-5070-N, 2016.

[65] S. Oszczepalski, "Origin of the Kupferschiefer polymetallic mineralization in Poland," *Mineralium Deposita*, vol. 34, no. 5-6, pp. 599–613, 1999.

Hindawi
Geofluids
Volume 2021, Article ID 5598069, 17 pages
https://doi.org/10.1155/2021/5598069

Research Article

Coupling Relationship between Multistage Fluid Activity and Reservoir Abnormally High-Porosity Zones in the Songtao–Baodao Region, Qiongdongnan Basin

Xu Chen,[1,2,3] **Yao Wang**,[4] **and Ao Su**[2,3]

[1]*Cooperative Innovation Center of Unconventional Oil and Gas (Ministry of Education & Hubei Province), Yangtze University, Wuhan 430100, China*
[2]*Key Laboratory of Exploration Technologies for Oil and Gas Resources, Ministry of Education, Yangtze University, Wuhan 430100, China*
[3]*School of Geoscience, Yangtze University, Wuhan 430100, China*
[4]*School of Advanced Manufacturing Engineering, Chongqing University of Posts and Telecommunications, Chongqing 400065, China*

Correspondence should be addressed to Ao Su; suao446@163.com

Received 20 January 2021; Revised 6 April 2021; Accepted 26 April 2021; Published 17 May 2021

Academic Editor: Rongxi Li

An abnormally high-porosity zone (AHPZ) is beneficial for petroleum exploration, especially for the deep tight reservoirs in a petroliferous basin. Because of lacking effective research methods, it is hard to analyze the formation process of AHPZs in different geological periods. From the perspective of the diagenetic fluid type and activity history, geochemical characteristics and fluid inclusions of diagenetic minerals were utilized to reconstruct the diagenetic fluid type and dynamic evolution. The ultimate goal is to study the genetic process of AHPZs in the Songtao–Baodao region of the Qiongdongnan basin, South China Sea. It was found that there are three sections of AHPZs at different burial depths, which are generally favorable for high-quality reservoirs. Moreover, it can be concluded that the AHPZs are closely related to multiple actions of various diagenetic fluids. The meteoric waters, organic acid, and thermal fluids facilitated the enlargement of porosity by dissolving minerals to form secondary pore spaces. The hydrocarbon fluids have positive effects on the preservation of pores by preventing cement from filling the pore space.

1. Introduction

The development of abnormally high-porosity zones (AHPZs) in sedimentary basins has always been an important topic, which is of great significance for high-quality reservoir predictions and commercial oil-gas exploration [1]. Main mechanisms for the formation of AHPZs commonly include sedimentation, grain coat, hydrocarbon filling, overpressure, and dissolution [2, 3]. Sedimentation can control original physical properties of the sandstone reservoir. In other words, the reservoir physical properties are closely related to the sedimentary environment. In addition, sedimentation also affects diagenetic alternation. For example, sandbody that contains high content of rigid particles, few argillaceous impurities, and coarser grain generally has a strong resistance to compaction during burial, thereby preserving more pores at the same burial depth. The cementation is generally weak in the middle of thick sandbody, and the pore is relatively well preserved [4]. Grain coat grows outward from the surface of skeleton grains. It can hinder the development of quartz cements and enable the pores to be effectively preserved in the middle-deep reservoirs [5]. During reservoir diagenesis, early hydrocarbon filling can hinder the flow of pore waters and cause ion supply and flow barriers, which would inhibit or even stop the precipitation of authigenic cements and thus effectively preserve the reservoir pore [6]. An important function of fluid overpressure is to reduce the effective stress on the formation. Effective stress is an important factor controlling the compaction of

clastic rock, so fluid overpressure can inhibit the compaction, which is beneficial to the preservation of reservoir space [7, 8].

The contribution of dissolution to an abnormally high-porosity zone lies in the dissolution of unstable minerals and the formation of additional secondary pores [9]. The geological factors controlling the AHPZ development are closely associated with the types and activities of diagenetic fluids [10]. The physical and chemical properties (such as acid, alkali, temperature, pressure, and components) of the fluid affect the reservoir diagenesis and control fluid-rock interaction. The fluids affecting the reservoir can be divided into organic and carbonic acid fluids [11, 12], meteoric water [13, 14], thermal fluids [15], H_2S generated by thermochemical sulfate reduction (TSR) [16], H^+ released by clay mineral conversion [17], acid generated by biodegradable hydrocarbons [18], and alkaline fluids [19]. Most AHPZs that developed in sedimentary basins are the result of the comprehensive superposition of different factors. Therefore, the analysis of the diagenetic pore fluid type and the evolution of the AHPZs in different geological periods are difficult to analyze and often ignored by scholars. Therefore, the key to better understanding AHPZ genesis is to clarify the fluid types and their large-scale activity in the geological periods. Because of the difference in source rock types, transport systems, thermal-burial-tectonic history, and hydrocarbon migration, the diagenetic fluid types and effective activity periods are different, which have a large influence on the lateral and vertical distributions of AHPZs.

The Qiongdongnan basin is one of the most important oil-bearing basins in the South China Sea. At present, there are few wells in the eastern part of the basin, and the degree of oil-gas exploration is low. There are few reports on the formation of AHPZ in this area. In terms of sedimentary facies and environment, previous authors have analyzed the good physical properties of a deep braided river reservoir [20, 21]. The high content of quartz in sandstone has a stronger compressive ability during compaction of the overburden strata; hence, the reservoir retains more pores [22]. In addition, compaction and cementation reduce reservoir porosity, and dissolution of silicate minerals such as feldspar and rock debris plays a constructive role in reservoirs with abnormally high porosity [22, 23]. The previous studies have not systematically analyzed the causes and distribution of AHPZ, which restricts the understanding of high-quality reservoir exploration. Based on the analysis of diagenetic fluid type and activity history, this study discusses the multistage dynamic evolution process of the abnormally high-porosity zone in the study area, which is of valuable and practical significance for high-quality reservoir exploration.

2. Geological Setting

The Qiongdongnan basin is located in the northwest continental margin of the South China Sea, covering an area of about 6.3×10^4 km^2. It is an extensional basin on the continental margin. Generally, this basin experienced two tectonic evolutionary stages: (1) the rift stage, from the Late Oligocene to Paleocene; (2) the depression stage, from the Miocene to Present [24]. It suffered from four successive tectonic episodes, including the Shenhu, Zhujiang, Nanhai, and Dongsha Movements [25]. The basin has normal faults in the lower part (Paleogene), which is overlain by Neogene sedimentary rocks within the depression. The boundary marked by the T60 forms an unconformity (Figure 1). The Cenozoic stratigraphy consists of Eocene (E_2), Lower Oligocene Yacheng Formation (E_3y), Upper Oligocene Lingshui Formation (E_3l), Lower Miocene Sanya Formation (N_1s), Middle Miocene Meishan Formation (N_1m), Upper Miocene Huangliu Formation (N_1h), Pliocene Yinggehai Formation (N_2y), and Quaternary Ledong Formation (Q_l), from bottom to top (Figure 2).

The study area is located in the Songtao–Baodao region in the eastern Qiongdongnan basin. This area is bounded by the Shenhu uplift and is adjacent to the Zhujiangkou basin. The burial histories of the eastern and western parts of the basin are different [25]. The western part experienced a slow burial at an early stage, followed a rapid burial in the late stage. In contrast, the eastern part went through a generally long-term, continuous burial. The geothermal gradient in the eastern basin (including the Songtao–Baodao region) is generally high, approximately 3.8~4°C/100 m. The current formation is hydrostatically pressured or weakly overpressured. The degree of exploration in the Songtao–Baodao region is low with few discovered petroleum structures (Figure 1). The main source rocks are coal measures in the Yacheng Formation and marine mudstones in the Lingshui Formation. The rock type of the reservoir sandstone is mainly feldspathic quartz sandstone, with a low content of rock debris (5.7%) and a medium to high compositional maturity. The textural maturity of the reservoir sandstone is relatively high because of its distance from the source area. The interstitial materials in the rock particles are mainly cement and argillaceous materials. The authigenic minerals are mainly carbonate cement, secondary quartz, and clay minerals [26].

3. Samples and Methods

Forty sandstone samples collected from the Songtao–Baodao region were used for petrologic characterization, diagenesis observation, and carbon isotope analysis, which were applied to the investigation of diagenesis observation, porosity type, and CO_2 origin. The well logs, strata division, stratigraphic age, vitrinite reflectance and measured temperature, formation tests, lithology, sandstone compositions, source rock data, and porosity-permeability data were collected from the CNOOC Research Institute. Eighteen sandstone samples from the three sections at unusually large depth in the Songtao–Baodao regions were collected; fluid inclusion analyses, including inclusion petrography, microscopic fluorescence spectrum analysis, and microthermometric measurements, were carried out. Fluid inclusion homogenization temperature (Th) combined with burial history was used to determine hydrocarbon filling time. In order to perform the diagenesis analysis, twenty samples were observed using a polarized optical microscope and an S4800 scanning electron microscope (SEM).

Carbon and oxygen isotopes of the carbonate cements were measured using a Delta Plus XL (Thermo/Finnigan) gas chromatography-carbon isotope mass spectrometer. CO_2 was collected from the selected sandstone samples using the acid solution method. The fused silica capillary column (PoraPLOT

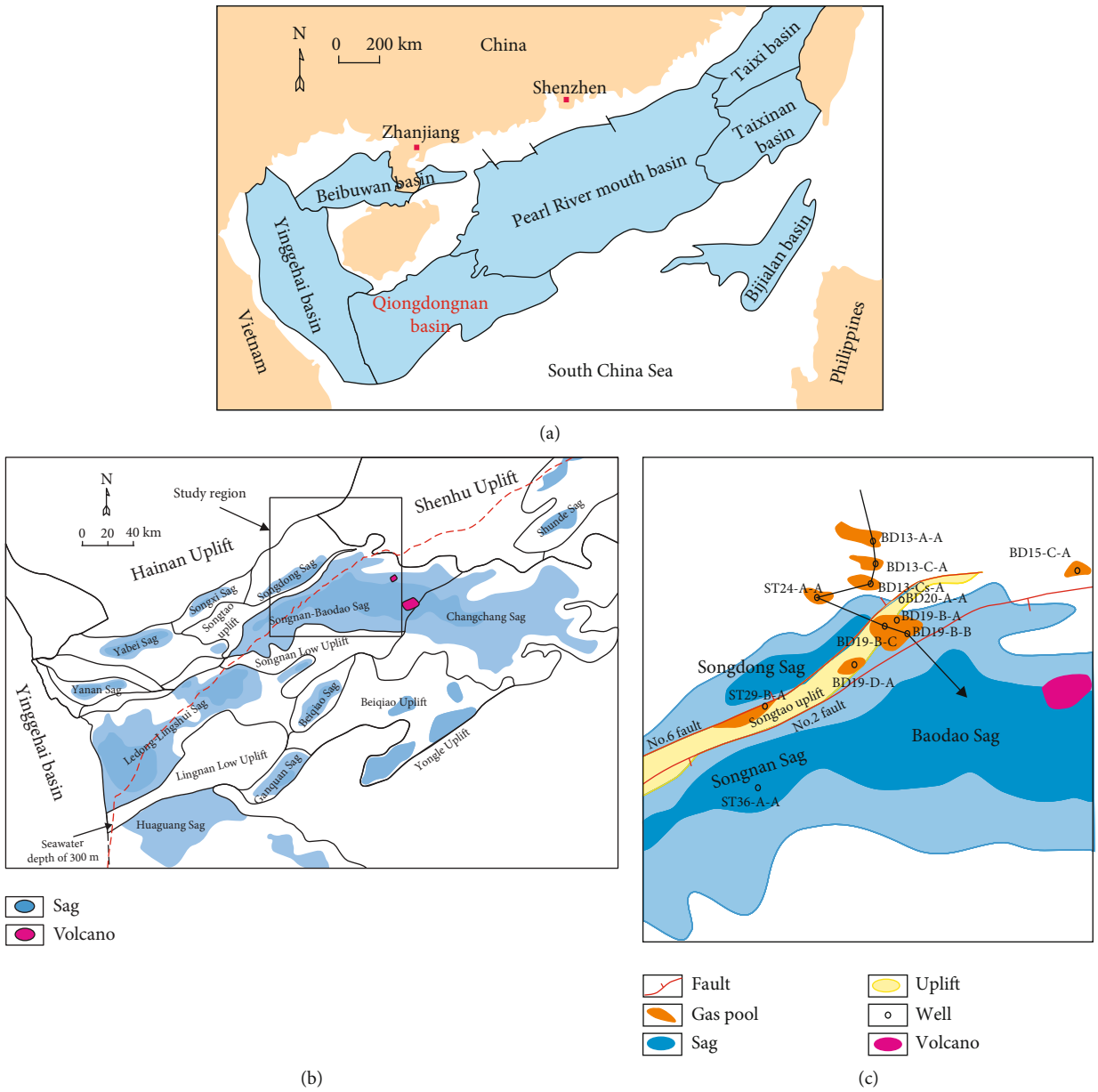

Figure 1: Continued.

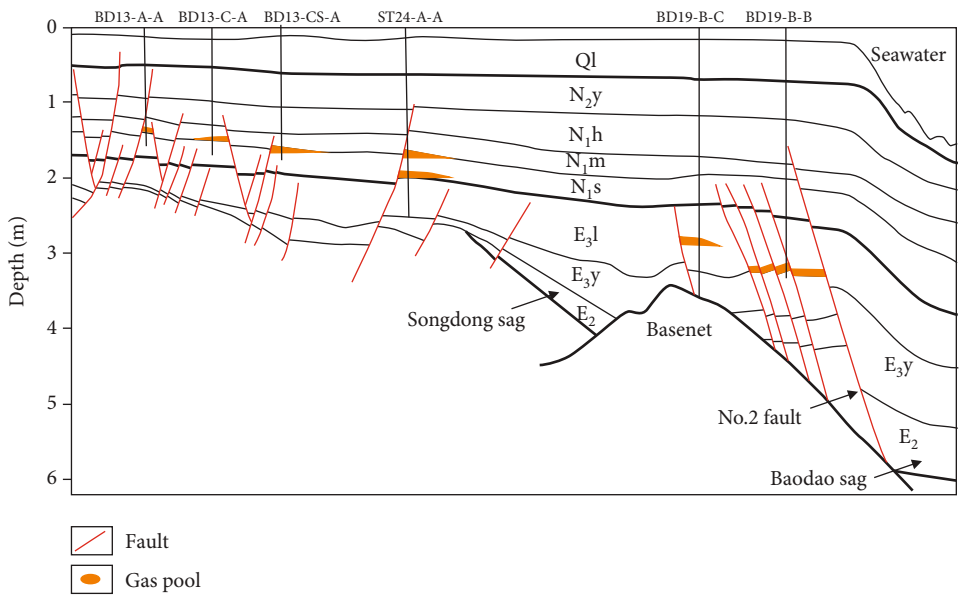

(d)

Figure 1: The location and geology of the Qiongdongnan basin: (a) map showing the Qiongdongnan basin in the South China Sea, (b) tectonic setting of the Qiongdongnan basin and location of the study area, (c) the Songtao–Baodao region and the profile location, and (d) the geological profile of the study area.

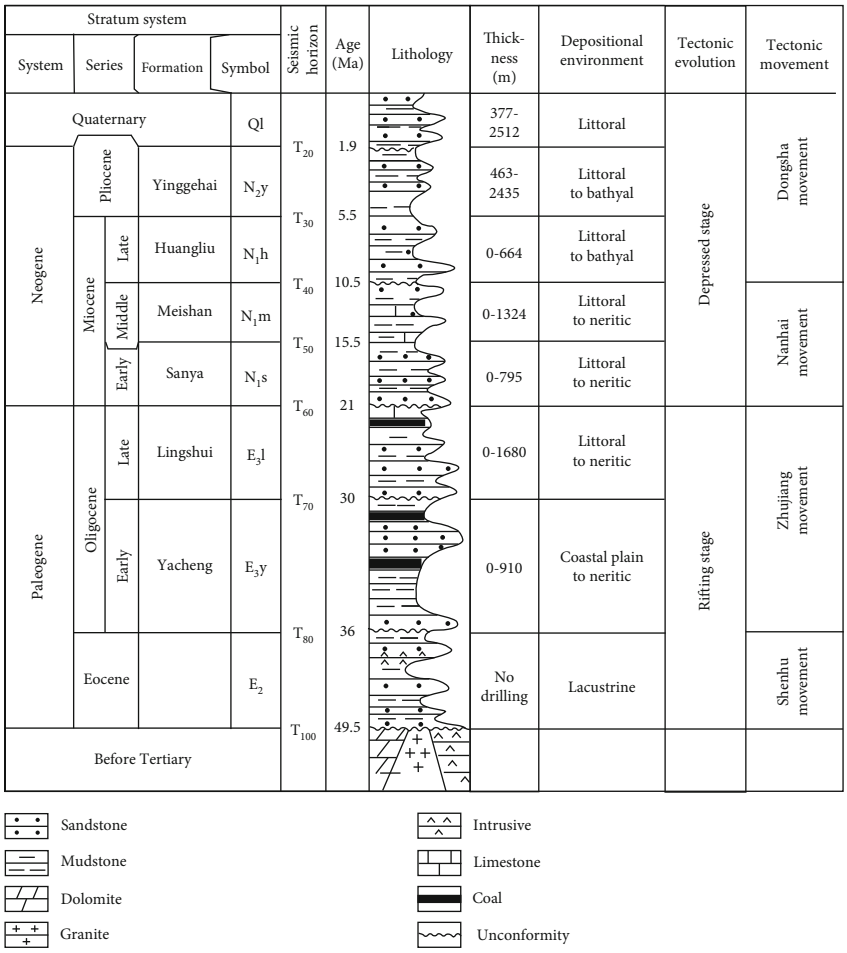

Figure 2: Stratigraphic composition and tectonic evolution in the Qiongdongnan basin.

Table 1: Diagenetic stages in the Yacheng region of the Qiongdongnan basin.

Diagenetic stage			Now geothermal temperature (°C)	Ro (%)	TAL	Tmax (°C)	Maturity	S (%)	I/S mixed layer type	Pore type	Depth (m)
Early stage	A	Early compaction and cementation	80	0.35	light-dark yellow < 2.6	405	Immature	70	Smectite	Primary pore	1600
	B	Early dissolution	115	0.5	dark-orange yellow 2.6-2.8	425	Half mature	40	Chaotic mixed		2400
Middle stage	A_1	Middle dissolution	140	0.7	dark-orange yellow 2.8-3	435	Low mature	25	Order mixed	Secondary pore	3200
	A_2		195	1.3	dark yellow-light brown 2.8-3	455	Mature	10	Superlattice order mixed		4500
	B	Late dissolution	>195	>1.3	light brown-brown > 4	>455	High mature	5			>4500

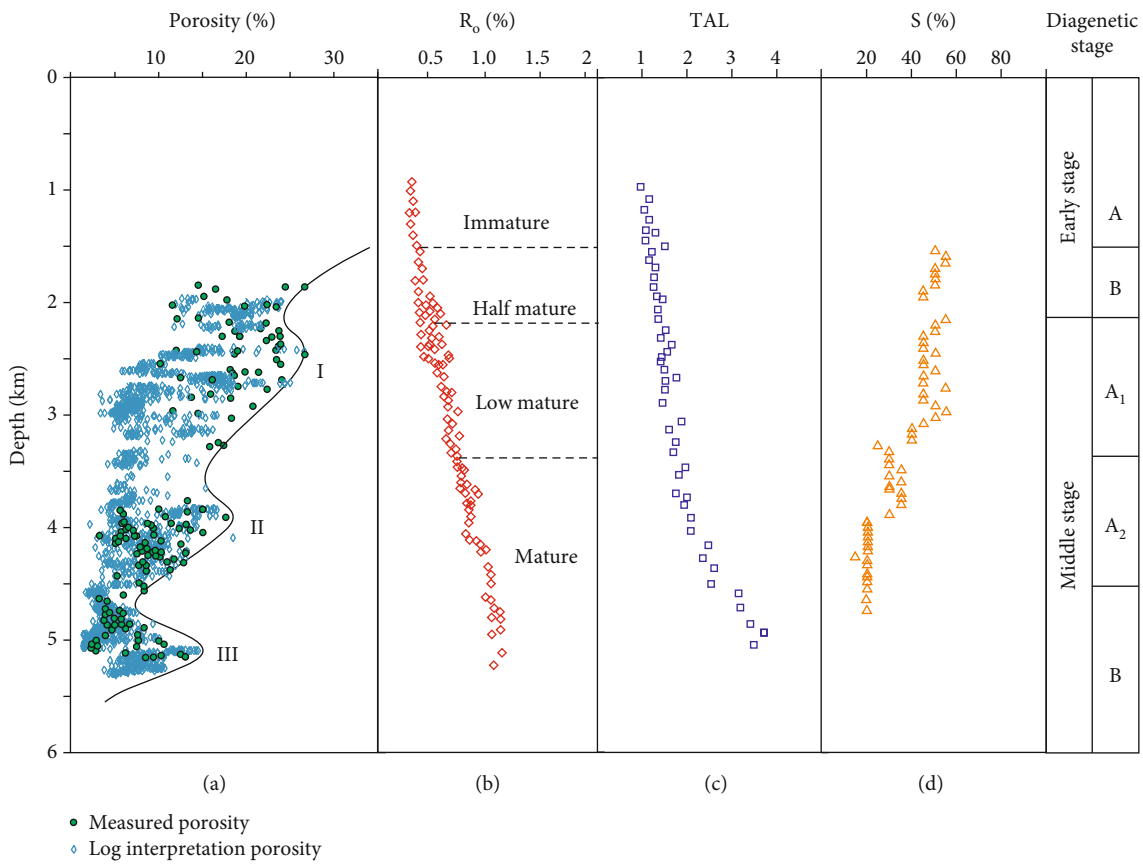

Figure 3: (a) The variation characteristics of porosity; (b) the thermal evolution of organic matter; (c) thermal alteration index from sporopollen color; (d) smectite mineral content of the illite/smectite mixed layer of the diagenetic stage in the Songtao–Baodao region of the Qiongdongnan basin. Note: Ro: organic vitrinite; TAI: thermal alteration index; S: illite/smectite mixed layer.

Q 30 m × 0.32 mm × 0.25 μm) was used, and the carrier gas was helium. The initial oven temperature was maintained at 50°C for 3 min, increased to 180°C at a rate of 15°C/min, and finally maintained for 15 min. Stable carbon isotopic values are reported in the customary ∂ notation in per mil (‰) relative to PDB (VPDB). Measurement precision was estimated to be ±0.3‰. The experiment was conducted at the Guangzhou Institute of Geochemistry, the Chinese Academy of Sciences.

Fluid inclusion analysis was carried out at the Key Laboratory of Tectonics and Petroleum Resource of Educational Ministry, China University of Geosciences. Fluid inclusion petrography was conducted using a Nikon 80I dual-channel fluorescence microscope equipped with transmitted and ultraviolet light. The main geochemical components of gas inclusions and gas-bearing inclusions were determined using a laser Raman microprobe. The homogenization temperature (Th) of fluid inclusions was measured using a LinkamTHMS600 cooling-heating stage at 20°C, i.e., room temperature. The initial heating rate was 15°C/min. The rate was set to 5°C/min when the vapor bubble in the fluid inclusion began to disappear. Measurement precision was estimated to be ±0.1°C.

4. Results

4.1. Diagenetic Stage. According to the industrial standard of the Chinese petroleum and natural gas industry (SY/T 5477-2003) [27], the diagenesis was analyzed by some parameters, such as the variation in the reflectivity of organic vitrinite (Ro), the thermal alteration index (TAI) from sporopollen color, the thermal evolution and pyrolysis parameters (Tmax), the smectite mineral content of the illite/smectite mixed layer (I/S), and the casting thin sections. The result was that the diagenetic process in the west of the Qiongdongnan basin can be divided into two stages, as shown in Table 1, the early diagenetic stage (including A and B stages) and the middle diagenetic stage (including A_1, A_2, and B stages); the corresponding depth is about 1600, 2400, 3200, 4500, and more than 4500 m (Table 1 and Figure 3).

4.2. AHPZs. AHPZ refers to the reservoir porosity exceeding that induced by the normal compaction curve with the increase in burial depth, and it is not completely equivalent to secondary porosity. The porosity variation in the Songtao–Baodao region could be obtained based on the well-logging and measured data. The plot of porosity vs. depth reveals three AHPZs at different depths (Figure 3(a)). The first AHPZ is located at 2250~3100 m with a maximum porosity close to 28%. The second and third AHPZs are located at 3700~4400 and 4800~5300 m, with porosities up to 18% and 20%, respectively. The reservoir porosity should be lower than 15% at depths below 3500 m by considering normal pore evolution regularity. This scenario suggests the

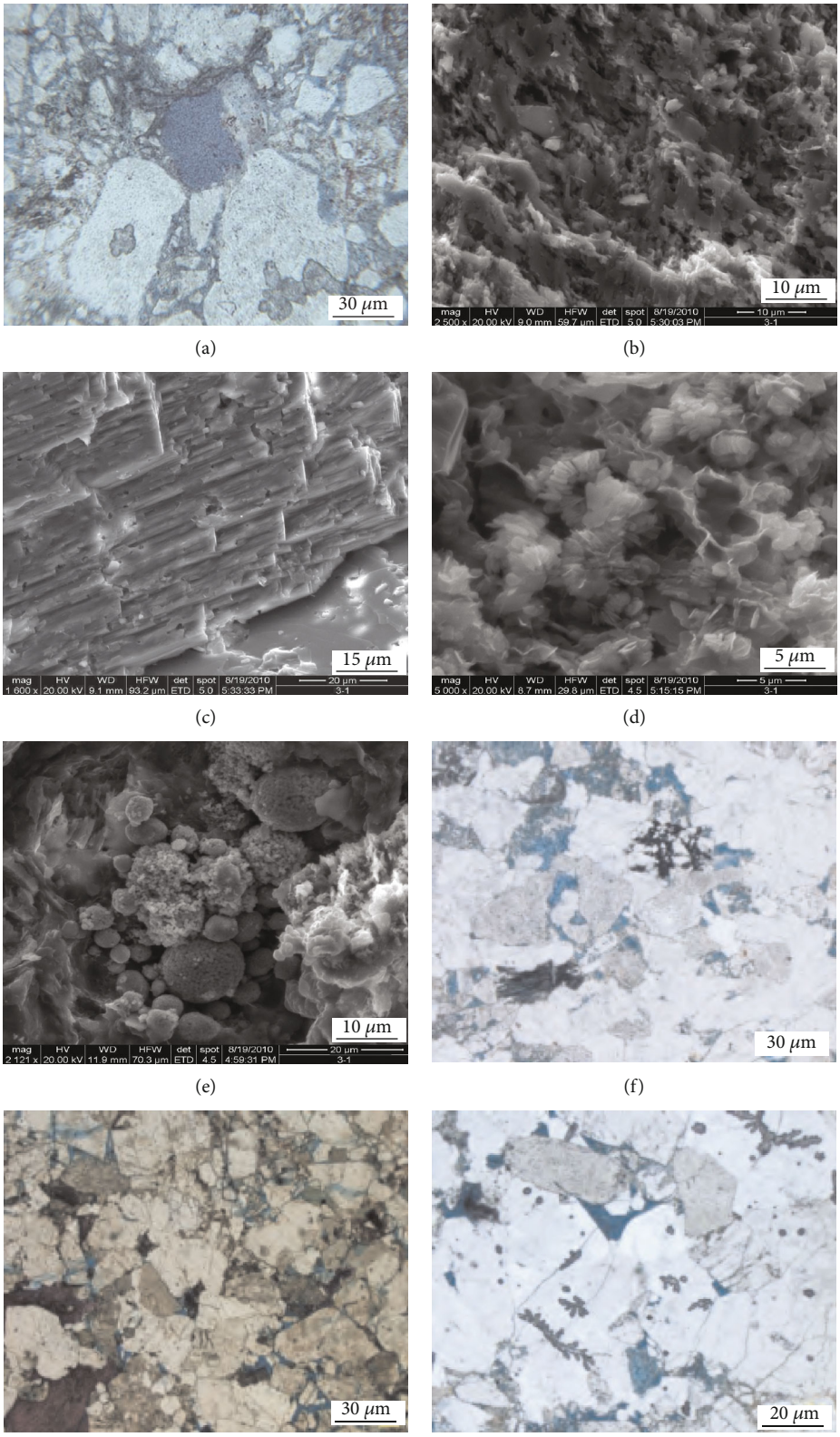

Figure 4: Continued.

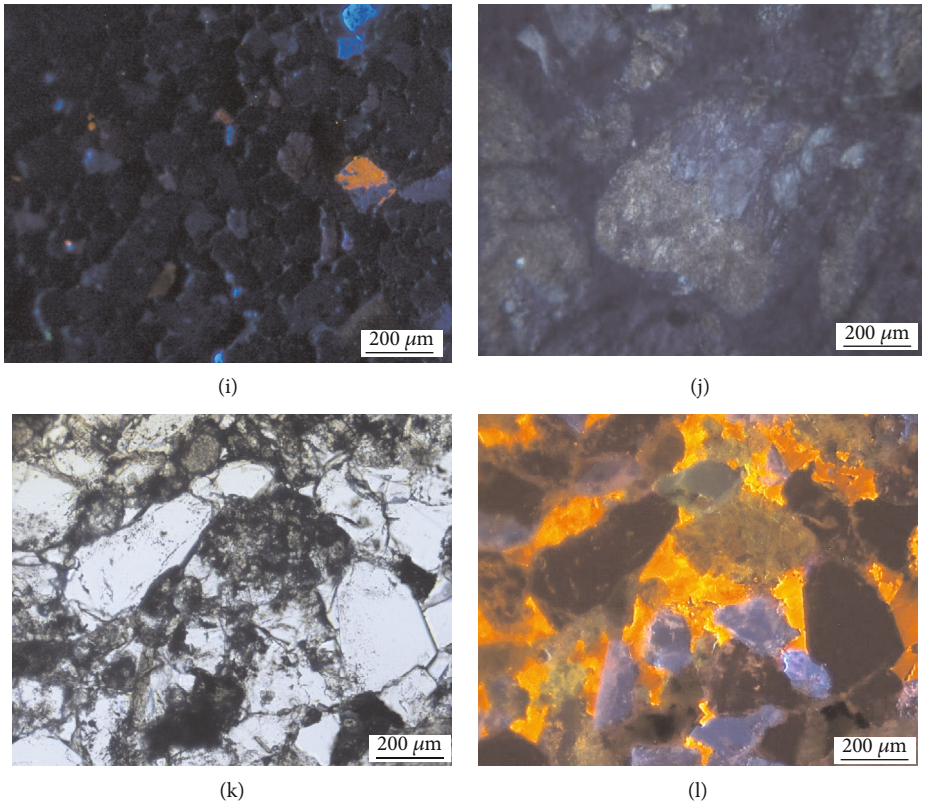

Figure 4: Thin section images of sandstone samples from the Songtao–Baodao region of the Qiongdongnan basin. (a) Blue cast slice; well BD15-C-A, 2268 m; feldspar dissolved into oversize molded hole. (b) Scanning electron microscopic image (SEM); well ST24-A-A, 2726 m; feldspar particles are dissolved. (c) SEM; well ST29-B-A, 2726 m; carbonate cement is dissolved. (d) SEM; well BD13-C-A, 2726 m; intergranular pores among kaolinite. (e) SEM; well ST36-A-A, 2813.2 m; berrylike pyrite. (f) Blue cast; well BD19-B-A, 4102 m; dissolved feldspar pores. (g) Blue cast; well BD19-D-A, 4102 m; dissolved feldspar pores and carbonate cement filling. (h) Blue cast; well BD19-B-B, 5092 m; dissolved feldspar and intergranular pores. (i) Cathode luminescence; well BD19-B-C, 2551.2 m; carbonate intragranular calcite cement filling the dissolved pores. (j) Orthogonal polarized light; well BD20-A-A, 2576 m; carbonate intragranular calcite cement filling the dissolved pores; well ST24-A-A, 2914.5 m. (k) Thin section; well BD19-B-B, 4100.1 m; carbonate intergranular calcite cement. (l) Cathode luminescence; well BD19-B-B, 4100.1 m; carbonate intergranular calcite cement filling the dissolved pores.

possibility of high-quality reservoirs in the middle-deep Qiongdongnan basin.

The first and second AHPZs are regional for the basin, dominated by primary pores, and followed by secondary dissolution pores. The secondary dissolution pores are mainly distributed in feldspar, rock debris, and carbonate cement, and some of them are even molded holes (Figures 4(a)–4(c), 4(g), and 4(h)). The third AHPZ is only locally developing at the Baodao 19-B structure belt and is dominated by secondary pores (Figure 4(h)). The first, second, and third AHPZs are in the middle diagenetic A1, A2, and B stages, respectively (Figure 3).

4.3. Fluid Inclusions. Fluid inclusions capture the original geofluids, which recorded the physical and chemical properties of fluid activity, such as temperature, pressure, and composition. Therefore, fluid inclusions can be used as one of the most important objects to study the geological information of paleofluid activity [28, 29]. There are three types of reservoir inclusions in the BD19-B area under microscope, including gas inclusions, oil inclusions, and CO_2 inclusions. Gas inclusions are well developed and mainly distributed in the cracks of quartz grains (Figures 5(a) and 5(b)). A large number of gas inclusions have been detected in both shallow Sanya and deep Lingshui reservoirs, which is the direct evidence of large-scale gas migration and accumulation. However, only a small amount of yellow fluorescent oil inclusion was detected in the Lingshui formation in the BD19-B structure (Figures 5(c) and 5(d)). Some three-phase CO_2 inclusions were also detected in the Lingshui reservoir (Figures 5(e) and 5(f)), indicating CO_2 filling events. Few CO_2 inclusions were found in the Sanya formation. The type of reservoir fluid observed by fluid inclusions is in good agreement with the natural gas composition of the present BD19-B structure.

5. Discussion

5.1. Reservoir Diagenetic Fluid Type and Evolution. In addition to its own properties, reservoir diagenetic fluid in the sedimentary basin is affected by external factors, including meteoric water, organic and carbonic acids, and thermal and hydrocarbon fluids [3, 4]. The property variations of diagenetic fluids in different geological periods have a large influence on the products of reaction between fluids and

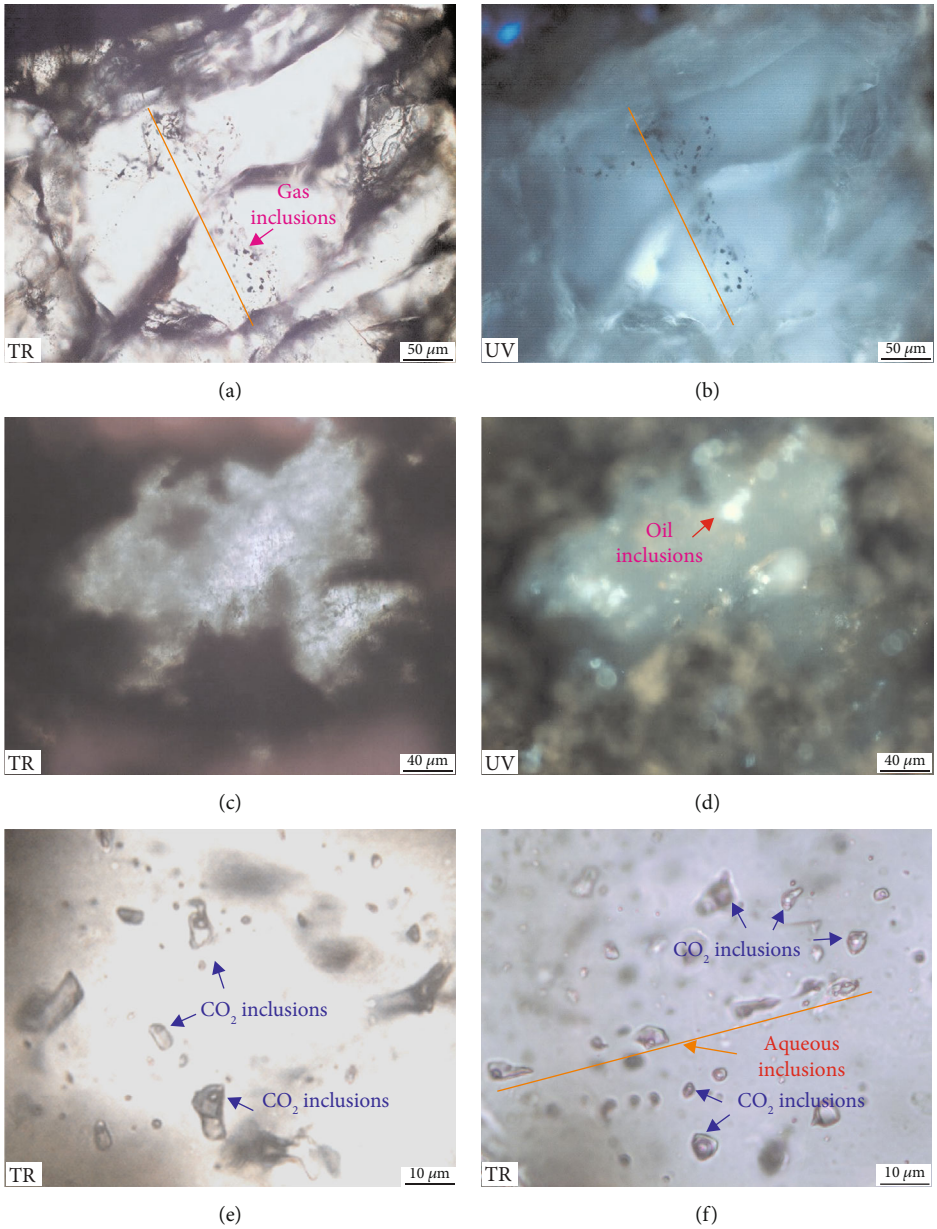

Figure 5: Fluid inclusion images of sandstone samples from the Songtao–Baodao region of the Qiongdongnan basin. TR: transmission light; UV: fluorescence. (a, b) Pure gaseous inclusions without fluorescence observed in quartz particle crack; well BD19-B-2, 3818 m. (c, d) Yellow fluorescent oil inclusions in quartz grains; well BD19-A-1, 3860 m. (e, f) Three-phase CO_2 inclusions developed in quartz particles and nearby associated aqueous inclusions; well BD19-B-1, 5155 m.

minerals in rocks. Therefore, geochemical information and mineral assemblages can be used to track the fluid types at different geological stages [30]. In this area, no obvious dissolution [25] of quartz particles suggests that minimal alkaline action was involved in the diagenetic process.

5.1.1. Organic Acid. Secondary dissolution pores in feldspar and rock debris were generally observed in three AHPZs, as well as the kaolinite and authigenic quartz near the secondary pores (Figure 4(d)), suggesting that these three AHPZs suffered from acid dissolution. Meanwhile, the relation between authigenic quartz content and depth reveals a high peak at 2250~3100 m which is in accordance with the first AHPZ (Figure 6), although the total content of authigenic quartz in the Songtao–Baodao region is low. The particles with each other show a point-line contact relationship, and no pressure dissolution or mass conversion of clay minerals at this depth range is observed (Table 1 and Figure 4). Therefore, the authigenic quartz at this depth range may form after the acid dissolution of feldspar and other minerals. These observations suggest that the dissolution was caused by organic acid. Under the action of anaerobic bacteria, organic carboxylic acid anions can be reduced to hydrogen sulfide ions, which would lead to the formation of pyrite by combining with iron ions

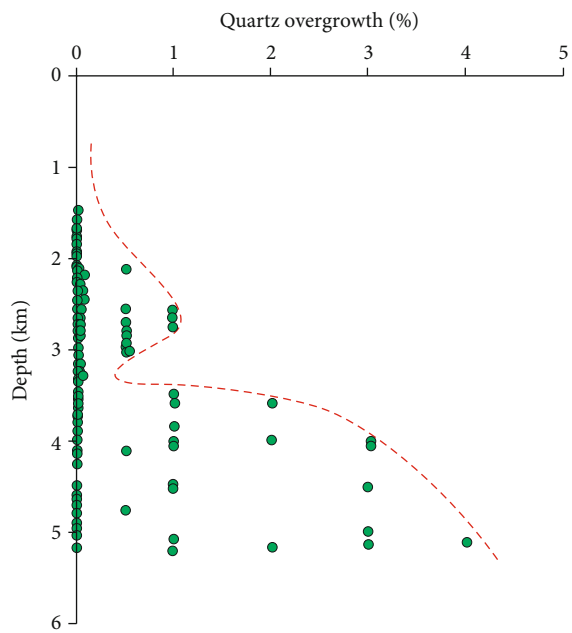

Figure 6: The variation of quartz authigenic enlargement percentage with depth in the Songtao 24-A and Baodao 19-B structure belt.

[31]. Although the content of pyrite in the first AHPZ is low, it is ubiquitous, as shown in Figure 4(e), with berrylike particles filling in pores, which also supports the involvement of organic acids.

When thermal evolution of organic matter reaches early maturity (Ro of 0.50%–0.70%), short-chain carboxylic acids will be released during kerogen degradation [32]. After the organic acid released from the source rock migrates into the reservoir, it dissolves the unstable materials, such as feldspar and rock debris, and produces secondary dissolution pores which improve reservoir quality. In the study area, the previous thermal simulation experiments show that the organic matter in the Lingshui and Yacheng Formations generated a large amount of organic acid, with an average of 3.8 mg of acid per gram of kerogen, dominated by highly soluble oxalic acid [24], which also supports the existence of organic acid in this area and the dissolution ability of the reservoir rock to dissolve.

In addition, the effective dissolution of organic acids generally occurs in the reservoir adjacent to the source rock, and the effect decreases as the distance from the reservoir to source rock increases. Using the Baodao 19-B structure belt as an example, the first AHPZ is distributed in the reservoir of the Sanya Formation, which is mainly affected by organic acid generated from the adjacent mudstone of the upper Lingshui Formation. The second AHPZ in the middle Lingshui Formation is mainly affected by the organic acids generated from its own mudstone, because the sand and mud frequently form interbeds in this formation. The third AHPZ is distributed in the reservoir of the lower Lingshui Formation, dominated by sand, and it is mainly affected by the organic acids generated from the mudstone in the middle Lingshui Formation and the coal-measure source rock of the Yacheng Formation. According to thermal evolution history, the dissolution history of organic acid can be obtained, as shown in Figure 7. Concerning this analysis, a large amount of organic acid is generated from organic matter when Ro ranges from 0.5% to 0.7%. The organic acid dissolution periods of three AHPZs are different. The first AHPZ was dissolved by organic acids roughly from the Late Miocene to the Late Pliocene. The second AHPZ was dissolved by organic acids from the Late Miocene to the Middle Pliocene. The third AHPZ was dissolved by organic acids from the Early to Middle Miocene and Late Miocene to the Middle Pliocene.

5.1.2. Meteoric Water. Large-scale meteoric water is an important factor for the development of AHPZs [33, 34]. During the basin evolution, the strata went through several tectonic uplifts and formed some unconformable surfaces [35]. At the end of the Oligocene (about 21 Ma), the Nanhai episode occurred in the basin and resulted in the strata uplift. The second AHPZ in the Lingshui Formation was uplifted to near the surface. In this geological period, the buried depth of the third AHPZ was about 1000 m and less affected by meteoric water [36, 37]. Therefore, the influence of meteoric water for the third AHPZ can be neglected. Another tectonic uplift occurred at 15.5 Ma (corresponding to the late stage of the Nanhai episode), when the first AHPZ was near the surface. The tectonic uplifts indicate that the first and second AHPZs were likely affected by meteoric water in the geologic history.

The diagenetic mineral assemblage of the water-rock reaction, such as carbonate cement, is a good tracer to track the fluid source. Carbonate cement in the study area is mainly calcite and ankerite, with a little dolomite, and the carbonate cement types are mainly intragranular calcite cement (in AHPZ I) and intergranular calcite cement (in AHPZ II) (Figures 4(j)–4(l)). The carbon isotopic value is different in different types of fluids; therefore, the carbonate cement precipitated by the fluids that provide the carbon will have different carbon isotopic values. Generally, the carbon in fluids originates from organic acid, meteoric water, and seawater. The carbon derived from the decarbonization of organic acids has a light carbon isotope with a $\delta^{13}C_{PDB}$ value as low as −8‰ to −23‰. The $\delta^{13}C_{PDB}$ provided by meteoric water generally ranges from −4‰ to −1‰. The $\delta^{13}C_{PDB}$ from seawater varies from 0 to 3‰ [38]. The oxygen isotope ($\delta^{18}O_{PDB}$) in carbonate cement is related to the formation temperature, the source of sedimentary fluid, and the diagenetic reformation in the later period [39]. Based on the types and characteristics of carbonate cement analysis, the measured carbon and oxygen isotope values of carbonate cement in the first and second AHPZs of the Baodao 19-B structure belt are shown in Table 2. The $\delta^{13}C_{PDB}$ value of the first AHPZ ranges from −3.4‰ to −0.4‰, indicating that the carbon was mainly provided by meteoric water and/or seawater. The $\delta^{13}C_{PDB}$ value of carbonate cement in the second AHPZ is lower than that of the first AHPZ, ranging from −7.9‰ to −2.2‰, suggesting that the carbon in the second AHPZ was derived from an organic carbon source.

Friedman and O'Neil suggested that oxygen isotopes in carbonate cements were determined by fractionation coefficients of the water-rock reaction, which relates to the formation

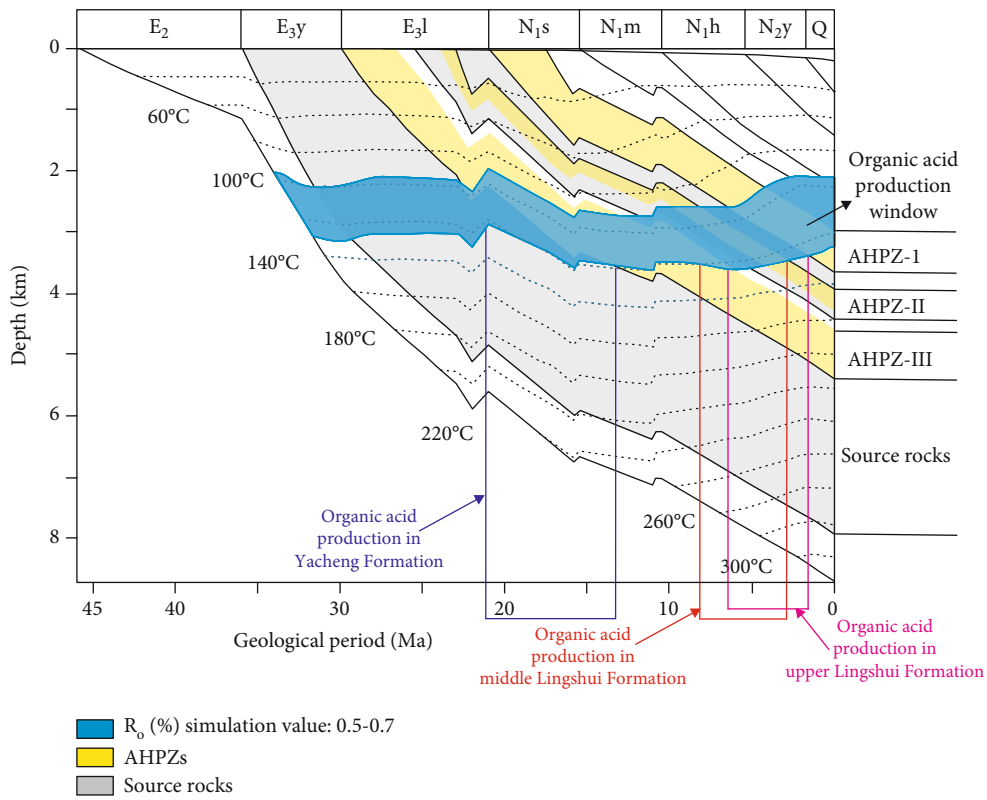

Figure 7: The burial and thermal histories of the Baodao 19-B structure belt.

Table 2: Carbon and oxygen isotopic composition of carbonate cement in the Baodao 19-B structure.

Well no.	Depth (m)	Sample location	Rock sample	Carbonate cement type	$\delta^{13}C_{PDB}$ (‰)	$\delta^{18}O_{PDB}$ (‰)
BD19-B-A	2538~2540	AHPZ-I	Borehole cuttings	Intragranular calcite cement	−2.8	−8.8
BD19-B-A	2530~2532	AHPZ-I	Borehole cuttings	Intragranular calcite cement	−2.8	−8.7
BD19-B-B	2520~2522	AHPZ-I	Borehole cuttings	Intragranular calcite cement	−2.4	−8.9
BD19-B-B	2646~2648	AHPZ-I	Borehole cuttings	Intragranular calcite cement	−0.3	−8.2
BD19-B-C	2550~2552	AHPZ-I	Borehole cuttings	Intragranular calcite cement	−3.1	−8.9
BD19-B-C	2698.0	AHPZ-I	Borehole cuttings	Intragranular calcite cement	−2.5	−9.7
BD19-B-C	2946.0	AHPZ-I	Borehole cuttings	Intragranular calcite cement	−3.4	−12.1
BD19-B-A	4189.0	AHPZ-II	Core	Intergranular calcite cement	−3.4	−10.2
BD19-B-A	4020.0	AHPZ-II	Borehole cuttings	Intergranular calcite cement	−7.9	−11.7
BD19-B-B	4100.0	AHPZ-II	Borehole cuttings	Intergranular calcite cement	−7.7	−12.2
BD19-B-B	4236.0	AHPZ-II	Core	Intergranular calcite cement	−2.2	−13.9

temperature and fluid oxygen isotopes [40]. The oxygen isotope value of the paleofluid can be deduced according to the $\delta^{13}O_{PDB}$ value and the formation temperature of carbonate cement. In this study, the formation temperatures of the first and second AHPZs were obtained from the homogenization temperature of aqueous inclusions in the dolomite (Figure 8). The formation temperature of the carbonate cement in the first AHPZ ranges from 70 to 120°C, and that of the second AHPZ ranges from 130 to 180°C. The oxygen isotope and formation temperature of the carbonate cement are plotted in Figure 9. The paleofluid oxygen isotope composition was obtained from the relationship. The oxygen isotope composition of the meteoric water is in accordance with the current rainfall value of the western Pacific [41], and the oxygen isotope composition of the seawater is the same as that of the current seawater. As shown in Figure 9, the paleofluid oxygen isotope value of the first AHPZ varies from −8‰ to +3‰. It is distributed in the mixing area of meteoric water and seawater. This phenomenon indicates that the pore fluids in the first AHPZ were mainly meteoric waters to high-salinity burial fluid in the process of

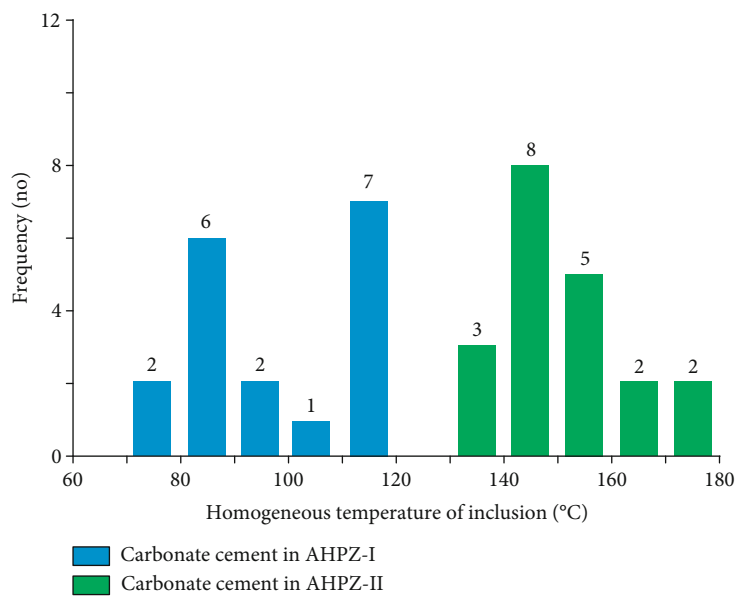

Figure 8: Homogenization temperature of the saltwater inclusion in the carbonate cement from the Songtao 29-B and Baodao 19-B structure belts.

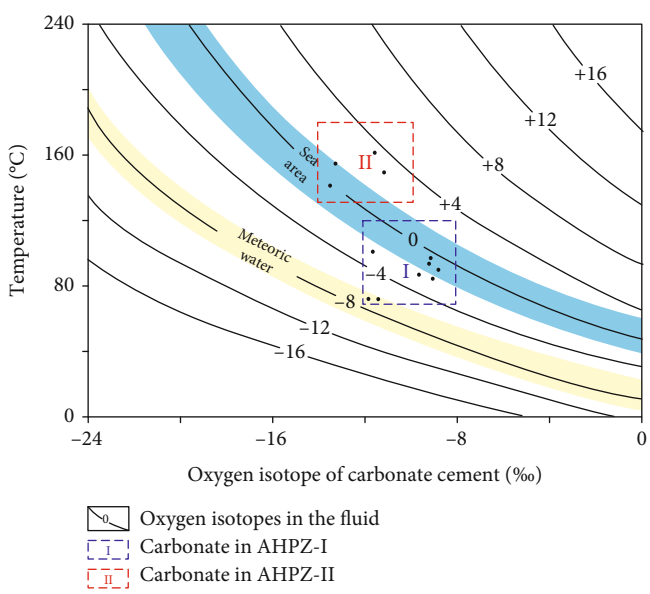

Figure 9: Diagram of the oxygen isotope and formation temperature of the carbonate cement as well as paleofluid from the Baodao 19-B structure belt.

gradual burial. The paleofluid oxygen isotope value of the second AHPZ ranges from −2‰ to +6‰, suggesting that it is seawater area with little input of meteoric water.

In addition, seawater and meteoric water could also be distinguished by salinity. The paleofluids trapped by fluid inclusions in the geological period retain the original physical and chemical properties. Therefore, the salinity of paleofluids (NaCl wt.%) can be calculated by the freezing point temperature (Tm) of the inclusions [42]. In this study, the Tm of aqueous inclusions in the first and second AHPZs were measured, and the salinity of fluids was calculated. Figure 10 shows the relationship between fluid salinity of aqueous inclusions in the first and second AHPZs. In this study, the threshold salinity of seawater and meteoric water was assumed to be 4%. The salinity of the paleofluid in the first AHPZ ranges widely from 0% to 15%, with an average value of 6.65%, indicating a mixture of seawater and meteoric water. However, the salinity of the paleofluid in the second AHPZ is relatively high, with an average value of 12.5% and a maximum of 21.5%, indicating that there was no significant input of meteoric water.

Generally, on the basis of the carbon and oxygen isotopic compositions and fluid inclusions in the carbonate cements, the origins of paleofluids in the first and second AHPZs are clarified. The paleofluids in the first and second AHPZs were mainly derived from seawater. In addition, the first AHPZ suffered from an external meteoric water at the near surface due to the tectonic uplift at the early diagenesis.

5.1.3. Thermal Fluid. Thermal fluid is a supercritical fluid and rich in a variety of minerals. It often carries high amounts of thermal energy, affecting the geothermal temperature. The Th of fluid inclusions reflects the geothermal temperature when the fluids are trapped as inclusions. Compared with the geothermal temperature, the thermal fluid activity in the basin could be determined, as shown in Figure 11. Geothermal temperatures were obtained from well drilling in the Baodao 19-B and 20-A structure belts. As shown in Figure 11, Th values of most fluid inclusions in the first AHPZ are lower than the corresponding temperatures at the same depth. However, about half of Th values in the second and third AHPZs is higher than the current testing temperature, even exceeding about 45°C. These scenarios indicate that the second and third AHPZs were affected by thermal fluids, but the first AHPZ was barely influenced by thermal fluids.

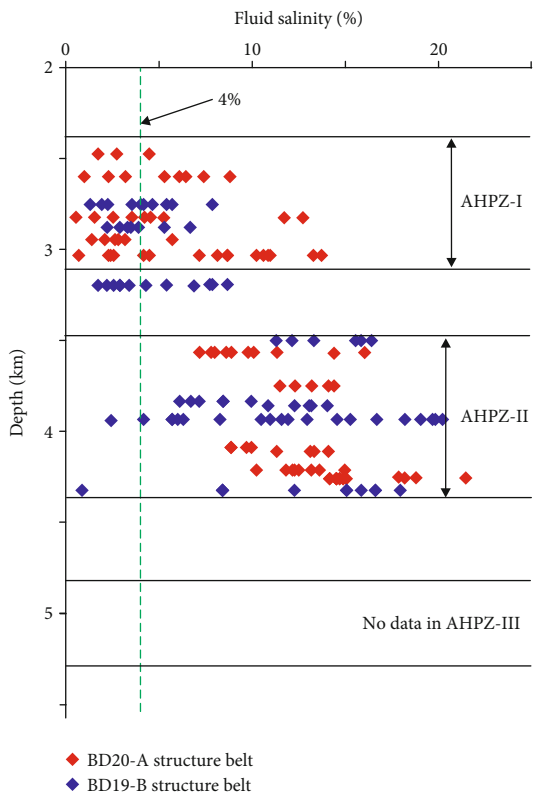

Figure 10: Relationship between fluid inclusion salinity and depth for the Baodao 20-A and 19-B structure belts.

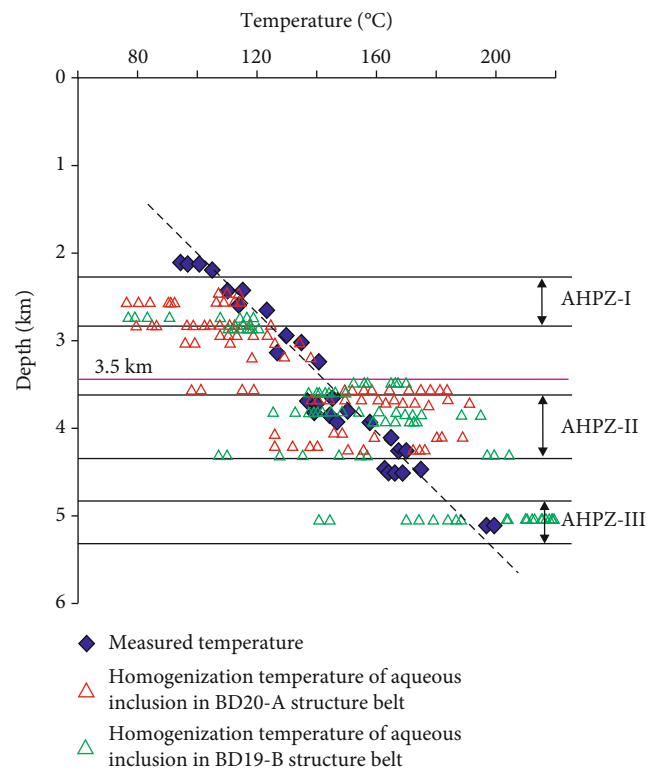

Figure 11: Relationship of the measured temperature, homogenization temperature of fluid inclusions, and buried depth in the Baodao 20-A and 19-B structure belts.

In addition, thermal fluid also greatly affects the dissolution in the reservoir due to its strong fluidity and the temperature-pressure properties. Strong fluidity can promote acid fluids to dissolve feldspar which results in more secondary pores. Meanwhile, the higher pressure and temperature can also improve the dissolution ability. This is also supported by observation of thin sections (Figures 4(f) and 4(g)). The feldspar and rock fragments were dissolved and formed dissolved pores in the second and third AHPZs, and the proportion of secondary pores to the total pores was relatively high. There is obviously high content of authigenic quartz in the second and third AHPZs, which is observably larger than in the first AHPZ (Figure 6). The abnormal overgrowth of quartz is the result of acidic dissolution. While it is impossible for organic acids to contribute so much silica, the abundant siliceous matter is likely the result of the dissolution of feldspar, rock debris, and other minerals by the active thermal fluids. Furthermore, the formation temperature of the quartz overgrowth zone may indicate the time of thermal fluids. Combining Th of inclusions in the quartz overgrowth, the active period of the thermal fluid in the Songtao–Baodao area was determined to be late stage (Figure 12).

It is noteworthy that the CO_2 content of the gas reservoirs in the third AHPZ in the Baodao 19-B belt is as high as 81.6%~87.9%. The carbon isotope value of CO_2 ranges from −7.5‰ to −6.9‰, with a $^3He/^4He$ value of 5.95×10^{-6} -8.75×10^{-6}, and an R/Ra ratio of 4.25–6.25 [26], which indicates an inorganic mantle CO_2 source [43], and may be related to the Miocene volcanic activity close to the No. 2 fault structure (Figure 1(d)). Rifting is always associated with volcanic activity, which may lead to the release of CO_2 from mantle sources. The fluid inclusion and burial history indicate that the CO_2 filling occurred in the late period (Figure 12), suggesting that the active period of thermal fluids (rich in CO_2) was also late. Under high-temperature and high-pressure conditions, the critical fluids rich in CO_2 have strong solubility to effectively dissolve feldspar and other minerals. This phenomenon is similar to that in a previous report stating that a large number of dissolution holes were discovered in high CO_2 reservoirs of the Huangliu Formation in the Dongfang gas field of the Yinggehai Basin [44, 45].

5.1.4. Hydrocarbon Fluid. The influence of hydrocarbon emplacement on diagenesis is still controversial [46]. Some scholars believe that hydrocarbon-filled pores would hinder the communication between inorganic ions and minerals [47]. Furthermore, authigenous minerals, such as quartz, illite, and carbonate cement, would be prevented from filling the pore space, and diagenesis would cease. However, other scholars have observed that hydrocarbon emplacement failed to inhibit the development of authigenic quartz and illite [48]. In this study, the fluid inclusions were used to help determine the period of hydrocarbon filling in the study area and also to analyze the effects of hydrocarbon emplacement on authigenic mineral development. The fluid inclusions in the study area may consist of gas, minor oil, and CO_2 inclusions.

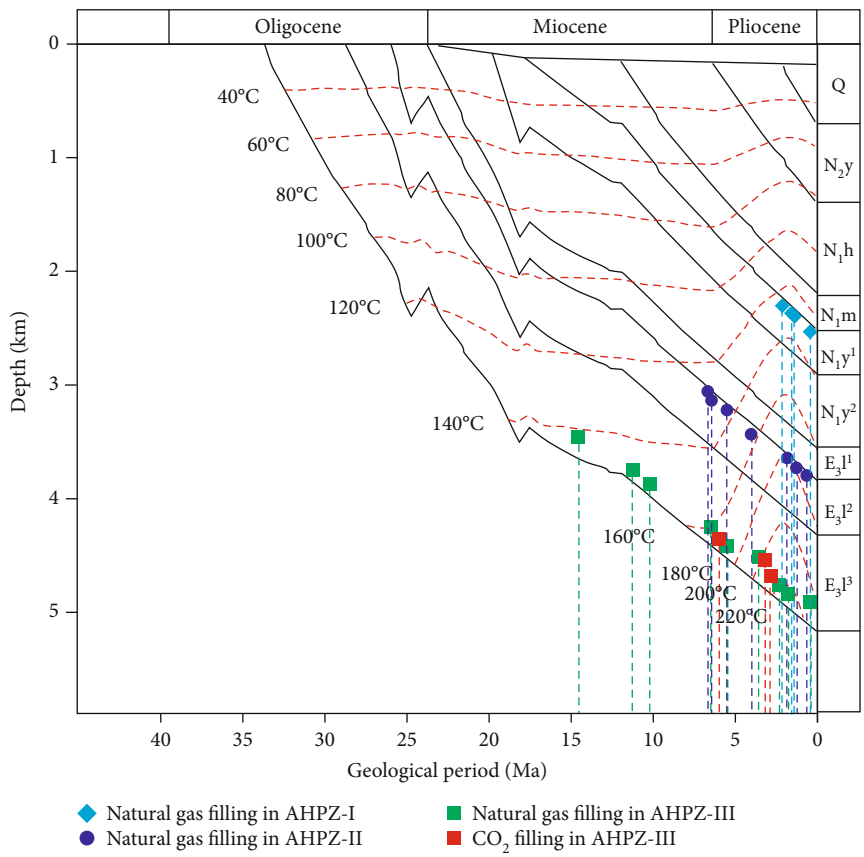

Figure 12: Natural gas filling period in the Baodao 19-A structure belt.

The inclusions present different shapes, including elliptical, triangular, and strips. The host minerals mainly include quartz grain cracks, quartz overgrowth zones, and carbonate cements (Figure 5). The development of hydrocarbon inclusions at different depths suggests that hydrocarbon migration and accumulation occurred in the geological periods. In this study, the hydrocarbons filling time in the Baodao 19-B structure belt were determined by combining the burial history and the Th of the aqueous inclusions coeval with the hydrocarbon inclusions (Figure 12). As shown in Figure 12, the time of hydrocarbon filling in the first AHPZ was after 2 Ma, in the Quaternary. The time of hydrocarbon filling in the second AHPZ was from the Early Pliocene to the present day. The time of hydrocarbon filling in the third AHPZ was from the Middle Miocene to the present day. In addition, the time of CO_2 filling was from the late Miocene to the present day. On the whole, the start time of hydrocarbon filling in the lower formation was in the early period, and that in the upper formation was in the late period, which also suggests that the lower Yacheng Formation may be the main source rock in the Songtao–Baodao structure belt.

The Th of aqueous inclusions in the quartz overgrowth and carbonate cement is similar to that of aqueous inclusions accompanying hydrocarbon inclusions, indicating that hydrocarbon filling in the study area fails to completely prevent the formation of authigenic minerals. The result may be related to gas (oil) saturation in the reservoir or more complex mechanisms. In this study, however, the carbonate cement demonstrates a certain negative correlation with gas saturation (Figure 13). The carbonate cement filling in pores is destructive to reservoir properties (Figures 4(i)–4(l)), and this negative relationship between the carbonate cement and gas saturation in the Baodao 20-A structure belt indicates that the hydrocarbon filling restrains the carbonate cement from filling of pores to a certain extent, which is favorable for reservoir porosity.

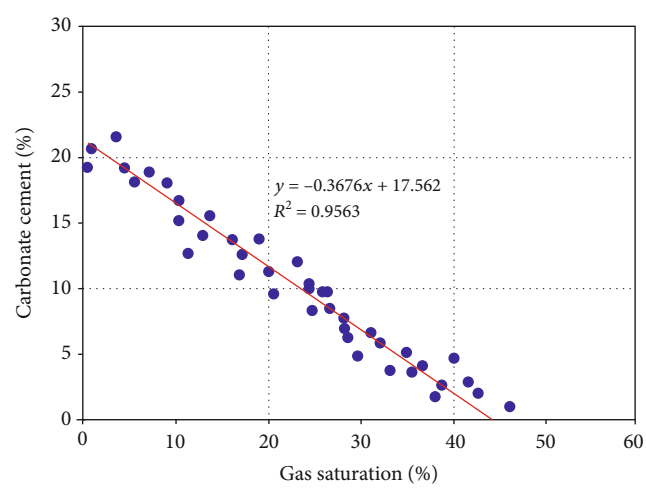

Figure 13: Relationship between the carbonate cement and gas saturation in the Songtao–Baodao region.

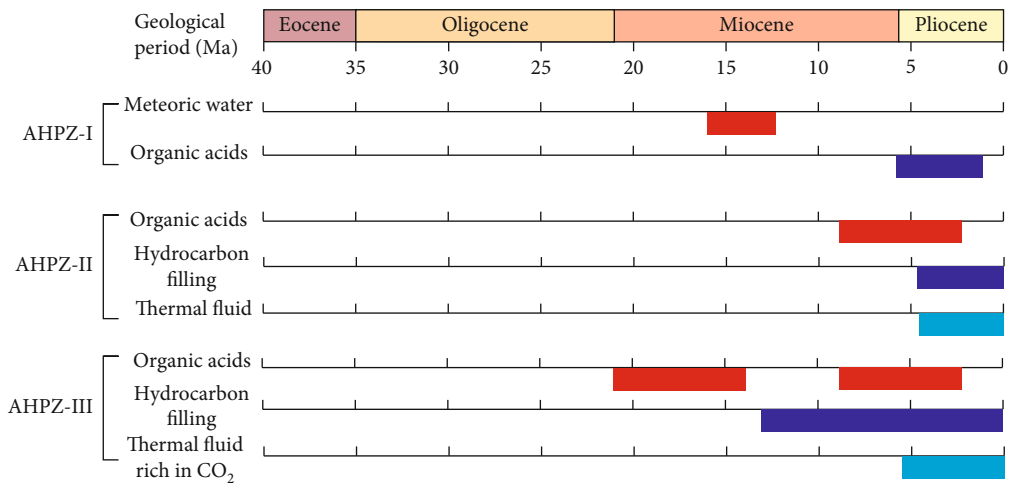

Figure 14: Diagenetic fluid types and their activity history for the Songtao–Baodao regions.

5.2. Formation Mechanism of AHPZs. The current AHPZs in the reservoir are the comprehensive results of various diagenetic fluid activities over geological periods. In this study, the diagenetic process of three AHPZs in the Songtao–Baodao region can be deduced according to the analysis of diagenetic pore fluid type and evolution (Figure 14).

Diagenetic fluids affecting the development of the first AHPZ included meteoric water, organic acid, and hydrocarbon. The meteoric water and organic acids dissolved feldspar minerals and thus led to secondary pores. The first AHPZ strata went through tectonic uplift in the Early and Middle Miocene and experienced dissolution caused by circulation of meteoric water in the shallower strata until the Middle Miocene. In the Late Miocene, plenty of organic acids were generated and expelled from the first mudstone member in the Lingshui Formation, entering the reservoir and dissolving minerals to form secondary pores. In the Quaternary, hydrocarbons began to fill the reservoir, preventing the pores from being filled and destroyed by carbonate cement to a certain extent. Finally, the first AHPZ was formed.

Organic acids, thermal fluids, and hydrocarbons were the main diagenetic fluids that led to the second AHPZ. The mechanism of organic acid dissolution and hydrocarbon filling affecting the second AHPZ is the same as that in the first AHPZ. Organic acids expelled from the second mudstone member of the Lingshui Formation in the Late Miocene caused dissolution in the second AHPZ, which was active until the Middle Pliocene. In the Early Pliocene, thermal fluid activity caused dissolution and enhanced the porosity. Meanwhile, hydrocarbon filling began to fill the reservoir, inhibiting carbonate cementation at the same time.

The third AHPZ is only found in some wells in the Baodao 19-B structure belt. The special geological location of the third AHPZ is close to the No. 2 fault where there was an active volcano and a high content of inorganic CO_2. Organic acids, thermal fluids rich in CO_2, and hydrocarbons have an important influence on the formation of AHPZ in the Baodao 19-B structure belt. In the Early Miocene, the source rock of the Yacheng Formation began to generate organic acids and caused reservoir dissolution, which was active until the Middle Miocene. In the Late Miocene, the second member mudstone of the Lingshui Formation started to generate organic acids and caused dissolution again, which was active until the Middle Pliocene. In the Middle Miocene, hydrocarbon filling inhibited the formation of carbonate cements. Meanwhile, the thermal fluid rich in mantle CO_2 began to dissolve minerals and formed secondary pores in the Pliocene, leading to the development of the third AHPZ.

6. Conclusions

The porosity variation, reservoir pore types, and corresponding diagenetic period are considered together for the identification of APHZs in the Songtao–Baodao region, eastern Qiongdongnan basin, South China Sea. There are three APHZs at depths of 2250~3100, 3700~4400, and 4800~5300 m. Moreover, the three APHZs were controlled by the multiple action of various diagenetic fluids, including meteoric water, dissolved organic acid from source rocks, thermal fluid rich in CO_2, and hydrocarbon fluids. In addition, it was concluded that three AHPZs in the Songtao–Baodao region resulted from various diagenetic fluids during different geological times.

Data Availability

Data are available on request from the corresponding author.

Conflicts of Interest

The authors declare no conflict of interest.

Authors' Contributions

X.C. and Y.W. analyzed the types and evolution of geological fluids and summarized the technical viewpoints; X.C. and A.S. analyzed the samples and organized geological data and jointly wrote the paper.

Acknowledgments

This research was funded by the Natural Science Foundation of Hubei Province, grant number 2020CFB372, and Open Foundation of Cooperative Innovation Center of Unconventional Oil and Gas (Ministry of Education & Hubei Province), grant number UOG2020-14.

References

[1] M. Hüpers, J. Ikari, B. Dugan, M. B. Underwood, and A. J. Kopf, "Origin of a zone of anomalously high porosity in the subduction inputs to Nankai Trough," *Marine Geology*, vol. 361, pp. 147–162, 2015.

[2] P. Dominic, S. Zhenbing, and S. D. Matthew, "Chemically-oscillating reactions during the diagenetic oxidation of organic matter and in the formation of granules in late Palaeoproterozoic chert from Lake Superior," *Chemical Geology*, vol. 470, pp. 33–54, 2017.

[3] G. H. Yuan, Y. C. Cao, Z. Jia, Y. Z. Wang, and T. Yang, "Research progress of abnormal high porosity zones in middle and deep clastic reservoirs in petroliferous basins," *Natural Gas Geoscience*, vol. 26, no. 1, pp. 28–42, 2016.

[4] L. Yang, L. Yu, D. Chen, K. Liu, P. Yang, and X. Li, "Effects of dolomitization on porosity during various sedimentation diagenesis processes in carbonate reservoirs," *Minerals*, vol. 10, no. 6, p. 574, 2020.

[5] P. J. Dowey, R. H. Worden, J. Utley, and D. M. Hodgson, "Sedimentary controls on modern sand grain coat formation," *Sedimentary Geology*, vol. 353, pp. 46–63, 2017.

[6] L. YOU, S. XU, C. LI, Y. ZHANG, Z. ZHAO, and P. ZHU, "Diagenesis-porosity evolution and "sweet spot" distribution of low permeability reservoirs: a case study from Oligocene Zhuhai Formation in Wenchang A sag, Pear River Mouth Basin, northern South China Sea," *Petroleum Exploration and Development*, vol. 45, no. 2, pp. 251–263, 2018.

[7] R. X. Li, S. Dong, D. Lehrmann, and L. Duan, "Tectonically driven organic fluid migration in the Dabashan Foreland Belt: evidenced by geochemistry and geothermometry of vein-filling fibrous calcite with organic inclusions," *Journal of Asian Earth Sciences*, vol. 75, no. 5, pp. 202–212, 2013.

[8] S. BARKER, S. COX, S. EGGINS, and M. GAGAN, "Microchemical evidence for episodic growth of antitaxial veins during fracture-controlled fluid flow," *Earth and Planetary Science Letters*, vol. 250, no. 1-2, pp. 331–344, 2006.

[9] S. M. Lange, S. Krause, A. C. Ritter et al., "Anaerobic microbial activity affects earliest diagenetic pathways of bivalve shells," *Sedimentology*, vol. 65, no. 4, pp. 1390–1411, 2018.

[10] U. Okyay and S. D. Khan, "Remote detection of fluid-related diagenetic mineralogical variations in the Wingate sandstone at different spatial and spectral resolutions," *International Journal of Applied Earth Observation and Geoinformation*, vol. 44, pp. 70–87, 2016.

[11] W. Patrick, H. Ulrike, K. Bastian, A. Dirk, and H. Christoph, "Critical evaluation of an upper Carboniferous tight gas sandstone reservoir: diagenesis and petrophysical aspects," *Marine and Petroleum Geology*, vol. 86, pp. 689–710, 2017.

[12] S. N. Ehrenberg, J. Zhang, and J. S. Gomes, "Regional porosity variation in Thamama-b reservoirs of Abu Dhabi," *Marine and Petroleum Geology*, vol. 114, article 104245, 2020.

[13] A. Berger, S. Gier, and P. Krois, "Porosity-preserving chlorite cements in shallow-marine volcaniclastic sandstones: evidence from Cretaceous sandstones of the Sawan gas field, Pakistan," *AAPG Bulletin*, vol. 93, no. 5, pp. 595–615, 2009.

[14] K. Violaki, J. Sciare, J. Williams, A. R. Baker, M. Martino, and N. Mihalopoulos, "Atmospheric water-soluble organic nitrogen (WSON) over marine environments: a global perspective," *Biogeosciences Discussions*, vol. 12, no. 10, pp. 3131–3140, 2015.

[15] H. Long, C. Xiang, J. Niu, and L. Wei, "Hydrothermal fluid flow and its influence on the hydrocarbon migration and accumulation along Binhai fault in Qikou sag, Bohai bay basin," *Acta Petrolei Sinica*, vol. 35, no. 4, pp. 673–684, 2014.

[16] C. C. Walters, F. C. Wang, K. Qian, C. Wu, A. S. Mennito, and Z. Wei, "Petroleum alteration by thermochemical sulfate reduction - A comprehensive molecular study of aromatic hydrocarbons and polar compounds," *Geochimica et Cosmochimica Acta*, vol. 153, pp. 37–71, 2015.

[17] J. W. Crompton, G. E. Flowers, D. Kirste, B. Hagedorn, and M. J. Sharp, "Clay mineral precipitation and low silica in glacier meltwaters explored through reaction-path modelling," *Journal of Glaciology*, vol. 61, no. 230, pp. 1061–1078, 2015.

[18] J. Peng, X. Wang, H. Han, S. Yin, Q. Xia, and B. Li, "Simulation for the dissolution mechanism of Cambrian carbonate rocks in Tarim basin, NW China," *Petroleum Exploration and Development*, vol. 45, no. 3, pp. 431–441, 2018.

[19] D. J. Smith, J. Naden, G. R. T. Jenkin, and M. Keith, "Hydrothermal alteration and fluid PH in alkaline-hosted epithermal systems," *Ore Geology Reviews*, vol. 89, pp. 772–779, 2017.

[20] Y. Chen, Y. X. Han, L. Z. Bian et al., "Geochemical characteristics and geochemical characteristics of the Paleogene sedimentary system in the northern South China Sea," *Oil & Gas Geology*, vol. 41, no. 5, pp. 1028–1037, 2020.

[21] L. Shao, A. Li, G. X. Wu, Q. Y. Li, C. L. Liu, and P. J. Qiao, "Sedimentary environment and provenance evolution of Qiongdongnan basin," *Acta Petroleum Sinica*, vol. 31, no. 4, pp. 548–552, 2010.

[22] Y. C. Zhang, X. D. Xu, J. Gan, J. T. Zhu, X. X. Guo, and X. H. He, "Geological characteristics, reservoir forming model and exploration direction of deep water gas field in Qiongdongnan basin," *Acta Geologica Sinica*, vol. 91, no. 7, pp. 1620–1633, 2017.

[23] X. M. Zeng, J. Yu, Y. Pan, X. W. Chen, and H. Zhang, "Study on the pore evolution and diagenetic facies of submarine fan in the northern slope of Lingshui sag," *Acta Sedimentologica Sinica*, vol. 36, no. 4, pp. 1198–1207, 2016.

[24] W. H. Li, Z. Z. Zhang, K. Zheng, and Y. C. Li, "geochemical characteristics and developmental models of the Eocene source rocks in the Qiongdongnan basin, northern south China sea," *Energy & Fuels*, vol. 31, no. 12, pp. 13487–13493, 2017.

[25] Y. Zhang, P. Wang, Y. Zhao, and Q. Z. Su, "Sedimentary formation and exploration significance of the Lingshui canyon system in the Qiongdongnan basin, northern South China Sea," *Journal of Oceanography*, vol. 37, no. 2, pp. 25–35, 2015.

[26] H. Su, H. Chen, X. Chen, H. P. Liu, Y. Liu, and M. Lei, "New insight into origin, accumulation and escape of natural gas in the Songdong and Baodao regions in the eastern Qiongdongnan basin, South China Sea," *Journal of Natural Gas Science and Engineering*, vol. 52, pp. 467–483, 2018.

[27] F. X. Ying, D. B. He, and Y. M. Long, *The industry standard of China and division of diagenetic stages in clastic rocks, SY/T5477-2003*, Petroleum Industry Press, Beijing, China, 2003.

[28] H. Ping, C. Li, H. Chen, S. C. George, and S. Gong, "Overpressure release: fluid inclusion evidence for a new mechanism for the formation of heavy oil," *Geology*, vol. 48, pp. 903–907, 2020.

[29] M. L. Frezzotti and S. Ferrando, "The chemical behavior of fluids released during deep subduction based on fluid inclusions," *American Mineralogist*, vol. 100, no. 2-3, pp. 352–377, 2015.

[30] J. Pszonka and M. Wendorff, "Carbonate cements and grains in submarine fan sandstones—the Cergowa beds (Oligocene, Carpathians of Poland) recorded by cathodoluminescence," *International Journal of Earth Sciences*, vol. 106, no. 1, pp. 269–282, 2017.

[31] A. Zarasvandi, Z. Fereydouni, H. Pourkaseb, M. Sadeghi, B. Mokhtari, and B. Alizadeh, "Geochemistry of trace elements and their relations with organic matter in Kuh-e-Sefid phosphorite mineralization, Zagros Mountain, Iran," *Ore Geology Reviews*, vol. 104, pp. 72–87, 2019.

[32] R. Hoffmann, D. K. Richter, R. D. Neuser et al., "Evidence for a composite organic-inorganic fabric of belemnite rostra: implications for palaeoceanography and palaeoecology," *Sedimentary Geology*, vol. 341, pp. 203–215, 2016.

[33] M. Oliveira and L. Ros, "Meteoric water and salt-dome-related diagenesis in tertiary turbidite reservoirs from the EspÍrito Santo basin, Brazil," *Journal of Sedimentary Research*, vol. 88, no. 12, pp. 1362–1380, 2018.

[34] S. W. Matthew and C. L. Kyger, "Isotopic and elemental evidence for meteoric alteration of a Pennsylvanian phylloid-algal mound holder formation, New Mexico, U.S.A," *Journal of Sedimentary Research*, vol. 85, no. 1, pp. 21–37, 2015.

[35] H. S. Shi, J. H. Yang, Y. C. Zhang, J. Gan, and J. H. Yang, "Geological knowledge innovation and a major breakthrough in deepwater natural gas exploration in Qiongdongnan Basin," *China Petroleum Exploration*, vol. 24, no. 6, pp. 691–698, 2019.

[36] J. X. Zhang, H. W. Yin, J. T. Zhu et al., "Effect of basement properties on fault structures: a case study of Qiongdongnan Basin," *Geological Journal of China Universities*, vol. 24, no. 4, pp. 563–572, 2018.

[37] B. B. Liu, X. H. Yu, J. F. Wu et al., "Half-graben types and sedimentary filling models in the continental margin basin of the northern South China Sea," *Journal of China University of Mining and Technology*, vol. 3, pp. 498–507, 2015.

[38] J. Hao, H. Liu, and P. L. Zou, "Mechanisms of natural gas accumulation and leakage in the overpressured sequences in the Yinggehai and Qiongdongnan basins, offshore South China Sea," *Earth Science Frontiers*, vol. 22, no. 1, pp. 169–180, 2015.

[39] P. Matteo, A. H. Amena, M. Daniel et al., "Impact of stylolitization on diagenesis of a lower Cretaceous carbonate reservoir from a giant oilfield, Abu Dhabi, United Arab Emirates," *Sedimentary Geology*, vol. 335, no. 15, pp. 70–92, 2016.

[40] J. Friedman and R. O'Neil, "Compilation of stable isotope fractionation factors of geochemical interest," *US Geological Survey Professional Paper*, vol. 440, no. 12, 1997.

[41] J. G. Ren, Y. P. Huang, Z. S. Fang, and X. B. Wang, "Oxygen and hydrogen isotope composition of meteoric water in the tropical West Pacific Ocean," *Acta Oceanologica Sinica*, vol. 22, pp. 60–64, 2000.

[42] K. Barbara, E. Elena, S. Jan, and H. Hanspeter, "Chemical accuracy obtained in an ab initio molecular dynamics simulation of a fluid by inclusion of a three body potential," *Chemistry*, vol. 4, no. 3, pp. 383–388, 1998.

[43] J. X. Dai, D. Z. Dong, Y. Y. Ni et al., "Some essential geological and geochemical issues about shale gas research in China," *Natural Gas Geoscience*, vol. 36, no. 6, pp. 745–760, 2020.

[44] Y. H. Xie, "Quantitative evaluation of capping ability of high temperature and high pressure cap rocks in Yinggehai basin," *Chinese Journal of Earth Sciences*, vol. 44, no. 8, pp. 2579–2589, 2019.

[45] K. Liu, Y. Sun, and Q. Q. Yu, "Characteristics of dissolutions of CO_2 geological storage applied to the Ordovician reef limestone in Bachu area of Tarim Basin," *Journal of Earth Sciences and Environment*, vol. 35, no. 3, pp. 1–4, 2013.

[46] D. Morad, F. H. Nader, M. Gasparrini et al., "Comparison of the diagenetic and reservoir quality evolution between the anticline crest and flank of an Upper Jurassic carbonate gas reservoir, Abu Dhabi, United Arab Emirates," *Sedimentary Geology*, vol. 367, no. 5, pp. 96–113, 2018.

[47] R. N. Greenberger, J. F. Mustard, E. A. Cloutis et al., "Hydrothermal alteration and diagenesis of terrestrial lacustrine pillow basalts: coordination of hyperspectral imaging with laboratory measurements," *Geochimica et Cosmochimica Acta*, vol. 175, no. 15, pp. 174–200, 2015.

[48] J. L. Soares, A. C. R. Nogueira, R. F. dos Santos, P. Sansjofre, M. Ader, and W. Truckenbrodt, "Microfacies, diagenesis and hydrocarbon potential of the Neoproterozoic cap carbonate of the southern Amazon craton," *Sedimentary Geology*, vol. 406, pp. 1–20, 2020.

Hindawi
Geofluids
Volume 2021, Article ID 5527299, 18 pages
https://doi.org/10.1155/2021/5527299

Research Article

Minerals Filling in Anhydrite Dissolution Pores and Their Origins in the Ordovician Majiagou Formation of the Southeastern Ordos Basin, China

Lihong Liu,[1,2] **Chunlian Wang**,[3] **Zhili Du**,[1] **and Jianghua Gong**[3]

[1]*Oil & Gas Survey, China Geological Survey, Beijing 100083, China*
[2]*Oil and Gas Research Center, School of Earth and Space Sciences, Peking University, Beijing 100871, China*
[3]*MNR Key Laboratory of Metallogeny and Mineral Assessment, Institute of Mineral Resources, Chinese Academy of Geological Sciences, Beijing 100037, China*

Correspondence should be addressed to Chunlian Wang; wangchunlian312@163.com

Received 20 January 2021; Revised 11 March 2021; Accepted 20 March 2021; Published 20 April 2021

Academic Editor: Guo Xiang Chi

Mold pore cementation is the key factor constraining the reservoir property in the study area. The anhydrite dissolution pores in the Ordovician Majiagou Formation of southeastern Ordos Basin are commonly filled by minerals such as dolomite, calcite, pyrite, and quartz accounting for more than 90% of the total molds resulting in significant porosity volume reduction. The anhydrite dissolution pores in the Jingbian Gas Field in the middle east of the basin, however, are rarely filled by minerals with more than 30% molds, remaining open to become good reservoir space. Studies reveal that the calcite filling in anhydrite dissolution pores has a relatively negative $\delta^{18}O$ value (-15.58‰~-8.96‰ VPDB) and negative $\delta^{13}C$ value (-7.56‰~0.26‰ VPDB), which is interpreted to be caused by thermochemical sulfate reduction (TSR). The higher homogenization temperatures (140-234°C) and high salinity (19.13-23.18 wt.% NaCl equivalent) of the primary inclusions in calcite confirm the above interpretation. Dolomite is the second most abundant carbonate formed as by-product of TSR, which is promoted by the precipitation of calcite and resulted enriched in Mg^{2+}/Ca^{2+} ratio in the pore water. Pyrite forms by the reaction of H_2S released from TSR with the Fe^{2+} in the horizon, which is supported by its cubic habit and relatively high $\delta^{34}S$ value (10.50‰~24.00‰VCDT). Quartz with relatively high homogenization temperature (113-154°C) is considered to precipitate in low-pH solution from calcite and pyrite precipitation after TSR. The southeastern Ordos Basin is much lower than the Jingbian Gas Field in paleogeographic location, which is submerged in the sea water of marine phreatic environments for a long time when sea water flooded from the southeastern direction. TSR occurs due to calcium sulfate enriched in pore water resulting in the minerals of dolomite, calcite, pyrite, and quartz filling in the molds leading to the low porosity and permeability of the study area.

1. Introduction

The anhydrite nodule-bearing dolomite is widely distributed in the Ordovician Majiagou Formation of southeastern Ordos Basin. The anhydrite nodule normally occurs in settings interpreted to be sabkhas [1, 2], intertidal to shallow subtidal [3], and even deeper subtidal settings [4]. The anhydrite nodules in the present case are formed in evaporative tidal flat facies but mostly leached by fresh water [5]. The nodular morphology suggests precursor gypsum or anhydrite. The gypsum is commonly dehydrated to anhydrite in the shallow burial condition; therefore, the nodules are normally filled by anhydrite when deep buried. Nevertheless, the anhydrite has been dissolved by fresh water during an episode of subaerial exposure during the Caledonian orogeny [6] forming the major reservoir space of the basin in the Ordos Basin. However, the anhydrite dissolution pores are commonly filled by minerals, such as dolomite, calcite, pyrite, and quartz, resulting in significant porosity and volume reduction. The minerals filling in molds are

conventionally interpreted to be formed in near surface conditions. However, the cementation of molds can occur at any time in the burial cycle from eogenesis through mesogenesis and into telogenesis.

The filling of anhydrite dissolution pores by calcite and dolomite can be interpreted as the replacement of sulfate by carbonate driven by various hydrological processes, such as bacterial sulfate reduction [7–9]. Pierre and Rouchy [7] interpreted the low $\delta^{13}C$ value from organic origin and the low $\delta^{18}O$ value caused by the large quantities of energy released during the bacterial sulfate reduction. It can also be the result of an active volcanogenic system [2] or even associated with cycling of seawater through hydrothermal anhydrite in mid-ocean ridges [10]. Late stage calcite replacement of evaporite nodules has also been reported to be associated with thermochemical sulfate reduction (TSR) [11, 12]. However, the most widely documented process is related to the meteoric water in the active phreatic zone but not in the deep subsurface [13–15]. The dissolution of sulfate and precipitation of minerals can significantly change the porosity and permeability of the horizon. To study the fabric and the formation process of replacement of evaporite is of economic and of scientific significance. Based on the outcrops and well cores in the southeastern Ordos Basin, thin section observation, stable isotopic analyses, scanning electron microscope (SEM), and fluid inclusion analyses are undertaken to study the time, process, and conditions of evaporite replacement to provide valuable information on the pore fluid properties and predict the reservoir quality.

2. Geological Background

The Ordos Basin, located in the middle-west of China, is the second largest basin in China with an area of 2.5×10^5 km^2 [16]. In the Ordovician Majiagou Formation, affected by the Helan Rift valley tension in the west of the basin, the rift shoulder rises forming the Central Uplift (also known as "L" shaped paleo-uplift group) [17–19]. Under the action of crustal equalization compensation, the compensating Shanbei Depression forms in the Middle East of the basin, which deposits anhydrite halite in drought-hot climate. The Jingbian Gas Field is located in the transitional zone between the Central Uplift and the Shanbei Depression (Figure 1). A set of dolomicrite to fine crystalline dolomite is developed in restricted to semirestricted platforms in the Jingbian Gas Field. The study area is located in the southeast of the basin far from the central uplift depositing anhydrite nodule-bearing dolomite in evaporite platform facies.

In the late Ordovician, the basin was uplifted and subjected to exposure for more than 140 My during Caledonian orogeny, forming a significant regional unconformity above the Majiagou Formation [6]. The Ordovician Majiagou Formation can be divided into six members. Member 6 is eroded in most regions and only found in the southern part of the basin with a thickness of 10 to 20 m. Members Ma_1 to Ma_5 are developed all over the basin and can be laterally traced for several kilometers. Owing to the periodic sea-level changes, a set of transgression–regressive cycles are deposited in the Majiagou Formation, in which Ma_1, Ma_3, and Ma_5 members are mainly composed of dolomite and anhydrite in evaporite platform facies, whereas the Ma_2, Ma_4, and Ma_6 members are dominated by limestone and dolomite in open platform facies (Figure 1) [16, 20]. Up to 10 submembers (Ma_5^1, Ma_5^2,…, Ma_5^{10}) have been identified in member 5 with cyclic carbonate-evaporite intervals related to the short term sea-level variations (Figure 1) [5]. The Ma_5^1 to Ma_5^4 submembers are mainly composed of fine microcrystalline dolomite, anhydrite, karst breccia, and anhydrite nodule-bearing dolomite. Because of the dissolution of anhydrite nodules in meteoric water, a favorable reservoir developed in the upper four submembers of the Ma_5 member, which became the major gas producing strata. Yican 1 well, drilled in 2014, produces 3.5×10^4 m^3 gas daily in Ma_5^1 and Ma_5^4 submembers where the anhydrite nodules, dolomite, and fractures are developed.

The anhydrite dissolution pores account for more than 90% of pore types both in the Jingbian Gas Field and the southeastern Ordos Basin. Mold pore cementation is the key factor constraining the reservoir property in the study area. The anhydrite dissolution pores in the Jingbian Gas Field are mostly filled by dolomite accounting for less than 70% of the total porosity with abundant pores remaining open, whereas the anhydrite dissolution pores of Yican 1 well are mainly filled by minerals accounting for more than 90% of the overall porosity in southeastern Ordos Basin, leading to the significant reduction of porosity (Figure 2) [21, 22]. Therefore, the porosity differences between the Jingbian Gas Field and the southeastern Ordos Basin are mainly caused by the filling degree of the anhydrite dissolution pores. Accurate analysis of the genesis of minerals filling in the pores is beneficial to understand the fluid activity process and predict effective reservoirs.

3. Samples and Methods

More than 60 samples from the Ordovician Majiagou Formation of Yican 1 well in the southeastern Ordos Basin over a depth of 2631 to 3132 m are examined by an optical microscope. Data from other wells of the Jingbian Gas Field were used for comparison.

Hand specimens of carbonates have been sampled selectively with a small drill to obtain samples from a very limited area. Samples used for carbon and oxygen analysis are mainly obtained from the gypsum molds and dolomite matrix. Powder samples (~30–50 mg per single sample) of limestone, dolostone, and anhydrite were extracted for carbon and oxygen isotope measurements. The powdered samples were heated to remove organic materials and then reacted with anhydrous phosphoric acid under vacuum to release CO_2 at 25°C for 24 h. The CO_2 was then analyzed for carbon and oxygen isotopes on a Finnigan MAT251 mass spectrometer. All carbon and oxygen data are reported in ‰ units relative to the Vienna Pee Dee Belemnite (VPDB) standard (Hoefs, 2009). The precision for both $\delta^{13}C$ and $\delta^{18}O$ measurements is better than ±0.1‰. Ultrafabrics were studied using a Melin-type scanning electron microscope (SEM) (Carl Zeiss AG) operated at 15–20 kV with a 10 nA beam curt and a working distance of 10 mm. The mineral composition was

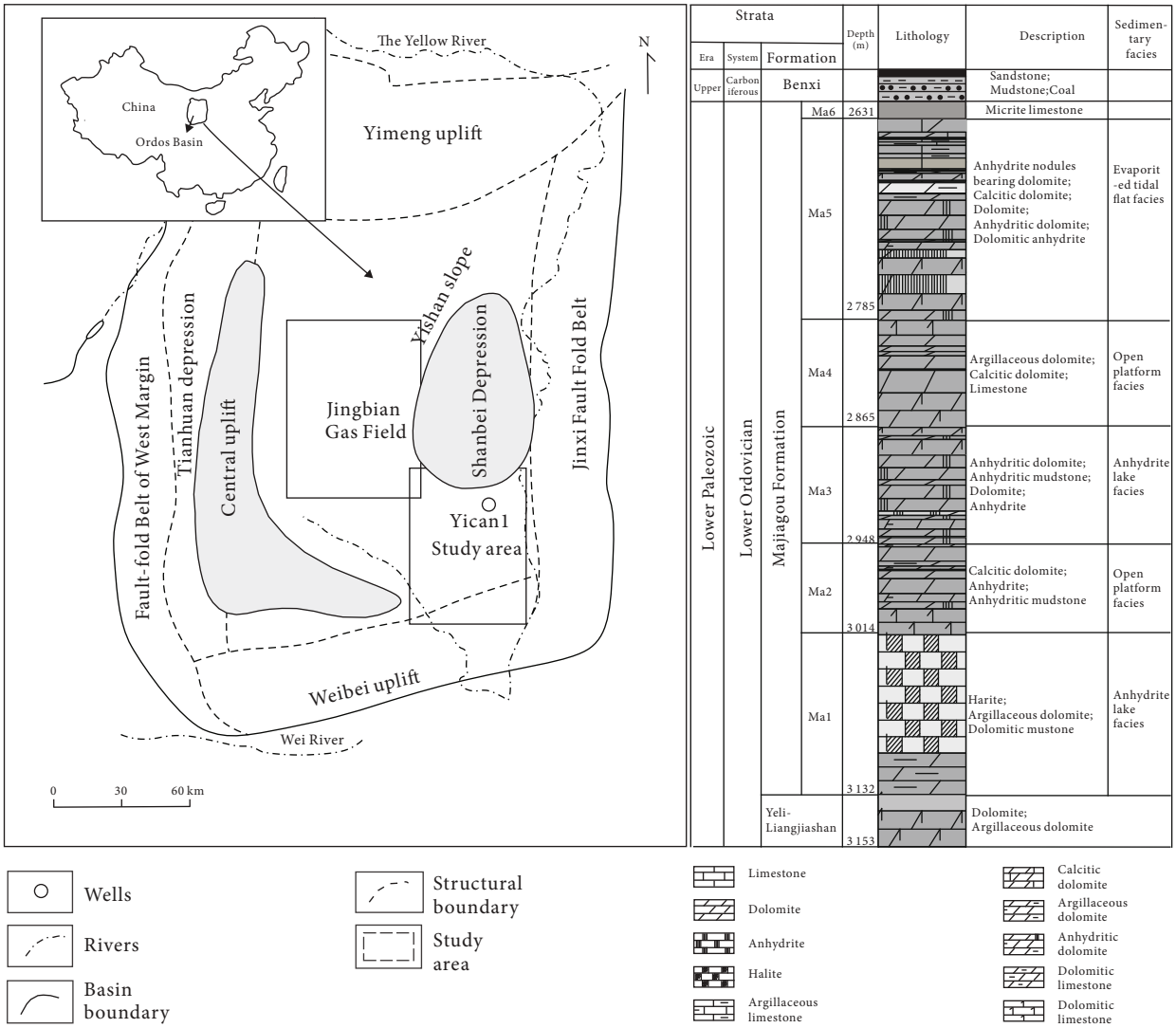

Figure 1: Simplified structural map of the Ordos Basin showing the study area and the Jingbian Gas Field [6] and the lithocolumn of the main sampled Yican 1 well.

observed by back scattered electron image (BSE), and the elemental concentrations and spatial variation of micron-sized spots were determined using energy-dispersive spectrometry (EDS) at the China University of Petroleum (College of Geosiences), which could generate high-resolution, high-magnification images revealing carbonate textures.

A total of 14 pyrite samples were analyzed for their sulfur isotope ratios. 30 mg of pyrite was mixed with Cu_2O at 1100°C under vacuum to produce SO_2. SO_2 was then analyzed on a Delta v plus Isotope Ratio Mass Spectrometer. The $\delta^{34}S$ values are reported relative to the Vienna-Canyon Biablo Troilite (V-CDT) standard [23]. The precision is better than 0.1‰.

Fluid inclusion heating-freezing analyses were conducted via a ZEISS Axioskop 40 A Pol with a Linkam THMS600 heating and cooling stages. An ultraviolet fluorescence system was used to discern hydrocarbon inclusions. The final melting temperature T_m and the homogenization temperature T_h were measured in all samples. Accuracy for measurements for homogenization temperature and melting temperature is ±1°C and ±0.1°C, respectively. The melting temperatures were converted to salinity values (equivalent wt.% NaCl) according to standard equations [23]. The bulk melting was close to the NaCl eutectic in most samples.

4. Results

4.1. Petrography. Anhydrite nodules primarily occur in thinly laminated dolomicrite, which also occur interlayered with anhydrite. The thinly laminated dolostones contain increasing amounts of anhydrite nodules from downward to upward of the unit. The nodules are spherical, ovoid, or, in some cases, elongate, ranging from 1 to 2 mm across (Figures 3(a)–3(d) and 4(a)–4(k)). Synsedimentary and early diagenetic nodular and contorted anhydrite structures are common diagnostic features of modern tidal environments [10]. The anhydrite nodules are partially or totally dissolved, where the carbonates display a vuggy internal

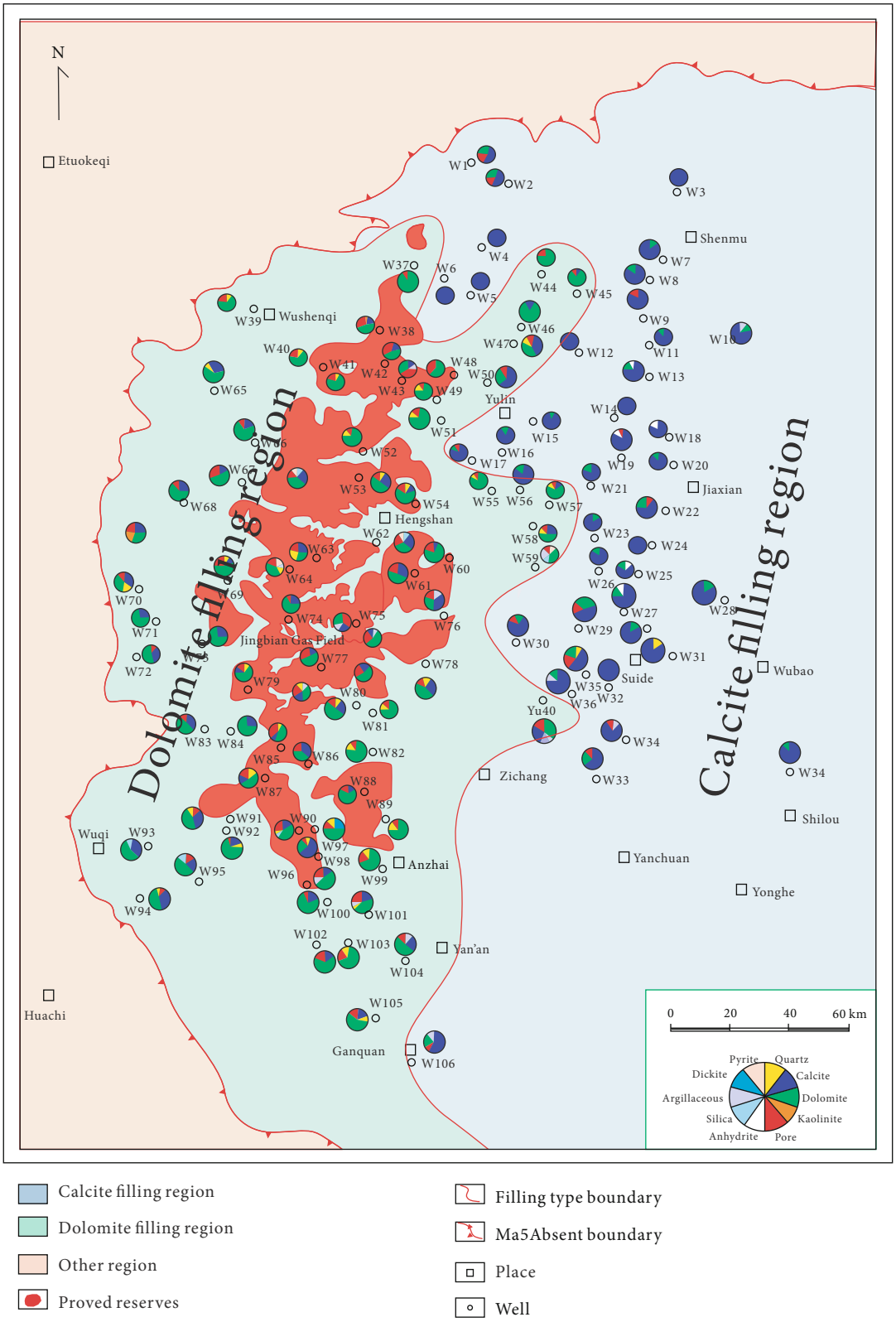

Figure 2: The distribution map of minerals filling in anhydrite dissolution pores in the Ordovician Majiagou Formation of Ordos Basin (modified from [21, 22]).

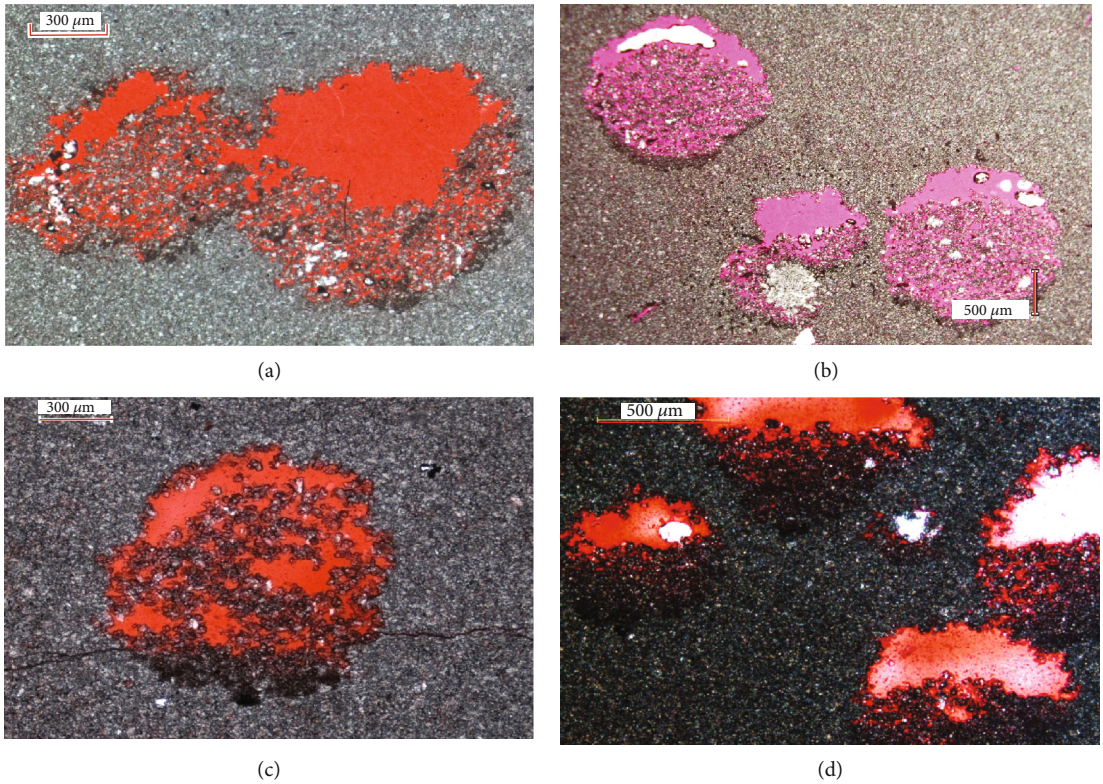

Figure 3: The occurring characteristics of anhydrite dissolution pores in the Ordovician Majiagou Formation in the Jingbian Gas Field (red and pink casting colors represent anhydrite dissolution pores).

microstructure, leaving molds to increase the overall reservoir properties. The anhydrite dissolution pores are more developed in the Jingbian Gas Field, which are rarely or partially filled by minerals (Figures 3(a)–3(d)). However, in the southeastern Ordos Basin, the molds are normally cemented by calcite, dolomite, quartz, etc. which resulted in the significant reduction of primary porosity in some core intervals.

4.1.1. Dolomite. Two types of dolomites are identified in the anhydrite dissolution pores. The first type is the fine crystalline dolomite at the bottom of the nodules (Figures 3(a)–3(d) and 4(c)–4(j)). The dolomite crystals at the bottom of the nodule are larger than the matrix dolomite with sizes ranging from 0.01 to 0.04 mm. The crystal density decreases, and the size increases from the bottom of the nodule towards the center of the mold. The fine crystalline dolomites are always at the bottom of the nodule as "seepage silts" forming the geopetal structures indicating the top of the horizon. The fine crystalline dolomite accounts for 60%-70% of the total nodule with the remaining pores open (Figures 3(a)–3(d)) or filled with other minerals (Figures 4(a)–4(k)). The pores are mainly filled with this type of dolomite in the Jingbian Gas Field with the remaining pores open (Figure 2). The remained pores account for 20%-30% of the nodule forming the major reservoir space of the unit.

The other type of dolomite occurs as euhedral dolomite crystals in the upper part of the nodules with crystal sizes in the range of 50-500 μm (Figures 4(c)–4(e)). The crystals are in rhombic morphology with cloudy surface. Fluorescent light images show that the hydrocarbon inclusions are abundant in the pores of seepage silt at the bottom of the nodule, and some are observed in the lattice defect of dolomite crystals (Figure 4(f)). Some dolomite crystals have slightly curved crystals with undulose extinction as saddle dolomites (Figure 4(g)).

4.1.2. Calcite. Different from the concentric structure defined by a succession of different types of quartz and carbonate phases documented in many literatures [10, 24], the nodules in this study are commonly composed of "seepage silt" at the bottom and carbonate phases and quartz at the top. The molds are formed by the dissolution of anhydrite and filled with blocky calcite spar (Figures 4(h)–4(j)). The calcite crystal morphology is outlined by the outer envelopes of the pore space. Individual crystal is normally coarse to very coarse crystalline of about 500-1000 μm in diameter. Some crystals are clear with crossed twinning apparently free of evaporite inclusions (Figure 4(h)). Many of the calcites contain primary hydrocarbon inclusions as shown in fluorescent light images (Figure 4(k)).

4.1.3. Quartz. The quartz is observed to fill the same pore or vug with calcite in direct contact with the long axes commonly perpendicular to the surface in which they lie as a single euhedral crystal (Figures 4(d) and 4(h)). The crystals are clear with few inclusions, which display unit or undulose extinction. The single euhedral crystal is mainly hexagonal, bipyramidal, and up to 0.5 mm long. SEM photos show the

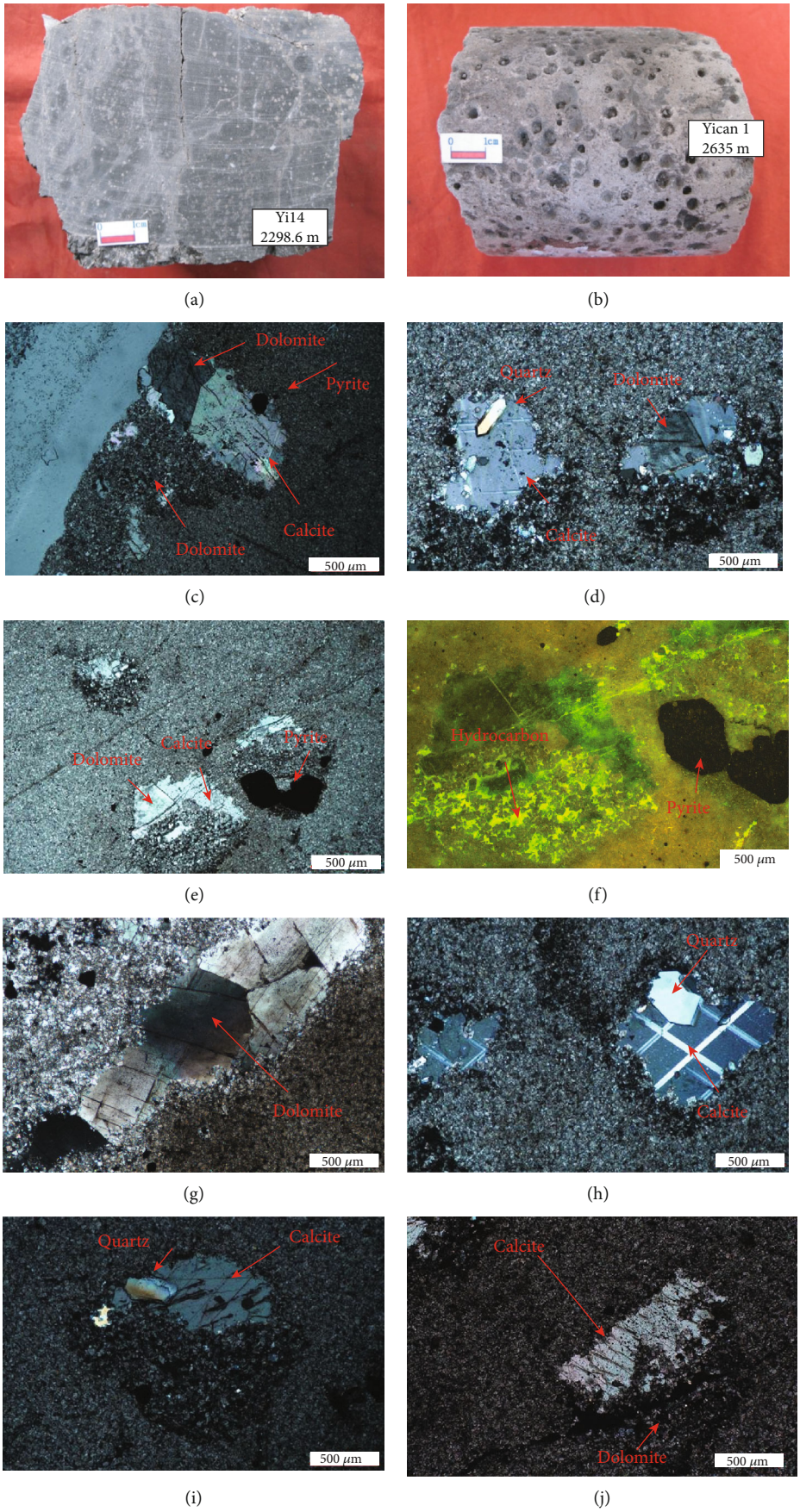

Figure 4: Continued.

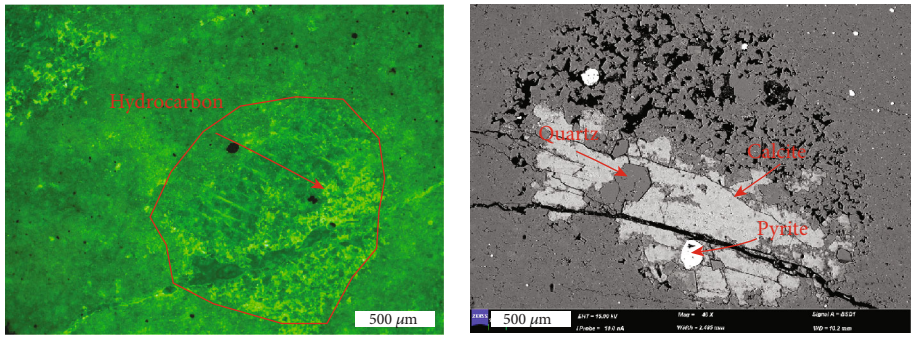

(k) (l)

Figure 4: Minerals filling in anhydrite dissolution pores of the Ordovician carbonate in Yican 1 well in the southeastern Ordos Basin. (a) Anhydrite nodule-bearing dolomite in Yi14 well, 2298.6 m, Ma_5^1. (b) Anhydrite dissolution pores in the core of Yican 1 well, 2635 m, Ma_5^1. (c) Anhydrite dissolution pores filled with dolomite, calcite, and pyrite in Yican 1 well, 2642.5 m, Ma_5^1, sample 96. (d) Anhydrite dissolution pores filled with dolomite, calcite, and quartz, 2641.4 m, Ma_5^1, sample 92. (e) Anhydrite dissolution pores filled with dolomite, calcite, and pyrite, 2642.5 m, Ma_5^1, sample 96. (f) Ultraviolet fluorescence photo shows hydrocarbon inclusions enriched in dolomite at the bottom of the nodule and lattice defect of calcite at the top of nodule, 2642.5 m, Ma_5^1, sample 96. (g) Saddle dolomite showing undulose extinction in the anhydrite dissolution pores, 2951.5 m, Ma_2, sample 242. (h) Calcite with crossed twinning and euhedral quartz filling in anhydrite dissolution pores, 2641.4 m, Ma_5^1, sample 92. (i) Anhydrite dissolution pores filled with calcite and quartz, 2642.5 m, Ma_5^1, sample 96. (j) Anhydrite dissolution pores filled with dolomite and calcite, 2640.9 m, Ma_5^1, sample 90. (k) Ultraviolet fluorescence photo shows hydrocarbon inclusions enriched in dolomite at the bottom of the nodule and lattice defect of calcite at the top of nodule, 2640.9 m, Ma_5^1, sample 90. (l) SEM photo of calcite, pyrite, and quartz filling in the anhydrite dissolution pores, 2641.4 m, Ma_5^1, sample 92.

high porosity in the fine crystalline dolomite at the bottom of the mold and the euhedral pyrite and quartz together with individual calcite crystal filling in the mold pore (Figure 4(l)).

4.1.4. Pyrite. Pyrite occurs as cubic crystals up to millimeter size scattered in laminated dolomicrite or in some cases within anhydrite dissolution pores (Figures 4(c) and 4(e)). The occurrence of pyrite is often accompanied by anhydrite, indicating its close association with the anhydrite dissolution. Under transmitted light, the crystal displays black color. Under SEM, the pyrite is white with Fe and S spectra identified from the EDS image (Figure 5).

4.1.5. Anhydrite. Anhydrite is found in nodules in the subsurface cores far from unconformity but rarely observed in nodules near the unconformity, indicating that the carbonate near the unconformity has undergone considerable late stage leaching of evaporite, resulting in the development of significant secondary porosity.

4.2. Geochemistry Data. Stable isotope compositions are determined for calcite cement and matrix dolomite. The data are plotted in Figure 6. The calcite cements have stable isotope values of $\delta^{18}O$ from -15.58‰ to -8.96‰ VPDB, average -12.12‰VPDB, and $\delta^{13}C$ from -7.56‰~0.26‰ VPDB, average -4.66‰ VPDB. Matrix dolomite has $\delta^{18}O$ from -10.95‰ to -6.75‰VPDB, average -8.47‰VPDB, and $\delta^{13}C$ from -6.87‰ to 0.18‰ VPDB, average -1.84‰ VPDB. Sulfur isotope analysis result shows that the $\delta^{34}S$ value of pyrite is between 10.50‰ and 24.00‰ VCDT with an average 17.33‰ VCDT ($n = 11$).

4.3. Homogenization Temperature of Fluid Inclusions. The fluid inclusions in calcite have a varied size of 1-10 μm but are mostly smaller than 5 μm as single or groups (Figures 7(a)–7(c)). Some fluid inclusions are two-phase liquid-gas inclusions, which can be classified as primary and secondary inclusions. The primary inclusions occur as a single inclusion in the crystal or isolated away from other inclusions (Figure 7(c)). The fluid inclusion assemblage (FIA) concept has also been used in the study as they are cooccurrence of different types of inclusions of the same origin in the same host minerals [25]. An ultraviolet fluorescence system was used to discern hydrocarbon inclusions. Under the optical microscope, liquid hydrocarbon inclusions show light brown or straw yellow in transmission light, and the gas hydrocarbon inclusions are commonly brown colors (Figure 7(d)). Some gas hydrocarbon inclusions show brownish black color in transmission light (Figures 7(e) and 7(f)), whereas under ultraviolet fluorescence light, the hydrocarbon always shows fluorescence color from green (Figure 7(g)), strong yellow (Figures 7(h) and 7(i)), to weak blue and orange color with increasing thermal evolution degree.

The homogenization temperatures of the primary inclusions in calcite and dolomite are in between 140 and 234°C ($n = 6$) and 190 and 193°C ($n = 2$), respectively (Table 1). The NaCl-equivalent salinities range from about 19.13 to 23.18 weight % approaching halite saturation. The quartz filling in the anhydrite dissolution pores had similar fluid inclusion homogenization temperatures as the associated calcite cements in a range of 113-154°C with an average 131°C ($n = 4$).

4.4. The Total Salinity of Formation Water. The total salinity of formation water has been analyzed as listed in Table 2. The total salinity of the formation water of the Ordovician Majiagou Formation in the southeastern Ordos Basin is very high, which can be up to 295.04 g/L, an average 150.31 g/L. The water type is mainly $CaCl_2$. The high salinity of the formation water shows that the $CaSO_4$ concentration is very high as shown in Table 2.

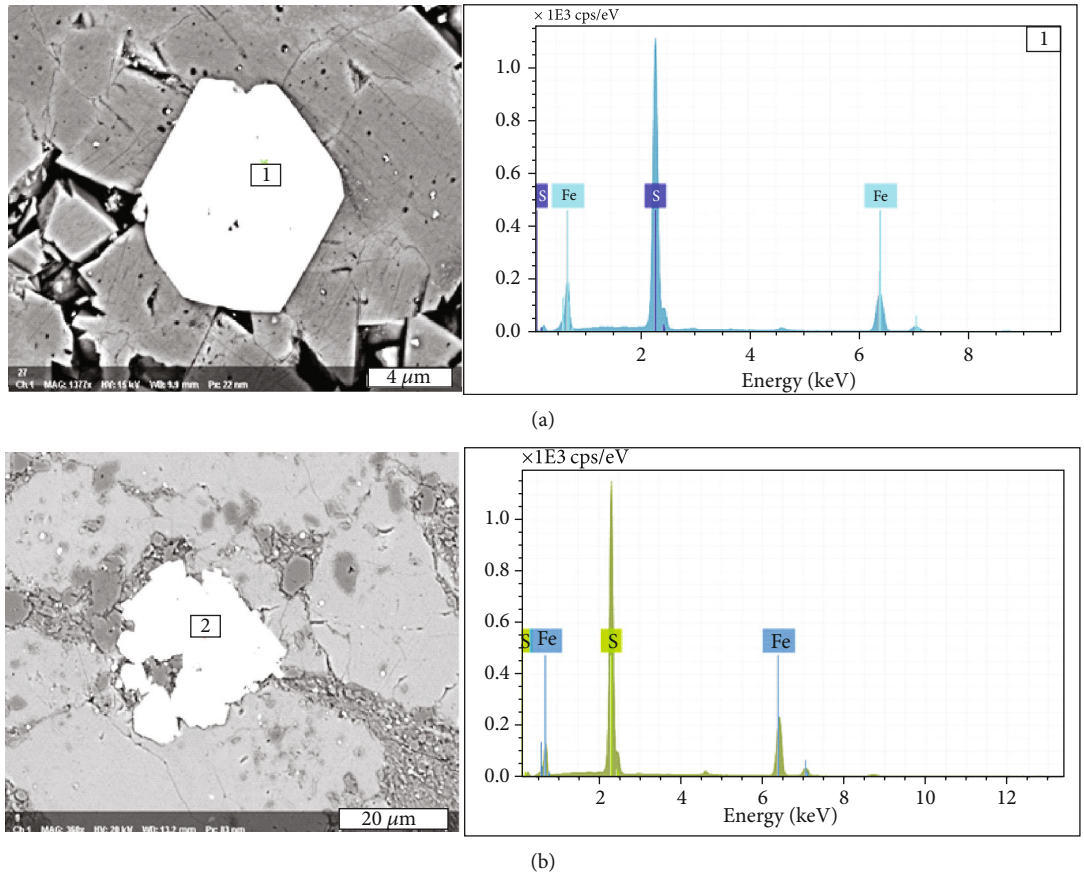

Figure 5: SEM and EDS analysis results of pyrite in Yican 1 well of the southeastern Ordos Basin. (a) Cubic pyrite in Yican 1 well, 2646.64 m, Ma_5^1. (b) Pyrite assemblage in Yican 1 well, 2684.86 m, Ma_5^4.

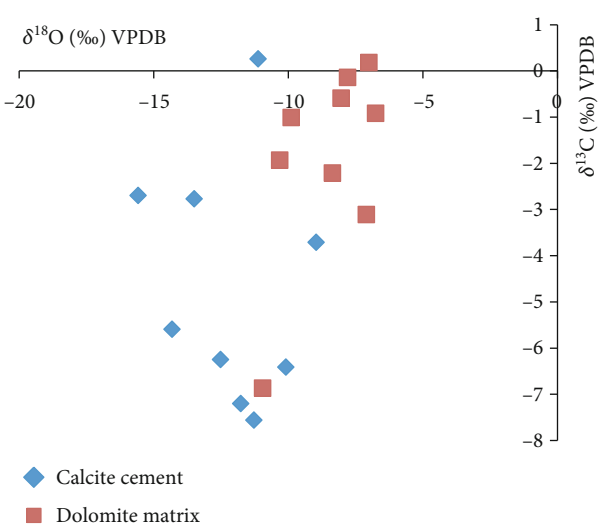

Figure 6: Cross-plot of $\delta^{18}O$ vs. $\delta^{13}C$ values of calcite cement and dolomite matrix of Yican 1 well in the southeastern Ordos Basin.

5. Discussions

Anhydrite nodule-bearing dolomite was interpreted to be formed by the penecontemporaneous dolomitization mode of the sabkha evaporative tidal flat [26]. The anhydrite and dolomite cyclical intervals are typical for shallow subtidal to supratidal evaporative settings. The dissolution molds are permeated by meteoric water during an episode of subaerial exposure during the Caledonian orogeny as they are restricted to the upmost 10 m below unconformity [6]. However, the cementation of the molds probably occurs in late burial settings.

5.1. Origin of Minerals Filling in Anhydrite Dissolution Pores

5.1.1. Calcite. The clean calcites containing no anhydrite inclusions suggest that they grow slowly in an open space where the anhydrite has been removed, which is confirmed by the existence of seepage silt at the bottom of the mold. The hydrocarbon inclusions in the calcite and in the residual pores at the bottom seepage silt indicate that the calcite probably precipitates when the hydrocarbon migrates to react with the dissolved sulfate in the pores. The original pore water in the Majiagou Formation would have been normal seawater to evaporative brines as the host rock consists of shallow marine platform limestone in the lower part of the formation and extensive evaporative facies in the upper part of the formation [27–29]. The initial pore fluid could have been diluted by meteoric water in much of the basin during the extended period of subaerial exposure [29]. The aqueous fluid inclusions in calcite filling in the molds, however, have

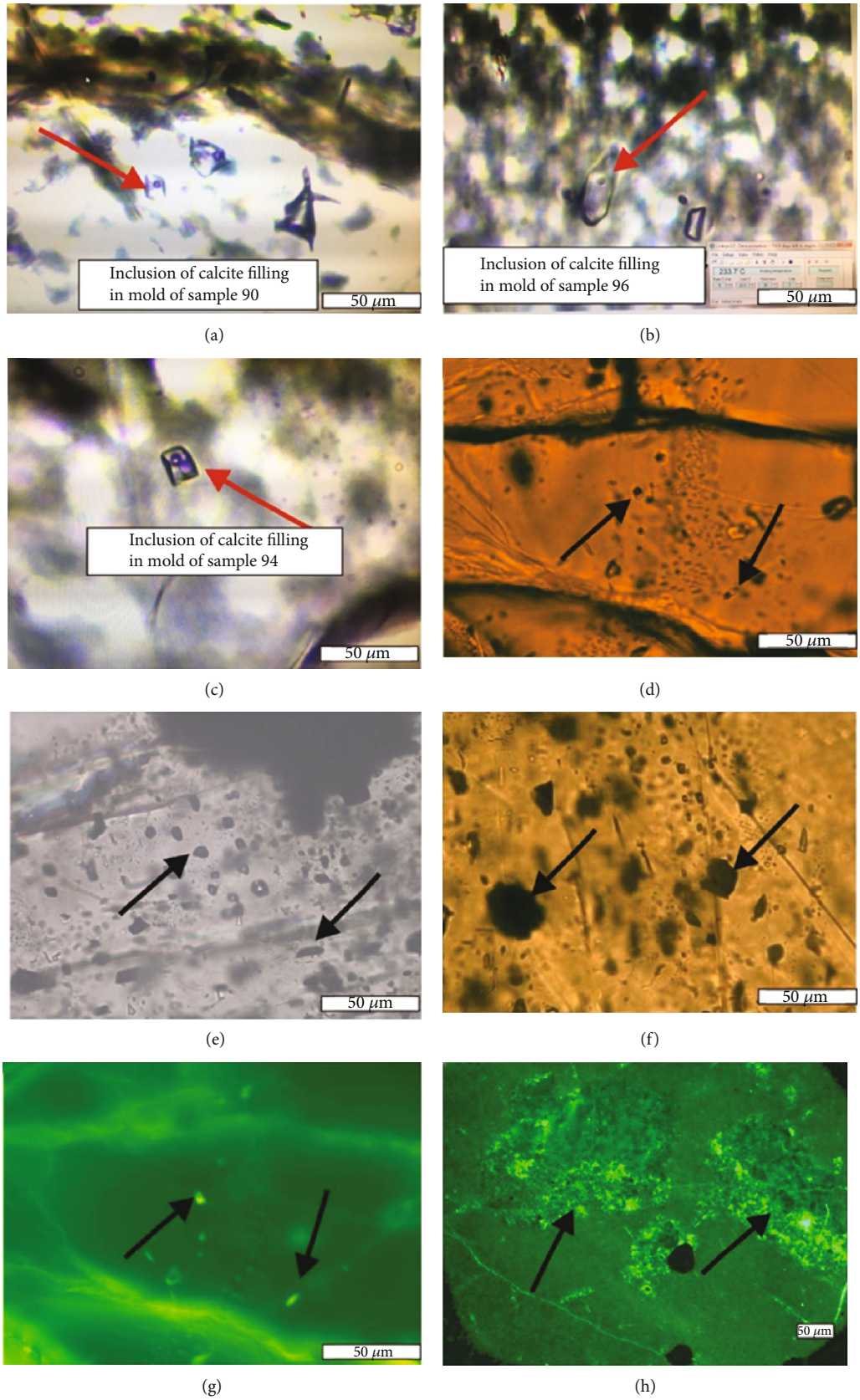

Figure 7: Continued.

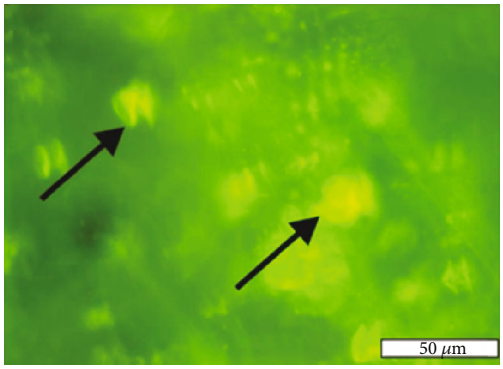

(i)

Figure 7: Characteristics of fluid inclusions in minerals filling in anhydrite dissolution pores in Yican 1. (a) Two-phase liquid-vaporous inclusions (WL+V) in calcite filling in anhydrite dissolution pores corresponding to Figures 4(j) and 4(k), 2640.9 m, Ma_5^1, sample 90. (b) Two-phase liquid-vaporous inclusions (WL+V) in calcite filling in anhydrite dissolution pores corresponding to Figure 4(i), 2642.5 m, sample 96. (c) Two-phase liquid-vaporous inclusions (WL+V) in calcite filling in anhydrite dissolution pores, 2641.8 m, sample 94. (d) Two-phase hydrocarbon inclusions of calcite filled in fracture showing light brown (OL) and black color (OV) in transmission light, 2642.5 m, sample 96. (e, f) Vaporous hydrocarbon inclusions (OV) of calcite showing black color in transmission light, 2635 m, sample 73. (g) Two-phase hydrocarbon inclusions of calcite filled in fracture showing light yellow (OV) and no fluorescence light (OV) in ultraviolet fluorescence light (the same thin section of (d)), 2642.5 m, sample 96. (h) Liquid hydrocarbon (OL) in the dolomite at the bottom of mold showing light green color in ultraviolet fluorescence light, 2641.8 m, sample 94. (i) Vaporous hydrocarbon inclusions (OV) of calcite showing yellow color in ultraviolet fluorescence light (the same thin section of (f)), 2635 m.

Table 1: Homogenization temperature of fluid inclusions in minerals filling in anhydrite dissolution pores in Yican 1 of the southeastern Ordos Basin.

No.	Samples	Minerals filling in molds	Homogenization temperature (°C)	Average (°C)	Melting temperature (°C)	Calculated salinity (%)	Average (%)
1	94	Dolomite	190	193	-17.3	20.45	21.81
2	94	Dolomite	196		-21.2	23.18	
3	90	Calcite	148	172	-15.6	19.13	21.03
4	90	Calcite	164		-15.6	19.13	
5	94	Calcite	174		-17.1	20.3	
6	94	Calcite	170		-18.4	21.26	
7	96	Calcite	140		-21.2	23.18	
8	96	Calcite	234		-21.2	23.18	
9	94	Quartz	113	131	-20.1	22.44	16.59
10	94	Quartz	129		-20.1	22.44	
11	96	Quartz	127		-18.7	21.47	
12	96	Quartz	154		10	0.02	

Table 2: Formation water composition of some wells of the Ordovician Majiagou Formation in the southeastern Ordos Basin.

Well	Formation	Section (m)	Ion content (mg/L)						Total salinity (g/L)	Water type
			K^++Na^+	Ca^{2+}	Mg^{2+}	Cl^-	HCO_3^-	SO_4^{2-}		
Yi 5	Ma_5^1	2317.0-2326.0	16749	79320	7660	180940	839	9529	295.04	$CaCl_2$
Yi 6	Ma_5^1	2295.0-2336.0	13522	66198	11951	167437	874	6556	266.54	$CaCl_2$
Yi 18	Ma_5^4	2358.0-2379.0	36382	10060	916	68225	530	10850	126.96	$CaCl_2$
Yi 8	Ma_5^1	2247.0-2257.0	17176	20623	3968	59278	204	20494	121.74	$CaCl_2$
Yi 14	Ma_5^1	2279.0-2300.0	9975	15090	1831	43619	394	4822	75.73	$CaCl_2$
Yi 12	Ma_5^1	1998.0-2034.5	2548	2347	610	8575	170	1607	15.86	$CaCl_2$

Table 3: Carbon and oxygen isotope results of calcite filling in mold and corresponding dolomite matrix in Yican 1 well in the southeastern Ordos Basin.

Samples	Depth (m)	Lithology	Formation	δ^{13}C of calcite in mold (VPDB ‰)	δ^{18}O of calcite in mold (VPDB ‰)	δ^{13}C of dolomite matrix (VPDB ‰)	δ^{18}O of dolomite matrix (VPDB ‰)
92	2641.38	Dolomicrite	Ma_5^1	0.26	-11.12	-0.59	-8.04
152	2688.00	Dolomicrite	Ma_5^4	-5.59	-14.32	-1.01	-9.89
164	2729.92	Dolomicrite	Ma_5^6	-7.56	-11.27	-6.87	-10.95
172	2731.80	Dolomicrite	Ma_5^6	-6.25	-12.52	-2.21	-8.36
186	2808.49	The fine crystalline dolomites	Ma_4	-2.70	-15.58	-1.93	-10.32
220	2821.06	The fine crystalline dolomites	Ma_4	-2.77	-13.49	-0.92	-6.75
228	2823.70	The fine crystalline dolomites	Ma_4	-7.20	-11.76	-0.14	-7.80
229	2823.80	The fine crystalline dolomites	Ma_4	-6.41	-10.09	0.18	-7.00
232	2945.62	The fine crystalline dolomites	Ma_3	-3.71	-8.96	-3.11	-7.10
Average				-4.66	-12.12	-1.84	-8.47

high T_h values (140-234°C) and high salinity (19.13-23.18 wt.% NaCl equivalent). The occurrence of fluids with salinities of higher than that of seawater (ca. 3.5 wt.%) is a direct indication of no influence of meteoric water. The exclusion of the involvement of meteoric water in spite of a substantial period of subaerial exposure suggests that the calcite filling in molds might have occurred after the subaerial exposure event and probably in the burial conditions. The homogenization temperature of calcite and dolomite is 140-174°C and 190-196°C, respectively, reflecting the deep burial diagenetic setting. The calcite filling in molds, therefore, is interpreted to have been precipitated from residual evaporative brine that had been locally preserved in the basin. Carbonate reservoirs with associated anhydrite, such as the anhydrite dissolution pores, are optimum sites for TSR, where the evaporative brines are remained in the pores.

This interpretation is further supported by the carbon and oxygen isotope composition of the calcite filling in the anhydrite dissolution pores. The presence of a possible hydrocarbons in the molds, together with its very low carbon isotopes (-7.56‰~0.26 VPDB) in calcite (Figure 6, Table 3) suggests that the calcite precipitation occurred in the presence of liquid hydrocarbons [30]. The oxygen isotope of calcite filling in anhydrite dissolution pores range from -15.58‰ to -8.96‰ VPDB, significantly negative to those in matrix dolomite, ranging from -10.96‰ to -6.75‰ VPDB (Figure 6, Table 3) indicating the effect of elevated temperatures, which drive the thermal fractionation of diagenetic carbonate [31–33]. The calcite, therefore, is most likely byproduct of TSR, where the hydrocarbon reacts with sulfate in residual pore water in high temperatures of deep burial condition. The porosity is lost due to the precipitation of authigenic calcite and dolomite.

The simplest TSR reaction can be written as [34]

$$nCaSO_4 + C_nH_{2n+2} \rightarrow nCaCO_3\ (\text{or } CO_2) + H_2S + (n-1)S + nH_2O. \quad (1)$$

The reaction provides the most reasonable explanation for both occurrences of authigenic calcite and oxidization of organic matter whose carbon is incorporated into the calcite [35, 36].

Although the lowest temperature for TSR is controversial, the available data indicate that as a generalization, the minimum temperature range of TSR is about 100-140°C [37]. Hence, in most geological settings, TSR occurs as soon as the temperature reaches this range, provided the necessary "ingredients" (sulfate, reactive organics, and some sulfur in a reduced form) are present [38]. Since uplifting and erosion in Caledonian, the Ordovician stratum is buried continuously until the late Cretaceous [39]) (Figure 8). Using geothermal gradients of 36°C/km and a surface temperature of 20°C, the temperature of 100°C reflects a depth of about 2200 m in early Triassic. TSR can proceed from 2200 m to the maximum depth of about 5000 m in late Cretaceous.

5.1.2. Dolomite. The fine crystalline dolomite at the bottom of the nodules is commonly interpreted to be formed by the dissolution of anhydrite and the reprecipitation of dolomite solute as "seepage silt." The composition of this dolomite, therefore, is the same as the matrix dolomite, whereas the

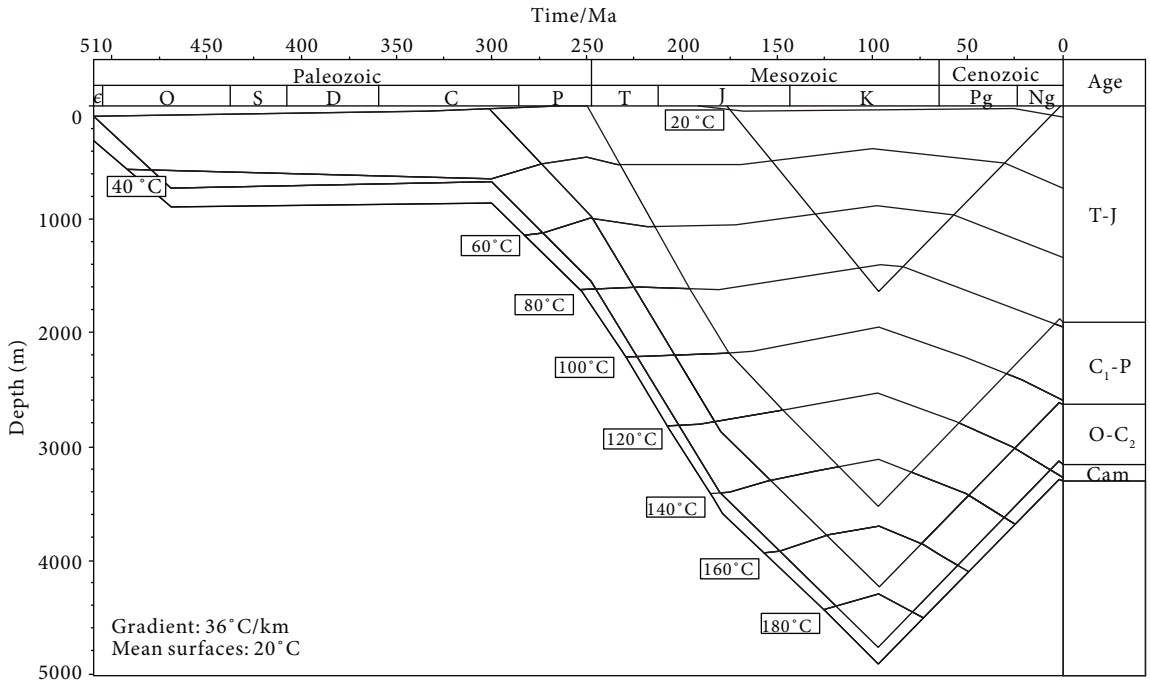

Figure 8: The burial history diagram of Yican 1 in the southeastern Ordos Basin (modified from [39]).

crystal size is commonly larger than that of matrix. The occurrence of seepage silts is a typical characteristic of meteoric water flushing in epigenetic stage.

The milky white, medium to coarse crystalline saddle dolomites in anhydrite dissolution pores are probably TSR dolomite. The abundant hydrocarbons in the pores of seepage silt at the bottom of the mold and in the lattice defect of dolomite crystals indicate simultaneously migration of hydrocarbons with the formation of crystalline dolomite. Saddle dolomite with undulose extinction is the typical characteristic of hydrothermal effect [33, 40], which is confirmed by its high homogenization temperature up to 193°C. Dolomite is the second most abundant carbonate formed as byproduct of TSR. TSR dolomite is almost exclusively restricted to the anhydrite-bearing dolomite associated with TSR calcite. Pressure solution is considered the chief source of Mg^{2+} for TSR dolomite [37]. The precipitation of calcite increases the Mg^{2+}/Ca^{2+} ratio in the pore water, which also promotes the dolomitization.

5.1.3. Pyrite. Pyrite is pervasively observed to occur as cubic, euhedral crystal (10-1000 μm) at the bottom of the mold or surrounding it. The cubic habit of pyrite (and the absence of framboidal pyrite) may indicate a nonbacterial origin with a relatively slow crystal growth rate during burial diagenesis at elevated temperatures.

Pyrite can be formed by the reaction of Fe^{2+} with S^{2-} as soon as in contact. S^{2-} can be originated from deep magma in volcanism [41], desulfurization of organic matter [42], bacterial sulfate reduction (BSR) [43, 44], or TSR. Previous studies reveal that the $\delta^{34}S$ of deep magma ranges from -5.6‰ to 5.5‰ [45]. The Ordos Basin is a stable cratonic basin, which excludes the possibility of volcanism. The pyrite formed by BSR commonly has a negative $\delta^{34}S$ value with an average from -42.7‰ to -5‰ [46, 47]. BSR is known from a multitude of geological settings that range in temperature from 0 to about 80°C [48, 49]. The homogenization temperature of fluid inclusions in calcite is between 140 and 234°C, in which the sulfate reduction bacteria cease to metabolize. The $\delta^{34}S$ value of TSR pyrite is commonly positive, which is reported to be from 8.9‰ to 23.4‰ of the pyrite from the Dengying Formation in Sichuan Basin [50] and 30‰ to 33‰ from the Upper Cambrian [36]. The pyrite in this study has a range of $\delta^{34}S$ from 10.50‰ to 24.00‰ with average 17.33‰ ($n = 11$), which can only be obtained from TSR.

H_2S is the most convincing and commonly known byproduct of TSR [51, 52]. However, the H_2S concentration is very low in Yican 1 well, which is only observed at 2823.7 m with low concentration. The most important reason for the widespread of pyrite and scarcity of H_2S is due to the presence of significant amount of Fe^{2+} in the horizon ($3387.5 \times 10^{-6} - 23112.5 \times 10^{-6}$) (Table 4). H_2S released from TSR is initially dissolved in the formation water in H^+ and S_2^{2-} form (Reactions (2) and (3)). The later will react with Fe^{2+} within seconds to minutes to form metal sulfides (Reaction (4)). H_2S is effectively removed as metal sulfide precipitation almost instantaneously, as soon and as long as base metals are available [38]. The Fe^{2+} content can be up to 23112.5×10^{-6} (Table 4) at the H_2S produced site of Yican 1 well, which abundantly assumed the H_2S released from TSR. The reaction between Fe^{2+} and H_2S reduces the concentration of H_2S and increases the pervasively occurrence of pyrite.

$$H_2S(aq) \rightarrow H^+ + HS^-, \quad (2)$$

$$2HS^- \rightarrow 2H^+ + S_{2-}^2, \quad (3)$$

Table 4: Geochemistry data of pyrite from Yican 1 in the southeastern Ordos Basin.

Samples	Depth (m)	Formation	Lithology	Pyrite $\delta^{34}S$ (VCDT, ‰)	Matrix $\delta^{13}C$ (VPDB, ‰)	Matrix $\delta^{18}O$ (VPDB,‰)	Matrix Fe × 10^{-6}	Matrix Mn × 10^{-6}
71	2634.7	Ma_5^1	Dolomicrite	11.90	/	/	/	/
72	2634.9	Ma_5^1	Dolomicrite	18.80	/	/	/	/
83	2637.4	Ma_5^1	Micrite limestone	11.10	-10.28	-10.62	15200.00	115.72
85	2638.7	Ma_5^1	Micrite limestone	20.00	-4.39	-10.44	8362.50	156.48
108	2646.6	Ma_5^1	Micrite limestone	-7.6	-1.44	-9.77	8312.50	224.88
122	2677.5	Ma_5^4	Dolomicrite	10.50	-0.86	-8.69	13950.00	99.42
249	2954.5	Ma_2	The fine crystalline dolomites	15.10	-0.46	-8.74	3387.50	85.24
308	3122.2	Ma_1	Dolomicrite	24.00	-3.25	-7.84	17450.00	139.44
314	3123.8	Ma_1	Dolomicrite	22.90	-3.92	-8.07	19412.50	257.64
320	3125.8	Ma_1	Dolomicrite	19.00	-4.90	-8.02	23112.50	258.48
321	3126.2	Ma_1	Dolomicrite	17.00	/	/	/	/
329	3128.76	Ma_1	Dolomicrite	20.30	-0.90	-7.50	9912.50	410.52

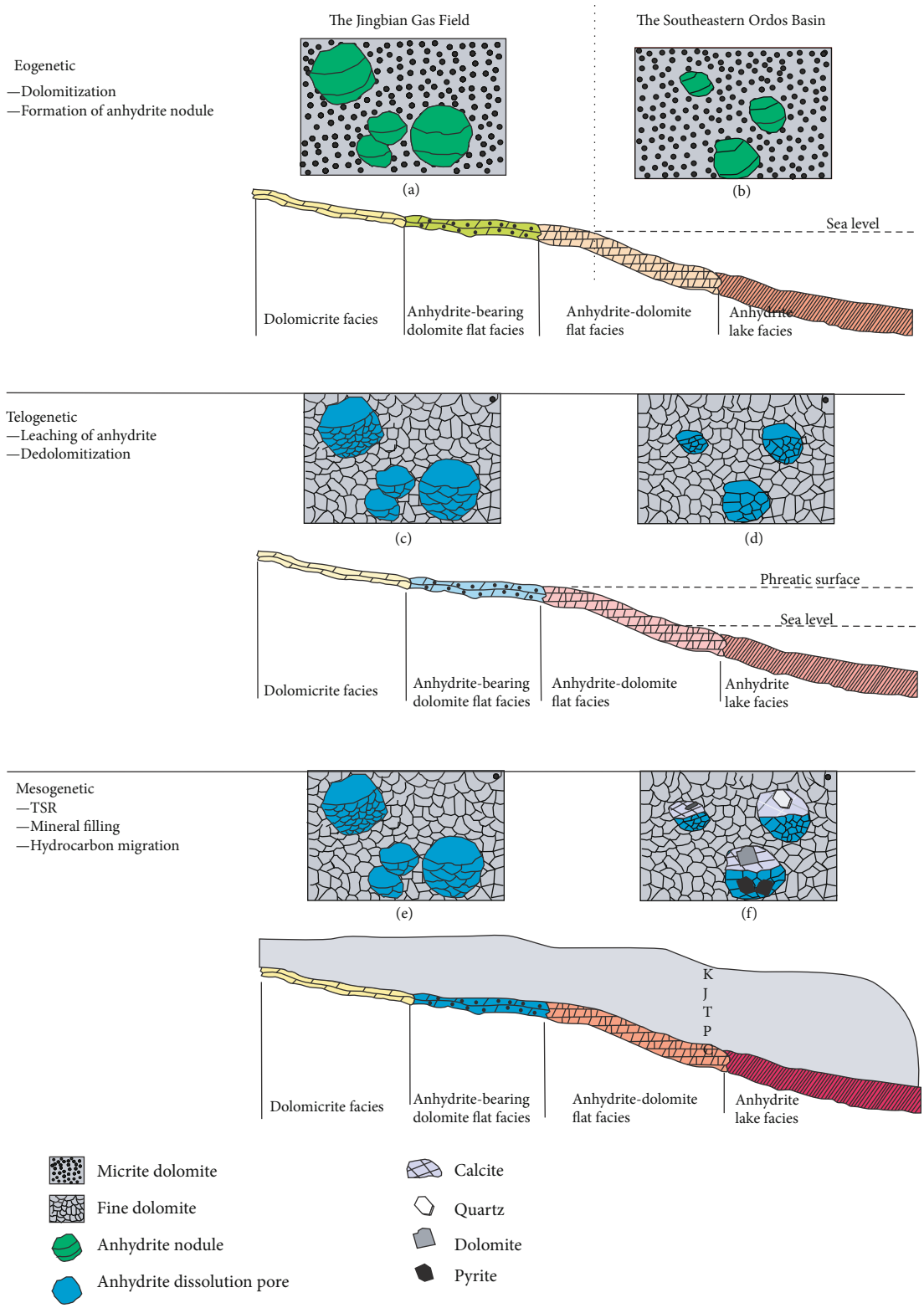

Figure 9: Diagenetic evolution comparison of minerals filling in anhydrite dissolution pores in the Ordovician Majiagou Formation of the southeastern Ordos Basin and the Jingbian Gas Field.

$$Fe^{2+} + S_{2-}^{2} \rightarrow FeS_2(pyrite). \quad (4)$$

5.1.4. Quartz. The silicification of evaporite is commonly thought to occur prior to significant burial (less than 500 m) [11]. Quartz is conventionally interpreted to be precipitated from solutions with higher silica concentrations from the dissolution of clastic quartz and other silicates of the mudstones or surrounding detrital deposits. The

dissolution and replacement of anhydrite by quartz, therefore, are indicative of the circulation of groundwater supersaturated in silica [24]. In the present case, the lack of anhydrite inclusions in quartz indicates that the quartz postdates the dissolution of anhydrite. The euhedral morphology of the quartz suggests that the quartz grows in sufficient space, where the anhydrite had probably been removed to form central hollows that later allows the euhedral crystals to grow. The relatively high homogenization temperature of fluid inclusions in quartz (113-154°C) strongly suggests that they are formed in deep burial conditions, which is probably related to TSR. Quartz is considered kinetically favorable to precipitate from low-pH solution [53–55]. H^+ released from calcite (Reaction (1)) and pyrite precipitation (Reaction (2) and (3)) is expected to locally decrease the pH value of the formation water, which is favorable for the precipitation of authigenic quartz. This can give a good explanation for the close temporal and spatial association of calcite and quartz [55]. In the present case, the authigenic quartz filling in anhydrite mold is, therefore, formed as a burial diagenetic process instead of an early diagenetic process.

5.2. Diagenesis Evolution and Comparison with the Jingbian Gas Field. The paleogeographic location of the southeastern Ordos Basin is much lower than that of the Jingbian Gas Field [56]. The sedimentary environment of the Jingbian Gas Field is mainly dolomicrite flat subfacies and anhydrite-bearing dolomite flat subfacies of the supratidal zone, whereas the southeastern Ordos Basin is mainly located in anhydrite-dolomite flat subfacies and anhydrite lake subfacies of intertidal zone (Figure 9). When the sea level decreases, the anhydrite nodules begin to form in the Jingbian Gas Field of supratidal zone. For longer evaporative time, the anhydrite nodules are more abundant, and the nodule size is larger in the Jingbian Gas Field (Figure 3, Figures 9(a) and 9(b)).

When uplifted in Caledonian orogeny in late Ordovician, the horizon experienced the leaching of meteoric water resulting in the anhydrite nodules dissolved, leaving the molds enriched in anhydrite dissolution water (Figures 9(c) and 9(d)). With the sea level increasing in Carboniferous-Permian, the southeastern Ordos Basin is flooded by the ocean from the south and east direction subsequently [22]. The formation is submerged in sea water of marine phreatic environments for a long time, leading to the pore water enriched in marine water. Owing to the periodic sea-level changes, the connate marine pore water is altered locally by minor amounts of evaporative water during shallow burial resulted in the pore water enriched in calcium sulfate (Table 2). Most minerals are preferentially hydrophilic so that a film of residual water lines the grain framework even in hydrocarbon gas-bearing reservoirs [57]. The amount of this residual water is generally ~10% of the pore volume of the rock. Reactions occurring in solution are generally many orders of magnitude faster than reactions between gases and solids [58]. Therefore, the hydrocarbons reacted with the dissolved anhydrite in solution in the residual water film rather than as a solid-gas reaction [34]. Since being uplifted in the Caledonian orogeny in the late Ordovician of the lower Paleozoic, the Ordos Basin experienced continuous burial until the deepest burial in the early Cretaceous, as shown in previous studies (Figure 8) [39]. The burial temperature has been above the minimum temperature of about 100°C in 2200 m of the early Triassic (using 36°C/km as a geothermal gradient and 20°C as surface temperature) necessary for TSR, the calcium sulfate enriched in pore water will react with hydrocarbons to form H_2S and CO_2. TSR will continue to the maximum burial of about 5000 m, equivalent to the temperature of 200°C. Calcite and dolomite are interpreted to be formed in late-diagenetic stage based on the petrographic and geochemical evidence investigated in this study (Figures 9(e) and 9(f)). The spatial distribution of calcite, along with that of secondary dolomite, authigenic quartz, and pyrite, in combination with carbon and oxygen data further indicates that the calcite in anhydrite dissolution pores is genetically related to thermochemical sulfate reduction.

In contrast to the southeastern Ordos Basin, the Jingbian Gas Field is located in the tectonic high in paleogeography, and the anhydrite dissolution water after leaching by meteoric water is taken away from its open system, leaving the molds open (Figure 9(e)). The sea water flooded in the southeastern direction has not emerged within the Jingbian region. The TSR reaction rarely occurs for the lack of dissolved sulfate in the pore water. Although some molds are also filled with minerals in the Jingbian Gas Field, the filling degree is much lower than that in the southeastern Ordos Basin (Figure 2). Therefore, the resultant porosity in the mold is preserved resulting in the high porosity and permeability of the Jingbian Gas Field (Figures 2 and 3).

6. Conclusions

The anhydrite nodule-bearing dolomite is widely distributed in the upper Majiagou Formation of the southeastern Ordos Basin. Nevertheless, the anhydrite dissolution pores are commonly filled by minerals such as dolomite, calcite, pyrite, and quartz, which resulted in significant porosity and volume reduction. The calcite filling in anhydrite dissolution pores is interpreted to be precipitated as TSR by-product, which is supported by its relatively negative $\delta^{18}O$ value (-15.58‰ ~-8.96‰ VPDB) and negative $\delta^{13}C$ value (-7.56‰~0.26‰ VPDB). The higher homogenization temperatures (140-234°C) and high salinity (19.13-23.18 wt.% NaCl equivalent) of the primary inclusions in calcite confirm the above interpretation. Dolomite is the second most abundant carbonate formed as a by-product of TSR, which is promoted by the precipitation of calcite and resulted enriched in Mg^{2+}/Ca^{2+} ratio in the pore water. Pyrite forms by the reaction of H_2S released from TSR with the Fe^{2+} in the horizon, which is supported by its cubic habit and relatively high $\delta^{34}S$ value (10.50‰~24.00‰). Quartz with relatively high homogenization temperature (113-154°C) is considered to precipitate in low-pH solution from calcite and pyrite precipitation after TSR.

The paleogeographic location of the southeastern Ordos Basin is much lower than that of the Jingbian Gas Field, which is submerged in the sea water of marine phreatic environments for a long time when sea water flooded from the

southeastern direction. Owing to the periodic sea-level changes, the connate marine pore water is altered locally by minor amounts of evaporative water during shallow burial resulted in the pore water enriched in calcium sulfate. The Jingbian Gas Field, however, is located in the tectonic high in paleogeography which has not been emerged by sea water. TSR rarely occurs for the lack of enriched pore water. Therefore, the resultant porosity in the nodule is preserved and rarely filled by other minerals resulting in the high porosity and permeability of the Jingbian Gas Field.

Data Availability

The data presented in this study are available on request from the corresponding author.

Conflicts of Interest

The authors declare no conflict of interest.

Authors' Contributions

Conceptualization, methodology, and writing of original draft were done by Lihong Liu. Investigation and writing (review and editing) were done by Chunlian Wang. Resources and funding were acquired by Zhili Du. Validation, visualization, and project administration were done by Jianghua Gong. All authors have read and agreed to the published version of the manuscript.

Acknowledgments

This work is supported by the National Natural Science Foundation of China (No. 41802173), Central Welfare Basic Scientific Research Business Expenses (No. KK2005), and China Geological Survey projects ((Nos. DD20160175, DD20190106, DD20190708, DD20190090, and DD20190606). The work is part of the outcome of the first author's PhD thesis (Peking University), under the guidance of Prof. Yongsheng Ma (Sinopec Co., Ltd.) and Prof. Bo Liu (Peking University), who are greatly acknowledged. We are grateful to Dr. Xuefeng Zhang for his constructive comments and suggestions that have significantly improved the manuscript. We would like to thank Hongguang Liu and Qicai Jiang of Peking University for picking minerals in the pores in dealing with samples. We heartily thank all those involved in the field study.

References

[1] T. M. Chowns and J. E. Elkins, "The origin of quartz geodes and cauliflower cherts through the silicification of anhydrite nodules," *SEPM Journal of Sedimentary Research*, vol. 44, pp. 885–903, 1974.

[2] M. A. Bustillo, J. Garcia-Guinea, J. Martinez-Frias, and A. Delgado, "Unusual sedimentary geodes filled by gold-bearing hematite laths," *Geological Magazine*, vol. 136, no. 6, pp. 671–679, 1999.

[3] J. H. Geeslin and H. S. Chafetz, "Ordovician Aleman Ribbon Cherts: an example of silicification prior to carbonate lithification," *SEPM Journal of Sedimentary Research*, vol. 52, pp. 1283–1293, 1982.

[4] R. G. Maliva, "Quartz geodes: early diagenetic silicified anhydrite nodules related to dolomitization," *SEPM Journal of Sedimentary Research*, vol. 57, pp. 1054–1059, 1987.

[5] H. P. Bao, C. Y. Yang, and J. S. Huang, ""Evaporation drying" and"reinfluxing and redissolving"—a new hypothesis concerning formation of the Ordovician evaporites in eastern Ordos Basin," *Journal of Palaeogeography*, vol. 6, pp. 279–288, 2004.

[6] Z. X. He, *The Evolution and Petroleum of Ordos Basin*, Petroleum Iindustry Press, Beijing, 2003.

[7] C. Pierre and J. M. Rouchy, "Carbonate replacements after Sulfate evaporites in the Middle Miocene of Egypt," *SEPM Journal of Sedimentary Research*, vol. 58, pp. 446–456, 1988.

[8] J. Peckmann, J. Paul, and V. Thiel, "Bacterially mediated formation of diagenetic aragonite and native sulfur in Zechstein carbonates (Upper Permian, Central Germany)," *Sedimentary Geology*, vol. 126, no. 1-4, pp. 205–222, 1999.

[9] A. C. Kendall, "Late diagenetic calcitization of anhydrite from the Mississippian of Saskatchewan, western Canada," *Sedimentology*, vol. 48, no. 1, pp. 29–55, 2001.

[10] J. K. Warren, *Evaporites: Sediments, Resources and Hydrocarbons*, Springer, Berlin, 2006.

[11] D. S. Ulmer-Scholle and P. A. Scholle, "Replacement of evaporites within the Permian Park City Formation, Bighorn Basin, Wyoming, USA," *Sedimentology*, vol. 41, no. 6, pp. 1203–1222, 1994.

[12] C. Cai, W. Hu, and R. H. Worden, "Thermochemical sulphate reduction in Cambro-Ordovician carbonates in Central Tarim," *Marine and Petroleum Geology*, vol. 18, no. 6, pp. 729–741, 2001.

[13] M. Harwoodg, "Calcitized anhydrite and associated sulphides in the English Zechstein First Cycle Carbonate (EZ1 Ca)," in *The Zechstein Basin with Emphasis on Carbonate Sequences. Contributions to Sedimentology 91*, H. Fiichtbauer and T. M. Peryt, Eds., pp. 61–72, E. Schweizerbart'sche Verlagsbuchhandlung (Nagele u. Obermiller), Stuttgart, 1980.

[14] M. R. Lee and G. M. Harwood, "Dolomite calcitization and cement zonation related to uplift of the Raisby Formation (Zechstein carbonate), northeast England," *Sedimentary Geology*, vol. 65, no. 3-4, pp. 285–305, 1989.

[15] P. A. Scholle, D. S. Ulmer, and L. A. Melim, "Late-stage calcites in the Permian Capitan Formation and its equivalents, Delaware Basin margin, West Texas and New Mexico: evidence for replacement of precursor evaporites," *Sedimentology*, vol. 39, no. 2, pp. 207–234, 1992.

[16] H. Yang, J. H. Fu, X. S. Wei, and J. F. Ren, "Natural gas exploration domains in Ordovician marine carbonates, Ordos Basin," *Acta Petrolei Sinica*, vol. 32, pp. 733–740, 2011.

[17] Z. Z. Feng, Z. D. Bao, and Q. F. Kang, "Palaeotectonics of Ordovician in Ordos," *Journal of Palaeogeography*, vol. 1, pp. 83–94, 1999.

[18] J. H. Fu and C. B. Zhen, "Evolution between North China Sea and Qilian Sea of the Ordovician and the characteristics of lithofacies palaeogeography in Ordos Basin," *Journal of Palaeogeography*, vol. 3, pp. 25–34, 2001.

[19] X. S. Wei, J. F. Ren, J. X. Zhao et al., "Paleo-geomorphologic characteristic evolution and geological significance of the Ordovician weathering crust in eastern Ordos Basin," *Acta Petrolei Sinica*, vol. 38, pp. 999–1009, 2017.

[20] Z. T. Su, H. D. Chen, Z. J. Ouyang, and X. Q. Jin, "Sequence-based lithofacies and paleogeography of Majiagou formation in Ordos Basin," *Geology in China*, vol. 39, pp. 623–633, 2012.

[21] Z. H. Li and J. M. Hu, "Characteristics of holes filling in Ordovician of Ordos Basin," *Geological Review*, vol. 57, pp. 444–456, 2011.

[22] J. F. Ren, H. P. Bao, L. Y. Sun, and B. X. Liu, "Characteristics and mechanism of pore-space filling of Ordovician Weathering crust karst reservoirs in Ordos Basin," *Marine Petroleum Geology*, vol. 17, pp. 63–69, 2012.

[23] J. Hoefs, *Stable Isotope Geochemistry*, Springer, Berlin, 2009.

[24] A. M. Alonso-Zarza, Y. Sánchez-Moya, M. A. Bustillo, A. Sopeña, and A. Delgado, "Silicification and dolomitization of anhydrite nodules in argillaceous terrestrial deposits: an example of meteoric-dominated diagenesis from the Triassic of Central Spain," *Sedimentology*, vol. 49, no. 2, pp. 303–317, 2002.

[25] G. Chi, L. W. Diamond, H. Lu, J. Lai, and H. Chu, "Common problems and pitfalls in fluid inclusion study: a review and discussion," *Minerals*, vol. 11, no. 1, p. 7, 2021.

[26] H. Bao, F. Yang, Z. Cai, Q. Wang, and C. Wu, "Origin and reservoir characteristics of Ordovician dolostones in the Ordos Basin," *Natural Gas Industry*, vol. 4, no. 2, pp. 106–119, 2017.

[27] F. Zengzhao, Z. Yongsheng, and J. Zhenkui, "Type, origin, and reservoir characteristics of dolostones of the Ordovician Majiagou Group, Ordos, North China Platform," *Sedimentary Geology*, vol. 118, no. 1-4, pp. 127–140, 1998.

[28] B. Q. Wang and I. S. Al-Aasm, "Karst-controlled diagenesis and reservoir development; example from the Ordovician mainreservoir carbonate rocks on the eastern margin of the Ordos basin, China," *AAPG Bulletin*, vol. 86, pp. 1639–1658, 2002.

[29] H. R. Qing, G. Chi, and S. Zhang, "Origin of coarse-crystalline calcite cement in Early Ordovician carbonate rocks, Ordos basin, northern China: Insights from oxygen and carbon isotopes and fluid inclusion microthermometry," *Journal of Geochemical Exploration*, vol. 89, no. 1-3, pp. 344–347, 2006.

[30] L. Jiang, W. Pan, C. Cai et al., "Fluid mixing induced by hydrothermal activity in the Ordovician carbonates in Tarim Basin, China," *Geofluids*, vol. 15, no. 3, 498 pages, 2015.

[31] L. A. Hardie, "Dolomitization; a critical view of some current views," *Journal of Sedimentary Research*, vol. 57, no. 1, pp. 166–183, 1987.

[32] P. W. Choquette and N. P. James, "Limestones-burial diagenetic environments," in *Diagenesis*, I. A. Mcilreath and D. W. Morrow, Eds., vol. 4, pp. 75–112, Geosci. Can. Reprint Ser., 1990.

[33] L. H. Liu, Y. S. Ma, B. Liu, and C. L. Wang, "Hydrothermal dissolution of Ordovician carbonates rocks and its dissolution mechanism in Tarim Basin, China," *Carbonates and Evaporites*, vol. 32, no. 4, pp. 525–537, 2017.

[34] R. H. Worden and P. C. Smalley, "H_2S-producing reactions in deep carbonate gas reservoirs: Khuff Formation, Abu Dhabi," *Chemical Geology*, vol. 133, no. 1-4, pp. 157–171, 1996.

[35] H. Irwin, C. Curtis, and M. Coleman, "Isotopic evidence for source of diagenetic carbonates formed during burial of organic-rich sediments," *Nature*, vol. 269, no. 5625, pp. 209–213, 1977.

[36] L. Jia, C. Cai, H. Yang et al., "Thermochemical and bacterial sulfate reduction in the Cambrian and Lower Ordovician carbonates in the Tazhong Area, Tarim Basin, NW China: evidence from fluid inclusions, C, S, and Sr isotopic data," *Geofluids*, vol. 15, no. 3, 437 pages, 2015.

[37] H. G. Machel, "Gas souring by thermochemical sulfate reduction at 140°C: discussion," *American Association of Petroleum Geologists Bulletin*, vol. 82, pp. 1870–1873, 1998.

[38] H. G. Machel, "Bacterial and thermochemical sulfate reduction in diagenetic settings – old and new insights," *Sedimentary Geology*, vol. 140, no. 1-2, pp. 143–175, 2001.

[39] Z. L. Ren, Q. Yu, J. P. Cui et al., "Thermal history and its controls on oil and gas of the Ordos Basin," *Earth Science Frontiers*, vol. 24, pp. 137–148, 2017.

[40] D. Zhu, Q. Meng, Z. Jin, and W. Hu, "Fluid environment for preservation of pore spaces in a deep dolomite reservoir," *Geofluids*, vol. 15, no. 4, 545 pages, 2015.

[41] K. Christof, O. Marcus, and A. G. Sarah, "Partitioning of arsenic between hydrothermal fluid and pyrite during experimental siderite replacement," *Chemical Geology*, vol. 500, pp. 136–147, 2018.

[42] S. Lubna, H. Itay, S. Ward et al., "Dynamics of pyrite formation and organic matter sulfurization in organic-rich carbonate sediments," *Geochimica et Cosmochimica Acta*, vol. 241, pp. 219–239, 2018.

[43] N. Wang, "The advances in the study of microbial dolomite," *Acta Petrologica et Mineralogica*, vol. 30, pp. 690–783, 2011.

[44] X. Zhang, Y. F. Zhou, and T. H. Chen, "An experimental study of the decomposition of gypsum as the function of contacted sulfate reducing bacterium and its metabolites," *Acta Petrologica et Min-Eralogica*, vol. 34, pp. 932–938, 2015.

[45] X. J. Meng, Z. Q. Hou, and Z. Q. Li, "Sulfur and lead isotope compositionsof the Qulong porphyry copper deposit, TiBet: implications for the sources of plutons and metals in the deposit," *Acta Geologica Sinica*, vol. 80, pp. 554–560, 2006.

[46] C. Pierre, J. M. Rouchy, and A. Gaudichet, "Diagenesis in the gas hydrate sediments of Blake Ridge: mineralogy and stable isotope compositions of the carbonate and sulfide minerals," in *proceedings of the ocean drilling program*, C. K. Paull, R. Matsumoto, and P. J. Wallace, Eds., vol. 164, pp. 139–146, Scientific Results, 2000.

[47] Z. Liu, D. Chen, J. Zhang et al., "Pyrite morphology as an Indicator of Paleoredox conditions and shale gas content of the Longmaxi and Wufeng Shales in the Middle Yangtze Area, South China," *Minerals*, vol. 9, no. 7, p. 428, 2019.

[48] J. R. Postgate, *The Sulfate-reducing Bacteria*, Cambridge University Press, Cambridge, 2nd edition, 1984.

[49] H. L. Ehrlich, *Geomicrobiology*, Marcel Dekker, New York, 2nd edition, 1990.

[50] Q. Liu, D. Zhu, Z. Jin, C. Liu, D. Zhang, and Z. He, "Coupled alteration of hydrothermal fluids and thermal sulfate reduction (TSR) in ancient dolomite reservoirs - an example from Sinian Dengying Formation in Sichuan Basin, southern China," *Precambrian Research*, vol. 285, pp. 39–57, 2016.

[51] Y. S. Ma, S. Zhang, T. Guo, G. Zhu, X. Cai, and M. Li, "Petroleum geology of the Puguang sour gas field in the Sichuan Basin, SW China," *Marine and Petroleum Geology*, vol. 25, no. 4-5, pp. 357–370, 2008.

[52] K. K. Li, C. Cai, D. Hou et al., "Origin of high H_2S concentrations in the Upper Permian Changxing reservoirs of the Northeast Sichuan Basin, China," *Marine and Petroleum Geology*, vol. 57, pp. 233–243, 2014.

[53] J. Ganor, T. J. Huston, and L. M. Walter, "Quartz precipitation kinetics at 180°C in NaCl solutions–implications for the

usability of the principle of detailed balancing," *Geochimica et Cosmochimica Acta*, vol. 69, no. 8, pp. 2043–2056, 2005.

[54] R. Wierzbicki, J. J. Dravis, I. al-Aasm, and N. Harland, "Burial dolomitization and dissolution of upper Jurassic Abenaki platform carbonates, deep Panuke reservoir, Nova Scotia, Canada," *AAPG Bulletin*, vol. 90, no. 11, pp. 1843–1861, 2006.

[55] F. Hao, X. Zhang, C. Wang et al., "The fate of CO_2 derived from thermochemical sulfate reduction (TSR) and effect of TSR on carbonate porosity and permeability, Sichuan Basin, China," *Earth-Science Reviews*, vol. 141, pp. 154–177, 2015.

[56] Z. T. Su, H. D. Chen, J. X. Zhao, J. Li, Q. Xu, and X. Gao, "Difference analysis of palaeokarst development in middle and south parts of Ordos Basin," *Fault-Block Oil & Gas Field*, vol. 17, pp. 542–547, 2010.

[57] J. S. Archer and C. G. Wall, *Petroleum Engineering Principles and Practice*, Graham & Trotman, London, 1986.

[58] A. C. Lasaga and R. J. Kirkpatrick, "Kinetics of geochemical processes," *Mineral. Soc. Am., Rev. Mineral*, vol. 8, p. 398, 1981.

Hindawi
Geofluids
Volume 2021, Article ID 5550271, 12 pages
https://doi.org/10.1155/2021/5550271

Research Article

A Rapid Cu Enrichment Mechanism from Cu-Bearing Brine in Kuqa Basin, Xinjiang, China: Controlled by Crystallized Sequence of Saline Minerals

Yangtong Cao and Haiming Xu

MNR Key Laboratory of Metallogeny and Mineral Assessment, Institute of Mineral Resources, Chinese Academy of Geological Sciences, Beijing 100037, China

Correspondence should be addressed to Yangtong Cao; cyt1941@126.com

Received 28 January 2021; Revised 14 March 2021; Accepted 16 March 2021; Published 26 March 2021

Academic Editor: Rongxi Li

Sediment-hosted copper deposit is usually related to arid climate, ancient saline lake basin, and brine. The Kuqa Basin filled with giant-thickness evaporite units is located in the northern Tarim Basin, Xinjiang, China. It is famous for sandstone-hosted Cu deposits formed by synsedimentary processes. However, our recent studies reveal that Cu enrichment is closely related to brine on the surface of clastic rocks in the basin. It is shown that green Cu mineral coexisting with halite and gypsum occurred in the fractured fault belts of sandstones or was precipitated with halite on the surface of maroon clay in the scallops of sandstone. By SEM, EDS, and geochemical analysis methods on Cu-mineralized solid samples and brines, respectively, combined with previous geological evidence, our studies demonstrate that green Cu mineral is paratacamite, and it occurred with gypsum, halite, secondary glauberite, natural copper, and probably lead chloride on the fractured fault belts of sandstones or surface of clay. Meanwhile, the precipitation of paratacamite is controlled by a crystallized sequence of saline minerals accompanying with evaporated-concentrated course of brine in which gypsum, secondary glauberite, paratacamite, and halite are crystallized in turn. The Cu-bearing brine derived from meteoric waters and ancient seawater has a powerful capacity to leach metallic ions from its surrounding rocks and can be formed in a very short time (10 days is OK) in normal pressure and temperature conditions; also, the cycle of surface-Cu enrichment (mineralization) is only a few months (no more than 5). These indicate that a rapid Cu enrichment mechanism from Cu-bearing brine occurs on the earth's surface of the evaporite basin. The mechanism might be supposed to make an enormous amount of metal mineralization in a short time if considered from a large-scale spatial viewpoint. By contrast with the lengthy geological period, the short evolutionary cycle of Cu enrichment (mineralization) is obviously different from the previous cognition.

1. Introduction

Sandstone-hosted Copper deposit is only the second largest to porphyry copper in the ultralarge copper ores of the world. It is mainly located in the 20°-30° latitudinal range on both sides of the equator. There are close relationships among Cu enrichment, arid climate, ancient saline lake basin, and brine [1–3]. The brine usually with low temperature derives from evaporated-concentrated seawater or leached rock salt by meteoric water in the ancient saline lake basin and becomes the main carrier for more kinds of metal ions such as copper [4–7]. It is reported that ions such as Cu, Fe, Zn, Ag, and Au migrate by clathrate forms in the brine, which has no substituted function on activation, migration, and enrichment of metal ions in the process of metal mineralization [8–14]. The Cu-bearing brine generally migrates along fractured fault belts, cross-bedding planes, and other paths and finally reaches favorable sites for Cu enrichment or mineralization.

The Kuqa Basin filled with giant-thickness evaporite deposits is located in the northern margin of Tarim Basin, Xinjiang Uygur Autonomous Region of northwestern China.

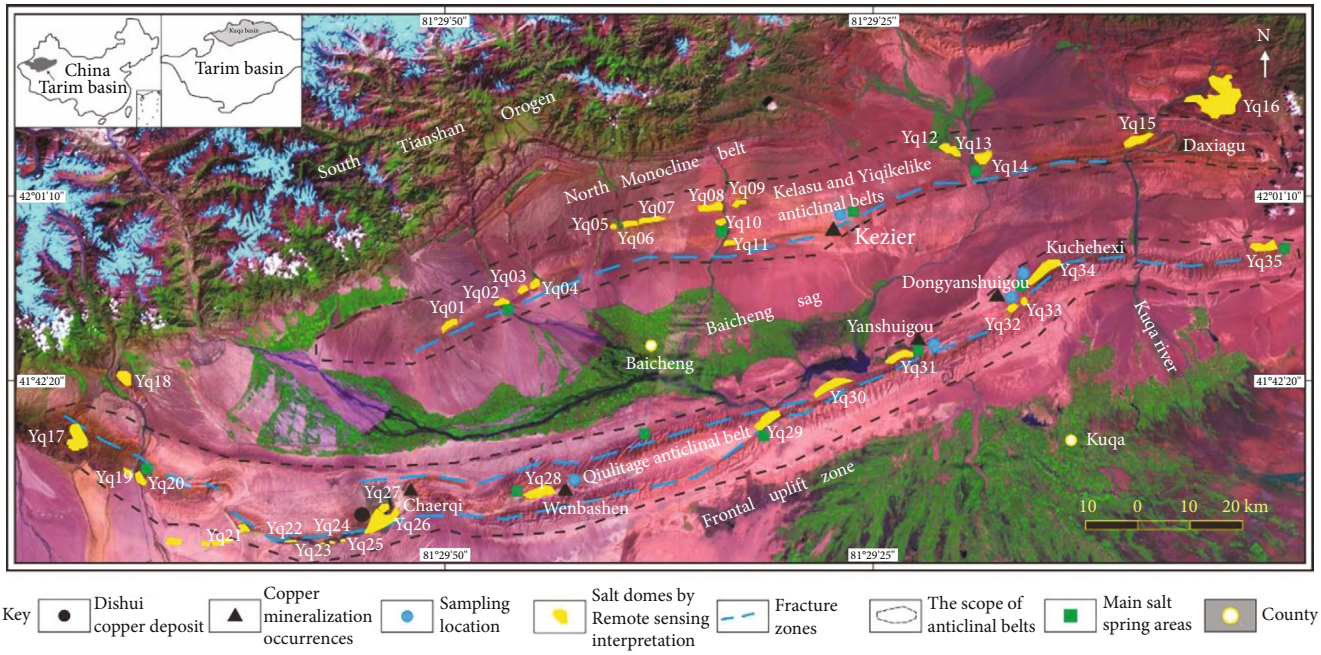

Figure 1: Schematic map of structure and sampling locations in Kuqa Basin.

These deposits contain a set of salt-bearing layers comprised of rock salt, gypsum rock, and clastic rocks [15, 16]. Influenced by tectonic activities and meteoric water, the evaporite was leached and dissolved, so it resulted in a series of salt springs and crystalline halite on the surface of the Neogene layers [17]. In recent studies on the evaporite and ore prospecting of potash, occasionally, we found a close relationship between Cu enrichment and brine, so some field investigations were carried out. The results show that there is a coexisting relationship among the green Cu mineral, halite, and gypsum. These minerals usually occur in fractured fault belts in the Neogene Jidike and Kangcun Formations comprised of clastic rocks. Previous studies have shown that the surface-Cu enrichment formed in the arid climate environment in the basin, and it originated from the Cu-bearing brine of the underlying evaporite units which migrated upward along fault belts to the surface [15, 16], but the cycle and era of Cu enrichment are unknown. Compared with the period of geological evolution, the mineralization cycle of Cu enrichment from beginning to ore formation is frequently studied over several tens to millions of years. However, recent research reveals that the surface-Cu enrichment has been formed in a very short time. Maybe a long period of Cu ore formation is needed, but these indicate a type of rapid Cu enrichment mechanism correlated with evaporation on the surface in the evaporite basin.

2. Geological Setting

The Kuqa Basin in Xinjiang is located in the tectonic belts between the South Tianshan Orogen and the Tarim Basin and is interpreted as a rejuvenated foreland basin [18–22]. The basin was initially opened in the Late Permian [21] and continued its formation until the Late Triassic [23]. It was finally established in the Jurassic [24]. In the Late Eocene, because of the tectonic effects due to the collision of the Indian and Eurasian plates [25], the Tarim Plate collided with the South Tianshan Orogen. In the Late Oligocene, sedimentation in the Kuqa Foreland Basin was resumed, thereby rejuvenating the Kuqa Foreland Basin. From north to south, the basin is characterized by a north monocline belt, the Kelasu and Yiqikelike anticlinal belts, the Baicheng sag, the Qiulitage anticlinal belt, and the frontal uplift zone (Figure 1). The two anticlinal belts are the main tectonic zones of the basin.

In ascending order, the stratigraphic units can be divided into the Kumugeliemu Group, Suweiyi Formation (Paleogene), Jidike Formation, Kangcun Formation, and Kuqa Formation (Neogene). The sediments are mainly interpreted as river-lake facies in the Paleogene [26]. The Kumugeliemu Group is comprised of giant-thickness evaporite series [15, 27, 28], and the Suweiyi Formation is composed of small amounts of rock salt, gypsum rock, fine sandstone, and siltstone. The Jidike Formation is composed of river-lake sediments, whereas the Kangcun and Kuqa Formations contain mainly piedmont facies composed of conglomerates, pebbly sandstone, siltstone, and mudstone.

The east-west orientation fault zones were developed in the basin where it was filled with evaporite, oil, and gas, so along the line of fault zones, a series of outcrops of salt domes were intruded onto surface rock units of the anticlinal axis in a tectonic compression setting (Figure 1). Salt springs can be observed everywhere on the earth's surface in the basin, and the Cu enrichment (mineralization) is mainly located in the two anticlinal belts, generally adjacent to salt domes (Figure 1). It is reported that the green Cu mineral is

(a) (b) (c) (d) (e) (f)

Figure 2: Continued.

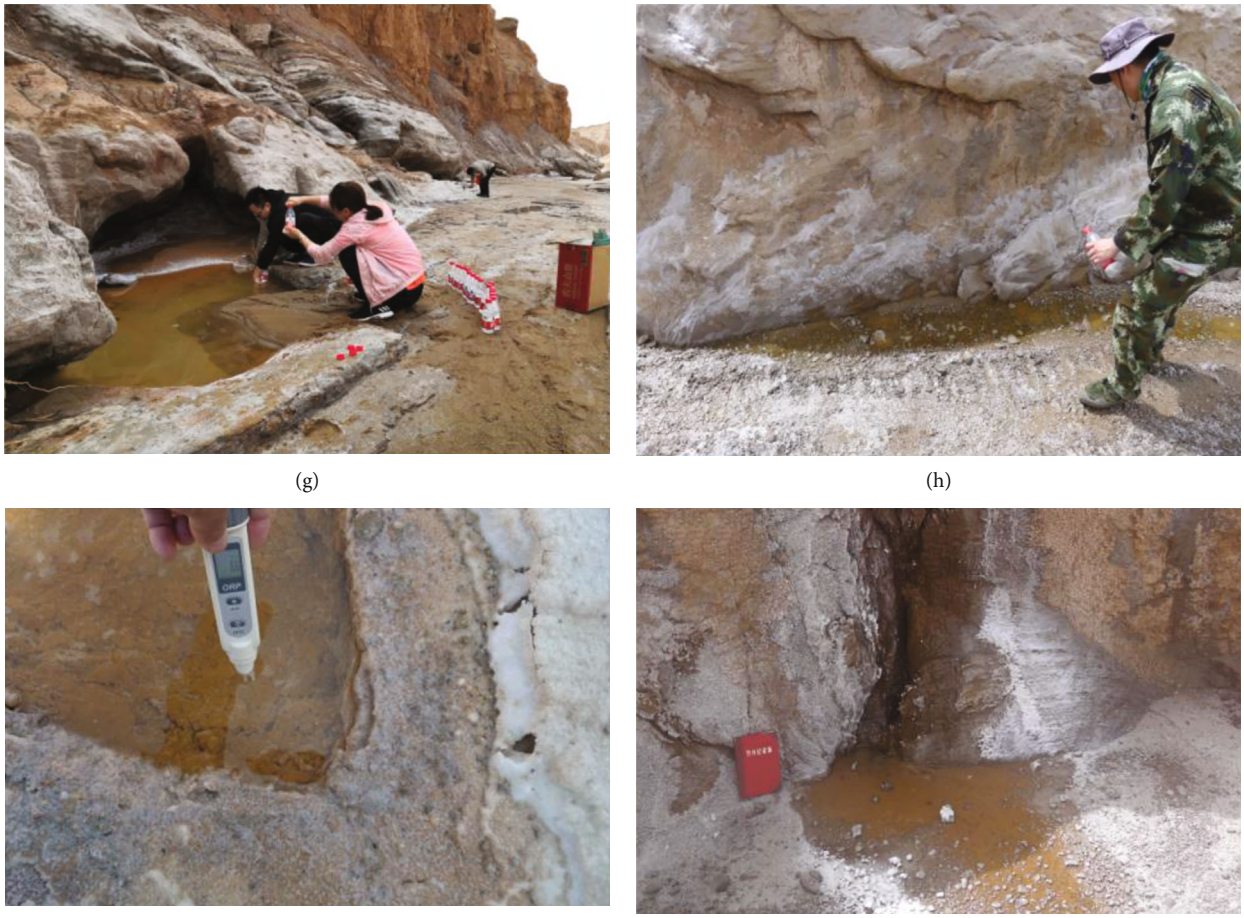

Figure 2: Sampling locations of brine and Cu-mineralized halite (gypsum). (a) Fractured fault belts of sandstone named "a" (the Kezier Cu mineralization occurrence); (b) Cu-mineralized halite (gypsum) of a site (sample no. KC-G_1); (c) fractured fault belts of sandstone named "b" (the Kezier Cu mineralization occurrence); (d) Cu-mineralized halite (gypsum) of b site (sample no. KC-G_2); (e) green Cu mineral and white halite on the surface of mud located in the scallops of sandstone (sample no. KC-G_3); (f) image magnification of photo (e); (g) the surface brine in the Kezier Cu mineralization occurrence; (h) the surface brine in the Dongyanshuigou Cu mineralization occurrence; (i) the surface brine in the Wenbashen Cu mineralization occurrence; (j) the surface brine in the east about 1.5 km away of Dongyanshuigou Cu mineralization occurrence.

paratacamite, commonly coexisting with halite and gypsum, which occurred in the gypsum veins of sandstones in the Jidike and Kangcun Formations [17].

3. Methods

Three representative samples (KC-G_1, KC-G_2, and KC-G_3) are selected from Cu-mineralized halite (gypsum) in the Cu mineralization occurrence named Kezier, northeastern Kuqa Basin (see Figure 1 for sampling locations, Figures 2(a)–2(f)). The samples (KC-G_1 and KC-G_2) are collected from fractured fault belts of the grey-white medium- to coarse-grained sandstone of the Kangcun Formation (Figures 2(a) and 2(c)). Sample KC-G_3 is a green crystalline mineral collected from the surface of maroon moist-mud located in concave of the grey-white medium- to coarse-grained sandstone. Field investigations show that the green Cu mineral coexists with halite as tasted with briny taste. The surface brines were, respectively, collected from Cu mineralization occurrences named Kezier, Wenbashen, Yanshuigou, and Dongyanshuigou, also the gully about 1.5 km away from Dongyanshuigou, where salt crystals can be seen all over the place. The part sites of samples are given in Figures 2(g)–2(j).

The analytical methods employed in this study include scanning electron microscopy (SEM), energy-dispersive X-ray spectroscopy (EDS), and hydrochemical analysis, for studying the possible geneses and enrichment mechanisms of copper. The solid samples were performed at the Key Laboratory of Deep-Earth Dynamics, Institute of Geology, Chinese Academy of Geological Sciences, Beijing, using the FEI Nova Nano SEM450 equipped with Gatan MonoCL4 and OXFORD X-Max (50 mm^2), and the backscattered electron (BSE) images were taken under operating voltage of 15-20 kV and the working distance of 13.5 mm. With regard to 13 surface brines, the component analysis on salt and metal ions (such as K^+, Na^+, Ca^{2+}, Mg^{2+}, SO_4^{2-}, Cl^-, and Cu^{2+}) was carried out at the MNR Key Laboratory of Metallogeny and Mineral Assessment, Institute of Mineral Resources,

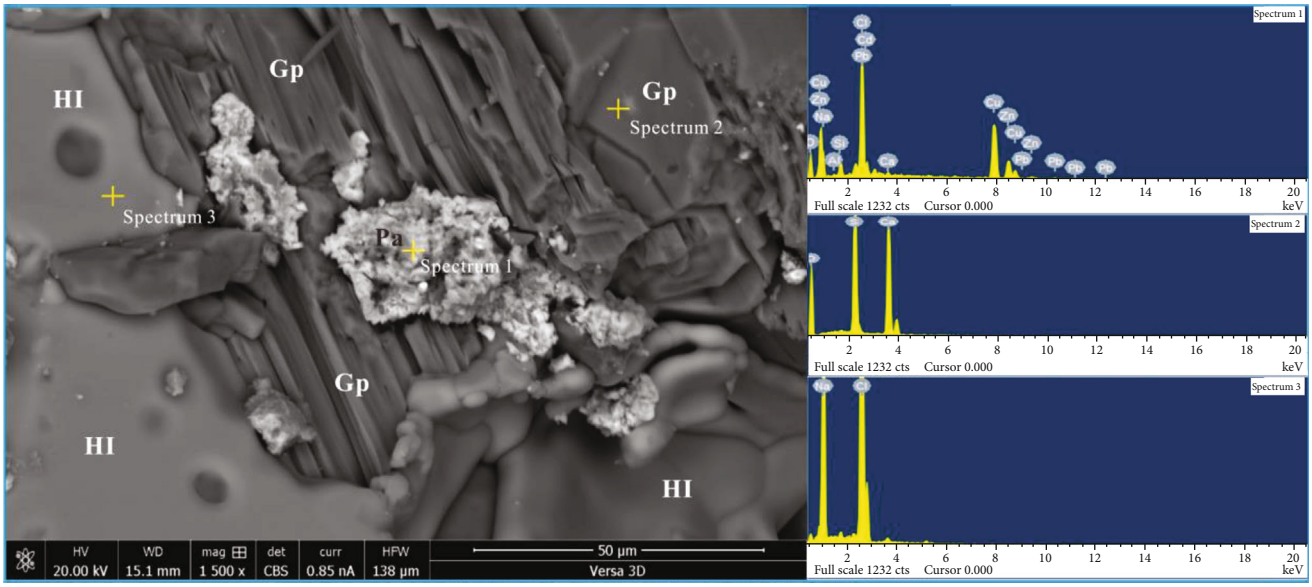

(a)

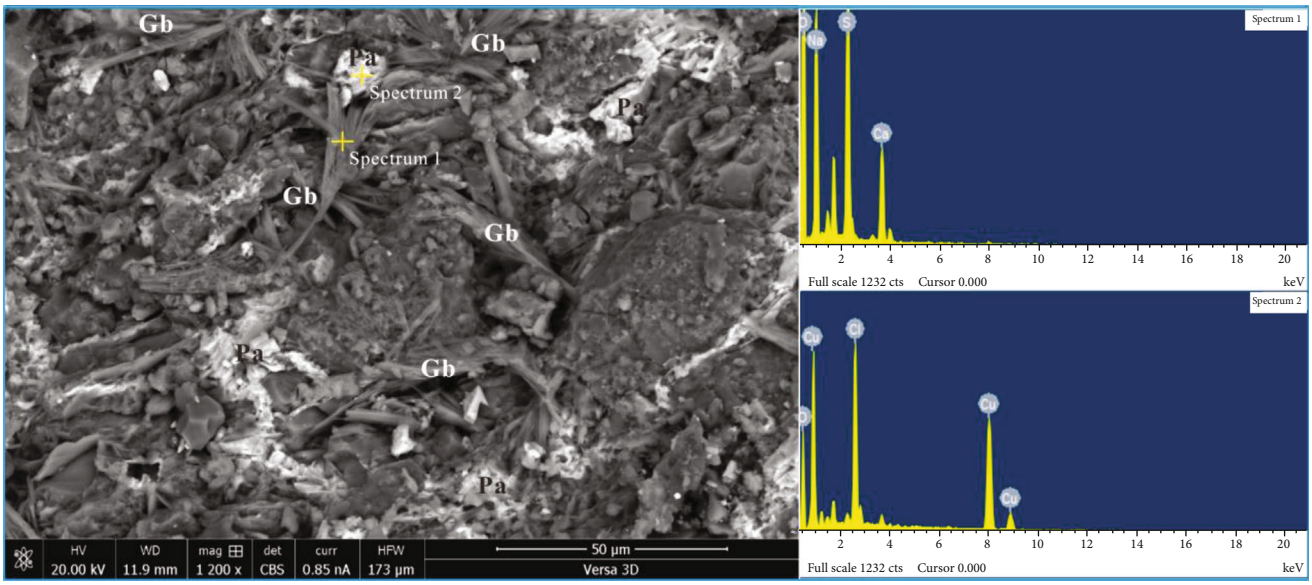

(b)

Figure 3: SEM and EDS analysis of sample KC-G_1. (a) and (b) are BSE images, whereas the rest of the graphs are EDS spectrums. Pa: paratacamite; Gp: gypsum; Gb: glauberite; HI: halite. (a) Left: SEM image; right: EDS graph. The white mineral, containing mainly Cu, Cl, O, and a few Si, Al, Ca, Pb, and Zn, is paratacamite (Cu_2 $(OH)_3$ Cl) and may contain clay minerals, Zn and Pb. The ash black mineral containing Ca, S, and O is gypsum ($CaSO_4{\cdot}2H_2O$). The grey mineral containing Na and Cl is halite (NaCl). (b) Left: SEM image; right: EDS graph. The radial material is glauberite ($Na_2SO_4{\cdot}CaSO_4$). The white mineral containing Cu, Cl, and O is paratacamite (Cu_2 $(OH)_3$ Cl).

Chinese Academy of Geological Sciences, Beijing, using the Inductively Coupled Plasma-Optical Emission Spectrometry (ICP-AES) (model: SPECTRO ARCOS SOP).

4. Results

The results on SEM and EDS analysis of 3 samples can be summarized and seen in Figure 3, Tables 1 and 2, Figure 4, Table 3, Figure 5, and Table 4. The results reveal that halite (abbreviated HI, the same below, Figure 3(a) and spectrum 3), gypsum or anhydrite (abbreviated Gp, the same below, Figure 3(a) and spectrum 2), glauberite (abbreviated Gb, the same below, Figure 3(b) and spectrum 1), and atacamite or paratacamite (abbreviated Pa, the same below, Figure 3(b) and spectrum 2) coexist in the sample KC-G_1. Combined with previous geological evidence on mineral analysis of Cu-bearing gypsum veins in sandstone of the basin [17], we conclude that the discoverable minerals of sample KC-G_1 are halite, gypsum, glauberite, and paratacamite. In addition, the white grain in Figure 3(a), containing mainly Cu, Cl, O, and a few elements such as Si, Al, Ca, Pb, and Zn (Table 1), is paratacamite (Cu_2 $(OH)_3$ Cl) and may contain clay minerals, Zn and Pb. In the same way, sample KC-G_2 contains halite, paratacamite, and natural copper

Table 1: The concentration of elements on grains in SEM of Figure 3(a).

Elements	Weight (%)	Mole (%)
	Spectrum 1	
OK	11.86	30.26
NaK	3.89	6.91
AlK	0.46	0.69
SiK	2.18	3.16
ClK	17.82	20.52
CaK	0.58	0.59
CuK	41.06	26.38
ZnK	15.77	9.85
CdL	2.32	0.84
PbM	4.07	0.80
Total	100.00	
	Spectrum 2	
OK	56.86	74.73
SK	20.14	13.21
CaK	23.00	12.07
Total	100.00	
	Spectrum 3	
NaK	41.63	52.38
ClK	58.37	47.62
Total	100.00	

Table 2: The concentration of elements on grains in SEM of Figure 3(b).

Elements	Weight (%)	Mole (%)
	Spectrum 1	
OK	60.71	72.91
NaK	18.08	15.11
SK	15.17	9.09
CaK	6.03	2.89
Total	100.00	
	Spectrum 2	
OK	23.96	51.50
ClK	17.13	16.62
CuK	58.91	31.88
Total	100.00	

(Figure 4, Table 3). Sample KC-G_3 contains halite, gypsum, probably lead chloride ($PbCl_2$), and paratacamite involved in a few elements Si, Al, Ca, K, Pb, and Zn (Figure 5, Table 4).

The main chemical components of thirteen surface brines are summarized in Table 5.

5. Discussion

5.1. Sources and Developmental Cycle of Cu-Bearing Brine. The evaporite in the Kuqa Basin formed from the evaporation of seawater in the Neo-Tethys Ocean. Salt springs and crystalline blooms occur throughout the earth's surface of the whole basin (Figures 1 and 2(g)). As a Mesozoic-Cenozoic evaporite basin, the Kuqa Basin is a favorable site for brine formed because of evaporite units composed of rock salt and gypsum rock. Cai et al. [29] analyzed the water of the Paleogene rock units in the Tarim Basin and showed characteristics of seawater including high average content of bromine and $Br * 10^3/Cl$, for example, respectively, 92 mg/l and 0.78 (Paleogene rocks) in comparison to 33.4 mg/l and 0.28 (Neogene rocks) and 15.3 mg/l and 0.09 (Quaternary units). The values are markedly different from those in the Neogene and Quaternary units. The salinity of water from the Neogene and Quaternary rock units is 202.94 g/l and 353.46 g/l, respectively [29], and is inferred to have originated from the near-surface where the salt concentrations are low. Therefore, salt in the brine must have originated from the dissolution of evaporite or from salt domes interacting with freshwater via surface fractures.

The brine is a type of compounded water from which derives meteoric waters and the Neo-Tethys Ocean seawater by research on its hydrogen and oxygen isotopes [23]. It has a powerful capacity to leach the metallic ions from its surrounding rocks, so an experiment was designed to verify it. 22 samples (such as rock salt, gypsum rock, sandstone, and mudstone) collected from different kinds of rocks were leached by saline in diverse days (Table 6). Because of 10% average value (Wt) on composition of sodium chloride in the Kuqa Basin by previous geochemical analysis on 135 surface-water samples [23], the saline with 10% sodium chloride (Wt) was made up to leach the metallic ions of samples. These results indicate that the concentration of Cu ion in the saline is changed accompanied with different samples or days in the conditions of 25°C (Table 6). The average value of Cu ion in the filtrate is 0.2532 (mg/l, the same below) in a 10-day period, accordingly 0.2571 in 20 days, 0.1815 in 30 days, and 0.2621 in 90 days, and the highest value is 0.6280. Compared with analysis results on 13 brine samples, the values of Cu ion among 3 samples collected from the Kezier area are much higher than those in the other areas, 0.315, 0.225, and 0.330 (Table 5). The value of composition is similar to that of filtrate obtained indoors; meanwhile, the Cu-bearing brine occurring on the surface of the Kezier area is revealed. In addition, our experiment demonstrates that the saline can extract Cu ion quickly from surrounding rocks and come into Cu-bearing saline in a very short time (only 10 days) compared with a long geological period, so too the brine. The copper is derived from not only clastic rocks but also evaporite (Table 6).

5.2. Genetic Mechanism of Cu-Mineralized Evaporite in Fractured Fault Belts of Sandstone. By the results of SEM and EDS, green Cu-mineralized samples are concluded with the main composition of paratacamite, natural copper, halite, gypsum, and glauberite. Because of powerful capacity for extracting mineral ions, sometimes the brine contains ions such as zinc, lead, silicon, and aluminum, so the crystalline paratacamite might contain a few clay minerals, zinc and lead. Paratacamite is generally associated with brine and arid climate. It is a secondary mineral that roots in the interaction

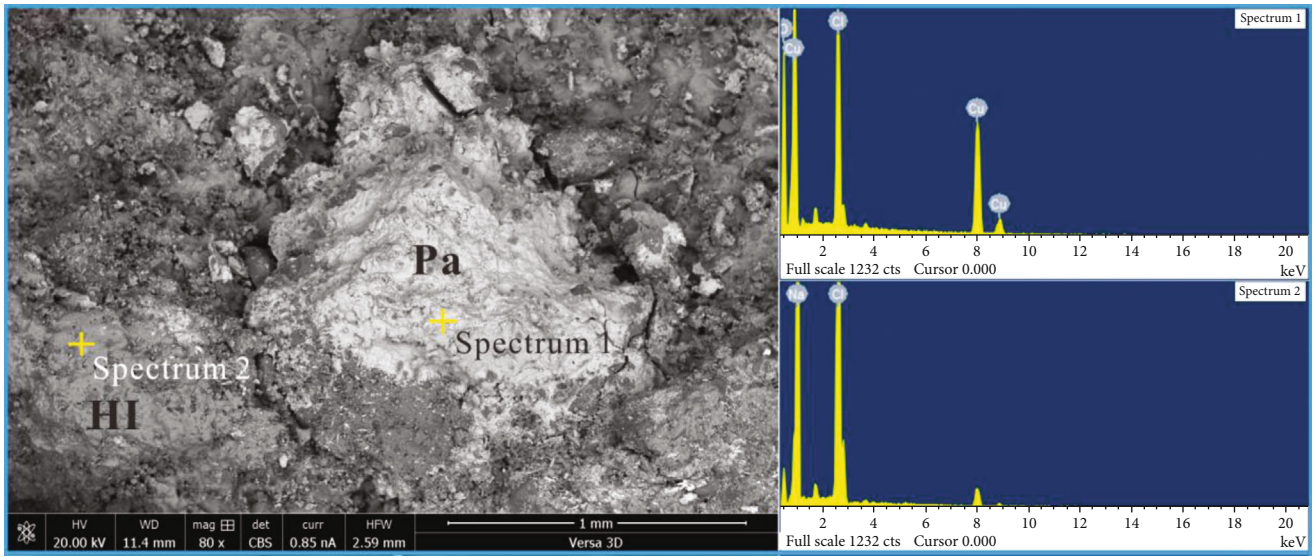

(a)

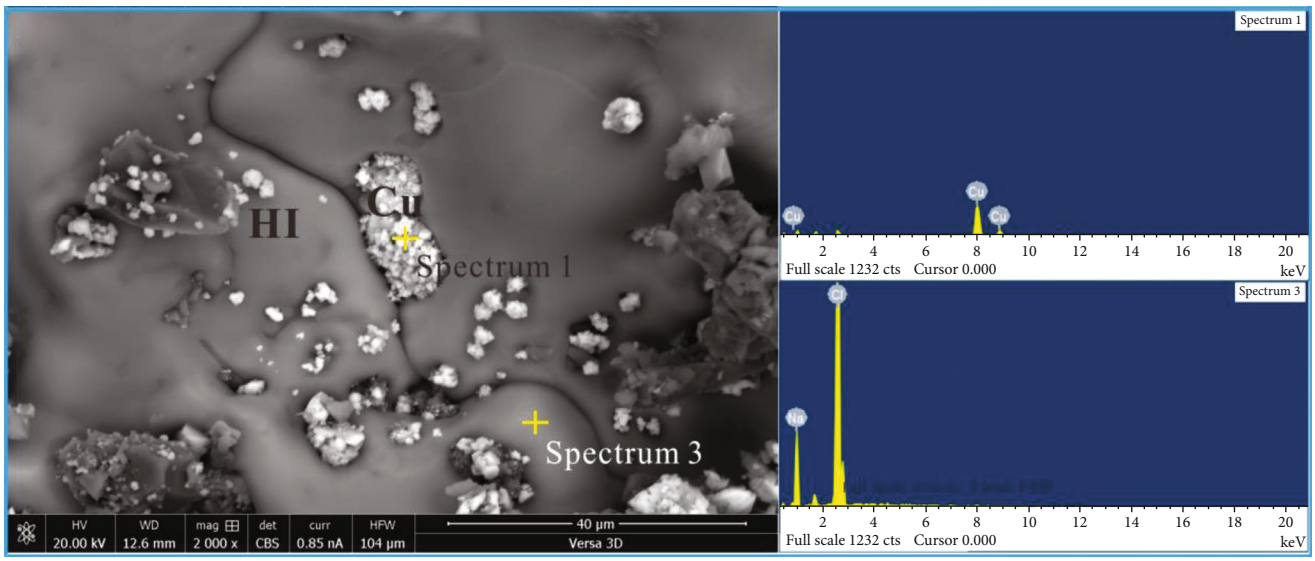

(b)

Figure 4: SEM and EDS analysis of sample KC-G_2. (a) and (b) are BSE images whereas the rest of the graphs are EDS spectrums. Pa: paratacamite; HI: halite; Cu: natural copper. (a) Left: SEM image; right: EDS graph. The white mineral containing Cu, Cl, and O is paratacamite (Cu_2 $(OH)_3$ Cl). The grey mineral containing Na and Cl is halite (NaCl). (b) Left: SEM image; right: EDS graph. The white mineral containing Cu is natural copper (Cu). The grey mineral containing Na and Cl is halite (NaCl).

of primary copper minerals and brine [30–33]. In the course of Cu-bearing brine migrated along the fractured fault belts of sandstone, paratacamite was separated out accompanying with crystallized salt minerals. Because the depositional sequence of salt minerals is controlled by their different solubility, such as gypsum, halite, and potassium-magnesium salt crystallized in turn, the occurrence of paratacamite must also be controlled for its chemical composition of element chlorine.

Based on the paragenetic sequence of the samples studied, gypsum crystallized first, followed by halite. The paratacamite occurs on the surface of the gypsum, as well as in pores that show evidence of enlargement from dissolution of gypsum (Figure 3(a)). The radial and acicular glauberite (Figure 3(b)) correspond to the secondary glauberite, formed through the interaction of brine enriched in Cl^- and Na^+ with an external fluid enriched in SO_4^{2-} and Ca^{2+} during later periods of evolution of the brine and after the crystallization of gypsum [34, 35]. These indicate that the paratacamite was precipitated after gypsum and that gypsum experienced dissolution after crystallization. Therefore, during the Cu-bearing brine migration along the fractured fault belts, the gypsum crystallized and subsequently dissolved by the residual brine, in which SO_4^{2-} and Ca^{2+} reacted with Cl^- and Na^+ in the residual brine to crystallize the secondary glauberite, so that the Cl^- became redundant after SO_4^{2-},

Table 3: The concentration of elements on grains in SEM of Figure 4.

Elements	Figure 4(a) Weight (%)	Mole (%)	Elements	Figure 4(b) Weight (%)	Mole (%)
	Spectrum 1			Spectrum 1	
OK	34.62	63.33	CuK	100.00	100.00
ClK	17.94	14.81	Total	100.00	
CuK	47.45	21.86		Spectrum 3	
Total	100.00		NaK	15.33	21.83
	Spectrum 2		ClK	84.67	78.17
NaK	35.50	45.91	Total	100.00	
ClK	64.50	54.09			
Total	100.00				

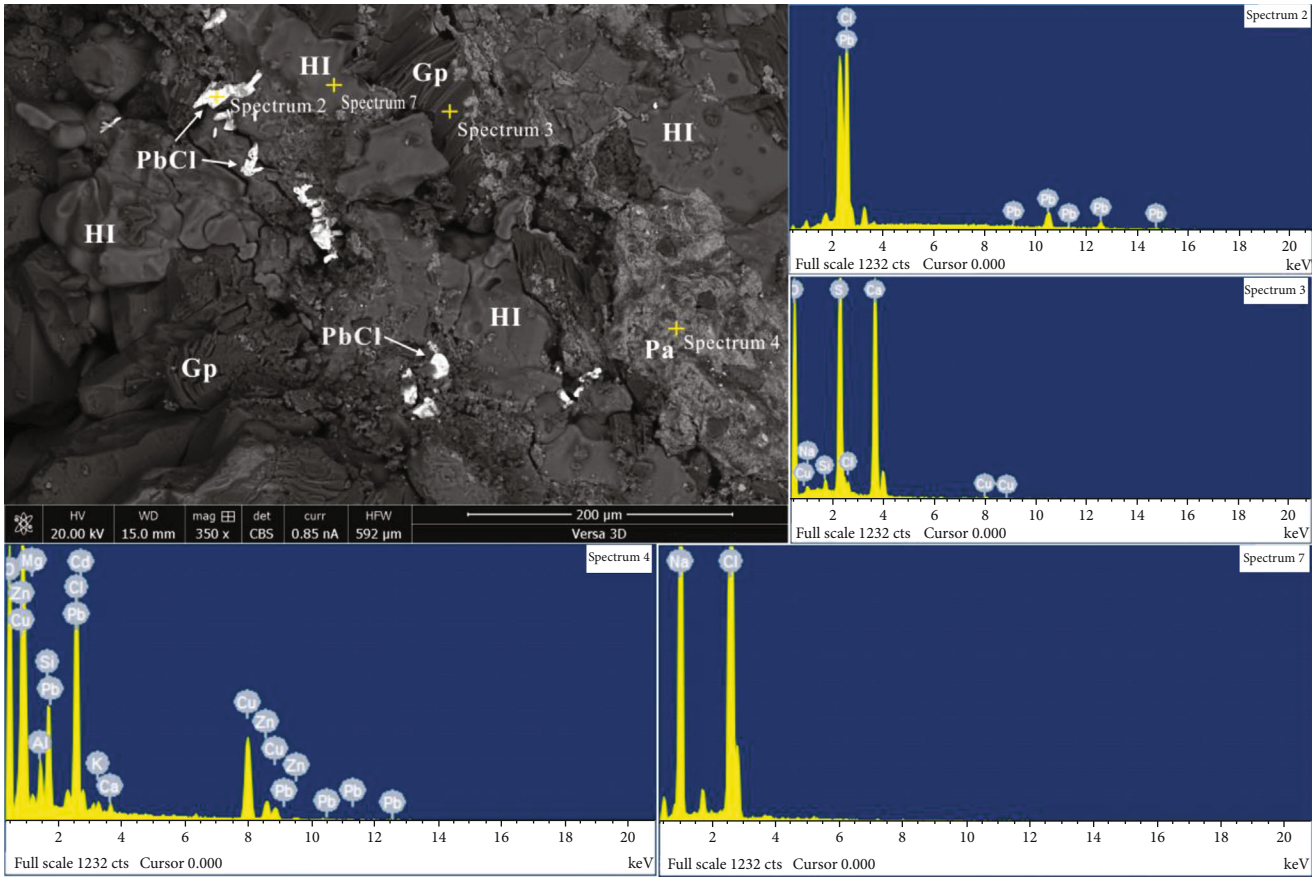

Figure 5: SEM and EDS analysis of sample KC-G_3. The upper left is a BSE image whereas the rest of the graphs are EDS spectrums. Gp: gypsum; Pa: paratacamite; HI: halite. The bright white mineral containing Pb and Cl might be $PbCl_2$. The white mineral, containing Cu, Cl, O, and a few Si, Al, Ca, K, Pb, and Zn, is paratacamite (Cu_2 $(OH)_3$ Cl) and may contain clay minerals, Zn and Pb. The grey mineral containing Na and Cl is halite (NaCl). The ash black mineral containing Ca, S, and O is gypsum ($CaSO_4{\cdot}2H_2O$).

Ca^{2+}, and Na^+ expended. The redundant Cl^- in the brine reacted with Cu and OH^- to form paratacamite. Finally, halite crystallized from the residual brine. Meanwhile, other metal ions such as lead and zinc might be precipitated by lead chloride ($PbCl_2$) (bright-white grains and its spectrum 2 in Figure 5), also the elements of clay minerals such as silicon and aluminum (white grains and their spectrum 1 in Figure 3(a)).

Halite, paratacamite, and natural copper are discovered in a paragenetic relationship in the sample KC-G_2 (Figures 4(a) and 4(b)), especially the natural copper that occurs on the surface of halite (Figure 4(b)). Some Cu grains lie in the pores of halite, and others do not. But compared with spectrums of halite in Figures 4(a) and 4(b), the spectral lines of sodium and chlorine are different from each other, and the sodium declined in spectrum 3 of Figure 4(b). All

Table 4: The concentration of elements on grains in SEM of Figure 5.

Elements	Weight (%)	Mole (%)
	Spectrum 2	
ClK	33.94	69.92
PbM	66.06	30.08
Total	100.00	
	Spectrum 3	
OK	63.65	79.57
SK	17.07	10.59
CaK	19.29	9.83
Total	100.00	
	Spectrum 7	
NaK	30.61	38.88
ClK	69.39	61.12
Total	100.00	
	Spectrum 4	
OK	43.41	69.62
MgK	0.92	0.97
AlK	2.16	2.05
SiK	4.84	4.42
ClK	12.82	9.28
KK	0.32	0.21
CaK	0.52	0.33
CuK	24.52	9.90
ZnK	6.75	2.65
CdL	1.00	0.23
PbM	2.74	0.34
Total	100.00	

the appearances are reflected in the EDS chart (Table 3). Based on the datum of Table 3, the atomic ratio of chloride to sodium is nearly 1 : 1 (54.09 : 45.91) (spectrum 2 in Figure 4(a)) and 3 : 1 (78.17 : 21.83) (spectrum 3 in Figure 4(b)), which showed an unbalanced feature of atomic amount between chloride and sodium. Enriched chloride that occurred in the halite indicates that some chloride ion in the brine reacted with Cu and OH^- to form paratacamite, and sodium ion reacted with Ca^{2+} and SO_4^{2-} to form the secondary glauberite. But the genetic mechanism of natural copper is still unknown at present.

5.3. Crystallized Cycle of Cu Mineralized on the Surface of Clay. The Cu deposit on the surface of maroon clay is observed in the scallops of grey-white medium- to coarse-grained sandstone in the Kezier area (Figures 1, 2(e), and 2(f), sample no. KC-G_3) on August 16, 2019. Field investigations show that green Cu mineral and white halite have already been precipitated on the surface of clay, but the clay is moist and the halite was precipitating along with the clay getting dryer and dryer. We infer that more and more halite must be crystallized on the argillaceous surface afterwards. In this way, it is offered as evidence that the halite must be crystallized later than the paratacamite. As we did not see the geological phenomenon at the same site when we did a field investigation during the whole of April of that year in the Kuqa Basin, therefore, the crystallized cycle of paratacamite is no more than 5 months (from April to August). These indicate that there is a rapid Cu enrichment mechanism from Cu-bearing brine at normal pressure and temperature (NPT) conditions in the earth's surface of the Kuqa Basin.

The rapid Cu enrichment on the surface of clay occurs in a stratified form but only occurs on the surface, not in the interior of the clay (Figure 2(f)). These hint that when the Cu-bearing brine which carried a little clay flowed along the sandstone's surface, the clay was deposited persistently in the scallop; correspondingly, the minerals were precipitated accompanying with the brine evaporation.

The mineral composed of elements Pb and Zn, maybe lead chloride, is paragenetic with paratacamite, halite, and gypsum in the sample KC-G_3 (Figure 5, Table 4). It indicates that the brine contains not only copper but also lead ions. Our research demonstrates again that the depositional metal minerals from brine are controlled by crystallized sequence of saline minerals.

Previous research on paratacamite from gypsum veins in sandstones of the Kuqa Basin is considered that the Cu-bearing brine comes from deeper rock units. It migrates upward along the fractured fault belts of sandstone to the surface and is concentrated in arid climate condition [17], but the developmental time and cycle of the brine are unknown. These make the developmental time and cycle of Cu enrichment uncertain. The cycle may be several to tens of millions years or persist in a more distant geologic period. Now, we realize that the growth cycle of Cu-bearing brine is about 3 months (sometimes only 10 days), and the cycle of Cu enrichment only needs no more than 5 months, also in normal pressure and temperature conditions. Pei et al. [36] put forward a type of mineralization mechanism (event geology stimulating anomalous ore-forming processes with economic super-accumulation of metals), and we also think the rapid Cu enrichment mechanism might make an enormous amount of metal mineralization come into being if considered from a large-scale viewpoint. Compared with the mineralization of hypothermal deposits, the surface-Cu enrichment with normal pressure and temperature is controlled by a crystallized sequence of saline minerals, and the cycle of Cu mineralization is only a few months. Even if the mineralization is in multiple stages, it is still a very short time compared to several to tens of millions years in the geologic period. These are different from the previous cognition of Cu enrichment or mineralization.

6. Conclusions

So we can draw some conclusions as follows:

(1) The surface-Cu enrichment showed by paragenetic sequence with paratacamite, gypsum, halite, secondary glauberite, natural copper, and probably lead chloride occurs on the fractured fault belts of sandstones or the surface of clay. It is a close relationship

Table 5: Main chemical components of the surface brine.

Sample numbers	K^+ (mg/l)	Na^+ (g/l)	Ca^{2+} (g/l)	Mg^{2+} (g/l)	SO_4^{2-} (g/l)	Cl^- (g/l)	Cu^{2+} (mg/l)
YSG-W1	112.76	31.51	2.60	0.80	4.89	53.12	<0.004
DYSG-W1	133.96	70.00	9.39	2.56	1.59	124.06	<0.004
DYSG-W2	134.30	66.62	9.23	2.54	1.68	124.70	<0.004
DYSG-W3	242.50	108.52	11.98	3.52	0.78	205.31	<0.004
DQ8-W1	115.82	31.65	2.62	0.78	4.95	51.90	<0.004
DQ8-W2	104.70	29.81	2.58	0.77	4.89	48.03	<0.004
WBS-W1	190.52	109.64	1.43	0.73	5.76	176.05	<0.004
WBS-W2	44.90	13.47	0.94	0.64	5.22	16.90	<0.004
KZE-W1	288.48	110.05	9.56	1.70	0.90	186.56	0.160
KZE-W2	293.04	109.40	9.60	1.69	0.90	189.66	0.315
KZE-W3	281.80	96.31	7.89	1.96	0.63	164.29	0.225
KZE-W4	295.22	96.71	9.93	2.16	0.72	167.35	0.330
KZE-W5	8.76	1.75	0.80	0.12	2.67	2.33	<0.004

Table 6: Concentration of Cu ion in the saline from different rocks leached and days.

Sample numbers	Lithology	Cu (mg/l)			
		10 days	20 days	30 days	90 days
0811KC-BCH-G7	Amaranthine rock salt	0.4368	0.3935	0.4132	0.1107
0811KC-BCH-G2	Celadon rock salt	0.4462	0.4622	0.2534	0.1621
0811KC-YSK-G5	Cyan-grey rock salt	0.3585	0.432	0.2928	0.1936
0811KC-YSKD-G5	Yellow-white silty gypsum rock	0.2593	0.2881	0.2043	0.1526
0811KC-YSKD-G6	Yellow-white silty gypsum rock	0.2683	0.298	0.1831	0.1132
0812KC-AGX-S10	Celadon silty gypsum rock	—	0.1555	0.0785	0.1953
0811KC-YSKD-G4	Celadon silty gypsum rock	0.1952	0.1122	0.0712	0.5266
0812KC-KCHX-G4	Grey-white medium- to coarse-grained sandstone with Cu mineralization	0.2682	0.2674	0.2017	0.2429
0812KC-KL2-G4-2		0.2525	0.2253	0.1554	0.2808
0812KC-KL2-G9		0.2915	0.2932	0.2107	0.2588
0812KC-AGX-TKD		0.2376	0.2071	0.1031	0.2031
0811KC-S1-G4	Celadon siltstone with Cu mineralization	0.2489	0.289	0.2373	0.6280
0812KC-KL2-G14A		0.2383	0.2944	0.1728	0.2871
0812KC-KCHX-G5	Grey-white medium- to coarse-grained sandstone with Cu mineralization	0.2712	0.2587	0.1691	0.3565
0812KC-AGX-TK3		0.2103	0.1891	0.1179	0.3446
0812KC-AGX-TK1		0.1970	0.1612	0.0793	0.2465
0812KC-KCHX-G2		0.1956	0.1322	0.0361	0.2838
0812KC-KCHX-G3		0.1826	0.0844	0.1294	0.2691
0812KC-AGX-S18	Celadon siltstone	0.2523	0.2601	0.2043	0.2938
0812KC-AGX-S16	Celadon gypseous siltstone	0.259	0.2921	0.2917	0.2256
0812KC-KCHX-G9	Celadon mudstone	0.2424	0.2671	0.1988	0.1197
0812KC-KL2-G5	Grey-white medium- to coarse-grained sandstone	0.2576	0.2934	0.1886	0.2712
Average values		0.2532	0.2571	0.1815	0.2621

between the Cu enrichment and Cu-bearing brine derived from leached rocks and evaporite units by meteoric waters and ancient seawater

(2) The occurrence of paratacamite is controlled by a crystallized sequence of saline minerals accompanying with evaporated and concentrated brine in which gypsum, secondary glauberite, paratacamite, and halite are crystallized in turn

(3) With normal pressure and temperature conditions, the Cu-bearing brine can be formed in a very short time (10 days is OK). The cycle of surface-Cu enrichment or mineralization is also only a few months (no

more than 5). These indicate a rapid surface-Cu enrichment from Cu-bearing brine in the evaporite basin. So the enrichment mechanism might be supposed to make an enormous amount of metal mineralization in a very short time if considered from a large-scale viewpoint. By contrast on the lengthy geologic period, the rapid enrichment mechanism is different from the previous cognition of Cu enrichment or mineralization

Data Availability

The experimental datum used to support the findings of this study is included in the manuscript and supplementary material.

Conflicts of Interest

The authors declare no conflict of interest.

Acknowledgments

This study was supported by the Basic Research Project for the Central Public Welfare Scientific Institutions (YYWF201716) granted by the Institute of Mineral Resources, CAGS, and the National Natural Science Foundation of China (41972082).

References

[1] J. K. Warren and R. H. Kempton, "Evaporite sedimentology and the origin of evaporite-associated Mississippi Vally-type sulfides in the Cadjebut mine area, Lennard shelf, Canning Basin, Western Australia," in *Basin Wide Diagenetic Patterns: Integrated Petrologic, Geochemical, and Hydrologic Considerations*, I. P. Montanez, J. M. Gregg, and K. L. Shelton, Eds., pp. 183–205, SEPM Special Publication, Tulsa OK, 1997.

[2] J. K. Warren, *Evaporites: Sediments, Resources, and Hydrocarbons*, Springer, Verlag Berlin Heidelberg, 2006.

[3] J. M. Zientek, M. L. Parks, H. L. Dicken, C. L. Dicken, and the US Geological survey global copper mineral resource assessment team, *Assessment of Undiscovered Copper Resources of the World*, vol. 619, U.S. Geological Survey Scientific Investigations Report, 2019, 2015 (ver.1.1, May 24, 2019).

[4] W. S. Xu, Z. J. Yao, and W. T. Han, "A study of the content characteristics of copper, lead, zinc, strontium and barium in sedimentary anhydrite and their activation and migration," *Geoscience*, vol. 5, pp. 79–90, 1991.

[5] K. X. Tan, *Geochemistry and Dynamics of Metallization on Copper Mineral of Sandstone*, Earthquake Public House, Beijing, 1998.

[6] F. Grandia, A. Canals, E. Cardellach, D. A. Banks, and J. Perona, "Origin of ore-forming brines in sediment-hosted Zn-Pb deposits of the Basque-Cantabrian Basin, northern Spain," *Economic Geology*, vol. 98, no. 7, pp. 1397–1411, 2003.

[7] P. N. Southgate, T. K. Kyser, D. L. Scott, R. R. Large, S. D. Golding, and P. A. Polito, "A basin system and fluid-flow analysis of the Zn-Pb-Ag mount Isa-type deposits of northern Australia: identifying metal source, basinal brine reservoirs, times of fluid expulsion, and organic matter reactions," *Economic Geology*, vol. 101, no. 6, pp. 1103–1115, 2006.

[8] H. L. Cao, R. M. Hua, B. Rao, and L. W. Qiu, "Preliminary experimental study on dissolution of metal elements in oil field brine of Jiyang depression, Shandong Province," *Geological Review*, vol. 48, pp. 444–448, 2002.

[9] W. Li, "Some problems on movement and enrichment of aurum," *Journal of Yunnan University (Natural Sciences)*, vol. 11, p. 30, 1989.

[10] J. W. Johnson, E. H. Oelkers, and H. C. Helgeson, "SUPCRT92: a software package for calculating the standard molal thermodynamic properties of minerals, gases, aqueous species, and reactions from 1 to 5000 bar and 0 to 1000°C," *Computers and Geoscience*, vol. 18, no. 7, pp. 899–947, 1992.

[11] A. A. Migdisov, A. E. Williams-Jones, and O. M. Suleimenov, "Solubility of chlorargyrite (AgCl) in water vapor at elevated temperatures and pressures," *Geochimica et Cosmochimica Acta*, vol. 63, no. 22, pp. 3817–3827, 1999.

[12] S. M. Archibald, A. A. Migdisov, and A. E. Willams-Jones, "An experimental study of the stability of copper chloride complexes in water vapor at elevated temperatures and pressures," *Geochimica et Cosmochimica Acta*, vol. 66, no. 9, pp. 1611–1619, 2002.

[13] H. R. Mark and P. James, "Sulfide mineral precipitation from hydrothermal fluids," *Reviews in Mineralogy & Geochemistry*, vol. 61, pp. 609–631, 2006.

[14] D. Asael, A. Matthews, S. Oszczepalski, M. Bar-Matthews, and L. Halicz, "Fluid speciation controls of low temperature copper isotope fractionation applied to the Kupferschiefer and Timna ore deposits," *Chemical Geology*, vol. 262, no. 3-4, pp. 147–158, 2009.

[15] Y. T. Cao, C. L. Liu, H. J. Yang, Q. Y. Gu, P. C. Jiao, and Y. H. Lu, "Identification and correlation of evaporites sedimentary cycle in Kuqa Basin of Paleogene and Neogene," *Journal of Palaeogeography*, vol. 12, pp. 31–41, 2010.

[16] Y. T. Cao, C. L. Liu, P. C. Jiao et al., "Evaporite deposition and potassium enrichment prospect from Upper Cretaceous to Paleogene in Yarkand Basin, Xinjiang," *Mineral Deposits*, vol. 35, pp. 300–314, 2016.

[17] Y. Cao, C. Liu, P. Jiao, and C. Wang, "Paratacamite from gypsum veins in sandstones of the Kuqa Basin, Xinjiang, China: implications for a new epigenetic Cu enrichment mechanism," *Resource Geology*, vol. 66, no. 2, pp. 114–126, 2016.

[18] C. Z. Jia, "Evolvement of slab structure in Tarim Basin," in *Corpus of Research on Modern Geology (First)*, Q. Dai, Q. R. Liu, and J. L. Li, Eds., pp. 22–31, Nanjing University Press, Nanjing, 1992.

[19] S. A. Graham, M. S. Hendrix, L. B. Wang, and A. R. Carroll, "Collisional successor basins of western China: impact of tectonic inheritance on sand composition," *Geological Society of America Bulletin*, vol. 105, no. 3, pp. 323–344, 1993.

[20] S. L. Cao, F. J. Chen, and C. R. Luo, "Numerical modeling of subsidence mechanism of a Meso-Cenozoic foreland basin in North Tarim," *Oil and Gas Geology*, vol. 15, pp. 113–120, 1994.

[21] H. F. Lu, D. Jia, D. S. Cai, S. M. Wu, and C. M. Chen, "Evolvement of slab structure in Paleozoic in Tarim Basin and in the west in Tianshan mountain," in *The New Evolvement of Petroleum Geology in Tarim Basin*, X. G. Tong, D. G. Liang, and C. Z. Jia, Eds., pp. 235–245, Science Press, Beijing, 1996.

[22] L. Huafu, D. G. Howell, J. Dong et al., "Rejuvenation of the Kuqa foreland basin, northern flank of the Tarim Basin,

Northwest China," *International Geology Review*, vol. 36, no. 12, pp. 1151–1158, 2010.

[23] C. L. Liu, P. C. Jiao, Y. T. Cao, and Y. Z. Chen, *Interior Report on Large-Scale Minerogenetic Conditions and Prediction Technique of Potash in Tarim Basin*, 2010.

[24] G. Q. He, M. S. Li, D. Q. Liu, Y. L. Tang, and R. H. Zhou, *Evolvement and Metallogenesis of Lithosphere in Paleozic in Xinjiang China*, Xinjiang Peoples Publishing House and Hongkong Culture and Educate House, Urumqi and Hongkong, 1994.

[25] L. Z. Guo, Y. S. Shi, H. F. Lu, Q. B. Li, J. X. Dai, and R. Q. Liu, "The two distances domino effect on India Slab and Tibetan Plateau," in *Corpus of Research on Modern Geology (First)*, Q. Dai, R. Q. Liu, and J. L. Li, Eds., pp. 1–7, Nanjing University Press, Nanjing, 1992.

[26] L. J. Zhang, D. L. Li, Y. S. Sun, and M. Chen, "Analysis of characteristics of sedimentary reservoir between Cretaceous and Palaeogene in the western part of the Kuqa depression," *Natural Gas Geoscience*, vol. 17, pp. 355–360, 2006.

[27] X. X. Zhou, "The features of tertiary halite-gypsum caprocks and their control on forming of oil and gas pools in Kuqa depression," *Journal of Palaeogeography*, vol. 2, pp. 51–57, 2004.

[28] L. J. Tang, Z. J. Jin, C. Z. Jia, X. J. Pi, and S. P. Chen, "Multicyclic salt tectonics and oil-gas accumulation in Tarim Basin," *Science China Series D*, vol. 34, pp. 89–97, 2004.

[29] C. F. Cai, B. W. Mei, T. Ma, and F. G. Zeng, "Origin and evolution of oilfield waters in the Tarim basin," *Geological Review*, vol. 43, pp. 650–656, 1997.

[30] L. Ye and T. G. Liu, "The discovery of atacamite in Xinjiang and its significance," *Acta Mineralogica Sinica*, vol. 17, pp. 78–81, 1997.

[31] X. Y. Li, Y. Jiang, and Y. G. Zhang, *Research Index Minerals of Copper Deposit: Atacamite in Arid Climates*, Xinjiang Nonferrous Metals, 2003.

[32] S. Y. Wang, Y. S. Wang, X. L. Zhong, and R. Zhao, "The function of the mineral characteristics of atacamite in the process of mine finding," *Xinjiang Geology*, vol. 21, pp. 251-252, 2003.

[33] K. Y. Bai and Z. X. Han, "Paratacamite of Kanggu'ertage gold deposit in the Xinjiang Uygur Autonomous Region of China," *North Western Geology*, vol. 40, pp. 114–117, 2007.

[34] J. Q. Zhu and W. X. Hu, "Types and geneses of glauberite in the Anning basin, Yunnan Province," *Journal of Hebei College of Geology*, vol. 12, pp. 34–42, 1989.

[35] Q. T. Yang, "The origin and analysis sedimentary environment analysis of glauberite," *Acta Sedimentologica Sinica*, vol. 7, pp. 137–141, 1989.

[36] R. F. Pei, Y. X. Mei, J. W. Li et al., "Event geology stimulating anomalous ore-forming processes with economic superaccumulation of metals," *Acta Geologica Sinica*, vol. 80, pp. 1509–1517, 2006.

Hindawi
Geofluids
Volume 2021, Article ID 5574772, 12 pages
https://doi.org/10.1155/2021/5574772

Research Article

Whether the Middle Eocene Salt-Forming Brine in the Kuqa Basin Reached the Potash-Forming Stage: Quantitative Evidence from Halite Fluid Inclusions

Yang Xu,[1] **Yangtong Cao**,[2] **and Chenglin Liu**[2]

[1]*State Key Laboratory of Nuclear Resources and Environment, East China University of Technology, Nanchang 330013, China*
[2]*MLR Key Laboratory of Metallogeny and Mineral Assessment, Institute of Mineral Resources, Chinese Academy of Geological Sciences, Beijing 100037, China*

Correspondence should be addressed to Yang Xu; geologyxu@163.com

Received 16 January 2021; Revised 23 February 2021; Accepted 4 March 2021; Published 10 March 2021

Academic Editor: Rongxi Li

The Kuqa Basin is an important potentially potash-bearing basin in China, and thick salt-bearing strata were deposited under the influence of multistage Tethyan transgression-regression cycles during the Eocene. At present, research on the process of potash formation in the Kuqa Basin has mostly focused on traditional salt mineralogy, whole-rock geochemistry, and evaporite sedimentary evolution characteristics. However, research on the original ore-forming parent fluid directly related to potash formation has not yet been carried out, directly hindering further evaluation of potash mineralization. Therefore, this paper takes the internal factors controlling potash formation as the starting point and analyzes the physical and chemical properties, such as the homogenization temperatures (T_h) and chemical compositions, of primary halite fluid inclusions. A total of 220 T_h data from fluid inclusions were obtained, and the temperatures ranged from 9.4 to 54.1°C, indicating a high-temperature brine environment conducive to the rapid deposition of the potash deposit. In total, 22 halite fluid inclusions were analyzed for chemical components. The highest KCl content reached 0.59%, which was higher than the lowest industrial grade of potassium-rich brine (0.5%), indicating that the brine experienced a high degree of evaporation and concentration during the salt-forming period and reached the potash precipitation stage. This paper provides quantitative data on the evolution of the sedimentary environment in the Kuqa Basin and supports future potash exploration.

1. Introduction

Global evaporites were concentrated in the Tethys region during the Mesozoic and Cenozoic, and in time and space, a series of evaporites and potash deposits developed sequentially from older in the west to younger in the east [1]. Although the Kuqa Basin, located on the northern branch of the eastern section of the Tethyan region, developed thick evaporite deposits in the Cenozoic, only some potassium minerals have been discovered to date and potash deposits with industrial mining value have not been found [2–4]. Liu et al. [5] proposed that the formation of potash deposits is the result of extremes in three coupled components: "climate, tectonics, and provenance". The Paleocene-Eocene thermal maximum (PETM) was the warmest global climate event in the Cenozoic, and this high-temperature event continued into the early Eocene, when temperatures began to slowly decrease until global warming occurred again in the middle Eocene climate optimum (MECO) [6–9]. There were favorable conditions for the formation of potash deposits in the Kuqa Basin during the Eocene, such as multistage provenance replenishment of Tethyan seawater and a relatively stable and enclosed tectonic structure [2, 10–12]. Many studies report that the Kuqa Basin has broad prospects for potash formation. However, the question of whether the Kuqa Basin reached the stage of potash precipitation currently remains controversial in the mineral deposit community. The most direct approach to answer this question is to determine the evolution stage of brine during the salt-forming period.

Salt-forming brine is primary brine concentrated after the precipitation of rock salt, and it is an ore-forming fluid with a higher evaporation degree than that of rock salt. Restoring salt-forming brine evolution is a direct and reliable method to evaluate the potential for potash formation. Halite fluid inclusions are a good geological archive of brine during the salt-forming period and can provide quantitative and reliable data for studying the temperature, chemical composition, and evolution characteristics of paleobrine associated with potash mineralization. Fluid inclusions are undoubtedly an excellent geological thermometer. At present, scholars in China and other countries have conducted considerable research and widely discussed methods for measuring T_h in halite fluid inclusions and its representative geological significance. Roberts and Spence [13], Lowenstein et al. [14], Zambito and Benison [15], and Zhang et al. [16] conducted research on the T_h of single-phase liquid fluid inclusions in primary halite crystals made artificially in the laboratory and collected from ancient and modern salt lakes, and they showed that the measured T_h quantitatively represents the brine temperature and is close to the atmospheric temperature. Moreover, a high-temperature environment is conducive to shortening the time interval from brine concentration to potash precipitation; so, high-temperature brine can be used as an important indicator of potash formation. This situation is obviously manifested in the northern Shanxi Basin, Sichuan Basin, and Lanping-Simao Basin and the Sakon Nakhon Basin in Laos [17, 18]. Single-phase fluid inclusion components can reflect chemical information during brine evolution and have been widely used in many applications, such as the study of ancient seawater or lake water chemical evolution. Lowenstein et al. [19] used the chemical compositions of halite fluid inclusions for the first time to restore the variations in Phanerozoic seawater. In addition, halite fluid inclusions have been used to study the brine evolution process in salt-forming basins [20–23].

Therefore, this paper takes the internal factors controlling potash formation as the starting point and comprehensively analyzes the evolution stage of middle Eocene salt-forming brine in the Kuqa Basin by studying the evolution patterns of the temperatures and the chemical compositions of halite fluid inclusions. This paper uses halite fluid inclusions for the first time to quantitatively and directly reconstruct various ion concentrations in the middle Eocene salt-forming brine, which has great significance for potash exploration in the Kuqa Basin.

2. Geological Setting

The Tarim Basin experienced multiple marine transgression-regression cycles associated with the Tethys during the Late Cretaceous-Paleogene [24]. Seawater invaded the southwestern Tarim Basin through the Alay Valley in the Late Cretaceous. When the sea level rose in the early Paleocene, the Tethyan transgression range expanded and extended to the Kuqa Basin (Figure 1). At present, the timing of the final retreat of seawater from the Tarim Basin is considered to have occurred between 47 and 33 Ma [24–27]. The key factor controlling the retreat was the northward spur of the Pamirs, not the collision between India and Eurasia [28–30]. The Paleogene transgression-regression cycles in the Kuqa Basin were intermittent, and during each regression, sedimentation in the basin gradually transformed from marine deposits to continental deposits.

The Kuqa Basin is a secondary basin adjacent to the southern Tianshan Mountains in the northern part of the Tarim Basin, and it extends in a nearly east-west direction [34, 35] (Figure 2). The stable tectonic environment created favorable depositional conditions for the formation of the Paleogene evaporite series. The deposition center was located in the central and western parts of the basin, and huge thick salt-bearing strata formed. Paleocene and Eocene strata are composed of the Talak and Xiaokuzibai Formations of the Kumugeliemu Group. Marine fossils (such as foraminifera and gastropods) have been found at the bottom of the Talak Formation; the Xiaokuzibai Formation is composed of purple-red sandstone, silty mudstone, limestone, brown-red silty mudstone, and thick gypsum rock and rock salt deposits, and marine microfossils are found in the middle part [36]. Zheng and Meng [37] established the precise magnetostratigraphy of Paleogene strata in the Kuqa Basin based on paleomagnetic data and determined the ages of the top and bottom of the Kumgeliemu Group, which are 38 Ma and 60.5 Ma, respectively. Teng et al. [38] and Li et al. [39] also proposed that the age of the boundary between the Paleogene Kumgeliemu Group and the Oligocene Suwei Formation is 38 Ma. Cao et al. [40] identified and compared Paleogene evaporite sedimentary cycles in the Kuqa Basin based on multiple drilling data from the Tarim Oilfield Company and developed a standard stratigraphic section of evaporite sedimentary cycles. Therefore, the formation age of salt-bearing strata from borehole DZK01 can be preliminarily determined to be middle Eocene.

3. Materials and Experimental Procedure

3.1. Materials. Rock salt samples used to measure T_h and the chemical compositions of fluid inclusions were collected from middle Eocene salt-bearing strata in borehole DZK01 (Figure 1). Borehole DZK01 is located in the northeastern Baicheng depression of the Kuqa Basin, and this is the first scientific research borehole in the basin to find potash deposits. The borehole mainly comprises mud-bearing rock salt, rock salt with gypsum and mud, gypsum-bearing argillaceous rock salt, and mud-bearing gypsiferous rock salt (Figures 3(a) and 3(b)).

Borehole samples were carefully selected, and the size, shape, and distribution characteristics of fluid inclusions were observed under a microscope and recorded to distinguish between primary and secondary fluid inclusions. Since halite with primary fluid inclusions is the most direct evidence to verify its originality, we placed selected primary halite samples into a desiccant for storage. Primary halite crystals are characterized by euhedral textures, and white smoky or cloudy, fluid inclusions are distributed along the growth surfaces of halite crystals in directional and regular strips. The sizes of individual inclusions vary, with diameters in the range of ~3 to 60 μm, and the inclusions are dominated by single-phase liquid inclusions, with few or no two-phase

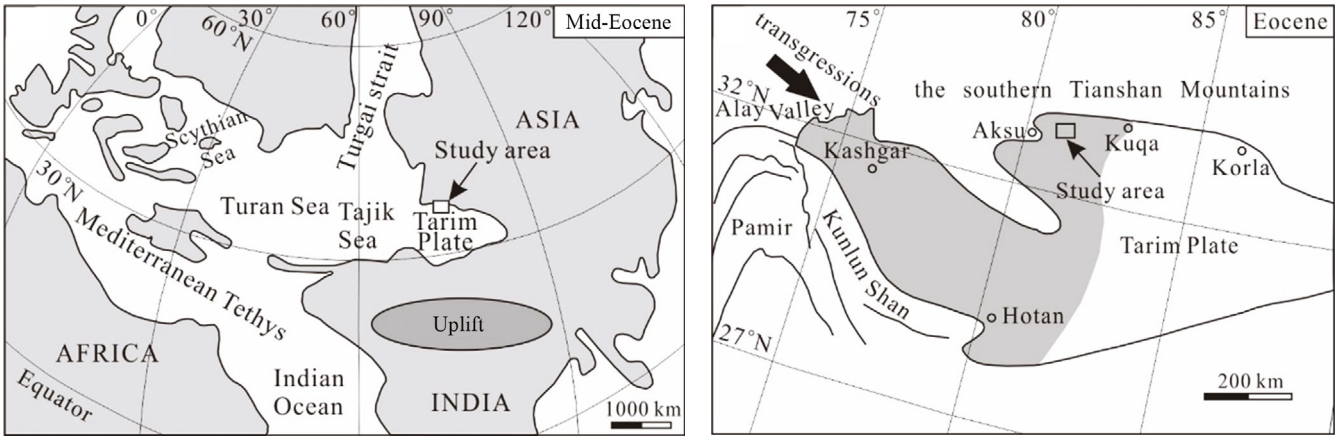

(a) (b)

Figure 1: (a) Paleogeographic sketch map of the mid-Eocene in the Tethyan realm (modified from [31, 32]); (b) Eocene paleogeographic map of the Tarim Plate (modified from [33]).

gas-liquid or three-phase gas-liquid-solid inclusions containing daughter crystals.

3.2. Experimental Procedure. The T_h values of halite fluid inclusions were measured at the State Key Laboratory of Nuclear Resources and Environment, East China University of Technology. A Linkam THMS600 instrument (made in England) was used, and the measured temperature range was at −196 to +600°C. The accuracies of freezing and T_h data were ±0.1°C and ±0.5°C, respectively. Before using cooling nucleation to measure T_h, we used a small hammer to split halite crystals along their cleavage planes into approximately 1 mm-thick slices. First, the halite cleavage slices were carefully observed under a microscope and photographs were taken to record all single-phase liquid fluid inclusions. Then, the selected cleavage slices were placed into a refrigerator (at −15°C to −20°C) for one week and the slices were quickly moved from the refrigerator to a prepared heating and cooling stage and frozen at −18°C until artificial nucleation bubbles appeared within the fluid inclusions. The initial heating rate was set to 0.5°C/min and then slowed to 0.1°C/min nearing 10°C until all observed artificial nucleation bubbles disappeared. Roberts and Spence [13] noted that the T_h of bubbles existing before cooling was abnormally high. Therefore, we chose fluid inclusions that featured artificial nucleation after cooling as the research subjects.

The determination of the chemical compositions of halite fluid inclusions was completed at the National Research Center for Geoanalysis. The laser ablation inductively coupled plasma mass spectrometry (LA-ICP-MS) method was used, and an Element 2 ICP mass spectrometer (Finnigan, Germany) and UP 213 laser (New Wave Company) were used. The diameter of the laser beam was 25 μm, the laser wavelength was 213 nm, and the pulse duration was 4 ns. Under laser ablation sampling conditions, high-purity helium gas was used as the carrier gas to optimize ablation and transmission efficiency. The actual energy acting on the samples was controlled between 0.03 and 0.06 mJ during the experiment, and the ablation energy density was controlled between 7 and 14 J/cm^2. Using the point ablation mode, the gas background acquisition time of each analysis point was approximately 15 s, and the signal acquisition time was 45 s. The calibration method involved internal standard-external standard combination methods [42, 43].

3.2.1. External Standard Method. The prepared standard solution was drawn into a pure quartz capillary tube and quickly sealed with epoxy resin. During the test and analysis, manufactured artificial fluid inclusions were attached to a glass sheet with double-sided adhesive and put into the laser ablation sample chamber together with test samples.

3.2.2. Internal Standard Method. Na was selected as the internal standard element for halite fluid inclusion samples, and the Na content was calculated to be at 141.62 g/L based on the theoretical value. The relative sensitivity between the standard calibration instrument and elements in the unknown sample was assumed to remain unchanged, that is, calibration was carried out according to the consistency of changes in the internal standard element and the elements to be measured [42, 44].

Figures 3(c) and 3(d) show fluid inclusions after laser ablation. Figure 4 shows the variation curve of the mass spectrum signal intensity with time during the analysis of typical halite fluid inclusions. From 1 to 14 s, the measured signal intensity is the background value; the signal intensities of the major elements Na, K, Mg, and Ca are very stable, and the signal intensities of trace elements Rb, Sr, and B fluctuate slightly. At 15 s, the signal intensities of Na, Mg, and Sr increase instantly and those of other elements remain stable; this is the result of laser ablation reaching the halite surface and releasing Na, Mg, and Sr. Then, the signal intensity of Na decreases slightly and the signal intensities of the other elements decrease quickly to the initial background values. From 26 to 33 s, when laser ablation reaches the fluid inclusion, the signal intensities of all major and trace elements increase significantly, especially K, Mg, Ca, and Sr. The signal

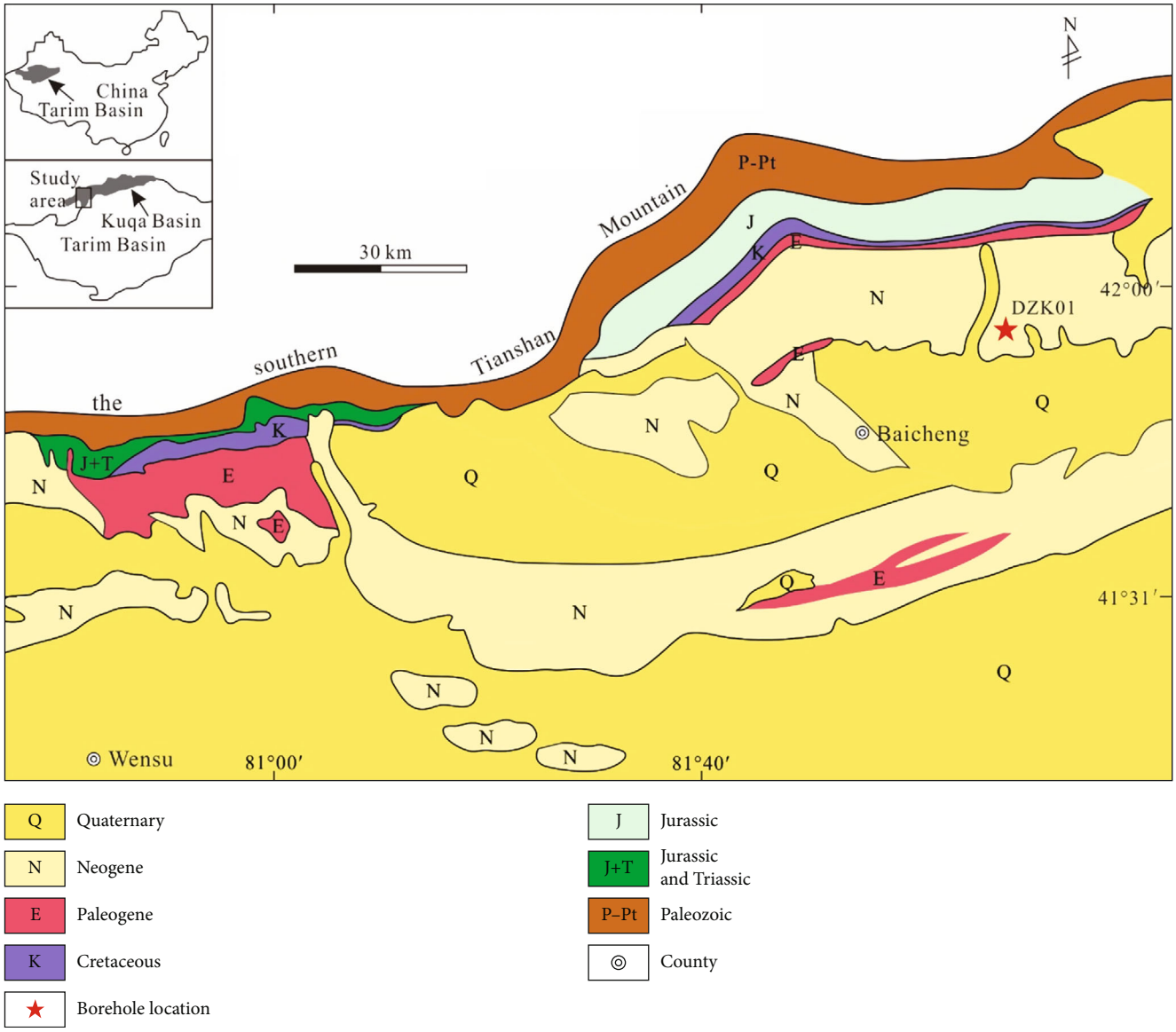

Figure 2: Simplified geological map of the Kuqa Basin [41].

intensities of these elements remain high for 7 s, indicating that there is abundant fluid available for ablation and that the inclusion is large.

4. Results

Approximately 15% of single-phase liquid fluid inclusions generated artificial nucleation vapor bubbles after cooling. In total, 220 T_h values were measured from artificially nucleated vapor bubbles in primary halite crystals from borehole DZK01 (Table 1) and the T_h values of the four stratigraphic intervals range from 11.1 to 47.1°C (S4, 1363 m), 13.2 to 52.3°C (S3, 1373 m), 15.3 to 36.2°C (S2,1382 m), and 9.4 to 54.1°C (S1, 1470 m). The corresponding average T_h values are 27.2°C, 31.2°C, 23.2°C, and 30.5°C. In this paper, each inclusion-rich band is regarded as an individual fluid inclusion assemblage (FIA) [46], showing that all primary fluid inclusions near the FIA formed almost simultaneously. The T_h range within each FIA is within 15°C, and 84% of FIAs have a range of less than 10°C. The T_h range measured within all FIAs yields an average value of 8.0°C, with a maximum value of 11.7°C and a minimum value of 4.6°C.

The chemical compositions of 22 fluid inclusions from 10 rock salt samples were determined by LA-ICP-MS (Table 2), and their sizes ranged from $\sim 30 \times 20\ \mu$m to $80 \times 30\ \mu$m. The chemical compositions of fluid inclusions in the same sample are quite different. Based on petrographic observations under the microscope, they come from different halite crystals in the same sample and information on paleobrine from different stages is captured during halite crystallization, such as the no. 18 and no. 19 fluid inclusions.

5. Discussion

5.1. Reliability and Stability of T_h Data. Damage or recrystallization occurs easily during burial and at depth due to the

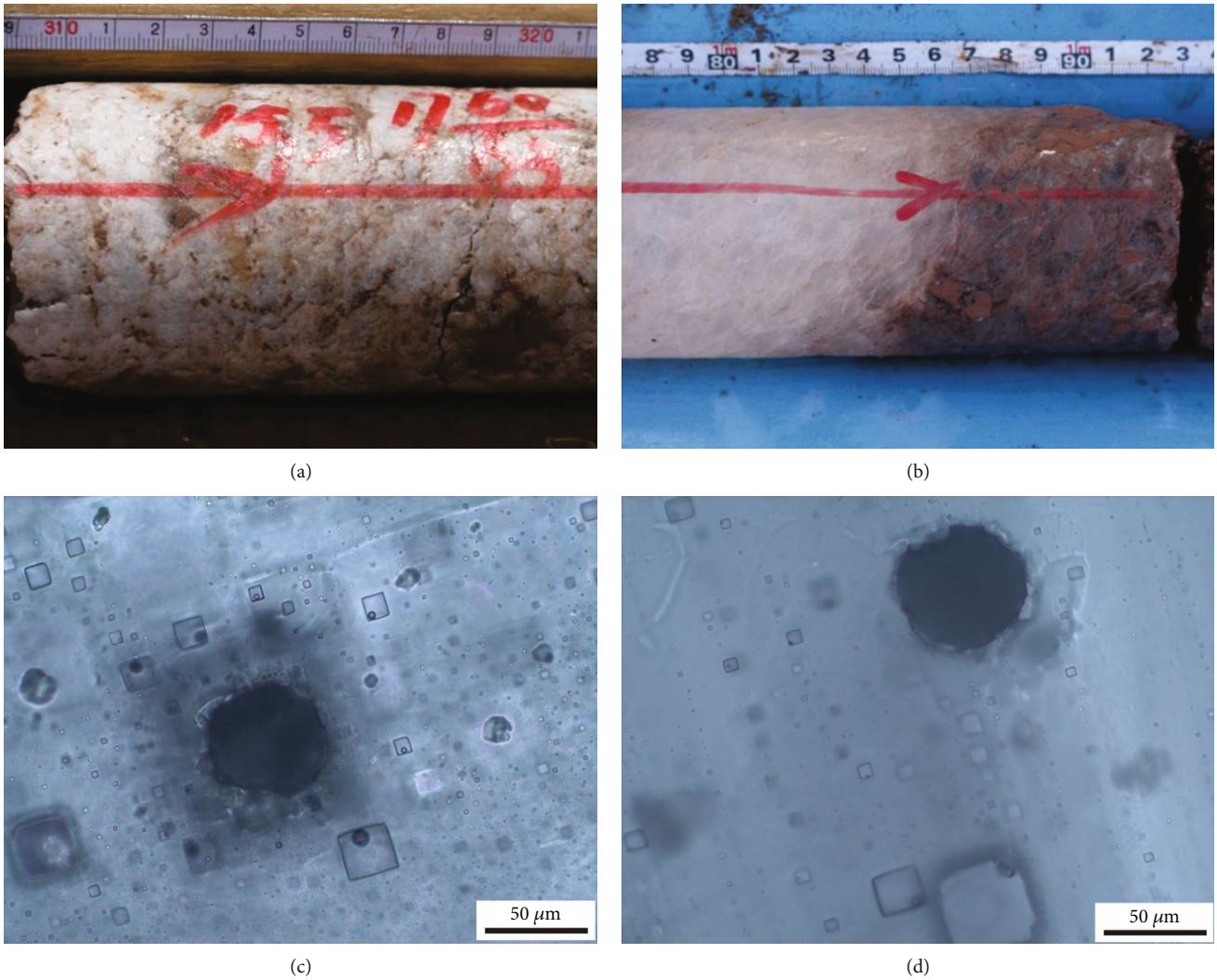

Figure 3: Characteristics of evaporite lithology and halite fluid inclusions from borehole DZK01 in the Kuqa Basin. (a) Gypsum rock with maroon boulder clay; (b) pure rock salt and rock salt with maroon boulder clay; (c, d) primary band-like fluid inclusions developed along growth faces of halite crystals and pits left on the surface of halite after laser ablation.

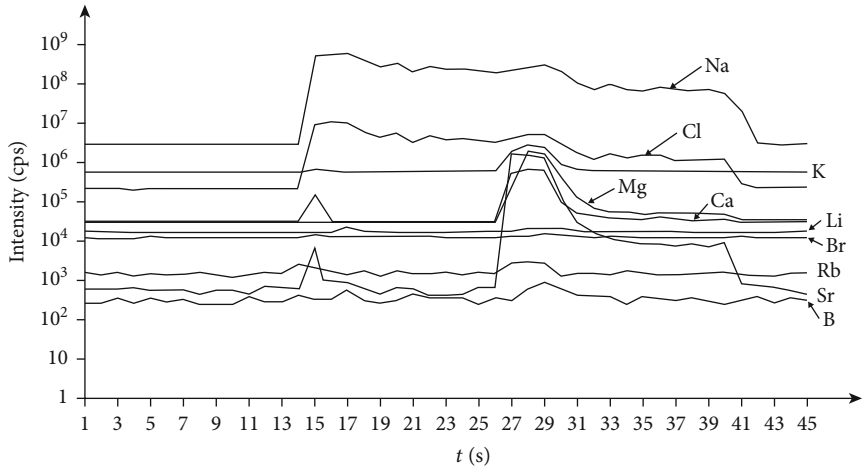

Figure 4: Mass spectral signal intensity versus time for a single fluid inclusion in halite (no. 4 fluid inclusion from 1385 m).

Table 1: T_h (°C) of middle Eocene halite primary fluid inclusions in borehole DZK01, Kuqa Basin.

Sample	Depth (m)	T_h (°C)/size (μm)	T_{hMAX} (°C)	T_{hMIN} (°C)	T_{hAVG} (°C)	T_{hRANGE} (°C)
S1	1363		47.1	11.1	27.2	
	FIA 1	11.1/16; 13.8/15; 14.1/29; 16.4/28; 17.2/28; 17.8/24; 18.1/20; 18.8/22				7.7
	FIA 2	19.5/22; 20.1/26; 20.5/18; 20.8/8; 21.3/12; 21.5/13; 22.2/15; 22.4/36; 22.6/42; 23.8/8; 24.1/6; 24.1/29; 24.2/28; 24.9/15; 25.1/19				5.6
	FIA 3	22.8/19; 23.7/10; 24.4/32; 24.6/16; 24.7/25; 28.3/22; 28.4/19; 28.5/28; 28.6/31; 28.7/30				5.9
	FIA 4	25.6/18; 26.3/33; 26.5/34; 26.7/20; 29.2/31; 30.2/21; 30.2/28; 30.3/20; 31.3/18				5.7
	FIA 5	30.8/16; 31.2/16; 31.5/17; 31.5/15; 31.6/19; 31.7/25; 31.7/15; 32.3/10; 33.2/18; 33.6/14; 33.8/10; 35.4/26				4.6
	FIA 6	37.2/10; 37.3/11; 39.9/16; 41.6/15; 42.7/23; 44.8/29; 47.1/18				9.9
S2	1373		52.3	13.2	31.2	
	FIA 1	13.2/27; 14.5/26; 14.6/23; 15.1/20; 15.5/19; 19.5/14; 21.2/34; 22.1/38				8.9
	FIA 2	20.8/18; 21.0/10; 23.4/41; 28.9/28; 29.5/27; 29.6/24; 29.6/23				8.8
	FIA 3	29.1/16; 29.8/25; 34.1/28; 34.2/12; 34.5/13; 35.1/18; 35.2/16				6.1
	FIA 4	35.3/26; 38.1/28; 38.1/23; 38.4/16; 45.6/20				10.3
	FIA 5	42.6/14; 45.8/7; 46.4/22; 47.6/19; 49.2/15; 52.3/31				9.7
S3	1382		36.2	15.3	23.2	
	FIA 1	15.3/24; 16.3/10; 16.4/9; 16.4/35; 16.6/33; 16.7/24; 17.2/26; 17.5/23; 17.6/18; 17.8/14; 18.4/10; 18.8/27; 19.1/28; 19.3/28; 19.5/25; 19.6/17; 19.6/16; 19.8/27; 20.5/8; 20.8/11; 22.3/19; 22.8/24; 23.8/25				8.5
	FIA 2	24.3/12; 24.3/18; 24.5/31; 24.8/48; 25.1/26; 26.1/27; 26.2/16; 27.3/29; 27.6/33; 31.4/15				7.1
	FIA 3	28.9/15; 31.2/14; 31.6/31; 31.6/32; 31.6/18; 32.7/26; 32.8/28; 36.2/20				7.3
S4	1470		54.1	9.4	30.5	
	FIA 1	9.4/24; 10.2/23; 14.5/25; 15.6/28; 15.7/12; 16.2/20; 16.3/28; 16.7/24; 17.3/33; 17.5/38; 17.8/36; 19.5/31; 20.7/46; 20.8/41; 21.1/27				11.7
	FIA 2	22.1/35; 22.2/24; 22.8/28; 23.1/24; 24.1/26; 24.3/15; 25.1/24; 25.9/16; 26.1/26; 26.2/17; 26.3/25; 26.5/26; 26.7/33; 27.2/37; 27.2/35; 27.8/26; 27.8/8; 28.1/8; 28.2/7; 28.5/24; 29.3/18; 29.3/23; 29.4/25; 30.1/29				8.0
	FIA 3	28.6/25; 28.9/15; 29.1/19; 30.2/38; 30.2/44; 30.3/35; 30.4/21; 30.5/20; 31.1/17; 31.7/22; 31.9/28; 32.4/23; 32.4/14; 32.5/15; 32.7/22; 32.8/10; 33.2/33; 34.5/29; 34.6/14; 35.4/41; 36.1/18; 36.4/22; 36.5/31; 36.6/27; 36.8/20; 37.6/31; 37.8/15; 38.1/24				5.7
	FIA 4	35.5/37; 35.6/34; 35.8/36; 38.4/16; 38.5/28; 40.8/24; 41.6/35; 41.8/10; 42.1/18; 44.8/27; 46.1/16; 46.1/28				10.6
	FIA 5	44.5/20; 45.3/26; 46.4/24; 47.6/23; 52.4/20; 54.1/29				9.6

T_{hMAX}: maximum homogenization temperature; T_{hMIN}: minimum homogenization temperature; T_{hAVG}: average homogenization temperature; T_{hRANGE}: range of T_h data; FIA: fluid inclusion assemblage.

deliquescent and solubility nature of rock salt and can affect the reliability and stability of T_h data, especially for ancient rock salt samples. The T_h data do not require pressure correction because rock salt forms in a shallow depositional environment and the temperatures captured by fluid inclusions under low-pressure conditions are approximately equal to T_h, thus providing a direct record of temperature during rock salt deposition. Primary fluid inclusions from the same inclusion growth band were captured contemporaneously [45]. However, multiple inclusion bands in primary halite crystals were not formed contemporaneously. Therefore, T_h data obtained from different inclusion bands are also diverse [45].

We use two methods to verify whether primary fluid inclusions have undergone damage or alteration from thermal reequilibration: thermal reequilibration analysis of the T_h data and evaluation of the relationship between the size and T_h of fluid inclusions. On the one hand, the consistency of the T_h data from individual FIAs can be used as an indicator for evaluating thermal reequilibration [45]. Goldstein and Reynolds [46] noted that approximately 90% of T_h data in individual FIAs have a fluctuation range of less than 15°C, indicating that primary fluid inclusions have not undergone alteration from thermal reequilibration. The T_h data in this paper meet this criterion (Table 1), as the temperature ranges of all T_h data from 19 FIAs are less than 15°C, with a minimum of 4.6°C and a maximum of 11.7°C. Therefore, the halite crystals have not been affected by thermal reequilibration. Furthermore, the relationship between the size and T_h of fluid inclusions can be used as another indicator to determine whether fluid inclusions have been affected by thermal

Table 2: Ion concentrations in halite fluid inclusions from borehole DZK01 in the Kuqa Basin.

Depth (m)	Inclusion no.	ρ (B)/(g/L)			ρ (B)/(mg/L)				
		K^+	Ca^{2+}	Mg^{2+}	Li^+	B^+	Rb^+	Sr^{2+}	Br^-
1370	1	0.23	1.16	0.42	0.12	1.62	0.44	23.52	12.64
1373	2	0.11	4.21	0.19	0.86	2.60	0.00	138.08	12.56
1374	3	0.12	0.17	0.13	0	0.98	0.07	4.74	2.55
1385	4	0.47	0.06	0.09	0.05	0.75	0.31	0.80	5.08
1415	5	0.26	3.09	0.53	1.80	1.18	0.15	115.89	10.33
1435	6	1.25	0.06	0.06	0.55	1.76	3.35	0.66	15.25
	7	0.30	0.04	0.03	1.23	0.52	1.94	0.54	6.41
	8	0.28	0.02	0.02	0.44	0.16	0.38	0.11	3.11
1436	9	0.27	0.02	0.01	0.06	0.07	0.26	0.16	6.06
	10	0.12	0.22	0.08	0.52	0.18	0.06	7.56	3.35
	11	0.07	0.05	0.05	0.27	0.19	0.13	0.94	4.72
1469	12	0.34	0.35	0.16	0.40	0.27	0.09	7.56	2.83
	13	0.10	0.65	0.10	0.04	0.12	0.05	17.39	3.65
1476	14	0.12	0.23	0.01	0.01	0.44	0.08	0.10	18.00
	15	0.27	0.68	0.13	0.15	0.04	0.05	15.62	7.45
	16	0.22	0.02	0.01	0.22	0.27	0.18	0.25	2.53
	17	0.14	0.78	0.20	0.44	0.16	0.04	16.17	4.07
	18	0.41	2.54	0.57	0.52	0.40	0.20	72.34	11.49
	19	3.07	0.46	0.86	6.67	34.09	10.62	3.32	48.52
	20	2.91	0.31	0.52	2.21	11.53	4.10	1.40	53.13
1478	21	0.71	0.11	0.15	0.37	2.65	0.40	0.84	7.05
	22	0.13	0.85	0.05	0.12	0.08	0.13	24.02	4.21

reequilibration. Large inclusions are more extendable than small inclusions, and fluid inclusions undergoing extension have a higher T_h than the original temperature at the time of formation [47]. In other words, if inclusions have undergone extension, large inclusions are more likely to produce higher T_h values than small inclusions. Our results show that there is no correlation between the size of fluid inclusions and the corresponding T_h (Figure 5). Therefore, thermal reequilibration did not alter or damage halite crystals, which further supports the rationality and stability of the T_h data. The T_h data from middle Eocene rock salt from borehole DZK01 may accurately reflect the brine temperatures during salt formation.

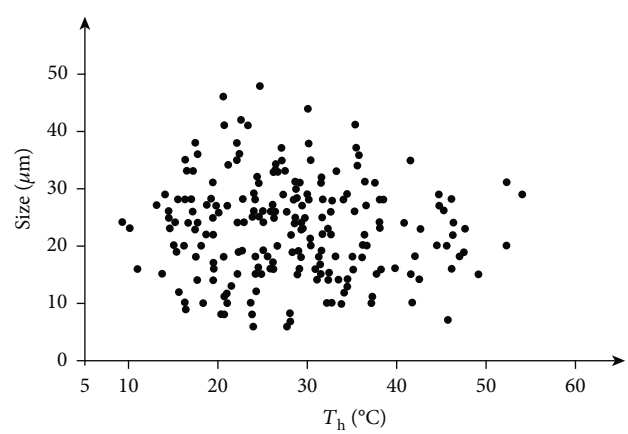

Figure 5: Crossplot of the T_h data against the size of fluid inclusions.

5.2. Significance of Paleobrine Temperature. The temperature of the brine during the salt-forming period can be directly and quantitatively reconstructed from the T_h values of halite fluid inclusions [15, 16, 48]. In addition, previous studies on modern salt lakes and laboratory halite crystals have shown that the highest T_h values of halite fluid inclusions are approximately equal to the highest brine temperature during the halite crystallization process [14, 45, 49]. Our results show that the T_h values of the 4 salt-bearing intervals are generally high (Figure 6), with an average value of 28.3°C and a maximum temperature of 54.1°C, which represent the average and high-temperature brine characteristics in the Kuqa Basin in the middle Eocene. Bougeois et al. [50] conducted a study on marine oyster fossils in the southwestern part of the Tarim Basin and showed that the average sea surface temperature during the middle Eocene was approximately 27–28°C. Therefore, the evidence supports our inference based on T_h data and indicates that our T_h data in the middle Eocene Kuqa Basin are reliable and reasonable.

Zhao et al. [17] studied halite fluid inclusions from 8 salt-bearing basins in China and other countries and used the T_h

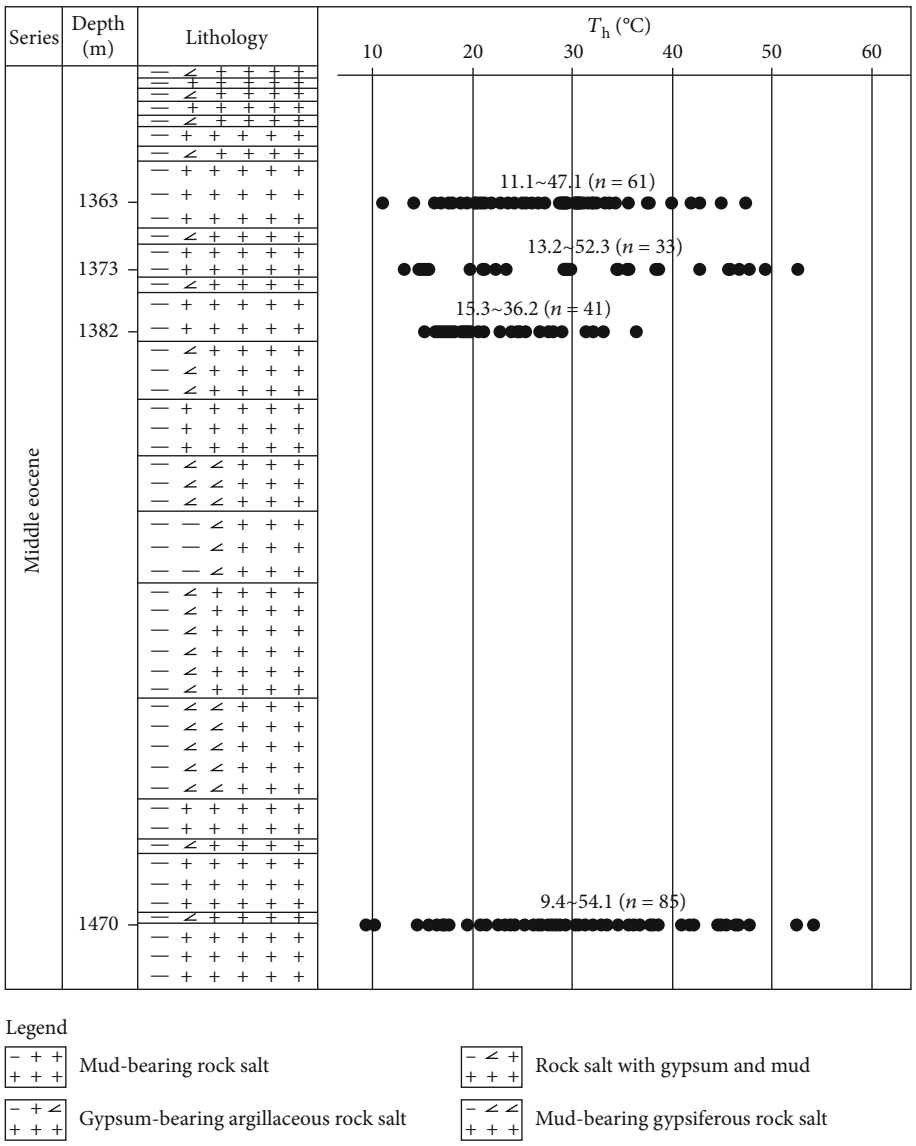

Figure 6: T_h data characteristics of primary fluid inclusions from middle Eocene halite in borehole DZK01, Kuqa Basin.

values to estimate the evaporation rate of ancient salt lakes, and the results showed that extremely high-temperature conditions (water and air temperatures) are conducive to rapidly concentrating salt lake brine, shortening the time interval from salt formation to potash formation, which is beneficial to the formation of potash deposits. Liu et al. [51] proposed that a hot and dry climate is a prerequisite for potash formation by ancient salt lake evaporation. The formation of many ancient and modern potash deposits is closely related to high-temperature paleobrine environments. For example, the highest paleobrine temperature of potash deposits in the Silurian Michigan Basin is 59°C [52], the highest paleobrine temperature of potash deposits in the Middle Cretaceous Korat Plateau is 62.1°C [53], and the highest paleobrine temperature of Quaternary Lop Nur potash deposits in the Tarim Basin is 58°C [54]. Therefore, the high-temperature conditions experienced during the middle Eocene salt-forming period in the Kuqa Basin may indicate relatively rapid evaporation rates. Moreover, potassium minerals, such as sylvite, carnallite, and syngenite, have been discovered in this stratum [55], indicating that the salt lake brine experienced high degrees of evaporation and concentration under the high-temperature conditions required for potash formation.

5.3. Significance of the Chemical Composition of Paleobrine. The elements K and Rb and the elements Sr and Ca have similar chemical properties, and they often displace each other in an isomorphic manner during continuous evaporation and the concentration of salt-forming brine. In addition, K is positively correlated with Mg and Br [56, 57]. Therefore, the linear relationships between K^+ and Mg^{2+}, K^+ and Rb^+, K^+ and Br^-, and Ca^{2+} and Sr^{2+} are often used to indicate the reliability of measured data [23, 58]. The ion concentrations that we tested showed good positive correlations (Figure 7), conforming to the evaporation and concentration patterns

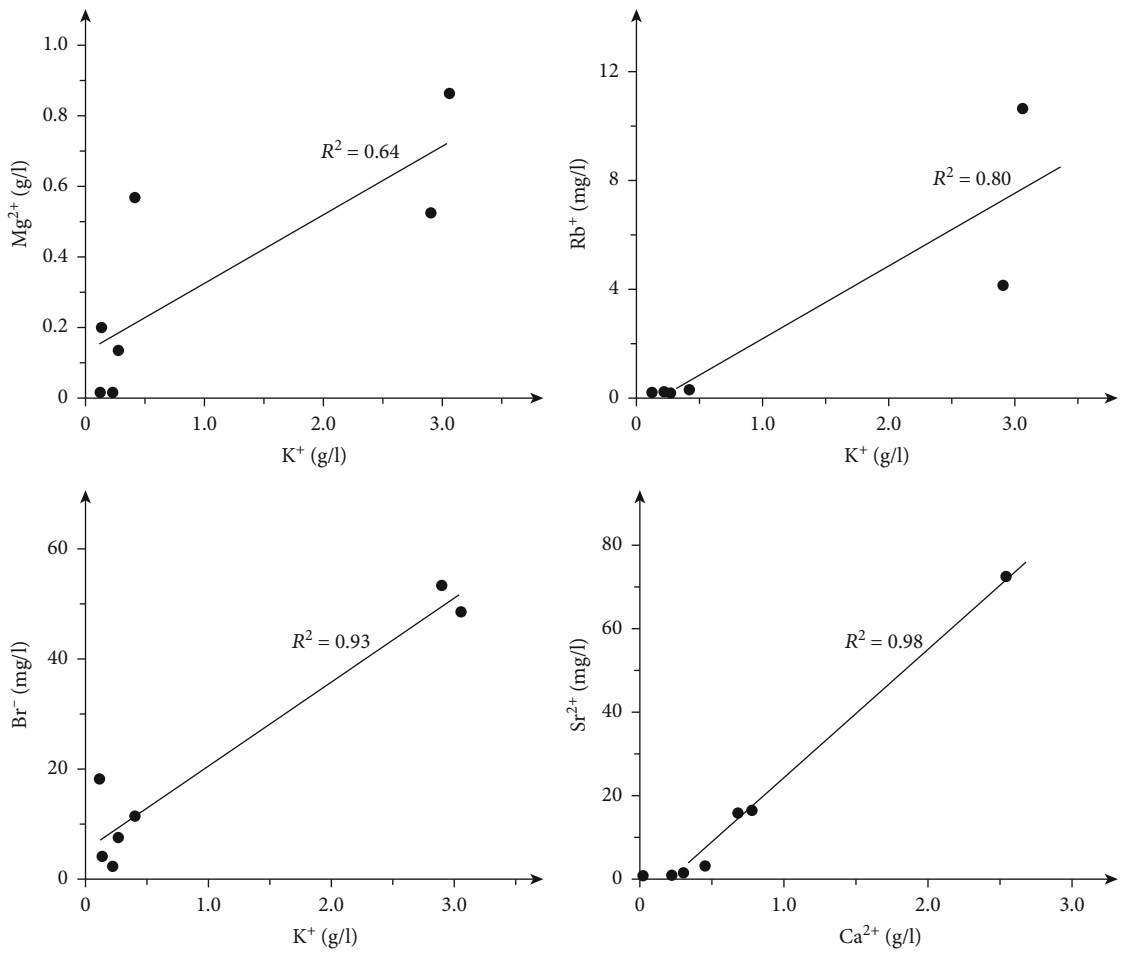

Figure 7: The relationships between K^+ and Mg^{2+}, Rb^+ and Br^-, and Sr^{2+} and Ca^{2+} in halite fluid inclusions from 1476 m in borehole DZK01.

of salt lake brine, indicating that our data have good reliability and validity.

The chemical compositions of halite fluid inclusions are characterized by high Ca^{2+} and Sr^{2+} concentrations, which may be due to the supply of terrestrial fresh water involved in the salinization process. Zhang et al. [12] and Xu et al. [59] systematically analyzed the carbon, oxygen, sulfur, and strontium isotope compositions of middle Eocene carbonate rocks and sulfate rocks and found that the provenance in the salt-forming environment was mostly a mixture of marine and continental sediments. The Br^- data from that study are compared with the chemical analysis results for the rock salt from borehole DZK01 [60], and the Br^- content in the latter is lower than the detection limit, whereas the Br^- content in the former is higher than the detection limit. This pattern is determined by the chemical properties of Br because Br rarely enters the crystal lattice of salt minerals but is present mainly in the form of brine.

The concentrations of other ions in the no. 19 and no. 20 fluid inclusions from the 1476 m halite sample are all the maximum values except for Ca^{2+} and Sr^{2+}; there are two reasons for this. On the one hand, salt lake brine generally undergoes evaporative concentration and desalination caused by the mixing of external water bodies during the evolution process. At 1476 m, the brine evaporates and evolves to a higher concentration stage and the concentrations of K^+, Mg^{2+}, Rb^+, and Br^- increase accordingly. In addition, a previous work discovered potassium minerals at 1476 m at the bottom of the borehole, which also confirmed the high degrees of evaporation and concentration of brine. On the other hand, due to the large sample collection interval, these ion concentrations did not show a good transitional relationship, indicating that the ion concentrations of inclusion nos. 19 and 20 differ greatly from those of other inclusions. The K^+ concentrations in the no. 19 and no. 20 fluid inclusions reach 3.07 g/L and 2.91 g/L, respectively, corresponding to KCl contents of 0.59% and 0.56%, respectively. Li et al. [61], based on the "specifications for salt lakes, salt mineral exploration (DZ/T0212—2002),", systematically collected recent survey results and research data on potassium-rich brine and summarized and determined the lowest industrial grade of potassium-rich brine (KCl ≥ 0.5%). It can be inferred that the evolution phase of ancient brine in the basin reached the stage of potash formation. In addition, Wu et al. [60] conducted a chemical analysis of rock salt samples from different depths in borehole DZK01 and showed that the rock salt at the bottom of the borehole has a high content of K^+, with a maximum of 0.34%. Xu et al. [55] studied the hydrogen and oxygen isotopes of primary fluid inclusions in halite

from borehole DZK01 and found that the salt-bearing strata at the bottom of the borehole had experienced a high degree of evaporation and that large amounts of potassium minerals precipitated. The interval that has good potential for potassium mineral formation is inferred to have good potential for potash formation. This is consistent with the K^+ concentration characteristics of halite fluid inclusions studied in this paper and further shows that brine had high degrees of evaporation and concentration in the early salt-forming period and reached the potassium-forming stage.

6. Conclusions

(1) The T_h data of measured primary halite fluid inclusions are accurate and reasonable, and these data can quantitatively reconstruct the temperature of salt-forming brine in the Kuqa Basin in the middle Eocene. The T_h of 220 fluid inclusions ranges from 9.4 to 54.1°C, reflecting a high-temperature brine environment that was conducive to the rapid deposition of potassium minerals

(2) The KCl content of salt-forming brine at the bottom of the borehole can reach up to 0.59%, which is higher than the lowest industrial grade of potassium-rich brine KCl (0.5%). Combined with previous research work, these results further show that salt-forming brine had high degrees of evaporation and concentration and reached the potash-forming stage

Data Availability

The data used to support the findings of this study are available from the corresponding authors upon request.

Conflicts of Interest

The authors declare that they have no conflicts of interest.

Acknowledgments

This study was supported by the National Natural Science Foundation of China (Grant no. 41902064) and the Scientific Research Foundation for PhD, East China University of Technology (Grant no. DHBK2018029) and an independent fund from the State Key Laboratory of Nuclear Resources and Environment (Grant no. 2020Z11).

References

[1] J. K. Warren, "Evaporites through time: Tectonic, climatic and eustatic controls in marine and nonmarine deposits," *Earth Science Reviews*, vol. 98, no. 3-4, pp. 217–268, 2010.

[2] Q. Liu, Y. H. Chen, Y. C. Li, Q. C. Lan, H. R. Yuan, and D. L. Yan, *Meso-Cenozoic terrigenous clastic rock-chemical rock salt deposits in China*, Beijing Science and Technology Press, Beijing, 1987.

[3] C. L. Liu, P. C. Jiao, Z. Q. Xuan, Y. T. Cao, and X. F. Zhao, "Paleogene potash mineral advances of evaporites in Kuqa Basin," *Geological Review*, vol. 59, no. 2, pp. 233-234, 2013.

[4] Y. Xu, C. L. Liu, P. C. Jiao, Y. Z. Chen, and Y. T. Cao, "Geochemical characteristics and potash formation analysis of Paleocene-Eocene evaporites in Kuqa depression of Xinjiang: a case study of borehole KL4," *Acta Petrologica et Mineralogica*, vol. 36, no. 5, pp. 755–764, 2017.

[5] C. L. Liu, Y. J. Zhao, X. M. Fang et al., "Plate tectonics control on the distribution and formation of the marine potash deposits," *Acta Geoligca Sinica*, vol. 89, no. 11, pp. 1893–1907, 2015.

[6] P. N. Pearson and M. R. Palmer, "Atmospheric carbon dioxide concentrations over the past 60 million years," *Nature*, vol. 406, no. 6797, pp. 695–699, 2000.

[7] M. Pagani, J. C. Zachos, K. H. Freeman, B. Tipple, and S. Bohaty, "Marked decline in atmospheric carbon dioxide concentrations during the Paleogene," *Science*, vol. 309, no. 5734, pp. 600–603, 2005.

[8] J. C. Zachos, G. R. Dickens, and R. E. Zeebe, "An early Cenozoic perspective on greenhouse warming and carbon-cycle dynamics," *Nature*, vol. 451, no. 7176, pp. 279–283, 2008.

[9] P. F. Sexton, R. D. Norris, P. A. Wilson et al., "Eocene global warming events driven by ventilation of oceanic dissolved organic carbon," *Nature*, vol. 471, no. 7338, pp. 349–352, 2011.

[10] J. X. Xu, H. Z. Ma, Y. K. Xiao et al., "Stable chlorine isotope and its research on applied geochemistry," *Journal of Salt Lake Research*, vol. 16, no. 1, pp. 51–59, 2008.

[11] Y. T. Cao, H. J. Yang, C. L. Liu, Q. Y. Gu, P. C. Jiao, and Y. H. Lu, "Response on sediment of evaporate in Kuqa Basin from Paleogene to Neogene period and Himalayan tectonic phase," *Acta Sedimentologica Sinica*, vol. 28, no. 6, pp. 1054–1065, 2010.

[12] H. Zhang, C. L. Liu, Y. T. Cao, H. W. Sun, and L. C. Wang, "A tentative discussion on the time and the way of marine regression from Tarim Bay during the Cenozoic," *Acta Geoscientica Sinica*, vol. 34, no. 5, pp. 577–584, 2013.

[13] S. M. Roberts and R. J. Spence, "Paleotemperatures preserved in fluid inclusions in halite," *Geochimica et Cosmochimica Acta*, vol. 59, no. 19, pp. 3929–3942, 1995.

[14] T. K. Lowenstein, J. Li, and C. B. Brown, "Paleotemperatures from fluid inclusions in halite: method verification and a 100,000 year paleotemperature record, Death Valley, CA," *Chemical Geology*, vol. 150, no. 3-4, pp. 223–245, 1998.

[15] J. J. Zambito IV and K. C. Benison, "Extremely high temperatures and paleoclimate trends recorded in Permian ephemeral lake halite," *Geology*, vol. 41, no. 5, pp. 587–590, 2013.

[16] H. Zhang, F. Lü, S. Mischke, M. Fan, F. Zhang, and C. Liu, "Halite fluid inclusions and the late Aptian sea surface temperatures of the Congo Basin, northern South Atlantic Ocean," *Cretaceous Research*, vol. 71, pp. 85–95, 2017.

[17] Y. J. Zhao, C. L. Liu, H. Zhang, Z. Q. Li, T. Ding, and M. Q. Wang, "The control of paleotemperature on potassium salt precipitation in ancient salt lakes," *Acta Petrologica Sinica*, vol. 31, no. 9, pp. 2751–2756, 2015.

[18] M. Q. Wang, Y. J. Zhao, C. L. Liu, and T. Ding, "Paleotemperature and sinificance of the evaporated seawater in salt-forming process of the forth member of Jialingjiang Formation in the eastern Sichuan Basin," *Acta Petrologica Sinica*, vol. 31, no. 9, pp. 2745–2750, 2015.

[19] T. K. Lowenstein, M. N. Timofeeff, S. T. Brennan, L. A. Hardie, and R. V. Demicco, "Oscillations in Phanerozoic seawater chemistry: evidence from fluid inclusions," *Science*, vol. 294, no. 5544, pp. 1086–1088, 2001.

[20] M. G. Siemann and B. Ellendorff, "The composition of gases in fluid inclusions of late Permian (Zechstein) marine evaporites in Northern Germany," *Chemical Geology*, vol. 173, no. 1-3, pp. 31–44, 2001.

[21] D. I. Cendón, C. Ayora, J. J. Pueyo, C. Taberner, and M. M. Blanc-Valleron, "The chemical and hydrological evolution of the Mulhouse potash basin (France): are "marine" ancient evaporites always representative of synchronous seawater chemistry?," *Chemical Geology*, vol. 252, no. 3-4, pp. 109–124, 2008.

[22] T. K. Lowenstein, L. A. C. Dolginko, and J. García-Veigas, "Influence of magmatic-hydrothermal activity on brine evolution in closed basins: Searles Lake, California," *Geological Society of America Bulletin*, vol. 128, no. 9-10, pp. 1555–1568, 2014.

[23] X. H. Sun, Y. F. Hu, C. L. Liu et al., "Argument that brine of salty lake in Sichuan Basin had reached crystallizing point of potash minerals during Triassic: evidence from chemical composition of fluid inclusions in halite," *Mineral Deposits*, vol. 35, no. 6, pp. 1157–1168, 2016.

[24] R. Bosboom, G. Dupontnivet, A. Grothe, H. Brinkhuis, and G. Villa, "Linking Tarim Basin sea retreat (West China) and Asian aridification in the late Eocene," *Basin Research*, vol. 26, no. 5, pp. 621–640, 2014.

[25] A. Yin, P. E. Rumelhart, R. Butler et al., "Tectonic history of the Altyn Tagh fault system in northern Tibet inferred from Cenozoic sedimentation," *Geological Society of America Bulletin*, vol. 114, no. 10, pp. 1257–1295, 2002.

[26] H. B. Zheng, R. Tada, J. T. Jia, C. Lawrence, and K. Wang, "Cenozoic sediments in the southern Tarim Basin: implications for the uplift of northern Tibet and evolution of the Taklimakan Desert," *Geological Society, London, Special Publications*, vol. 342, no. 1, pp. 67–78, 2010.

[27] J. M. Sun, B. Windley, Z. L. Zhang, B. H. Hu, and S. H. Li, "Diachronous seawater retreat from the southwestern margin of the Tarim Basin in the late Eocene," *Journal of Asian Earth Sciences*, vol. 116, pp. 222–231, 2016.

[28] B. Carrapa, P. G. De Celles, X. Wang et al., "Tectono-climatic implications of Eocene Paratethys regression in the Tajik basin of central Asia," *Earth and Planetary Science Letters*, vol. 424, pp. 168–178, 2015.

[29] J. M. Sun, W. G. Liu, Z. H. Liu, and B. H. Fu, "Effects of the uplift of the Tibetan Plateau and retreat of Neotethys Ocean on the stepwise aridification of mid-latitude Asian interior," *Bulletin of the Chinese Academy of Sciences*, vol. 26, no. 9, pp. 39–46, 2017.

[30] X. Chen, H. Chen, X. Lin et al., "Arcuate Pamir in the Paleogene? Insights from a review of stratigraphy and sedimentology of the basin fills in the foreland of NE Chinese Pamir, western Tarim Basin," *Earth-Science Reviews*, vol. 180, pp. 1–16, 2018.

[31] H. A. Abels, G. Dupont-Nivet, G. Xiao, R. Bosboom, and W. Krijgsman, "Step-wise change of Asian interior climate preceding the Eocene-Oligocene Transition (EOT)," *Palaeogeography, Palaeoclimatology, Palaeoecology*, vol. 299, no. 3-4, pp. 399–412, 2011.

[32] J. Dercourt, L. E. Ricou, and B. Vrielynck, *Atlas Tethys Paleoenvironmental Maps: Expanatory Notes*, Gauthiervillars, Paris, 1993.

[33] H. Z. Wang, *Atlas of the paleogeography of China*, China Cartographic Publishing House, Beijing, 1985.

[34] S. A. Graham, M. S. Hendrix, L. B. Wang, and A. R. Carroll, "Collisional successor basins of Western China: impact of tectonic inheritance on sand composition," *Geological Society of America Bulletin*, vol. 105, no. 3, pp. 323–344, 1993.

[35] L. Huafu, D. G. Howell, J. Dong et al., "Rejuvenation of the Kuqa Foreland Basin, northern flank of the Tarim Basin, Northwest China," *International Geology Review*, vol. 36, no. 12, pp. 1151–1158, 1994.

[36] Y. M. Zhang, G. Z. He, and Z. R. Wang, "Analysis of the tertiary salt rock system and potassium fertilizer in Kuqa Basin," *Northwestern Geology*, vol. 26, no. 4, pp. 44–52, 1982.

[37] M. Zheng and Z. F. Meng, "Magnetostratigraphy of tertiary system in Baicheng, Xinjiang," *Acta Sedimentologica Sinica*, vol. 24, no. 5, pp. 650–656, 2006.

[38] Z. H. Teng, L. P. Yue, D. F. He, X. Q. Deng, and X. W. Bian, "Magnetostratigraphic research of Cenozoic section of Kuche River area, South Xinjiang," *Journal of Stratigraphy*, vol. 21, no. 1, pp. 55–62, 1997.

[39] Z. Li, Q. C. Wang, D. X. Wang, and W. Lin, "Depositional record constraints on Late Cenozoic uplift of Tianshan and tectonic transformation in Kuqa Depression, West China," *Acta Sedimentologica Sinica*, vol. 21, no. 1, pp. 38–45, 2003.

[40] Y. T. Cao, C. L. Liu, H. J. Yang, Q. Y. Gu, P. C. Jiao, and Y. H. Lu, "Identification and correlation of the Paleogene and Neogene evaporites sedimentary cycles in Kuqa Basin, Xinjiang," *Journal of Palaeogeography*, vol. 12, no. 1, pp. 31–41, 2010.

[41] Y. Xu, C. L. Liu, Y. T. Cao, and H. Zhang, "Quantitative temperature recovery from middle Eocene halite fluid inclusions in the easternmost Tethys realm," *International Journal of Earth Sciences*, vol. 108, no. 1, pp. 173–182, 2019.

[42] M. Y. Hu, H. L. He, X. C. Zhan, X. T. Fan, G. Wang, and Z. R. Jia, "Matrix normalization for in-situ multi-element quantitative analysis of zircon in Laser Ablation-Inductively Coupled Plasma Mass Spectrometry," *Chinese Journal of Analytical Chemistry*, vol. 36, no. 7, pp. 947–953, 2008.

[43] X. H. Sun, M. Y. Hu, C. L. Liu et al., "Composition determination of single fluid inclusions in salt minerals by laser ablation ICP-MS," *Chinese Journal of Analytical Chemistry*, vol. 41, no. 2, pp. 235–241, 2013.

[44] H. P. Longerich, S. E. Jackson, and D. Gunther, "Inter-laboratory note. Laser ablation inductively coupled plasma mass spectrometric transient signal data acquisition and analyte concentration calculation," *Journal of Analytical Atomic Spectrometry*, vol. 11, no. 9, pp. 899–904, 1996.

[45] K. C. Benison and R. H. Goldstein, "Permian paleoclimate data from fluid inclusions in halite," *Chemical Geology*, vol. 154, no. 1-4, pp. 113–132, 1999.

[46] R. H. Goldstein and T. J. Reynolds, "Systematics of fluid inclusions in diagenetic minerals," *Society for Sedimentary Geology*, vol. 26, no. 1, pp. 23–47, 1994.

[47] E. Roedder, "The fluids in salt," *American Mineralogist*, vol. 69, no. 5, pp. 413–439, 1984.

[48] Y.-j. Zhao, H. Zhang, C.-l. Liu, B.-k. Liu, L.-c. Ma, and L.-c. Wang, "Late Eocene to early Oligocene quantitative paleotemperature record: evidence from continental halite fluid inclusions," *Scientific Reports*, vol. 4, article 5776, 2014.

[49] X.-h. Sun, Y.-j. Zhao, C.-l. Liu, P.-c. Jiao, H. Zhang, and C.-h. Wu, "Paleoclimatic information recorded in fluid inclusions in halites from Lop Nur, Western China," *Scientific Reports*, vol. 7, no. 1, article 16411, 2017.

[50] L. Bougeois, M. de Rafélis, G. J. Reichart, L. J. de Nooijer, F. Nicollin, and G. Dupont-Nivet, "A high resolution study of trace elements and stable isotopes in oyster shells to estimate Central Asian Middle Eocene seasonality," *Chemical Geology*, vol. 363, pp. 200–212, 2014.

[51] C. L. Liu, Z. Q. Xuan, Y. T. Cao et al., "Research on potash exploration at China land mass—potash alteration and pattern of eastern Tethys Ocean, China," *Geology of Chemical Minerals*, vol. 37, no. 4, pp. 193–197, 2015.

[52] A. B. Losey and K. C. Benison, "Silurian paleoclimate data from fluid inclusions in the Salina Group halite Michigan Basin," *Carbonates Evaporites*, vol. 15, pp. 28–36, 2000.

[53] H. Zhang, C. Liu, Y. Zhao, S. Mischke, X. Fang, and T. Ding, "Quantitative temperature records of mid Cretaceous hothouse: evidence from halite fluid inclusions," *Palaeogeography, Palaeoclimatology, Palaeoecology*, vol. 437, pp. 33–41, 2015.

[54] C. L. Liu, Y. Z. Chen, W. S. Chen, P. C. Jiao, M. L. Wang, and S. D. Li, "Studies of fluid inclusions in glauberite of middle-upper Pleistocene strata and their paleoclimatic significance in Lop Nur salty lake, Xinjiang, NW China," *Acta Mineralogica Sinica*, vol. 26, no. 1, pp. 93–98, 2006.

[55] Y. Xu, Y. T. Cao, C. L. Liu, and P. C. Jiao, "Provenance and degree of evaporation and concentration of Eocene salt lake in the Kuqa Basin," *Acta Geologica Sinica*, vol. 92, no. 8, pp. 1617–1629, 2018.

[56] P. D. Deckker, A. R. Chivas, J. M. G. Shelley, and T. Torgersen, "Ostracod shell chemistry: a new palaeoenvironmental indicator applied to a regressive/transgressive record from the gulf of Carpentaria, Australia," *Palaeogeography Palaeoclimatology Palaeoecology*, vol. 66, no. 3-4, pp. 231–241, 1988.

[57] H. T. You, R. H. Cheng, and C. L. Liu, "Review of Paleosalinity recovering methods," *World Geology*, vol. 21, no. 2, pp. 111–117, 2002.

[58] L. Shen, C. Liu, L. Wang, Y. Hu, M. Hu, and Y. Feng, "Degree of brine evaporation and origin of the Mengyejing potash deposit: evidence from fluid inclusions in halite," *Acta Geologica Sinica - English Edition*, vol. 91, no. 1, pp. 175–185, 2017.

[59] Y. Xu, Y. T. Cao, C. L. Liu, H. Zhang, and X. Nie, "The history of transgressions during the Late Paleocene-Early Eocene in the Kuqa Depression, Tarim Basin: constraints from C-O-S-Sr isotopic geochemistry," *Minerals*, vol. 10, no. 9, p. 834, 2020.

[60] K. Wu, C. L. Liu, P. C. Jiao et al., "Geochemical characteristics and ore-prospecting indicators of salt-bearing series in No.1 exploratory drill hole of Kuqa Basin, Xinjiang," *Mineral Deposits*, vol. 33, no. 5, pp. 1011–1019, 2014.

[61] B. Y. Li, X. L. Deng, F. Wang et al., "Types, exploration techniques and suggested industrial indexes of deep-seated potassium-rich brine," *Geology and Exploration*, vol. 55, no. 6, pp. 1426–1435, 2019.